

CHEMIA

**STUDIA
UNIVERSITATIS BABEȘ-BOLYAI
CHEMIA**

4/2013

EDITORIAL BOARD
STUDIA UNIVERSITATIS BABEȘ-BOLYAI
CHEMIA

ONORARY EDITOR:

IONEL HAIDUC - Member of the Romanian Academy

EDITOR-IN-CHIEF:

LUMINIȚA SILAGHI-DUMITRESCU

EXECUTIVE EDITOR:

CASTELIA CRISTEA

EDITORIAL BOARD:

PAUL ȘERBAN AGACHI, Babeș-Bolyai University, Cluj-Napoca, Romania

LIVAIN BREAU, UQAM University of Quebec, Montreal, Canada

HANS JOACHIM BREUNIG, Institute of Inorganic and Physical Chemistry,
University of Bremen, Bremen, Germany

MIRCEA DIUDEA, Babes-Bolyai University, Cluj-Napoca, Romania

JEAN ESCUDIE, HFA, Paul Sabatier University, Toulouse, France

ION GROSU, Babeș-Bolyai University, Cluj-Napoca, Romania

EVAMARIE HEY-HAWKINS, University of Leipzig, Leipzig, Germany

FLORIN DAN IRIMIE, Babeș-Bolyai University, Cluj-Napoca, Romania

FERENC KILAR, University of Pecs, Pecs, Hungary

BRUCE KING, University of Georgia, Athens, Georgia, USA

ANTONIO LAGUNA, Department of Inorganic Chemistry, ICMA, University of
Zaragoza, Zaragoza, Spain

JURGEN LIEBSCHER, Humboldt University, Berlin, Germany

KIERAN MOLLOY, University of Bath, Bath, UK

IONEL CĂTĂLIN POPESCU, Babeș-Bolyai University, Cluj-Napoca, Romania

CRISTIAN SILVESTRU, Babeș-Bolyai University, Cluj-Napoca, Romania

<http://chem.ubbcluj.ro/~studiachemia/>; studiachemia@chem.ubbcluj.ro
http://www.studia.ubbcluj.ro/serii/chemia/index_en.html

YEAR
MONTH
ISSUE

Volume 58 (LVIII) 2013
DECEMBER
4

S T U D I A
UNIVERSITATIS BABEȘ-BOLYAI
CHEMIA

4

Desktop Editing Office: 51ST B.P. Hasdeu, Cluj-Napoca, Romania, Phone + 40 264-40.53.52

CUPRINS – CONTENT – SOMMAIRE – INHALT

IULIA-MARIA BODEA, CĂLIN-CRISTIAN CORMOȘ, Applications of Chemical Looping Combustion to Energy Conversion Processes.....	7
CLAUDIU CRISTIAN BOTAR, Analysis of the Aerosol Transport and Topology of Their Deposit in the Lungs Via CFD Technique in Nonstationary Flow Conditions	23
CĂLIN I. ANGHEL, DANIELA J. CHELARU, Metamodeling Level of Pollution Based on Operating Parameters of a Thermo Power Station.....	41
SIMION DRĂGAN, Kinetic Analysis of Thermal Decomposition of the Limestone and Precipitate Calcium Carbonate	53
ADINA GHIRIȘAN, Settling of Coagulated Dilluted Yeast Suspensions	63
MARIA GOREA, IOANA OLIVIA RUJONI, NICOLAE HAR, MARCEL IOAN BENEĂ, Synthesis and Characterization of Cordierite for Diesel Filters	71
DANA-MARIA SABOU, IOAN BĂLDEA, On the Oxidation of Glutathione by Chromium (VI), in Aqueous Solutions of Perchloric Acid.....	81
ZSOLT TASNÁDI-ASZTALOS, ÁRPÁD IMRE-LUCACI, ANA-MARIA CORMOȘ, MIHAELA DIANA LAZĂR, PAUL-ȘERBAN AGACHI, Thermodynamic Study and Kinetic Modeling of Bioethanol Steam Reforming	101
RAMONA-ELENA TATARU-FARMUS, MIHAELA DRĂGAN, SIMION DRĂGAN, ILIE SIMINICEANU, Kinetics of Carbon Dioxide Absorption into New Amine Solutions	113

DUMITRU BULGARIU, CONSTANTIN RUSU, LAURA BULGARIU, Adsorptive Characteristics of Histosol Modified by Simple Chemical Treatments For Ni(II) Removal from Aqueous Media	121
ANA MARIA BARGAN, GABRIELA CIOBANU, CONSTANTIN LUCA, EUGEN HOROBA, Influence of the Citric Acid on the Cerium Substituted Hydroxyapatite Morphology	137
MARCEL BENEĂ, RAMONA IENCIU, VIORICA RUSU-BOLINDEȚ, Mineralogical and Physical Characteristics of Roman Ceramics from Histria, <i>Basilica Extra Muros Sector</i> , West-East Section (Romania).....	147
CONSTANTIN MĂRUȚOIU, LAURA TROȘAN, VASILICA-DANIELA TOADER, ZAHARIE MOLDOVAN, ALEXANDRU I. TURZA, CLAUDIU TANASELIA, IOAN BRATU, Scientific Investigation of Pigments Employed for „Crucifixion” Processional Flag Painting from the Ethnographic Museum of Transylvania Heritage	161
JULIETA DANIELA CHELARU, LUCIAN BARBU-TUDORAN, LIANA MARIA MUREȘAN, Protection of Artistic Bronzes by Artificial Patina and Wax....	173
FLORIN HANC-SCHERER, ADRIAN NICOARĂ, Coupled Voltammetric and Electrogravimetric Investigation of Copper Behavior in Carbonate-Bicarbonate Solutions	183
IOANA FORT, ILEANA ELISABETA SILAI, DORINA CASONI, GRAZIELLA L. TURDEAN, Electrochemical Study of Isoprenaline and Epinephrine at Platinum-Nanoparticles-Chitosan Modified Graphite Electrode	193
ILEANA ELISABETA SILAI, GRAZIELLA LIANA TURDEAN, DORINA CASONI, Electrochemical Behavior of Some Catecholamines Investigated by Cyclic and Square-Wave Voltammetry	203
ION ROPOTA, MIHAI BRATU, DRAGA DRAGNEA, OVIDIU DUMITRESCU, OVIDIU MUNTEAN, MARCELA MUNTEAN, Recycling Solid Wastes as Polymer Composites	213
IOANA STOICA, IONUȚ BANU, GRIGORE BOZGA, An Analysis of the Stabilization Mechanism of Reverse Flow Reactors with Application in Catalytic VOC Combustion	227
CAMILLE STRADY, ADINA STEGARESCU, CRISTIAN SILVESTRU, ANCA SILVESTRU, New Copper(I) Complexes with Organophosphorus Ligands with XpnsO Skeleton.....	243
NICOLETA BICAN-BRIȘAN, TEODORA ENACHE, CRISTINA ROȘU, New Copper(I) Concentration of Particulate Matter Associated to a Crossroad Traffic from Cluj-Napoca City	253
ANDRA TĂMAȘ, SORINA BORAN, Intensification of Convective Heat Transfer in Straight Pipes by Using Some Turbulence Promoters.....	265
ONUC COZAR, NICOLAE CIOICA, CLAUDIU FILIP, CONSTANTIN COȚA, XENIA FILIP, Structural FT-IR and ¹³ C CP/MAS NMR Investigation of Native Starch with Plasticizers Before and Post Extrusion Process.....	275

Studia Universitatis Babes-Bolyai Chemia has been selected for coverage in Thomson Reuters products and custom information services. Beginning with V. 53 (1) 2008, this publication is indexed and abstracted in the following:

- Science Citation Index Expanded (also known as SciSearch®)
- Chemistry Citation Index®
- Journal Citation Reports/Science Edition

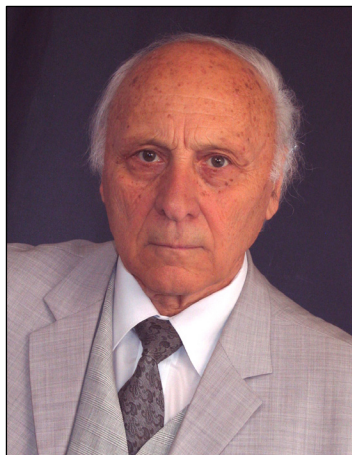
Professor Emeritus PhD Eng. Liviu Literat at the 85th Anniversary

In 2013 Professor Emeritus Liviu Literat celebrates his 85th anniversary. His life has been devoted to the development of the chemical engineering and chemistry education in Romania and he is known as the founder of the Chemical Engineering Education in Cluj-Napoca University Center.

He was born on the 9th of September 1928 in Vințu de Jos as the descendant of an old family of priests, teachers and professors who significantly contributed to the development of the national culture and tradition in the Făgăraș County.

Professor Liviu Literat performed his first studies at the Andrei Șaguna College in Brașov and in 1947 became baccalaureate of the National College George Barițiu in Cluj. His university studies have been performed at two of the top Romanian universities: the Victor Babeș University from Cluj, Faculty of Chemistry, where he graduated in 1951 the Chemistry-physics specialization, and the University of Bucharest, where he graduated in 1963 Chemical engineering within the program of study Technology of Inorganic Materials. In 1966 he became PhD in chemistry with the thesis entitled *Physical-chemical study on some reducing non-stoichiometric aluminum oxides*, working with the Academician Raluca Ripan. These steps of education have been followed by research training and post doctoral studies with Academician Ilie Murgulescu and Academician Costin C. Nenițescu.

Professor Literat Liviu started his academic career at Victor Babeș University from Cluj as teaching assistant (1950) and continued to ascend the steps of the higher education hierarchy. He became Professor in 1974 and head of the departments: Organic Chemistry and Technology (1977-1985), Chemical Engineering (1990-1992), Chemical Engineering and Oxide Materials Science (1992-1995) at Babeș-Bolyai University, Faculty of Chemistry and Chemical Engineering. From 1995 he is Consultant Professor and from 2011 he is Professor Emeritus of the Babeș-Bolyai University. As founder of Chemical Engineering School from Cluj, he established several programs of study: Technology of Building Materials (1971), Organic and Inorganic Technology (1977), Science and Engineering of Oxide Materials (1990) and he was the founder of Departments of Chemical Engineering (1990) and Chemical



Engineering and Oxide Materials Science (1993). He put the basis for research and designing activities in chemical engineering at Cluj, for master and doctorate studies, being the first scientific doctorate advisor in chemical engineering from the University Center Cluj-Napoca.

Professor Literat Liviu has gained high recognition from the scientific community for his contributions, both to fundamental and applied research, especially in the fields of material science, chemical engineering and physical–chemistry. These contributions include over 130 scientific papers published in journals, 75 applied research reports, 5 grants, 3 patents and 15 books (university textbooks, treaties, monographs, history of sciences and education). Some of the subjects of his research consist in: heterogeneous catalysis, sorption, extraction, reactions in solid phase, with applications to the study of processes of interface and of nano-systems, synthesis and studies of a new class of refractory oxide compounds with deviation from stoichiometry associated to original contributions to the theory and the concept of the stoichiometry for nanometric oxide systems, establishing new similitude criteria and criteria equations for carriers of electrical load through molecular and convective mechanism both in stationary and transitory regime, development of concepts and application of the dimensional analysis, contributions to the technique of chemical, punctual, qualitative and quantitative analysis of the micro-phases from composite systems.

Professor Liviu Literat was founder member, president and Honorary President of the Society of Chemical Engineering from Romania – Cluj branch, Honorary Member of the Academy of Technical Sciences from Romania, founder member of ASTR – Cluj-Napoca branch, Member of the European Federation of the Chemical Engineering; Society of Chemistry from Romania, Association of Sciences People from Romania "Transylvania" subsidiary of Romanian Academy, Scientific Association of the Engineers and Technicians, National Council of the Engineers and Technicians, member in the editorial board of the Scientific Bulletin of Polytechnic Institute Cluj, *Studia Universitatis Babeş-Bolyai Seria Chemia* and *Romanian Journal of Materials*.

The education, research and management work performed by Professor Liviu Literat reveals an outstanding character who showed a constant commitment to share his energy and wisdom not only to the benefit of the Alma Mater Napocensis community but also to the whole Romanian higher education system.

At the 85th anniversary of the distinguished personality who made history for the chemical engineering education, during more than half of the century, the colleagues from the Faculty of Chemistry and Chemical Engineering of Cluj-Napoca wish to honor his celebration and show him their highest consideration and gratitude. Happy Birthday and Long Life Professor Liviu Literat!

Cristea V. Mircea

Department of Chemical Engineering

*Dedicated to Professor Liviu Literat
On the occasion of his 85th birthday*

APPLICATIONS OF CHEMICAL LOOPING COMBUSTION TO ENERGY CONVERSION PROCESSES

IULIA-MARIA BODEA^a, CĂLIN-CRISTIAN CORMOȘ^{a,*}

ABSTRACT. Among various carbon capture technologies, chemical looping combustion (CLC) is a promising option to reduce both energy and cost penalties for CO₂ capture. This technique uses an oxygen carrier (usually a metallic oxide) for fuel oxidation followed by reoxidation of reduced oxygen carrier by air and/or steam. Both fuel and air reactors are operated in fluidised conditions. This paper investigates the optimisation of process operation conditions for two CLC cases, one based on natural gas and one based on syngas as fuels. The investigated CLC processes using various metallic oxides (e.g. iron, nickel, copper and mangan oxides) as oxygen carriers are aiming to find optimum process conditions (pressure, temperature, oxygen carrier flow rate, molar ratio among reactants, oxygen carrier concentration in the solid phase etc.) for an almost complete fuel conversion as well as for total decarbonisation of the used fuel.

Keywords: *Energy conversion with carbon capture, Chemical looping combustion (CLC), Oxygen carriers, Optimisation of process operation conditions.*

INTRODUCTION

In the last decade, significant progress has been made towards a better understanding of the world climate and of the long-term impact of climate change. There is now evidence that the mean annual temperature at the earth's surface increased over the past 200 years. This temperature increase is commonly known as global warming. It has been established that emission of greenhouse gases (CO₂, NO_x, SO_x, CH₄) are the main contributor to global warming, and CO₂ is the most prevalent of these gas emissions. Statistics indicate that the CO₂ emissions resulting from human activity have led to an increase in the atmospheric CO₂ concentration, from a pre-industrial level of 280 to 380 ppm [1].

^a *Universitatea Babeș-Bolyai, Facultatea de Chimie și Inginerie Chimică, Str. Kogălniceanu, Nr. 1, RO-400084, Cluj-Napoca, Romania, * cormos@chem.ubbcluj.ro*

There are several ways in which to reduce anthropogenic CO₂ emissions: increase the use of renewable sources of potential energy, such as hydro-, wind and solar power; promote CO₂ uptake in biomass; switch from fossil fuels to biomass; expand the nuclear power sector; and finally, reduce global energy intensity. However, it is likely that society will remain highly dependent on fossil fuels for some time to come [2]. Hence an additional alternative to reduce the net emissions of CO₂ has been suggested: combining the use of fossil fuels with CO₂ capture and storage (CCS), which would yield to low carbon sources of heat and power [2].

A number of known techniques can be used to carry out this separation, but a major disadvantage with most of these techniques is the large amount of energy that is required to obtain CO₂ in pure form, which means that the efficiency of power plants decrease with about 8–12 net electricity percentage points [2]. Combustion of fossil fuels (coal, lignite, oil, natural gas) release a massive amount of carbon as carbon dioxide into the atmosphere. It is estimated that fossil fuel-based power generation contributes today to about one-third of the total carbon dioxide released.

In order to capture CO₂, there are currently a number of available processes as follows: (i) pre-combustion, in which the fuel is decarbonized prior to combustion, (ii) oxy-fuel combustion, which uses pure oxygen obtained from cryogenic air separation and (iii) post-combustion separation, which separate CO₂ from the flue gases using different approaches. These techniques are energy intensive, resulting in a significant decrease of the overall energy conversion efficiency and as a result in a price increase of the produced electricity. For instance, gas-liquid absorption using alkanolamines (e.g. monoethanol-amine - MEA, methyl-diethanol-amine - MDEA) which are the most technologically and commercially mature CO₂ capture processes has as major negative impact the high heat duty needed for solvent regeneration (in the range of 3 to 4 MJ/kg CO₂). Considering all these factors, chemical-looping combustion (CLC) appears to have the potential for delivering a most efficient and low cost technology. This process was initially proposed to increase thermal efficiency in power generation stations, but later on was identified as having inherent advantages for CO₂ separation with minimum energy losses [1].

The chemical looping combustion is implying the usage of several interconnected circulated bed reactors, as presented in Figure 1 (for the case of gaseous fuels like natural gas or syngas resulted from catalytic reforming / gasification processes). The fuel (either gaseous, liquid and solid) is introduced to the fuel reactor where it reacts with an oxygen carrier (OC) to convert the fuel to CO₂ and H₂O. The gas phase resulted from the fuel reactor is cooled, water condense separated and CO₂ stream is ready for storage (inherent CO₂ capture is one of the most attractive feature of chemical looping systems). The reduced stage of the solid carrier is then pneumatically transported to a separate reactor where it is oxidized back to its original state. The reoxidation

process can be made by air, steam or a combination of both. The energy integration between fuel and air reactors is a key aspect of this technology (the reactions in the fuel reactor are mainly endothermic and the oxygen carrier reoxidation is always exothermic), solid flow being used as heat transport media [3-4].

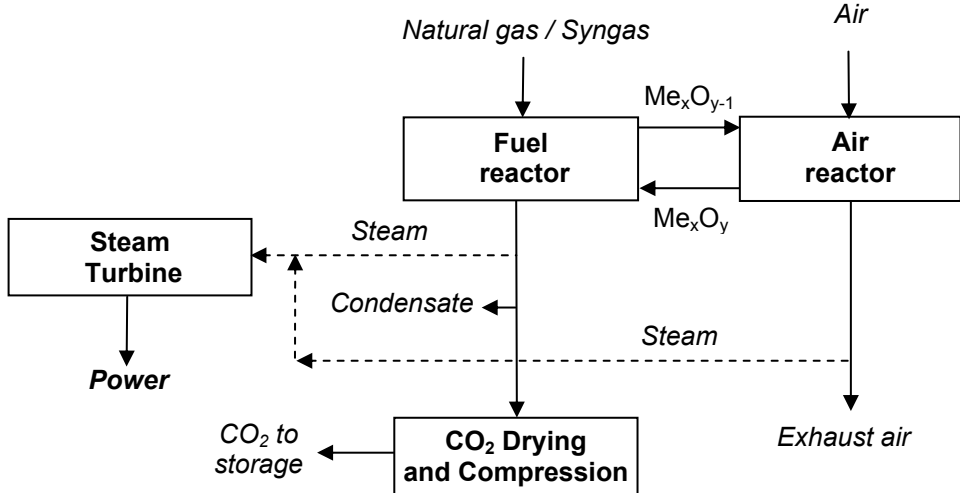
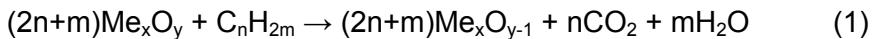


Figure 1. Chemical looping combustion (CLC) of gaseous fuels

In the fuel reactor, the oxygen carrier is reduced by the fuel to lower oxidation stage. This paper is investigating gaseous fuels like natural gas or syngas [5]. The fuel (hydrocarbon) oxidation reaction is the following:



Me_xO_y is a metal oxide and Me_xO_{y-1} represents its reduced form.

The reduced form of the oxygen carrier is pneumatically transported to a separate reactor where it is regenerated (reoxidation) by air according to the reaction 2. Reoxidation can be done also with steam.



The reoxidised oxygen-carrier is then closing the cycle being transported back to the fuel reactor. The reduction process in the fuel reactor (reaction 1) can be either endothermic or exothermic, depending on the oxygen carrier and the fuel, while the oxidation process in the air reactor (reaction 2) is exothermic [5-6]. In theory, the oxygen carrier can be used indefinitely. However, the solid material must be renewed by a makeup flow of new material due to undesirable attrition / fragmentation or reactivity loss [6]. The usage of an inert support for the oxygen carrier is significantly improve the mechanical strength.

In chemical-looping combustion (CLC), a metal oxide is used as an oxygen carrier which transfers oxygen from the combustion air to the fuel [7]. The main advantage with CLC compared to normal combustion is that CO₂ is inherently separated from the other flue gas components, i.e. N₂ and unused O₂ and thus, costly equipment and efficiency losses for separation of CO₂ are avoided [8]. Although the advance of the CLC technology involved works carried out at different research levels, continuous operation in a CLC prototype is necessary to demonstrate the validity of this technology and to verify the usefulness of the particles developed. The CLC process was first successfully demonstrated by Lyngfelt et al. at Chalmers University, Sweden, in a 10 kWh prototype during 100 h of continuous operation burning natural gas and using nickel based oxygen carrier particles [9].

Most research to date on CLC is mainly concentrated on gaseous fuel, and CLC applications with solid fuels, e.g. coal, biomass, are still limited [10]. In the development of suitable oxygen carrier material it is important to test a significant number of materials with varying metal oxide/support combinations and production conditions [8]. OC was the basis for CLC and acted as oxygen conductor as well as energy carrier in CLC, which is composed of the active metal oxides and inert support. Until now, Fe₂O₃, CuO and NiO are widely used in CLC as the active oxygen carriers, and a variety of inert materials have been reported as the inert supports for OC, such as Al₂O₃, SiO₂, ZrO₂, etc. among which, Al₂O₃ is recognized as one of the most promising supports [10].

A number of materials have been identified as suitable OC in a CLC system: metal oxides based on iron, nickel, manganese, copper or cobalt, supported on alumina, zirconia, silica, titania, or bentonite. An OC must withstand a high number of redox cycles, both chemical and physically, in order to be used in a CLC process. Thermodynamic characteristics of the metallic oxides vs. temperature is an important aspect, Ellingham diagrams being used. In addition, other characteristics such as high oxygen transport capacity, complete fuel conversion to CO₂ and H₂O, negligible carbon deposition, good properties for fluidization (no presence of agglomeration) and easy preparation to reduce costs are also important [7].

There are some important criteria for the selection of oxygen-carrier particles. The basic requirements for OC are mechanical stability, lowest possible costs and high oxygen transport capacity [11]. The thermodynamic equilibrium for the reaction with the fuel has to be favorable in order to achieve high fuel conversion to CO₂ and H₂O. Metal oxide systems which are feasible for use as oxygen carriers in CLC are Mn₃O₄/MnO, Fe₂O₃ / Fe₃O₄, NiO / Ni, CuO / Cu and CoO / Co. Also the rate of oxidation and reduction has to be sufficiently fast. Otherwise the amount of oxygen-carrier needed in the reactors would be too large. Moreover the oxygen transfer capacity needs to be sufficient. Since the proposed reactor system consists of fluidized beds, the

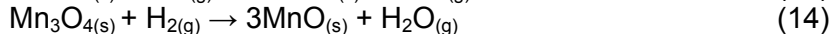
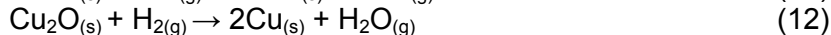
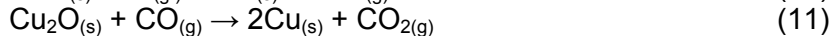
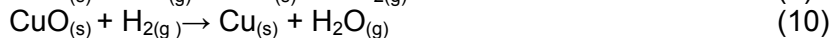
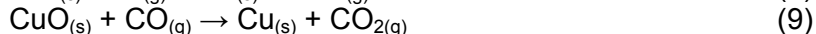
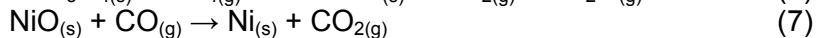
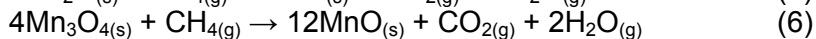
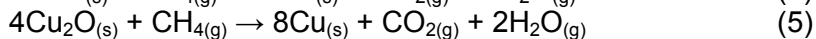
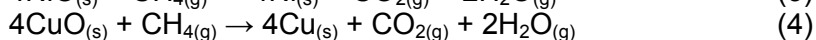
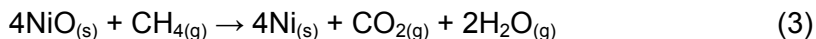
particles need to have a low tendency for fragmentation and attrition. It is also vital that they do not agglomerate under real reaction conditions [9]. In view of maintaining a sufficient fuel reactor temperature for a high conversion rate, CuO has been highly appraised and intensively studied for the exothermic characteristics of its reduction reaction with various fuels [7]. In a CLC system, the solid circulation between the reactors has to be sufficient to transport the adequate amount of oxygen for fuel combustion, and to transfer sufficient sensible heat from the air reactor to the fuel reactor for those oxide systems where the reaction in the fuel reactor is endothermic [9].

In the manufacture process of the oxygen carriers, the metal oxides are combined with an inert which acts as a porous support providing a higher surface area for reaction, and as a binder for increasing the mechanical strength and attrition resistance [12-13]. Temperature variations in the oxygen carrier particles during their reduction and oxidation in a chemical-looping combustion system are equally important to the overall process. In this work, the inert solid used for the preparation of oxygen carriers have been considered Al_2O_3 .

RESULTS AND DISCUSSION

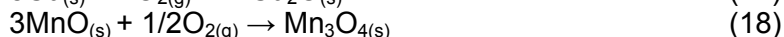
This paper describes two chemical looping combustion systems of the carbon dioxide capture using a natural gas-based and a syngas-based chemical looping combustion system. The processes are identical in design; the difference is in terms of substance used as oxygen carrier and the fuel used (syngas and natural gas). The evaluated oxygen carriers are copper oxide (CuO , Cu_2O), nickel oxide (NiO) and manganese oxide (Mn_3O_4) [14-16]. The process is composed of two interconnected fluidized bed reactors as shown in Figure 1.

The fuel comes in contact with the oxygen carrier in the fuel reactor. The reduction of the oxygen carrier takes place at about 750-850°C, according to the chemical reactions (the first four reactions are for the case of natural gas used as fuel, the next reactions are for the case of syngas used as fuel):



The stream which leaves the reactor is sent to a flash separator where the solid phase is separated from the gas phase. The rich CO₂ stream leaves the flash to the top and is sent to a heat recovery steam generation. The CO₂ hot stream is then cooled down with cooling water, at around 40°C, the temperature is achieved by using a series of heat exchangers (heat recovery steam generator - HRSG). The steam obtained in heat recovery steam generators by cooling the hot streams reaches a steam turbine where heat is converted into electricity. The exhausted steam leaves the turbine, then it is condensed and recycled back in the cycle (steam – Rankine cycle).

The CO₂ cooled stream is sent to a compression unit, which has 3 compression stages with intercoolers. In the first stage the gas is compressed from 14 bar to 20 bar. The stream is cooled at 40°C and enters in a flash separator, used to remove the water from the process. Cooling and separation are made after each stage of compression. In the second stage the pressure is increased from 20 bar to 70 bar, then the pressure reaches in the third stage 120 bar. The compression stages were used instead of one compressor because one compressor needs more energy to achieve 120 bar than 3 compression stages. Another argument is to avoid the overheating of the compressors. The solid stream coming from the bottom of the flash separator is sent to the air reactor where is oxidized with air at 850-950°C, according to the following reactions:



The oxygen carrier obtained is recycled to the reduction reactor (fuel reactor). The gas stream leaves the cyclone to the top and is sent, like the CO₂ stream, to a heat recovery steam generator. The generated steam is then expanded in a steam turbine to produce the ancillary power. The natural gas and the syngas composition used in the mathematical modeling and simulation are presented in Table 1. ChemCAD was used as simulation software. As calculation model for simulation of the process, thermodynamic equilibrium was chosen, the thermodynamic package being selected considering the range of operating parameters (e.g. pressure, temperature) as well as the chemical species present in the system.

1. Syngas chemical looping combustion

The first process simulated used syngas as fuel. In order to evaluate the effect of the oxygen carrier flow on the reactor temperature Figure 2 shows the temperature curve in the fuel reactor due to the oxygen carrier flow. Various oxygen carriers were evaluated (CuO, Mn₃O₄, NiO and Cu₂O).

The results suggest a logarithmic influence between inlet oxygen carrier flow and the temperature, the temperature increase with the oxygen carrier (OC) load. The temperature tends to become stable when the maximum conversion of the oxygen carrier is reached. This conclusion is important for the practical operation on the chemical looping unit.

Table 1. Fuel characteristics used in analysis

Fuel	Parameters	Values
Natural gas	Temperature (°C)	30.00
	Pressure (bar)	15.00
	Gas composition (% vol.)	
	Methane	89.00
	Nitrogen	0.89
	Carbon dioxide	2.00
	Ethane	7.00
	Propane	1.00
	I-Butane	0.05
	N-Butane	0.05
	I-Pentane	0.005
	N-Pentane	0.004
	Hexane	0.001
	Hydrogen Sulfide	0.00001
Syngas	Temperature (°C)	30.00
	Pressure (bar)	31.50
	Gas composition (% vol.)	
	Methane	0.01
	Nitrogen	5.14
	Carbon dioxide	4.47
	Carbon monoxide	61.34
	Hydrogen	28.09
	Water	0.02
	Argon	0.93

As shown in Figure 2, the temperature in the fuel reactor is influenced by the oxide used as oxygen carrier. With the increasing in amount of OC, from 10% OC to 90% OC (expressed in mass percentages from the total solid), the difference between the variation of the temperatures increase due to the reduced material flow through the reactor. This fact is important in order to find a suitable trade-off between the OC concentration and the temperature profile.

The Figure 3 shows the variation of temperature in the air reactor due to the air flow. The temperature in the air reactor decrease with the increasing of the air flow, because of the exothermic reaction in the reactor. As for the case of the fuel reactor, the solid material flow through the reactor influences the temperature profile.

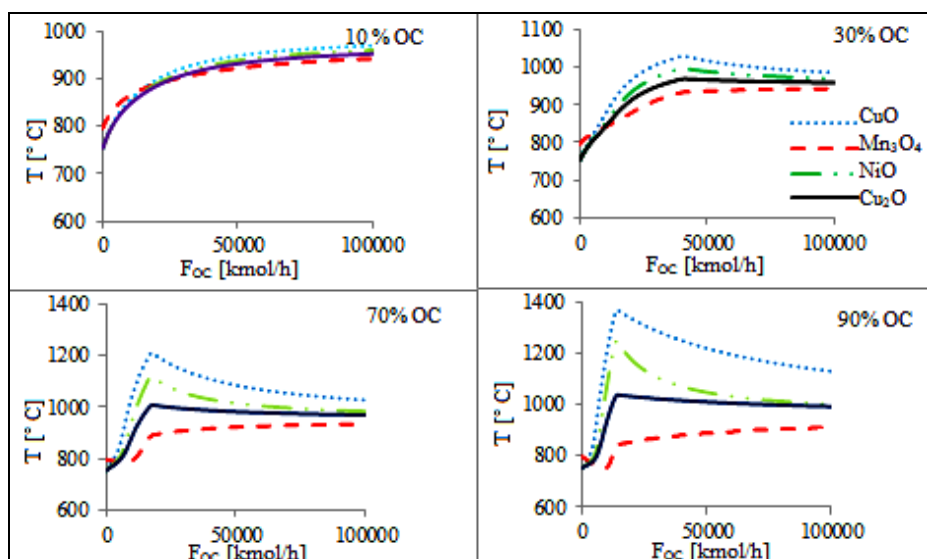


Figure 2. Variation of temperature in the fuel reactor due to the oxygen carrier flow with different concentrations

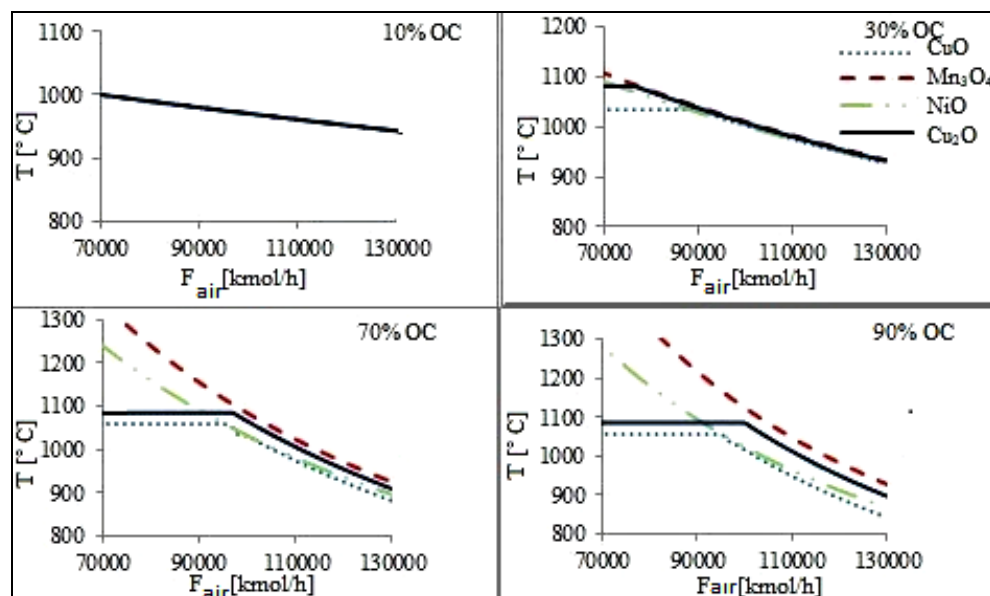


Figure 3. Variation of temperature in the air reactor due to the air inlet flow

In view of maintaining a sufficient fuel reactor temperature for a high conversion rate, CuO has been highly appraised and intensively studied for the exothermic characteristics of its reduction reaction with various fuels [17]. The exothermic character of both fuel and air reactors simplify the energy management of the whole process and increase the overall energy efficiency. In the following text, the evaluation was concentrated on using the copper oxide as oxygen carrier in chemical looping.

Figure 4 describes the variation of CO molar fraction due to oxygen carrier flow, at different pressures. The CO molar fraction decreases with the increasing of OC. The trends are similar with the increasing of the pressures, in the range of 2 to 32 bar. As can be noticed from Figure 4, the influence of pressure is rather limitate on the process.

A similar trend is observed also for hydrogen molar fraction (see Figure 5). As can be noticed from Figure 5, hydrogen molar fraction increases, reaches a maximum, and then the slope has a downward trend to zero (total conversion). Figure 5 shows also the influence of syngas pressure over the process, as the pressure increases the hydrogen oxidation process is more favorable. The influence of pressure for syngas looping combustion is of great importance considering that the most efficient gasification / catalytic reforming technologies are running at hight pressure (up to 40 bar).

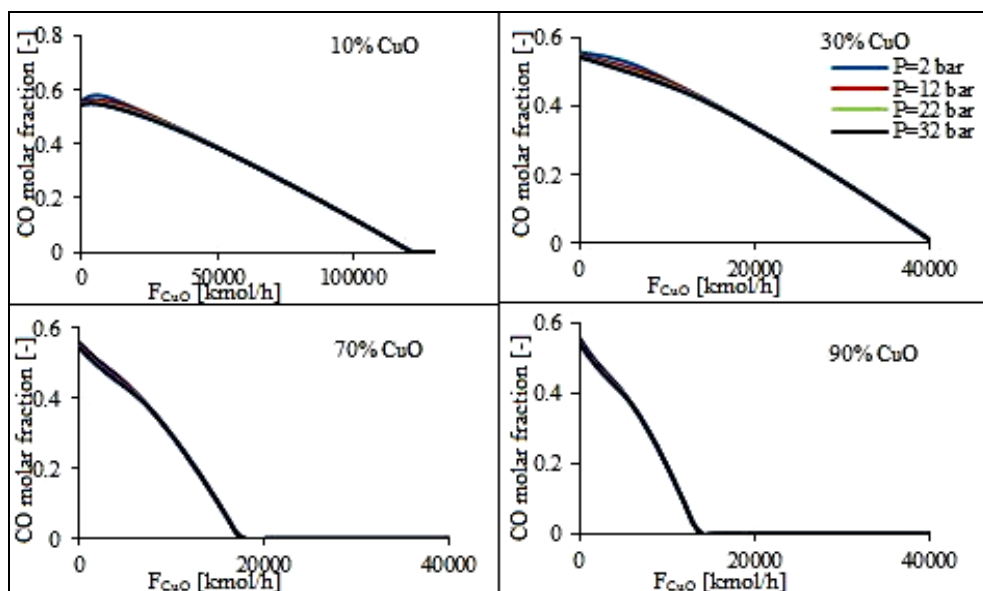


Figure 4. Variation of CO molar fraction as a function of CuO inlet flow

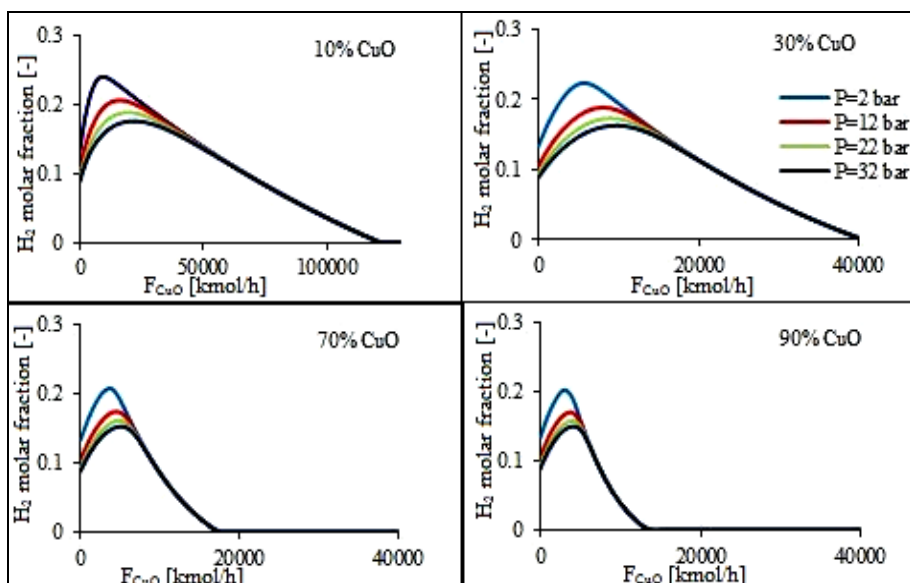


Figure 5. Variation of H₂ molar fraction as a function of CuO inlet flow

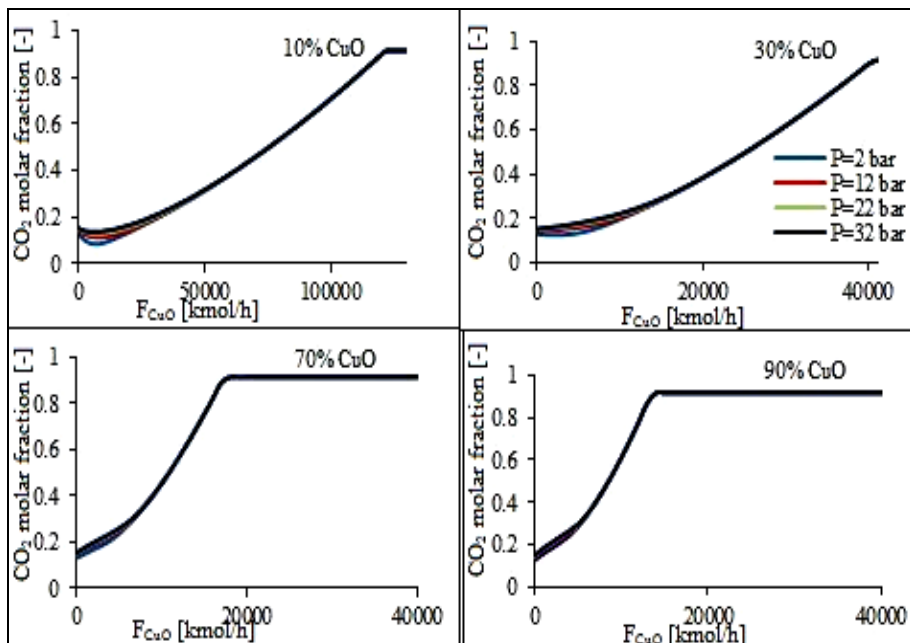


Figure 6. Variation of CO₂ molar fraction as a function of CuO inlet flow

The CO_2 molar fraction increases with the increasing of the CuO flow, the CO_2 fraction reaches 99%. The CO_2 is influenced by the pressure just at low flows of CuO. As presented in Figures 2 - 6, these numerical evaluations are of significant importance to establish the process conditions (pressure, temperature, solid and gaseous flows etc.).

2. Natural gas chemical looping combustion

Figure 7 illustrates the trend of the temperature in the fuel reactor, due to the oxygen carrier for natural gas-based chemical looping. The fuel reactor temperature increases with the increasing of OC. The temperatures tempt stability below 1000°C . The highest temperature in the fuel reactor is achieved using CuO as oxygen carrier, while the lowest temperature is obtained with Mn_3O_4 as OC. The temperature variation based on OC influence is visible with the decreasing of inert material in the OC inlet flow.

Figure 8 shows the variation of temperature in the air reactor due to the air flow. The temperature decreases with the increasing of the OC inlet flow. As presented already for syngas-based chemical looping combustion, the concentration of OC has an important influence on temperature profiles in both reactors. The operational conditions (e.g. oxygen carrier concentration in the solid phase) have to be modulate in a such a way to maximize the fuel conversion (which generally imply a temperature increase) but not to cause sintering of the solid and maintaining a suitable mechanical strenght to prevent particle fragmentation.

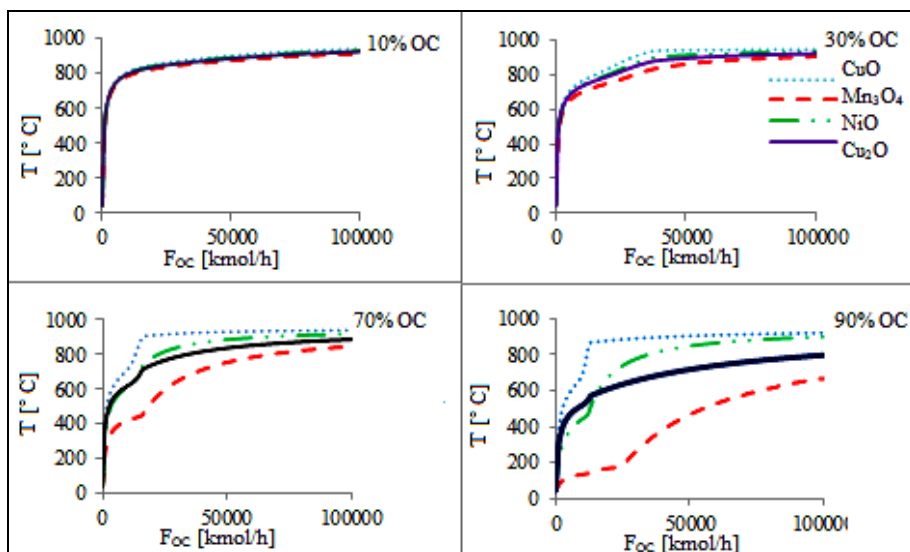


Figure 7. Variation of temperature in the fuel reactor due to the oxygen carrier flow

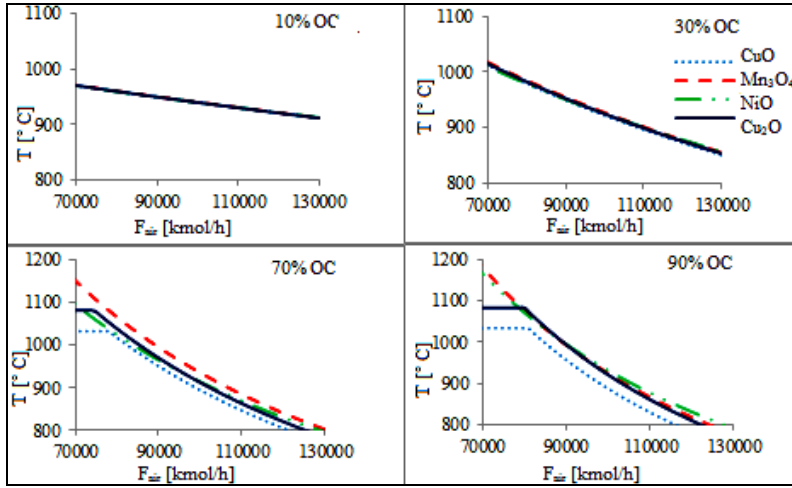


Figure 8. Variation of temperature in the air reactor due to the air flow

Figure 9 shows the variation of CH_4 molar fraction as a function of CuO inlet flow at different pressures. The CH_4 molar fraction decreases with the increasing in CuO . The influence of pressure was analysed in the range 2 to 32 bar. The oxygen carrier flow has to be selected in a such a way to ensure an almost total fuel oxidation. As can be noticed from Figure 9, the increase of pressure implies the increase of OC flow to ensure a total oxidation of the fuel.

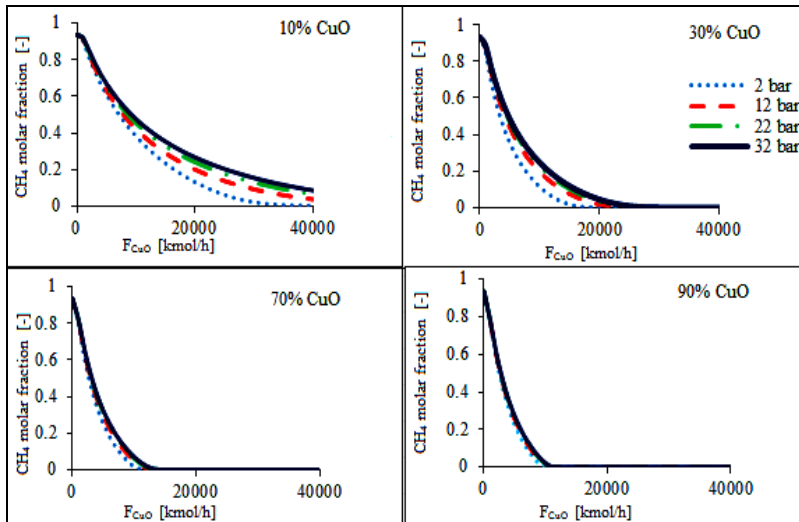


Figure 9. Variation of CH_4 molar fraction as a function of CuO inlet flow at different pressures

Figures 10-11 describe the variation of CO and H₂ molar fractions as a function of oxygen carrier (CuO) flow. These chemical species are formed in the natural gas oxidation process and then are they are finally oxidised to carbon dioxide and water. The behavior of carbon monoxide and hydrogen molar fractions is similar, the trend is to increase up to a maximum fraction, then they are reduced to a minimum concentration, close to zero. The molar fraction is influenced by the pressure, the increase of the pressure decreases the range in which these molar fractions varies. These results are important for evaluation of pressure influence on chemical looping combustion conditions.

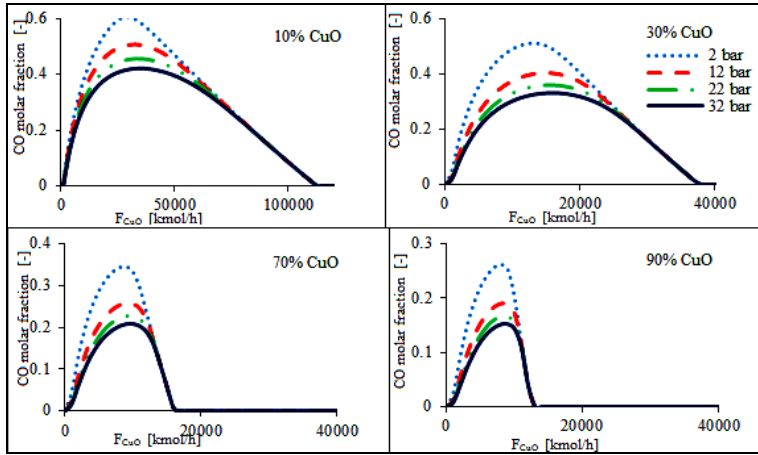


Figure 10. Variation of CO molar fraction as a function of CuO inlet flow

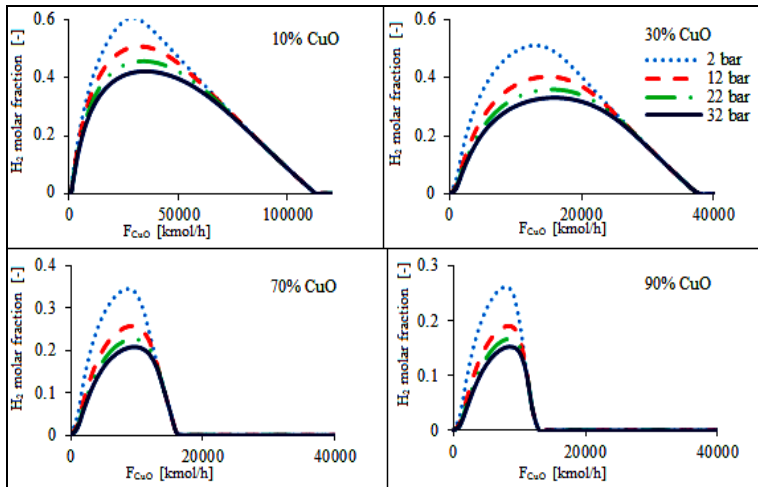


Figure 11. Variation of H₂ molar fraction as a function of CuO inlet flow

The Figure 12 describes the variation of CO₂ molar fraction as a function of CuO inlet flow at various pressures. The molar fraction increases with the increasing of the inlet flow of CuO. The trend is similar with increasing pressures, but without a significantly difference.

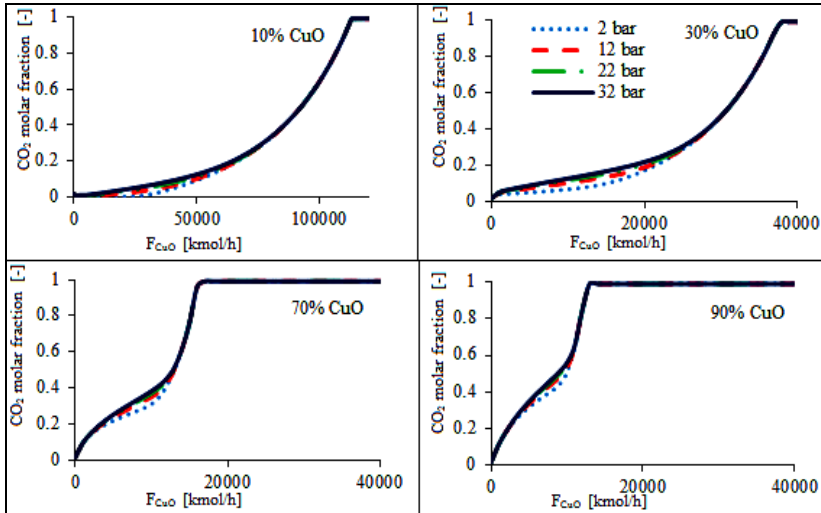


Figure 12. Variation of CO₂ molar fraction as a function of CuO inlet flow at different pressures

Table 2. Overall plant performance indicators

Main plant data	Units	Iron	Nickel
Natural gas flow rate	t/h	38.708	38.708
Natural gas LHV	MJ/kg	46.502	
Natural gas thermal input (A)	MW _{th}	500.00	500.00
Steam turbine	MW _e	164.13	164.21
Purge gas expander	MW _e	291.87	291.84
Gross power output (B)	MW _e	456.01	456.05
Ancillary power consumption (C)	MW _e	247.11	246.49
Net power output (D)	MW _e	208.90	209.56
Net electrical efficiency (D/A*100)	%	41.78	41.91
CO₂ capture rate	%	99.07	99.07
Specific CO₂ emissions	Kg/MWh	1.85	1.81

As presented in above evaluations, the numerical assessments (based mainly on thermodynamic factors) of various oxygen carriers for gaseous fuel chemical looping combustion are extremely useful for optimization of the experimental conditions to ensure both an almost total fuel conversion and a high energy efficiency. The optimised values of the process parameters can be then used for performance assessment of industrial-scale chemical looping combustion cases.

As an illustrative case, Table 2 presents the overall plant performance indicators for natural gas looping combustion using iron and nickel oxides as reported in a previous study [6], the evaluations being based on optimised process conditions as reported in this paper.

CONCLUSIONS

Chemical looping combustion is one promising techniques used to combine fuel combustion and pure CO₂ production in situ allowing for CO₂ sequestration. This technique has significantly higher energy efficiency and lower energy and cost penalties compared with other carbon capture methods (e.g. physical or chemical gas-liquid absorption in both pre- and post-combustion capture configurations).

This paper investigates the behavior of various oxygen carriers used for natural gas and syngas chemical looping combustion in terms of optimising process conditions e.g. temperature, pressure, molar ratio between the reactants, oxygen carrier composition etc. For instance, the ratio between the oxygen carrier and the support is of paramount importance for process conditions (e.g. reactor temperature and heat transfer between the fuel and air reactors) and overall performance indicators. The assessment was based on numerical methods using an thermodynamic approach for the calculations. The results of the evaluation can be successfully used for optimization of the process parameters (pressure, temperature, fuel to OC ratio, oxygen carrier concentration etc.) in order to maximize the fuel conversion and overall plant energy efficiency.

ACKNOWLEDGMENTS

This work was supported by a grant of the Romanian National Authority for Scientific Research (CNCS – UEFISCDI), project number PN-II-ID-PCE-2011-3-0028: “*Innovative methods for chemical looping carbon dioxide capture applied to energy conversion processes for decarbonised energy vectors poly-generation*”.

REFERENCES

1. M.M. Hossain, H.I. de Lasa, *Chemical Engineering Science*, **2008**, 63, 4433.
2. C. Linderholm, T. Mattisson, A. Lyngfelt, *Fuel*, **2009**, 88, 2083.
3. H. Leion, T. Mattisson, A. Lyngfelt, *International Journal of Greenhouse Gas Control*, **2008**, 2, 180.
4. M. Igglund, H. Leion, T. Mattisson, A. Lyngfelt, *Chemical Engineering Science*, **2010**, 65, 5841.
5. A. Abad, T. Mattisson, A. Lyngfelt, M. Johansson, *Fuel*, **2007**, 86, 1021.
6. I.M. Bodea, C.C. Cormos, *Studia UBB Chemia*, **2012**, LVII, 47.
7. P. Gayan, C. Dueso, A. Abad, J. Adanez, L.F. de Diego, F. Garcia-Labiano, *Fuel*, **2009**, 88, 1016.
8. P. Cho, T. Mattisson, A. Lyngfelt, *Fuel*, **2004**, 88, 1215.
9. L.F. de Diego, F. Garcia-Labiano, P. Gayan, J. Celaya, J. M. Palacios, J. Adanez, *Fuel*, **2007**, 86, 1036.
10. B. Wang, H. Zhao, Y. Zheng, Z. Liu, R. Yan, C. Zheng, *Fuel Processing Technology*, **2012**, 96, 104.
11. J. Bolh ar-Nordenkampf, T. Pr oll, P. Kolbitsch, H. Hofbauer, *Energy Procedia*, **2009**, 1, 19.
12. A. Abad, T. Mattisson, A. Lyngfelt, M. Ryden, *Fuel*, **2006**, 85, 1174.
13. L.F. de Diego, F. Garcia-Labiano, J. Adanez, P. Gayan, A. Abad, B.M. Corbella, J.M. Palacios, *Fuel*, **2004**, 83, 1749.
14. M. Broda, A. Kierzkowska, C. M uller, *Environmental Science and Technology*, **2012**, 46, 10849.
15. D. Jing, T. Mattisson, M. Ryden, P. Hallberg, A. Hedayati, J. Van Noyen, F. Snijkers, A. Lyngfelt, *Energy Procedia*, **2013**, 645.
16. M. Pans, P. Gay an, A. Abad, F. Garc ia-Labiano, L. de Diego, J. Ad anez, *Fuel Processing Technology*, **2013**, 115, 152.
17. L.S. Fan, "Chemical looping systems for fossil energy conversions", **2010**, Wiley-AIChE.

*Dedicated to Professor Liviu Literat
On the occasion of his 85th birthday*

ANALYSIS OF THE AEROSOL TRANSPORT AND TOPOLOGY OF THEIR DEPOSIT IN THE LUNGS VIA CFD TECHNIQUE IN NONSTATIONARY FLOW CONDITIONS

CLAUDIU CRISTIAN BOTAR^a

ABSTRACT. Therapy of lung pathology, based on the active aerosols, is one of the most efficient ways of treatment when aerosols are delivered directly into the area where the disease is installed. Only in this way the medical practice could be optimized. Predicting the behavior of a particular device for aerosol delivery and/or describing accurately the aerosol transport and deposition along the respiratory tract represent the key for achieving a successful and modern medical practice. The problem of modeling and simulation of aerosol behavior along the pulmonary tract has not been solved yet. A more detailed knowledge of the mechanisms of aerosol deposition in different parts of the respiratory tract during breathing cycles is necessary and essential in establishing different therapeutic strategies for drug delivery via aerosol particles. Accordingly, the aim of this paper was to investigate, through modern means, the aerosol transport and deposition along the respiratory tract in non-stationary conditions. CFD and CAD techniques have been employed for simulating regional deposition of particles, as functions of aerosol characteristics, ventilation parameters, and respiratory system morphology. The mathematical approach for airflow simulations over the pulmonary tract considered a modified k - ϵ model with incorporated non-stationary features. Simulations were made for single and multiple respiratory cycles, in order to identify the transport and exact aerosol deposition topology along the pulmonary airways. The results reveal the topology of aerosol deposition zones along the 3D computational domain and the characteristics of the air-aerosol mixture flow.

Keywords: *CFD, aerosol transport, lung topology, unsteady-state simulation*

^a *Universitatea Babeş-Bolyai, Facultatea de Chimie și Inginerie Chimică, Str. Kogălniceanu, Nr. 1, RO-400084 Cluj-Napoca, Romania, cbotar@chem.ubbcluj.ro*

INTRODUCTION

Lung diseases are the most prevalent diseases of the human body. Found in different forms (Singh, 2003; Martonen, 2003; Sturm and Hofmann, 2004, etc.) lung diseases are generally related to pathogens and pollutants presence in the breathing air. Due to the increased incidence of lung diseases, public health must identify new ways of treatment, which should be characterized by increase efficiency and use of non-invasive techniques. Furthermore, modern medicine, in case of lung pathology, requires in depth understanding of lung physiology and breathing phenomena and aerosol transport and deposition.

Therapy of the lung pathology, based on the active aerosols, was observed to be more effective than other means of treatment. Moreover, when aerosols are delivered directly into the area where the disease is localized (Harrington, 2006; Hiller, 1992) then the treatment is has increased efficiency.

Prediction of aerosols transport along the pulmonary airways could contribute to treatment optimization through topology identification upon which aerosols are transported and deposited along the lung airways.

Understanding and accurate description of the phenomena which contribute to realization of the breathing process represents the key for the implementation of a successful technique that could be used for prediction of aerosol transport and deposition. Accordingly, experimental investigations have been addressed for description of aerosol transport in both physiological conditions (ICRP, 1994, Smith 1997), and pathological conditions (Chalupa, 2004). The degree of accuracy and prediction in case of experimental investigations is ranging from case to case. Phenomena as diffusion and convection are generally characterizing the transport of breathing air in the lungs. Their influence has been extensively investigated. Researchers (Heyder, 1988; Ultman, 1985) concluded that the co-existence of the two phenomena, when experimental investigation is chosen as technique of analysis, makes difficult to detect the role of each mechanism in terms of transport and deposition of aerosols in the respiratory tract. Therefore, experimental investigation proved to be most often ineffective for optimizing medical practice in case of lung pathology treatment, either for adults or children (Park, 2007; Shiller-Scotland, 1994).

Experimental methods applied to investigate aerosol deposition in lungs allow only measuring the total aerosol fraction deposited along the respiratory tract (Gebhart, 1989; Heyder, 1978). Experimental techniques of this type, defined as "aerosol bolus techniques" are not capable of measuring the amount of aerosols deposited at certain levels of pulmonary tract for a complete breathing cycle. This is a major drawback of experimental techniques. Moreover, there are several technical and ethical issues related to the "in vivo" investigation, it is invasive, inefficient in terms of cost, accuracy and reproducibility of measurements. All these contribute to the conclusion that

methods of experimental investigation are most often an inefficient method of investigation when zones of aerosol deposition and their topology along the respiratory tract are intended to be established.

Given the complexity of aerosols flow and of pulmonary tract geometry, an experimental estimate of aerosol transport is still a difficult task. Effective prediction of inhaled aerosol deposition zones depends mainly on accurately description of lung geometry and breathing process. In this area, an essential contribution has been made through continuous increase of computers power and development of specific software. This encouraged more and more scientists to be active in the field and to contribute to the development of knowledge regarding prediction of aerosol transport and deposition in lungs (Lee, 2002). Another essential factor contributing to increasing solutions accuracy was the development of medical imaging techniques and the development of three-dimensional geometry reconstruction methods. Based on these two factors, computer simulation is able to handle all technical issues affecting experimental investigation. In addition, it provides a detailed image of the breathing process and useful information on how certain processes take place (such as active detection of the aerosol particles route in drug therapy). This is just one essential feature of the mathematical models that makes them effective tools for identifying a proper treatment. Using computer simulation, the effect of each morphometric parameter of the breathing process for any type and size of aerosol particle, can be revealed. Therefore, computer simulation remains one of the most important method in studying breathing and transport of aerosols in human lungs; it contributes to understanding and predicting the development of aerosol transport related phenomena and in the same time to the improvement of the human health (Hiller, 1992).

Prediction of aerosols deposition through mathematical modeling and simulation can be approached in a variety of ways; usually mathematical models cover one-dimensional to three-dimensional scales. Studies based on analytical models have provided useful information on overall effectiveness, regional and generation-specific particle number deposition efficiencies. Single-path analytical models applied to adults were developed by Yeh and Schumacher (1980). Multiple-path analytical models were developed by Koblinger and Hofmann (1990). However, analytical models cannot predict zonal heterogeneity on the number of aerosol particle deposition. More than that, as it was concluded by Heyder et al. (1988), the aerosol bolus dispersion processes are dependent rather to the volume inhaled than to the time variance.

Subsequently, due to development of computational fluid dynamics (CFD) techniques, models that allowed a significant increase in solutions resolution, going beyond the analytical models, have been implemented. Mainly, the CFD techniques were used to investigate regions of the pulmonary tree (Grgic, 2004; Heenan, 2004), or units of the lung (Balášházy, 2003; Darquenne

and Paiva, 1996; Zhang, 2002). But, there are also models that are integrating larger areas of the pulmonary tract, such as the region between proximal segments of the main airway up to 10th bifurcations order (Geng, 2011).

Between models which are considering complex lung geometries there is the stochastic model of Hofmann, et al. (2002), which is based on detailed morphometric measurements of the bronchial tree and acinar region. This model considers the variation of all geometric parameters to simulate regional deposition of aerosol particles. In contrast, it disregards the dispersion of particles. Particles are considered to move with the same speed as the main flux of air.

The dispersion of particles was introduced into calculations by Brand (1997) and Heyder (1988). Sarangapani and Wexler (2000) showed the significance of dispersion on the total deposition of inhaled particles. In the same time dispersion increases mainly the deposition of fine particles.

Processes as mixing and streaming of disperse particles during a breathing cycle determine how far the inhaled aerosol penetrates into the lung and consequently where in the pulmonary region the aerosol particles are deposited (Sarangapani and Wexler, 2000). As a consequence, the mathematical models dealing with particle deposition in pulmonary region of the airways must consider dispersion since it is the fundamental transport mechanism that enables their presence in the airways region.

Another important factor in modeling of aerosol particle transport and deposition is the cyclical characteristic of breathing. Efforts have been made to model aerosol transport and to characterize regional submission. In general, these models have considered a single breath cycle (Park and Wexler, 2007a); but there are also models that consider the deposition of particles for several respiratory cycles (Park and Wexler, 2007b). Accurate estimates of regional particle dosimetry for one or more respiratory cycles cannot be made without taking into account the amount of particles deposited during transport along the pulmonary tract. However, there is the study of Park and Wexler (2008), which used a semi-empirical model, in which total and regional particle dosimetry was estimated for particles between 0.01-10 micro meters, in conditions when equilibrium was established in the respiratory system along multiple breathing cycle's conditions. Nevertheless, the study covers just the particle transport profiles and cumulative mixing intensities, which represents only a framework for understanding particle transport and deposition during multiple breaths.

In light of these arguments, more detailed knowledge of the mechanisms of aerosol deposition in different parts of the respiratory tract during the breathing cycle is necessary, yet essential in establishing different therapeutic strategies for drug delivery via aerosol particles for pulmonary diseases.

Taking into account the above discussion, the aim of this paper is to analyze the aerosol transport and deposition along the respiratory tract in non-stationary conditions, for single and multiple respiratory cycles using CFD.

MATERIAL AND METHODS

Simulations were performed on a 3D geometry of the human pulmonary tract; the pulmonary tract geometry being reconstructed based on computer tomography (CT) images.

The CT images were collected from a 51 years old patient, who presented pulmonary pathology. The chest CT images correspond to slices in the axial plane with a distance of 0.23 mm apart. Each image was analyzed and processed using Matlab software, resulting in a data set representing the diameters of the trachea and bronchi along the entire geometry. Computer aided design (CAD) techniques have been used to reconstruct the patient airways in 3D. The computational fluid dynamics (CFD) technique was assigned to simulate the airflow and aerosol deposition inside the trachea-bronchial tree of the patient. Unsteady state conditions have been applied at the inlet of the 3D lung geometry.

1. Lung geometry reconstruction

The objective of 3D reconstruction of pulmonary tract geometry based on CT images was to get the 3D volume of the patient airways, replicating as closely as possible the complexity of the pulmonary airways geometry. The reconstruction of the lung geometry was performed using SolidEdgeV20 software. An approximation was made for the cross-sectional shapes of distal branches, which were considered ellipsoidal or circular as appropriate.

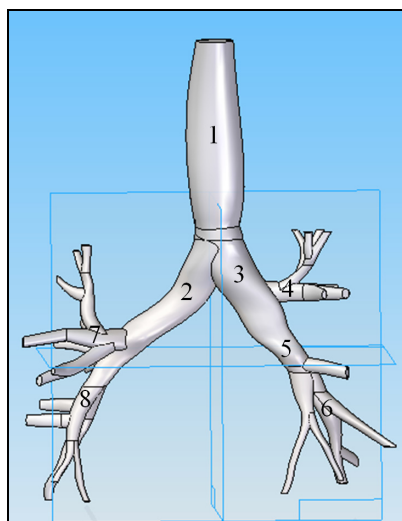


Figure 1. The reconstructed geometry of lung airways based on CT images: 1-Trachea, 2-Left main bronchus, 3-Right main bronchus, 4-Right secondary bronchus, 5-Medial lobe of right lung, 6-Inferior lobe of right lung, 7-Superior lobe of left lung, 8-Inferior lobe of left lung

The lung geometry was discretized using Gambit software. The surface mesh was generated using the Quad/Tri/Pave face surface scheme and smoothed using the length-weighted Laplacian algorithm. The volume mesh was generated using the Tet/Hybrid/Tgrid scheme. The reconstructed geometry of the pulmonary airways is shown in Figure 1.

2. Mathematical modeling approach

Airflow over the pulmonary tract was simulated using a $k-\varepsilon$ model, modified with incorporated non-stationary features. Thus, fluctuations in air flow between inspiration and expiration periods were considered. A user defined function has been used in order to incorporate the real transient profile of the air velocity during inspiration and expiration periods.

2.1. Transport Equations for the $k - \varepsilon$ model

The following transport equations have been used to obtain the turbulence kinetic energy, k , and its rate of dissipation, ε :

$$\frac{\partial}{\partial t}(\rho k) + \frac{\partial}{\partial x_j}(\rho k u_j) = \frac{\partial}{\partial x_j} \left[\left(\mu + \frac{\mu_t}{\sigma_k} \right) \frac{\partial k}{\partial x_j} \right] + G_k + G_b - \rho \varepsilon - Y_M + S_k \quad (1)$$

and
$$\frac{\partial}{\partial t}(\rho \varepsilon) + \frac{\partial}{\partial x_j}(\rho \varepsilon u_j) = \frac{\partial}{\partial x_j} \left[\left(\mu + \frac{\mu_t}{\sigma_\varepsilon} \right) \frac{\partial \varepsilon}{\partial x_j} \right] + C_{1\varepsilon} \frac{\varepsilon}{k} (G_k + C_{2\varepsilon} G_b) - C_{2\varepsilon} \rho \frac{\varepsilon^2}{k} + S_\varepsilon \quad (2)$$

where:

- G_k represents the generation of turbulence kinetic energy due to the mean velocity gradients. It is calculated according to the following equation:

$$G_k = -\overline{\rho u_i u_j} \frac{\partial u_j}{\partial x_i} \quad (3)$$

- G_b represents the generation of turbulence kinetic energy due to buoyancy. It is calculated as follow:

$$G_b = \beta g_i \frac{\mu_t}{Pr_t} \frac{\partial T}{\partial x_i} \quad (4)$$

where Pr_t is the turbulent Prandtl number for energy and g_i is the component of the gravitational vector in the i^{th} direction.

The coefficient β , representing the coefficient of thermal expansion, has the following form:

$$\beta = -\frac{1}{\rho} \left(\frac{\partial \rho}{\partial T} \right)_p \quad (5)$$

For ideal gases, equation (4) reduces to:

$$G_{\rho} = -g_t \frac{\mu_t}{\rho P \tau_t} \frac{\partial \rho}{\partial x_t} \quad (6)$$

- Y_M represents the contribution of the fluctuating dilatation in compressible turbulence to the overall dissipation rate, calculated as:

$$Y_M = 2\rho\varepsilon M_t^2 \quad (7)$$

where M_t is the turbulent Mach number, defined as:

$$M_t = \sqrt{\frac{k}{a^2}} \quad (8)$$

where a represent the speed of sound.

The coefficients $C_{1\varepsilon}$, $C_{2\varepsilon}$, and $C_{3\varepsilon}$ are constants, σ_k and σ_ε are the turbulent Prandtl numbers for k and ε , respectively, and S_k and S_ε are user-defined source terms.

2.2 Model Constants

The model constants $C_{1\varepsilon}$, $C_{2\varepsilon}$, σ_k and σ_ε have the following default values (Fluent 6.3 User's guide, 2006):

$$C_{1\varepsilon} = 1.44, \quad C_{2\varepsilon} = 1.92, \quad \sigma_k = 1, \quad \sigma_\varepsilon = 1.3 \quad (9)$$

$C_{3\varepsilon}$ is calculated according to the following relation :

$$C_{3\varepsilon} = \tanh \frac{u}{v}. \quad (10)$$

The differential equations were discretized in the manner of finite element method. Mass flow boundary conditions have been specified at the geometry inlet. The trachea-bronchial tree wall was treated as rigid and the no-slip condition was imposed to its boundary.

The flow conditions are considered to be isothermal and incompressible. Transitional and turbulent flow is expected, that may be enhanced by the geometry at the bifurcations. To evaluate the transitional and turbulent flows in the system, a dispersed turbulence model has been considered.

2.3. The dispersed turbulence model

In our case, the concentrations of the secondary phase - the aerosol is dilute in the air continuous phase. Therefore, in order to appropriate model the flow inside the trachea-bronchial tree we used the dispersed turbulence model. In this case, inter-particle collisions are considered negligible. The primary phase is influencing the secondary phase random movement. Mass balance of the secondary phase can be characterized according to the characteristics of primary phase and the fraction of particle relaxation and eddy-particle interaction times.

Several assumptions are taken into account when dispersed method is used for modeling turbulence. These assumptions are the following ones:

- the use of standard $k - \varepsilon$ model, supplemented with additional terms including the interphase turbulent momentum transfer, to describe the turbulent predictions for the continuous phase;
- the prediction for turbulence quantities for the dispersed phases are obtained using the Tchen theory of dispersion;
- when dealing with turbulent multiphase flows, the momentum exchange terms consider the correlation between instantaneous distribution of the dispersed phases and the turbulent fluid motion.
- a phase-weighted averaging process is introduced for modeling the dispersion in turbulent multiphase flow.

2.4. Turbulence in the Continuous Phase

The mass balance considers the eddy viscosity. The form of the Reynolds stress tensor for the continuous phase q is the following one:

$$\overline{\tau}_{ij}^q = -\frac{2}{3}(\rho_q k_q + \rho_q \mu_{t,q} \nabla \cdot \vec{U}_q) \delta_{ij} + \rho_q \mu_{t,q} (\nabla \vec{U}_q + \nabla \vec{U}_q^T) \quad (11)$$

where \vec{U}_q is the phase-weighted velocity.

The turbulent viscosity $\mu_{t,q}$, in equation (9) takes the following form for the continuous phase q :

$$\mu_{t,q} = \rho_q C_\mu \frac{k_q^2}{\varepsilon_q} \quad (12)$$

and a characteristic time of the energetic turbulent eddies is defined as:

$$\tau_{t,q} = \frac{3}{2} C_\mu \frac{k_q}{\varepsilon_q} \quad (13)$$

where ε_q is the dissipation rate and $C_\mu = 0.09$ (Fluent 6.3 User's guide, 2006).

The length scale of the turbulent eddies is:

$$L_{t,q} = \sqrt{\frac{3}{2} C_\mu} \frac{k_q^{3/4}}{\varepsilon_q} \quad (14)$$

The equations for turbulence estimation, according to the modified $k - \varepsilon$ model, could be written as follows:

$$\frac{\partial}{\partial t} (\alpha_q \rho_q k_q) + \nabla \cdot (\alpha_q \rho_q \vec{U}_q k_q) = \nabla \cdot \left(\alpha_q \frac{\mu_{t,q}}{\sigma_k} \nabla k_q \right) + \alpha_q G_{k,q} - \alpha_q \rho_q \varepsilon_q + \alpha_q \rho_q \Pi_{k,q} \quad (15)$$

and

$$\frac{\partial}{\partial t} (\alpha_q \rho_q \varepsilon_q) + \nabla \cdot (\alpha_q \rho_q \vec{U}_q \varepsilon_q) = \nabla \cdot \left(\alpha_q \frac{\mu_{t,q}}{\sigma_\varepsilon} \nabla \varepsilon_q \right) + \alpha_q \frac{\varepsilon_q}{k_q} (C_{1\varepsilon} G_{k,q} - C_{2\varepsilon} \rho_q \varepsilon_q) + \alpha_q \rho_q \Pi_{\varepsilon,q} \quad (16)$$

The terms Π_{kq} and $\Pi_{\varepsilon q}$ represent the influence of the dispersed phases on the continuous phase q , and $G_{k,q}$ is the production of turbulent kinetic energy.

The term Π_{kq} takes the following form, M representing the number of secondary phases:

$$\Pi_{kq} = \sum_{p=1}^M \frac{\rho_{pq}}{\alpha_q \rho_q} (\langle \vec{v}_q'' \cdot \vec{v}_p'' \rangle + (\vec{U}_p - \vec{U}_q) \cdot \vec{v}_{dr}) \quad (17)$$

which can be simplified to:

$$\Pi_{kq} = \sum_{p=1}^M \frac{\rho_{pq}}{\alpha_q \rho_q} (k_{pq} - 2k_q + \vec{v}_{pq} \cdot \vec{v}_{dr}) \quad (18)$$

where k_{pq} is the covariance of the velocities of the continuous phase q and the dispersed phase p (calculated from equation 24 below), is the relative velocity, and is the drift velocity (defined by equation 29 below).

$\Pi_{\varepsilon q}$ has the following form:

$$\Pi_{\varepsilon q} = C_{3\varepsilon} \frac{\rho_q}{\rho_q} \Pi_{kq}, \quad (19)$$

where $C_{3\varepsilon} = 1.2$.

2.5. Turbulence in the Dispersed Phase

The turbulent kinetic energy, the dispersion coefficients, and the correlation functions of the dispersed phase are evaluated using the time and length scales characterizing the motion. The particle relaxation time in relation with inertial effects in the dispersed phase p has the following form:

$$\tau_{F,pq} = \alpha_p \rho_q K_{pq}^{-1} \left(\frac{\rho_p}{\rho_q} + C_V \right) \quad (20)$$

The Lagrangian integral time, is defined as:

$$\tau_{t,pq} = \frac{\tau_{t,q}}{\sqrt{1 + C_\beta \xi^2}} \quad (21)$$

where

$$\xi = \frac{|\vec{v}_{pq}| \tau_{t,q}}{L_{t,q}}, \quad (22)$$

and

$$C_\beta = 1.8 - 1.35 \cos^2 \theta \quad (23)$$

where θ is the angle between the mean particle velocity and the mean relative velocity (Fluent 6.3 User's guide, 2006).

The ratio between these two characteristic times is written as:

$$\eta_{pq} = \frac{\tau_{c,pq}}{\tau_{F,pq}} \quad (24)$$

Following Simonin (1990), FLUENT writes the turbulence quantities for dispersed phase p as follows:

$$k_p = k_q \left(\frac{b^2 + \eta_{pq}}{1 + \eta_{pq}} \right) \quad (25)$$

$$k_{pq} = 2k_q \left(\frac{b + \eta_{pq}}{1 + \eta_{pq}} \right) \quad (26)$$

$$D_{t,pq} = \frac{1}{3} k_{pq} \tau_{c,pq} \quad (27)$$

$$D_p = D_{t,pq} + \left(\frac{2}{3} k_p - b \frac{1}{3} k_{pq} \right) \tau_{F,pq} \quad (28)$$

$$b = (1 + C_v) \left(\frac{\rho_p}{\rho_q} + C_v \right)^{-1} \quad (29)$$

and $C_v = 0.5$ is the added-mass coefficient.

2.6. Interphase Turbulent Momentum Transfer

The turbulent drag term for multiphase flows $K_{pq}(\vec{v}_p - \vec{v}_q)$ is modeled as follows, accordingly to both dispersed p and continuous q phases:

$$K_{pq}(\vec{v}_p - \vec{v}_q) = K_{pq}(\vec{U}_p - \vec{U}_q) - K_{pq} \vec{v}_{dr} \quad (30)$$

The drift velocity is represented by the second term on the right-hand side of Equation (28), where:

$$\vec{v}_{dr} = - \left(\frac{D_p}{\sigma_{pq} \alpha_p} \nabla \alpha_p - \frac{D_q}{\sigma_{pq} \alpha_q} \nabla \alpha_q \right) \quad (31)$$

In the above equation the D_p and D_q phase's characteristic diffusivities, and σ_{pq} represent the dispersion Prandtl number.

In FLUENT, in case of Tchen theory in multiphase flows application, the diffusivities $D_p = D_q$ have the same value $D_{t,pq}$ and the dispersion Prandtl number σ_{pq} takes the default value of 0.75.

2.7. Boundary and initial conditions

The lung 3D model was imported in GAMBIT, a preprocessing software released by ANSYS, where the surface was meshed using the Quad/Pave algorithm. Then, the model volume was meshed with the use of the Tet/Hybrid/Tgrid algorithm, and the boundary conditions were set accordingly to the model region.

The working fluid is the air. Initial velocity profiles were specified as user defined functions developments.

The aerosol was injected in the air at the beginning of the first breathing cycle. The aerosol particles are modeled as a dilute dispersed phase flow in which the particle motion is controlled by fluid force and external forces acting on particles.

RESULTS AND DISCUSSION

The computation of the airflow field and aerosol particles dynamics, during breathing cycles, has been performed using the geometric parameters acquired from CT images.

A breathing cycle consists of one inspiration and one expiration period.

The respiration was simulated using a user-defined flow velocity function, which profile can be seen in Figure 2.

An unsteady-state air-particle mixture flow was simulated assuming a singular injection of the aerosols along the z-axis of the lungs geometry. The maximum amplitude of the breathing flow velocity was considered 9.8 m/s. The diameter of the particles was considered to be 0.1 μm. Two simulation scenarios have been considered: one of a single breathing cycle and the other of 4 breathing cycles.

The period for one breathing cycle was considered 3s, corresponding to the typical human inspiration-expiration sequence when resting.

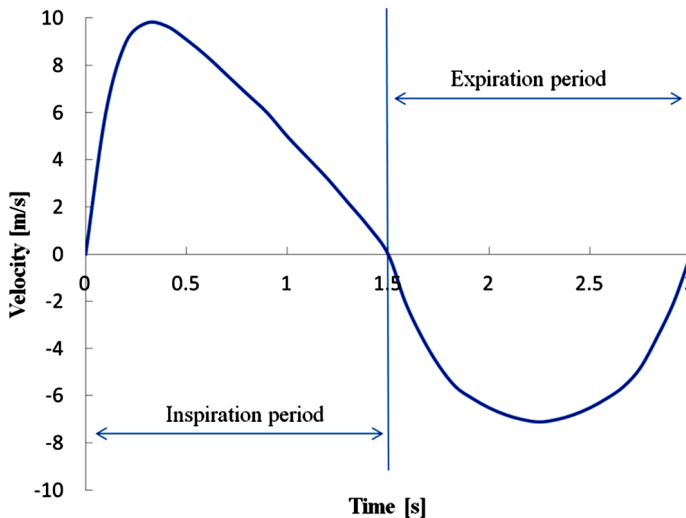


Figure 2. Profile of user defined function for air velocity

The domain of the 3D lung airways geometrical extent is presented in Table 1, considering the origin of the domain in the center of the 3D geometry, in an horizontal plane which intersects the geometry at the level of the main secondary bifurcation of the bronchi (see figure 1) of the investigation pulmonary tract geometry,

Table 1. Simulated lung airways geometry domain extent

Domain extents			
Xmin (cm)	-10.43	Xmax (cm)	11.30
Ymin (cm)	-6.20	Ymax(cm)	6.09
Zmin (cm)	-8.48	Zmax (cm)	18.60

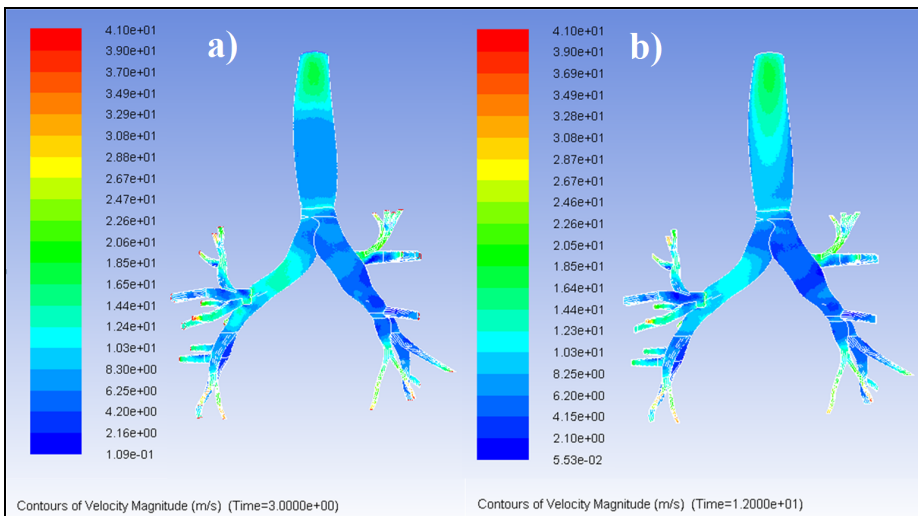


Figure 3. Contours of velocity magnitude along the simulated domain for 1 breathing cycle (a) and for 4 breathing cycles (b)

In order to predict the evolution of the fluid field, the nonlinear system of transport equations has been solved for dynamic state conditions.

The flow features could be observed in Figure 3 where the contours of velocity magnitude are illustrated for single cycle and for 4 breathing cycles.

In order to have a quantification of the air velocity values distribution, the histograms of velocity magnitude (Figure 4 - lower part) have been represented along the entire geometry domain extent in order to emphasize in a more comprehensive manner the differences between single cycle and 4 cycle breathing scenarios.

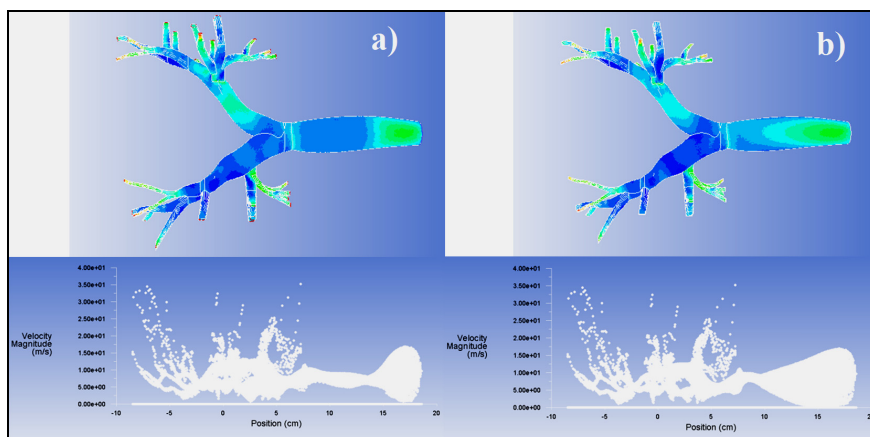


Figure 4. Histograms of velocity magnitude distribution for 1 breathing cycle (a) and for 4 breathing cycles (b)

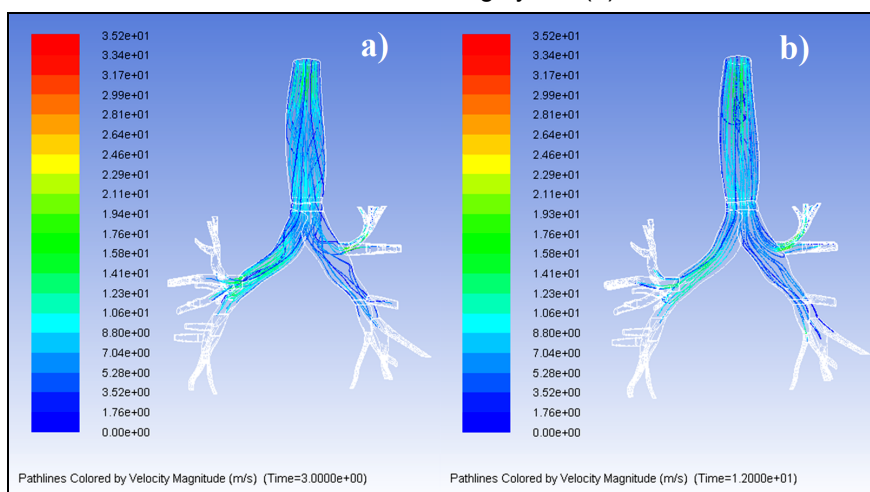


Figure 5. Path lines of the velocity magnitude for 1 breathing cycle (a) and for 4 breathing cycles (b)

Consistent differences are revealed in the upper and middle sections of the geometry, where initial aerosol injection and geometrical configuration of trachea-bronchial tree are strongly influencing the distribution of flow patterns. The flow characteristics could be also identified based on the profile of velocity magnitude path lines distribution (Figure 5). In Figure 5 (b), the case of the 4 breathing cycles, the uniformity of flow patterns could be observed. This suggests that the hydrodynamic equilibrium is established. Therefore, the results obtained for 4 breathing cycles are approaching in a more realistic manner the “reality” related to aerosol transport and deposition.

The distribution of aerosols mass fraction in the bulk of fluid (represented as contours of H₂O<liquid> mass fraction) along the simulated domain can be evaluated in Figure 6. The single and 4 cycles breathing simulations reveal different levels of aerosols mass fraction distribution in the air flux. Differences appear due to aerosol deposition and loss through expiration.

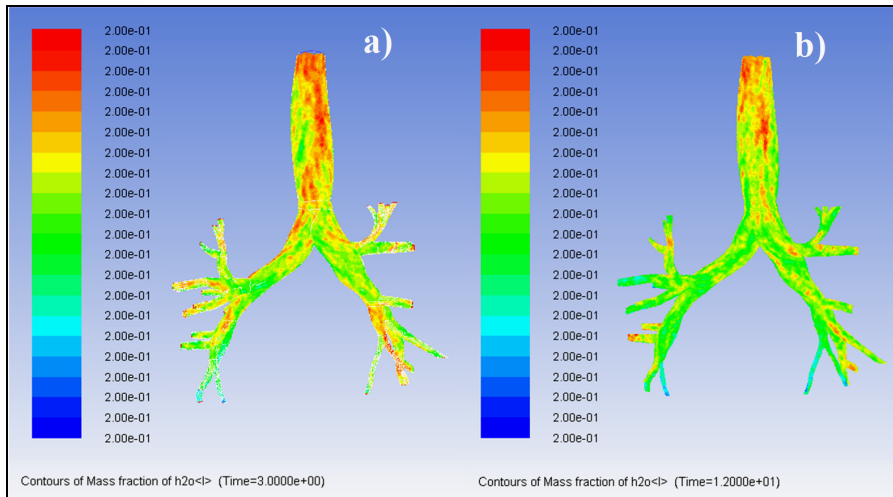


Figure 6. Contours of aerosols mass fraction distribution along the simulated domain for 1 breathing cycle (a) and for 4 breathing cycles (b)

The quantification of aerosols deposition could be done based on aerosol mass imbalance profiles, presented in Figure 7.

A precise evaluation of the aerosol deposition topography may be done through the profiles of the histograms of aerosol mass imbalance along the entire geometry extent, which are represented in Figure 8. The histograms have been realized along the axis x, y, and z, to cover the entire trachea-bronchial tree geometry. In this way, if needed, one can accurately identify regions or distances from the geometry inlet where preponderantly aerosol usually deposits.

To identify the trajectories of aerosol particles, their pathlines along the simulated airway geometry have been generated and presented in Figure 9. These can be thought of as a "recording" of the path of the fluid elements in the flow over a certain period of time. As it can be observed in Figure 9 (a), for single respiratory cycle simulation, the direction under which aerosol particles are predominantly distributed is strongly influenced by the geometrical configuration of the pulmonary tract and initial turbulence created by aerosol injection.

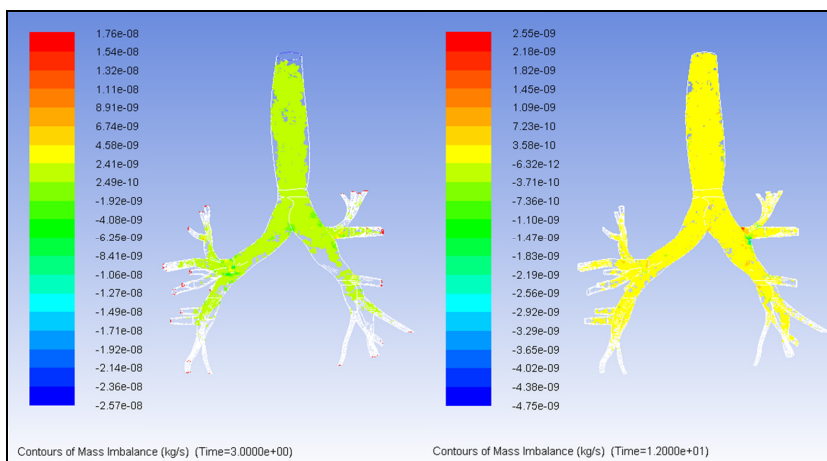


Figure 7. Profiles aerosol mass imbalance along the simulated domain for 1 breathing cycle (a) and for 4 breathing cycles (b)

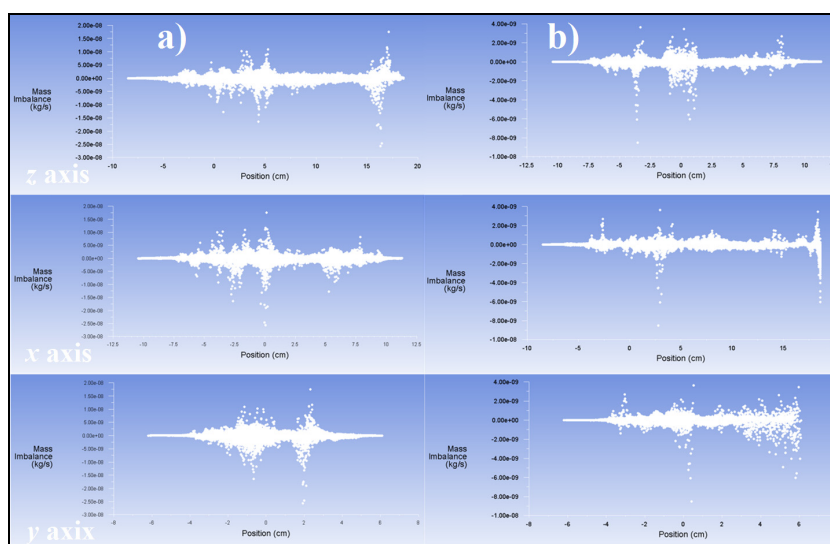


Figure 8. Histograms of aerosol mass imbalance along the z, x, y axes of the simulated domain for 1 breathing cycle (a) and for 4 breathing cycles (b)

After hydrodynamic equilibrium was established during the 4 respiratory cycles (Figure 9 (b)), a nearly uniform distribution of aerosol particles was observed. This characteristic reinforces the conclusion that an analysis that considers the results obtained from multi-cycle simulation is more appropriate to provide predictability and support for therapeutic decision, because it covers the real behavior of the phenomena involved in the breathing process.

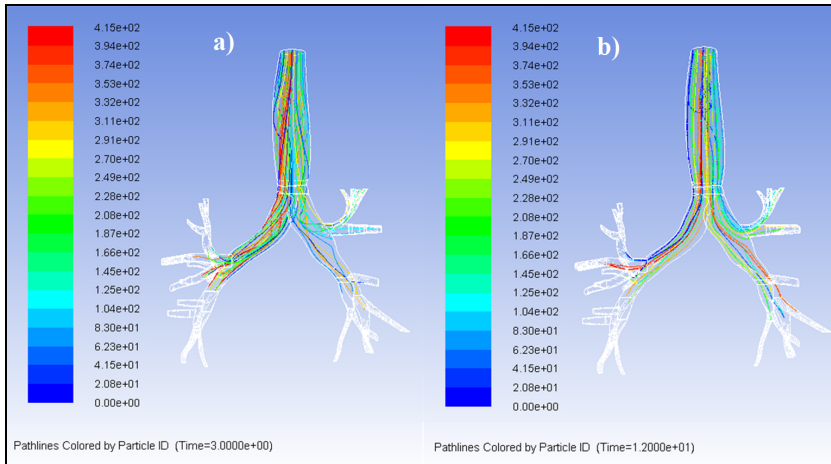


Figure 9. Path lines colored by the particles ID along the simulated geometry in case of single breathing cycle

This type of analysis could be done for all kinds of lung geometrical configurations, and in consequence this approach could be successfully used by physicians to optimize their treatment schemes, by identifying specific for each patient the aerosol transport and deposition characteristics.

CONCLUSIONS

Today, identifying ways in which prediction and monitoring of various human diseases is possible through noninvasive means represents a very important goal related to optimizing the medical practice. Along this path, CFD technique represents a very important tool. Both engineering and medicine are benefiting from its use, first of all because of its non-invasive nature, and second because of its capabilities, which arise from the possibility of characterization of fluid flow and particle transport and deposition topography.

Mathematical models based on CFD technique can be of great value when simulating regional deposition of particles, as functions of aerosol characteristics, ventilation parameters, and respiratory system morphology.

In this paper, besides the CFD technique, the CAD technique has been employed in the research. Based on it, the tridimensional real lung geometry was reconstructed from CT images. The 3D CT images based geometry was used to provide boundaries for the development of flow and aerosol transport phenomena. The mathematical approach for airflow simulations over the pulmonary tract considered a modified $k-\varepsilon$ model with incorporated non-stationary features. The unsteady state flow conditions have been imposed by

means of a user defined function for the inlet velocity profile. Two scenarios were analyzed, the first one of a single respiratory cycle, and the second one, of four respiratory cycles.

The air-aerosol particles mixture was modeled as a dilute dispersed phase flow. The particle motion was considered to be controlled by fluid forces and by the external forces acting on particles.

The evaluation of the fluid field behavior has been done through contours of velocity magnitude and through histograms of the velocity magnitude distribution.

Comparing the two breathing scenarios, consistent differences were revealed in the upper and middle sections of the geometry. In case of the 4 cycles breathing scenario, the hydrodynamic equilibrium was established. Therefore, 4 cycles breathing scenario could be used for a more realistic evaluation of aerosol transport and deposition along the lung geometry.

Analyzing the mass fraction of aerosol distribution along the simulated geometry, different levels of aerosol mass fraction have been observed when the two scenarios were simulated. The quantification of aerosol deposition has been done based on aerosol mass imbalance on axial profiles. The topology of the deposition sites has been accurately identified based on mass imbalance histograms, which have been represented for all spatial directions, covering in this way the entire extent of the trachea-bronchial tree geometry. Accordingly, the medical practice and/or aerosol generating devices can be optimized to enable the achievement of the expected results.

NOMENCLATURE

- u – overall velocity vector (m/s);
- ρ – density (kg/m³);
- k – turbulence kinetic energy (J/kg) ;
- ε – rate of dissipation;
- μ_t – turbulent viscosity (Pa/s);
- μ – dynamic viscosity (Pa/s);
- x – space coordinate (m);
- t – time coordinate (s);
- v – component of the flow velocity parallel to the gravitational vector (m/s);
- a – speed of sound (m/s);
- U – Free-stream velocity (m/s);
- I – turbulence intensity.

REFERENCES

1. Balásházy, I. et al., *Journal of Applied Physiology*, **2003**, 94, 1719.
2. Brand, P. et al., *European Respiratory Journal*, **1977**, 10(2), 460.
3. Chalupa, D.C. et al., *Environmental Health Perspectives*, **2004**, 112(8), 879.
4. Darquenne, C., Paiva, M., *Journal of Applied Physiology*, **1996**, 80, 1401–1414.
5. FLUENT 6.3 User's Guide (2006).
6. Grgic, B. et al., *Journal of Aerosol Science*, **2004**, 35, 1025.
7. Geng, T. et al., *Journal of Aerosol Science*, **2011**, 42(11), 781.
8. Harrington, L. et al., *Journal of Aerosol Science*, **2006**, 37, 37.
9. Heenan, A.F. et al., *Journal of Aerosol Science*, **2004**, 35, 1013.
10. Heyder, J. et al., *Journal of Applied Physiology*, **1988**, 64, 1273.
11. Hiller, F., "Therapeutic aerosols: An overview from a clinical perspective", Marcel Dekker: NewYork, **1992**, pp. 289–306.
12. Hofmann, W. et al., *Journal of Aerosol Science*, **2002**, 33(2), 219.
13. ICRP, "Human Respiratory Tract Model for Radiological Protection", ICRP Publication 66. Ann. ICRP, **1994**, 24 (1-3).
14. Koblinger, L., Hofmann, W., *Journal of Aerosol Science*, **1990**, 21, 661.
15. Lee, D.Y., Lee, J.W., *Journal of Aerosol Science*, **2002**, 33(9), 1219.
16. Martonen, T. et al., *Advanced Drug Delivery Reviews*, **2003**, 55(7), 829.
17. Park, S.S., Wexler, A.S., *Journal of Aerosol Science*, **2007a**, 38(2), 228.
18. Park, S.S., Wexler, A.S., *Journal of Aerosol Science*, **2007b**, 38(5), 509.
19. Park, S.S., Wexler, A.S., *Journal of Aerosol Science*, **2008**, 39, 266.
20. Sarangapani, R., Wexler, A.S., *Toxicological Sciences*, **2000**, 54(1), 229.
21. Schiller-Scotland, Ch.F., *Toxicology Letters*, **1994**, 72(1–3), 137.
22. Simonin, C., Viollet, P.L., *Numerical Methods for Multiphase Flows*, **1990**, 91, 65.
23. Singh, S., *Current Anaesthesia & Critical Care*, **2003**, 14(2), 74.
24. Smith, J.R.H. et al., *Journal of Aerosol Science*, **1997**, 28(S1), S431.
25. Sturm, R., Hofmann, W., *Bulletin of Mathematical Biology*, **2004**, 69(1), 395.
26. Ultman, J.S. "Gas transport in the conducting airways. In: L. A. Engel, and M. Paiva (Eds.), *Gas Mixing and Distribution in the Lung*", Dekker: NewYork, **1985**, pp. 63–136.
27. Yeh, H., Schumacher, G., *Bulletin of Mathematical Biology*, **1980**, 42, 461.
28. Zhang, Z. et al., *Journal of Aerosol Science*, **2002**, 33, 257.

*Dedicated to Professor Liviu Literat
On the occasion of his 85th birthday*

METAMODELING LEVEL OF POLLUTION BASED ON OPERATING PARAMETERS OF A THERMO POWER STATION

CĂLIN I. ANGHEL^{a,*}, DANIELA J. CHELARU^a

ABSTRACT. In process industries objectives as improving performance, reducing pollutant emission or predicting feasible operating conditions requires analysis based on complicated mathematical models and procedures. For quickly but reliable assessments besides of cumbersome approaches of potential support are so-called metamodeling techniques. The paper presents a metamodeling procedure belonging to artificial intelligence in a minimax approach able to assess predictions, trend and correlations to establish a safety-operating domain. The proposed procedure was compared with a robust total least squares regression based on principal component analysis. Numerical experiments are related to dependencies between the level of pollution and operating parameters of a thermo power station.

Keywords: *metamodeling, minimax probability, regression, classification, prediction, harmful level of pollution, operating parameters.*

INTRODUCTION

Many industrial activities produce pollutant emissions that affect the quality of environment and human health. Improving process quality and performance, predicting trends or feasible operating domain are important targets in process industries. Generally solving such problems requires complicated models, expensive analysis and simulation together with cumbersome correlations of many operating parameters and pollutant emissions concentration. In order to reach a high level of accuracy often these analyses becomes computational burden. To address such a challenge,

^a *Universitatea Babeş-Bolyai, Facultatea de Chimie și Inginerie Chimică, Str. Kogălniceanu, Nr. 1, RO-400084 Cluj-Napoca, Romania, * canghel@chem.ubbcluj.ro*

approximation-empirical or metamodeling techniques are often used. These models of reduced order developed for expensive simulation process in order to improve the overall computation efficiency are also known as “surrogate” models [1-3]. A metamodel replaces a true functional relationship $g: \mathfrak{R}^n \mapsto \mathfrak{R}$ and know values $y_i = g(x_i)$ at some selected input variables usually called sampling points ($\mathbf{X} = \{x_1, \dots, x_m\}$, $\mathbf{X} \in \mathfrak{R}^n$), by an empirical mathematical expression $\tilde{g}(x)$ that is much easier to evaluate. Thus, “surrogates” of the objectives functions can replace the original functional relationship as, $g(x) = \tilde{g}(x) + \varepsilon(x)$. Based on correlated input-output values, parameters of the model are fit to approximate the original data in a best possible way. Among the well-known metamodeling techniques, it can be mentioned: response surface, radial basis function, Gaussian process also known as kriging, high dimensional model representation, artificial neural network, genetic algorithms, support vector machine and many others. The main goal of this paper is to implement a metamodel-based approach able to represent the behaviour of pollution level according some operating parameters into a unit plant. For unity and generality the level of pollution due to the pollutant emission will be assess by the harmful level of pollution. The metamodel based on artificial intelligence methods in a minimax manner is able to assess predictions, trends and dependencies between pollutant emission concentrations and operating parameters. Much more the metamodel can be used into a first step for approximation of optimal domain in which a unit plant can be safely operated. Comparative numerical experiments with a powerful total least squares regression based on principal component analysis (TLS-PCA) are presented. The numerical examples are related to some pollutant emission concentrations expressed by a harmful level of pollution and some operating parameters of an industrial thermo power station. The implementation of the procedure and numerical experiments were developed as a user-friendly computer application in MATLAB language. The results point out the ability of proposed procedure at least into: (1) predicting parameters of interest to facilitate monitoring purposes, (2) approximating trends and correlated dependencies between pollutant emission concentrations and operating parameters to ensure feasible performance.

RESULTS AND DISCUSION

Theoretical foundation

The core of procedure is based on a novel type of pattern recognition machine developed in a minimax manner. The procedure casts both regression (numerical values as outputs) and classification problems (class labels as

outputs) into a unified technique. Basic principles of these types of classification approach named minimax probability machine and regression approach named minimax probability machine regression were previously published [4-5]. Some depicted and proved advantages of the implemented procedure over many regression procedures must be mentioned: (a) avoids the specific problems such as over-fitting and local minima, (b) relative less influenced by outliers, (c) provides an explicit direct upper bound on the probability of misclassification of new data, without making any specific distribution assumptions (d) good generalisation ability. Detailed principles also a basic flowchart of implemented procedure and others were previously presented [6-8]. In the present paper only fundamentals principles will be presented.

For predictive purposes, a minimax regression approach was built as in Strohmann and. Grudic [5] by maximising the minimum probability of future predictions to be within some bound ($\pm\epsilon$) of the true regression function. Starting from some unknown regression function formally expressed as $f: R^d \rightarrow R$ and

$$f \Rightarrow y = f(z) + \rho \quad (1)$$

the task is to construct an approximation for y as \hat{y} such that for any

$$z \in R^d, \hat{y} = \hat{f}(z). \quad (2)$$

To avoid some mathematical limitations based on a kernel formulation minimax probability machine regression model will approximate this function not into a real Euclidean space but into a space of high dimension, named as feature space, by:

$$f \Rightarrow \hat{f} \Rightarrow \hat{y} = \hat{f}(z) = \sum \beta_i K(z_i, z) + b_k \quad (3)$$

Here $K(z_i, z) = \Phi(z_i) \cdot \Phi(z)$ in the feature space is so-called kernel function satisfying Mercer's conditions. By this kernel function we simply map data from a real Euclidean space into a higher dimensional space named as feature space through a non-linear mapping function $\Phi(\dots)$. In this context, a kernel represents a legitimate inner product into a high dimensional feature space, that is basically a Hilbert space. The others, β_i are weighting coefficients and ' b_k ' offset of the minimax regression model, obtained as outputs of the minimax probability machine regression from the learning data. The nonlinear regression function (eq.3) is only a formal basic function formulation. Because $\Phi(\dots)$ is done implicitly, all related computations would be carried by kernel function into a high dimensional feature space. Instead of ' d ' features now ' n ' features represent inputs vectors and the kernel map evaluates at all of the other training inputs. Generating two classes that are obtained by shifting the dependent variable $\pm\epsilon$ the regression problem was

reduce to a binary classification problem into features space. The regression surface is interpreted as being the boundary that separates the two classes, **successfully** and **wrongly** predicted. Into this feature space, a linear classifier-surface between the two classes of points corresponds to a high non-linear decision-hyper plane into original Euclidean input space. Therefore, a linear regression into the features space corresponds to a cumbersome and high non-linear regression into a real Euclidean space.

If a binary classifier is built to separate the two sets of points (**successfully** and **wrongly** predicted), then finding a crossing point \hat{y} at where the classifier separates these classes for some inputs named as $\mathbf{z} = (z_1, \dots, z_d)$, is equivalent to finding the output of the regression model for these inputs for any $z_i \in \mathbf{R}^d$. Basically as was stated in minimax probability machine by Lanckriet [4] into a binary classification problem of \mathbf{z} random vectors, with \mathbf{z}_1 and \mathbf{z}_2 denoting random vectors from each of two classes as $\mathbf{z}_1 \in \text{Class 1}$ and $\mathbf{z}_2 \in \text{Class 2}$, a hyper plane can separates these points, with maximal probability in respect to all distributions having mentioned means \bar{z}_1, \bar{z}_2 and covariance matrices $\Sigma z_1, \Sigma z_2$. This hyperplane

$$H(\mathbf{w}, b) = \{ \mathbf{z} | \mathbf{w}^T \cdot \mathbf{z} = b \}, \text{ where } \mathbf{w} \in \mathbf{R}^n \setminus \{0\} \text{ and } b \in \mathbf{R} \quad (4)$$

that separates the two classes of points with maximal probability with respect to all distributions must to obey the conditions:

$$\max_{\alpha, \mathbf{w} \neq 0, b} \alpha \quad s.t. \quad \begin{cases} \inf_{\mathbf{z}_1 \left(\bar{z}_1, \Sigma z_1 \right)} \text{Prob} \left\{ \mathbf{w}^T \cdot \mathbf{z}_1 \geq b \right\} \geq \alpha \\ \inf_{\mathbf{z}_2 \left(\bar{z}_2, \Sigma z_2 \right)} \text{Prob} \left\{ \mathbf{w}^T \cdot \mathbf{z}_2 \leq b \right\} \geq \alpha \end{cases} \quad (5)$$

Related to a minimax probability machine approach the classifier must to minimise this misclassification probability by an optimal separating hyperplane, named minimax probabilistic decision hyperplane. The implemented procedure operates on two data sets: (1) training (learning) data to establish the best model-choosing the best mapping function $\Phi(\dots)$ and (2) testing to evaluate the errors.

The procedure is conducted in a crude manner, without outliers' detection. To ensure a good distribution of the data the simulations were realised based on data cyclic randomly divided into a number of distinct learning and testing subsets. The errors were estimated by testing rather than by calculation during the training steps (learning and testing) in order to build and estimate the model. To carry out the most basic testing method

(simple testing) a random percentage of the database (10-30%) is set aside and used in testing step. The implementation was developed as a user-friendly computer application in MATLAB software and works in multiple cyclic steps (“ k ” cyclic experiments). The performance of procedure was investigated based on the following model validation metrics:

- relative error between the predicted (outputs) and the corresponding test t values

$$RE = \left(\frac{(Y_{predicted} - Y_{test})}{Y_{predicted}} \right) \times 100 [\%]. \quad (6)$$

- simple equivalent linear dependency between the predicted (outputs) and the corresponding test values:

$$Y_{predicted} = a \cdot Y_{test} + b, \quad (7)$$

where a and b represents the slope and intercept of the equivalent linear dependency model, respectively. Better predictions, means a index close to unity and b index close to zero value. The performance criterions are evaluated with all values reconvered into the original real Euclidian R^d space. To obtain generalisation the best models will be establish after a number of “ k ” cyclic experiments (simulations). Formally, the best model means model that performs best. It involves best kernel function, kernel parameters and outputs. Basically as previously mentioned Lanckriet, et al. [4] one typically has to choose manually or determine it by tenfold cross validation. This time we preferred a simple-empirical principle for setting the type of the kernel function. The best model over these “ k ” cyclic simulations and the corresponding output values emerged from the procedure was chosen as the *best model*. Long random trials ($k > 100$) do not get improved accuracy and predictions that are more reliable. According some statements [9,10] we limit the trials to $k = \leq 100$. The proper size and selection of the training set (randomly divided into learning and test subsets) is very important to increase the performance of the algorithm. Regarding this, there are no an agreed approached concerning the dimension and the selection of the training set. However, it is a commonly agreed idea, which states that training set must be sufficiently large compared with the number of features/variables.

Case study

This section presents a numerical application of proposed metamodeling technique, related to pollutant emission concentrations and operating parameters of a thermo power station. The acquired data consists of a multivariate set of pollutant emission concentrations measured on the top of an industrial stack of a thermo power station and operating parameters. The statistics of this data set

are presented in Table 1. The data set contains 64 daily measured values of operating parameters as: temperature of gaseous releases (T_G) coke content of C, S, humidity, coke specific caloric power and pollutant emission concentrations for SO_2 , NO , NO_x , and CO . A general level of pollution from a gaseous release source may be done reporting current values of pollutant emission to the critical concentration C_R representing the value of the 'dangerous concentration' of particular interest. This general level of pollution named harmful level of pollution (*HLP*) were assessed by the following basic relation [7]:

$$HLP = \sum_{i=1}^n C_i / C_{ai} \quad (8)$$

where, C_i current pollutant concentration, C_{ai} admissible/critical pollutant concentration and n the number of considered pollutants.

Table 1. The main values of pollutant emissions and operating parameters

Parameters (operating conditions)					
	<i>Percentage content of coke analyse</i>				<i>Coke specific caloric power</i>
	T_G [°C]	C [%]	S [%]	Humidity [%]	[kcal/kg]
<i>Range</i>	269 ÷ 136	20.8 ÷ 19	2.88 ÷ 2.32	26.1 ÷ 23	1875 ÷ 1740
<i>Mean value</i>	200.1	20.3	2.50	24.8	1799
<i>Standard deviation</i>	55.18	0.43	0.112	0.78	36.34
Pollutant emission concentrations [ppm]					
	SO₂	NO	NO_x	CO	
<i>Range</i>	726 ÷ 145	134 ÷ 54	208 ÷ 77	399 ÷ 70	
<i>Mean value</i>	391.7	97.4	130	152.6	
<i>Standard deviation</i>	158.5	22.23	34.52	73	
<i>Critical concentration</i>	400	140	230	200	

The critical values of polluting emissions are reported to industrial pollutant emissions for solid fuel elements in burning type II installations according to *Romanian HG- 541/2003*

According eqs.(8) an accepted level of pollution means *HLP* close to unity. Numerical application was developed according with this harmful level of pollution (*HLP*). After the model is generated on random training database, it is used to predict on random test database. In other words it is random validated. This time the kernel type that yields to the best performance (eqs.6-7) was an exponential radial basis function with standard width kernel (σ) tuned using 10-fold cross validation. The results were compared with those obtained by a well-known total least squares regression based on principal component analysis (*TLS-PCA*). To ensure a real comparison between these procedures, they were conducted to work on the same learn and test subsets. Table 2 presents the main conditions and results of procedures for the best model obtained after cyclic simulations.

Table 2. The main results and conditions of predictions for best metamodel

	TLS-PCA	Minimax metamodel
Criteria of performance on test data set		
<i>Range of relative errors RE (eq.6)</i>	-140÷40 [%] based on Fig. 2	-5,377÷0 [%] based on Fig. 1
<i>Coefficients of equivalent linear dependency (eq.7)</i>	a = 0.754 b = 1.115 based on Fig. 2	a = 1 b = -0,029 based on Fig. 1
Criteria of performance on unseen-validation data set		
<i>Range of relative errors RE (eq.6)</i>	-1441÷41 [%]	-5,377÷10 [%]
<i>Coefficients of equivalent linear dependency (eq.7)</i>	a = 1.918 b = -1.746	a = 0.992 b = 0,028
<i>Formal kernel functions – exponential radial basis function</i>		
$K(\mathbf{x}_i, \mathbf{x}_j) = \exp\left(-\frac{\ \mathbf{x}_i - \mathbf{x}_j\ ^2}{2\sigma^2}\right)$		

Results related to test data reveal relative good performance for both procedures. Predicted and test harmful level of pollution (*HLP*) are in reasonable agreement because range of relative errors of both procedures presents a good adjustment. However *TLS-PCA* depicts a high range of relative errors than our procedure (Table 2 and Fig. 1-2). Results of predictions on unseen-validation data set (Table 2) are a little worse than those previously reported. Our metamodel retrieves this drawback by the range of relative errors less than 10% which suggest good generalisation capability. The dependency between predicted and corresponding test values illustrated based on simple equivalent linear dependency reveals also reasonable accurate results. Certainties of predicted values are established in a 95 % confidence interval. Regarding the robust regression technique, the results (Table 2) suggest a poor generalisation capability. By these reasons, only our metamodel was utilised into new correlated predictions to assess dependencies between the harmful level of pollution (*HLP*) and some operating parameters of a thermo power station (Fig. 3-4). Until now, all predictions reflecting dependencies and trends are correlated. Based on proved generalisation capability of our metamodel we extend a well-known principle of artificial neuronal network as in [11] to examine the effect of any individual input of interest on the output variable. This means to establish an uncorrelated functional dependency. This may be very difficult in reality or in some cases impossible to do in other way.

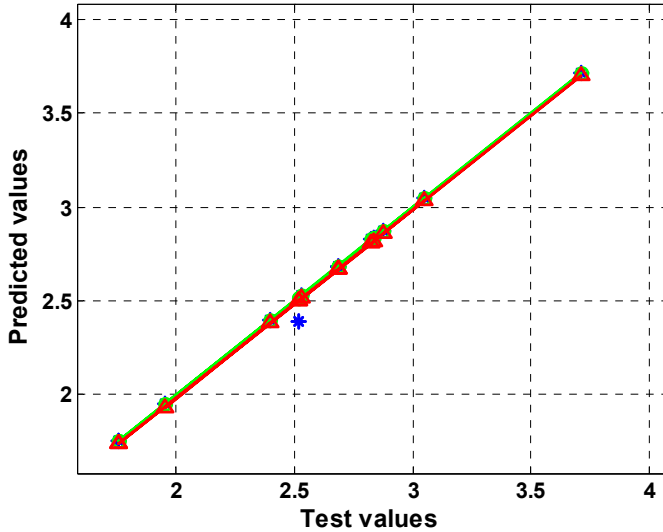


Figure 1. The performance of metamodel on test set.
 red ∇ - simulated values; blue * - test/predicted values;
 green \circ – ideal hypothetical simple equivalent linear dependency

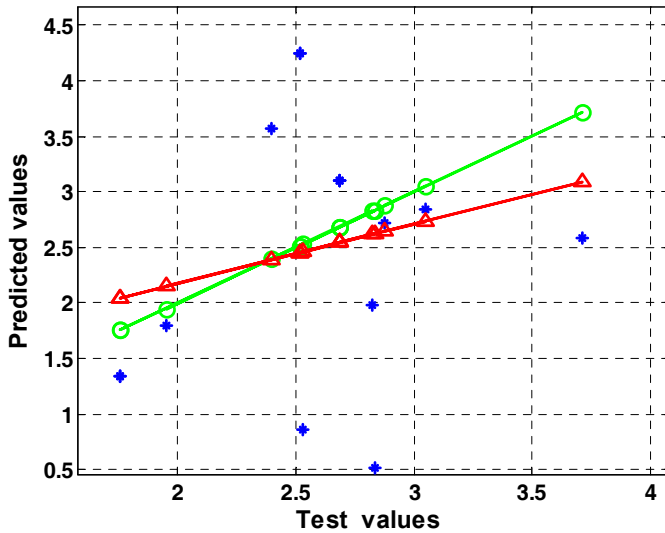


Figure 2. The performance of robust regression technique on test set.
 red ∇ - simulated values; blue * - test/predicted values;
 green \circ – ideal hypothetical simple equivalent linear dependency

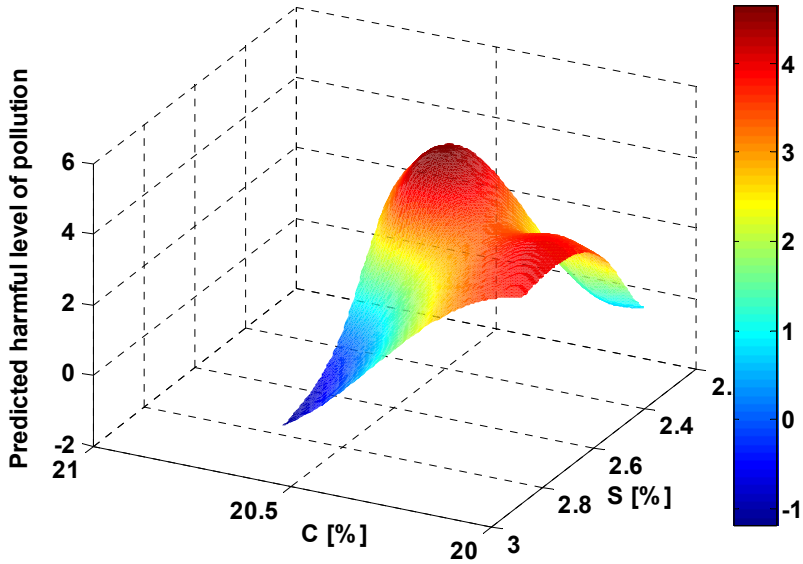


Figure 3. Correlated predicted dependencies between HLF and (C, S) content.

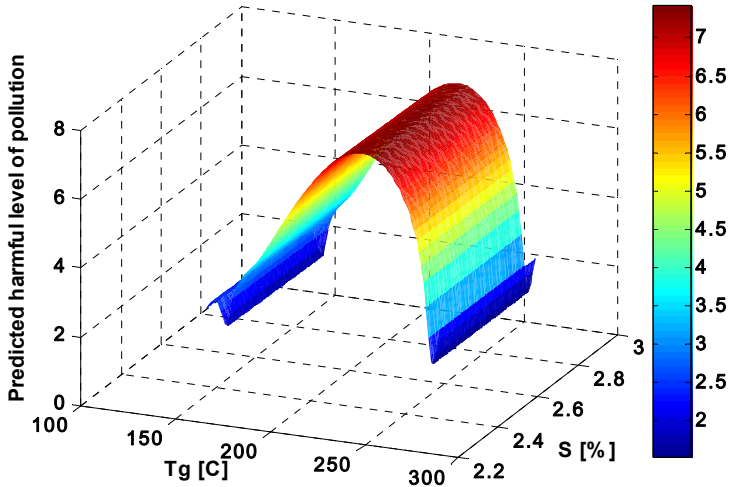


Figure 4. Correlated predicted dependencies between HLF and (T_G, S) content.

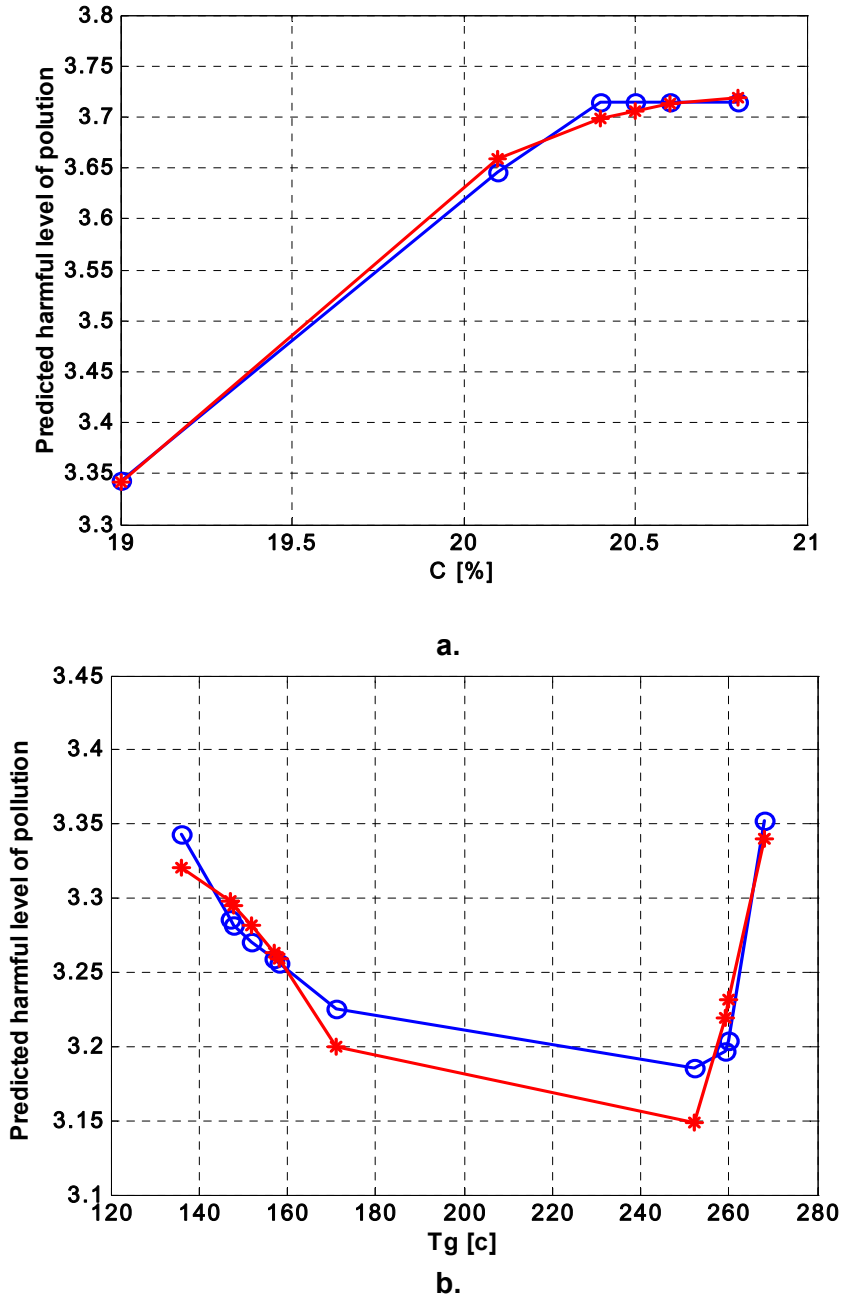


Figure 5. Uncorrelated functional dependency between harmful level of pollution (*HLP*) and some functional parameters.
 blue o – predicted values of *HLP*; red * - polynomial fitted values.

Analysing correlated dependencies (Fig. 3-4) between harmful level of pollution (*HLP*) and some operating parameters we can identify that correlated dependencies of T_G , S produce a level of pollution higher than those due to C , S . Based on these correlated dependencies and others many times it is possible to adjust some operational parameters to decrease the dangerous level of pollution.

Regarding the effect of an individual input of interest on the harmful level of pollution the solution involves the use of the best metamodel (that preserves the best non-linear interactions between all variables) to perform virtual experiments. These virtual experiments predict outputs variations (Fig. 5) with any individual input variable (keeping the values of the other input variables at constant values within their range-usually at their nominal-mean values in the training data). This time inputs of interest were chosen operating parameters as: coke content of C (Fig. 5a) and temperature of gaseous releases T_G (Fig. 5b). As a result, our metamodeling procedure can be promoted as a valid procedure for simple monitoring activities or quickly assessment of feasible operational parameters of a thermo power station into a reasonable level of pollution. It is clear by the values of harmful level of pollution (*HLP*) that basically thermo power station works in a wrong way. Therefore future developments based on optimisation tasks need to establish a feasible and safety operating domain.

CONCLUSIONS

The paper presents the feasibility of applying a novel metamodeling procedure to estimate dependencies of concentration of pollutant emissions generalised into a harmful level of pollution and operational parameters of a thermo power station without the relational physics or analytic being explicitly or known. By principle this metamodeling procedure, represents a pattern recognition and classification task. The procedure casts both regression and classification problems into a unified technique able to predict trends, correlations and various dependencies. The procedure performs highly complex mappings into high dimensional space on nonlinearly related data, by inferring subtle relationships between input and output parameters. Used it with an appropriate policy related to environmental protection it could leads to a drop from industrial pollutant emissions and hence to decrease the atmospheric level of pollution.

This procedure can be a promising alternative for engineers dealing with risk pollution to work out optimal feasible operating conditions according to the regulations and beyond this one to other engineering domains. Because of these, we consider opportune to promote our procedure as predictive tool towards real engineering applications at least as a simple preliminary investigation before any cumbersome operational optimisation of process.

REFERENCES

1. T. Chena, K. Hadinoto, W. YAN W, Y. MA, *Computers & Chemical Engineering*, **2011**, 35, 502.
2. N.V. Queipoa, R.T. Haftka, W. Shyy, T. Goel, R. Vaidyanathan, P.C. Tucker, *Progress in Aerospace Sciences*, **2005**, 41, 1.
3. G.G. Wang, S. Shan, *ASME Transactions, Journal of Mechanical Design*, **2007**, 129, 370.
4. G.R.G. Lanckriet, E.L. Ghaoui, C. Bhattacharyya, M.I. Jordan, *Journal of Machine Learning Research*, **2002**, 3, 555.
5. T.R. Strohmann, G.Z. Grudic, in: S. Thrun, S. Becker, K. Obermayer (Eds.), *Advances in Neural Information Processing Systems*, **2003**, 15, MA: MIT Press, Cambridge, 769.
6. C.I. Anghel, Al. Ozunu, *Chemical Paper*, **2006**, 60, 410.
7. C.I. Anghel, *Revista de Chimie*, **2006**, 57, 773.
8. C.I. Anghel, M.V. Cristea, *Revista de Chimie*, **2010**, 61, 87.
9. A. Bordes, S. Ertekin, J. Weston, L. Bottou, *Journal of Machine Learning Research*, **2005**, 6, 1579.
10. Y-J. Lee, O.L. Mangasarian, RSVM: Reduced Support Vector Machines, Computer Sciences Department, University of Wisconsin, Madison, WI 53706, **2000**, olvi@cs.wisc.edu.
11. H.K.D.H. Bhadeshia, *Statistical Analyses. Data Mining*, **2009**, 1, 296.

*Dedicated to Professor Liviu Literat
On the occasion of his 85th birthday*

KINETIC ANALYSIS OF THERMAL DECOMPOSITION OF THE LIMESTONE AND PRECIPITATE CALCIUM CARBONATE

SIMION DRĂGAN^a

ABSTRACT. In this paper, decomposition reaction of limestone and precipitate calcium carbonate (PCC) was investigated, using thermo gravimetric analysis technique. All experiments were performed in isothermal conditions, within a temperature range of 973-1173 K, with main diameters of granules: 63 μ m, 180 μ m, and 450 μ m. The temperature influence was found using Arrhenius law. The reaction rate constant k and activation energy E_a have been determined. The values were found to be between: $k=1.8 \times 10^{-3}$ - $4.4 \times 10^{-3} \text{ s}^{-1}$, $E_a=139,9$ KJ/mol for limestone and $k=2.1 \times 10^{-3}$ - $6.5 \times 10^{-3} \text{ s}^{-1}$, $E_a=124,9$ KJ/mol for PCC, according to the values reported in the literature.

Keywords: *Ca-looping process, calcium oxide as adsorbent of the CO₂, decomposition reaction, rate constant, activation energy.*

INTRODUCTION

Increasing atmospheric CO₂ emissions from fossil fuel combustion systems is responsible for the effect on global warming. Calcium oxide (CaO) is recognized as an efficient carbon dioxide adsorbent and separation of CO₂ from gas stream [1,2].

The Ca-looping process is a promising technique for reducing CO₂ emissions from the power generation sector. The basic idea of the calcium looping process is to use calcium oxide as sorbent of the CO₂ to form CaCO₃, and regeneration of the sorbent (calcination of CaCO₃). Utilization of calcium-based adsorbent in a process based on chemical looping from the gas stream through the calcination and carbonation process is extensively applied in the gas purification process [2,3,4].

^a "Babeş-Bolyai" University, Faculty of Chemistry and Chemical Engineering, Arany Janos 11, 400028 Cluj-Napoca, sdragan@chem.ubbcluj.ro

Thermal decomposition of limestone has been the subject of many studies over the years due to its importance in the industry and lately it is well known that calcium carbonate is used in calcium looping CO₂ capture systems [5,6,7,8].

The most used adsorbents are different assortments of natural and synthetic calcium carbonate: limestone, dolomite, precipitate calcium carbonate, etc. Under identical experimental conditions, the reactivity of these adsorbents is significantly influenced by their chemical structure and composition.

The kinetics of calcination is complicated by several factors which are: decomposition temperature, concentration of CO₂, sizes of the solids particle and also impurities. Calcination is favored by the high temperature as it is an endothermic reaction which needs low decomposition pressure of CaCO₃ in order to drive the equilibrium reaction forward [10].

Calcium oxide is an efficient carbon dioxide adsorbent, especially at high temperature. The temperature for decomposition of the adsorbent is a function of its origin, particle size and chemical reactivity.

Kinetic studies of different limestones have been investigated by many researchers [6,7,10,11,12] but there has not been reported work on that of precipitate calcium carbonate which is abundantly present in waste deposits of NP fertilizer industry.

In this research study, the potential of waste precipitate calcium carbonate, sources for CaO adsorbent compared with natural limestone was investigated. Since the microstructure of the solid adsorbent has an important influence over its reactivity, the main objectives of this work are the kinetic analysis of the process of natural and precipitate calcium carbonate (PCC) decomposition.

The decomposition process was realized at temperatures between 973-1173 K and atmospheric pressure in a TGA. Evolution of the decomposition degree during the heating and calcination intervals of the limestone and PCC sample for three particle size was established.

RESULTS AND DISCUSSION

The chemical composition of the limestone and precipitate calcium carbonate (PCC) has been determined and is summarized in Table 1.

Table 1. Composition of limestone and precipitate calcium carbonate

Carbonate source	Composition			
	CaCO ₃ [%]	Fe ₂ O ₃ [%]	Al ₂ O ₃ [%]	SiO ₂ [%]
Limestone Săndulești - Turda	97	1,8	0,88	0,3
Precipitate Carbonate (waste) PCC	CaCO ₃ [%] 96,7	Fe ₂ O ₃ [%] 0,8	NH ₄ NO ₃ [%] 1,2	humidity[%] 0,7

To determine the crystallographic structure and to compare the two types of carbonates has been carried out the structure analysis. IR spectra are shown in Figure 1.

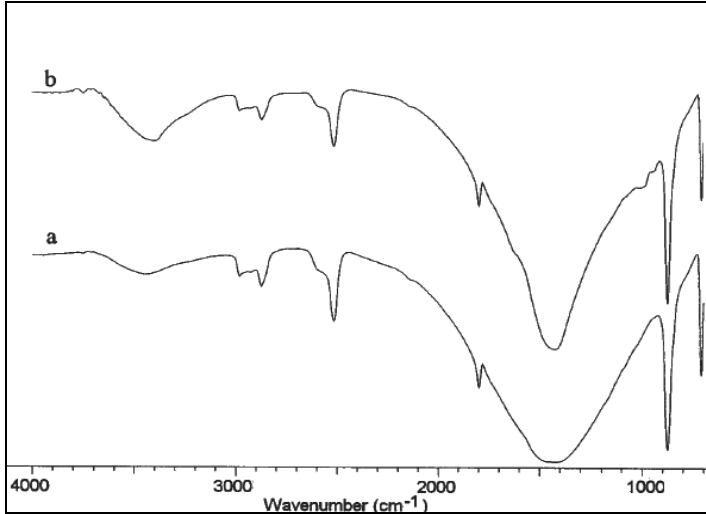


Figure 1. IR spectra of calcium carbonate. a.) - precipitated calcium carbonate (waste) of NP fertilizer industry; b) – natural limestone from Săndulești-Turda

IR spectra shows that chemical and crystallographic structure of the two types of carbonates are not significantly different. They presented same maximum and minimum absorbance curve, precipitated calcium carbonate wider band corresponding wavelength 1450 cm^{-1} can be attributed to the degree of crystallinity lower than that derived its rock.

Evolution of the limestone and PCC decomposition for all grain sizes was followed by means of decomposition degree η_D . On the basis of the material balance, the decomposition degree η_D can be described by equation (1):

$$\eta_D = \frac{m_S^0 - m_S}{m_S^0 \cdot \bar{x}_{PC}^0} = \frac{1}{\bar{x}_{PC}^0} \left(1 - \frac{m_S}{m_S^0} \right) \quad (1)$$

where: m_S^0, m_S – initial and at a given moment sample mass [mg];

\bar{x}_{PC}^0 – mass fraction of the calcination losses (0,4397-limestone and 0,41427PCC) was determined as arithmetical average in four values obtained samples subjected to calcination at 1323 K for two hours.

The particle sizes and temperature influence on the decomposition degree are presented in figures 2, 3, 4, 5.

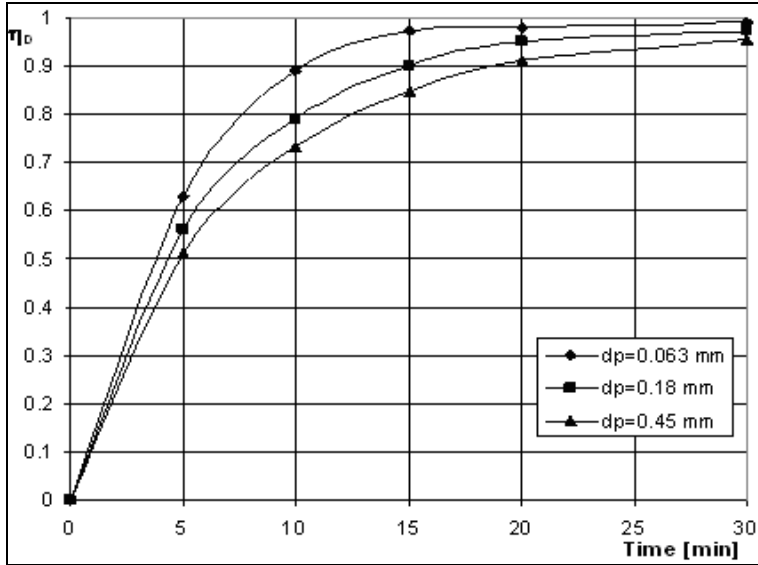


Figure 2. Effect of particles sizes on the decomposition degree of limestone at $T_c=1173$ K.

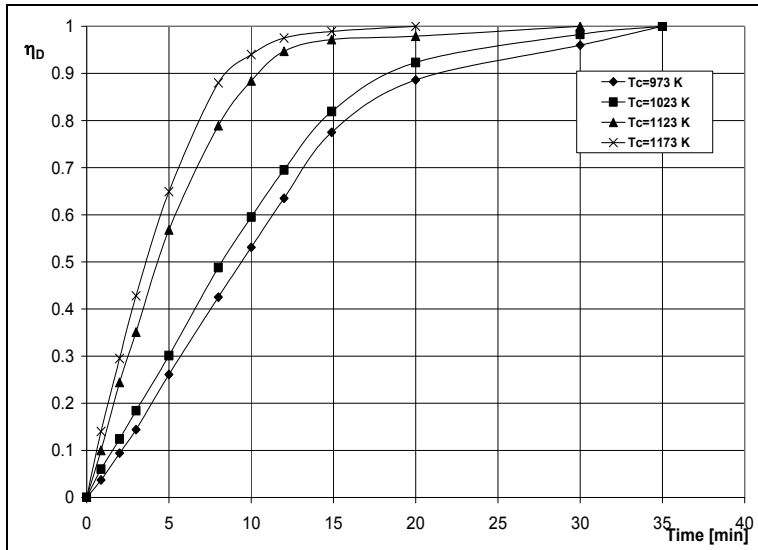


Figure 3. Effect of temperature on the decomposition degree of limestone granules with $d_p=0.063$ mm

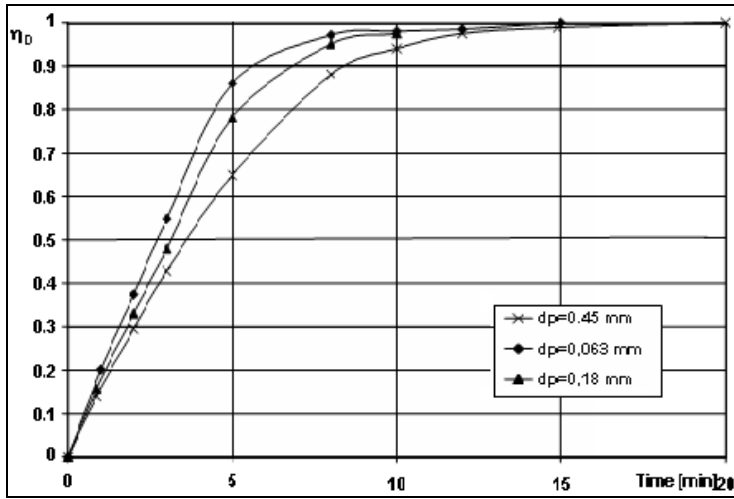


Figure 4. Effect of particles sizes on the decomposition degree of PCC at $T_c=1173$ K

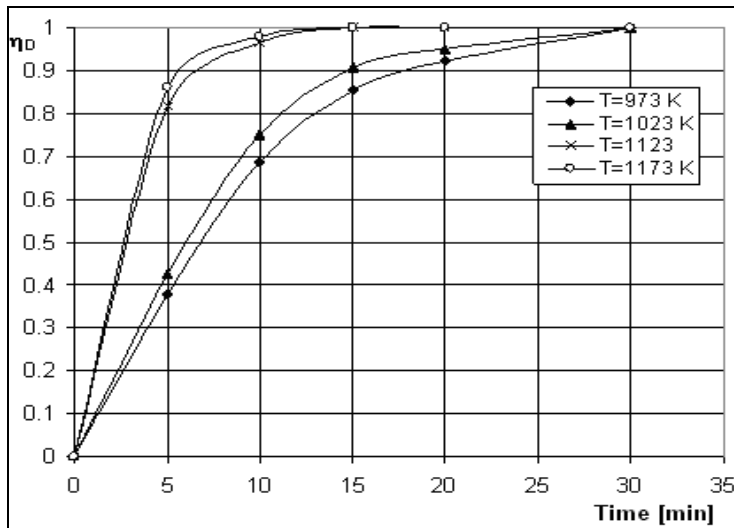


Figure 5. Effect of temperature on the decomposition degree of PCC granules with $d_p=0.063$ mm

The kinetic curves η_D - τ presented in figures 2 and 4, shown a influence of the grain size on the decomposition degree. Decomposition degree increased as the particle size is smaller. It is also observed that the time taken for maximum decomposition degree of the smallest particle size is shorter compared to

the sample with larger particle size. Particle sizes become a factor to the thermal decomposition process as it determines the surface area of the sample. Smaller particles size has large surface area that contributes to high efficiency of heat transfer.

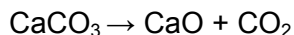
The results presented in figures 3 and 5 shown significant temperature influence on the decomposition degree for both carbonate samples. With an increase in temperature, the decomposition degree increases rapidly at temperature over $T=1123$ K, reaching values higher than 0.90 in the first ten minutes. The difference which appears between two types of carbonates samples was attributed to the different structure of the granules. In all cases the reached decarbonation degree was higher than 0.95 at 30 minutes.

It can accelerate the process by reducing the thermal or heat resistance and other resistance such as mass transfer or gas diffusion.

Kinetics analysis is important as the process involves thermal effect to the sample. The process takes place once the heat supplied is enough. Thus, the kinetic energy needs to be analyzed so that best operating condition by controlling particle size and operating temperature can be implemented.

In this work, kinetic analysis of thermal decomposition was described using Arrhenius law.

For irreversible decomposition reaction:



the rate of disappearance of CaCO_3 can be represented by equation:

$$r_{\text{CaCO}_3} = -\frac{dc_{\text{CaCO}_3}}{d\tau} = k \cdot c_{\text{CaCO}_3}^n \quad (2)$$

where k is the reaction rate constant and n reaction order.

For a first order irreversible type reaction the integrated form of equation 2 is given in equation 3:

$$-\int_{c_{\text{CaCO}_3}^0}^{c_{\text{CaCO}_3}} \frac{dc_{\text{CaCO}_3}}{c_{\text{CaCO}_3}} = k \cdot \int_{\tau=0}^{\tau} d\tau \quad \text{or} \quad -\ln \frac{c_{\text{CaCO}_3}}{c_{\text{CaCO}_3}^0} = k \cdot \tau \quad (3)$$

In terms of decomposition degree η_D we can write:

$$\ln(1-\eta_D) = -k \tau \quad (4)$$

where k is the reaction rate constant and has a unit of s^{-1} for first order reaction

The kinetic curves plotted in $\ln(1-\eta_D)$ vs τ coordinates, figures 6 and 7, gives a straight line graph with slope equal to k . The values obtained are presented in the Table 2.

Table 2. Effect of temperature on reaction rate constant

Temperature, K	Rate constant $k \times 10^3, s^{-1}$	
	Limestone	PCC
973	1.8	2.1
1023	2.1	2.5
1123	3.3	5.4
1173	4.4	6.5

The values of k increase with temperature due to increase the porosity of solid particles due to diffusion of CO_2 from the interior to surface of solids, so increase the heat transfer to the interior of particles.

The linear relationship of figure 6 and 7 having average regression coefficient R^2 higher than 0,97, confirmed that the decomposition of Sandulesti limestone and precipitated calcium carbonate (waste) of NP fertilizer industry at temperature range studied followed a first order reaction [13].

The temperature influence on the reaction rate constant has been found to be well described by Arrhenius equation:

$$k = k_0 \cdot e^{-\frac{E_a}{RT}} \tag{5}$$

where: k_0 –pre-exponential or frequency factor;
 E_a -the activation energy;
 R –gas constant;
 T - absolute temperature.

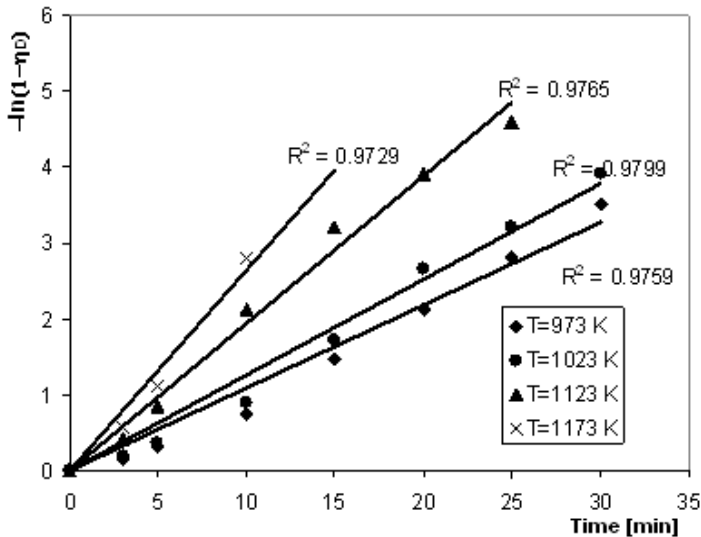


Figure 6. Determination of reaction rate constant at various temperature of limestone decomposition

The value of activation energy E_a is a good measure sensitivity of a given reaction to temperature changes. A plot of $\ln k$ - $1/T$ coordinate yields values of frequency factor k_0 and activation energy E_a , by taking the natural logarithm of equation 5:

$$\ln k = \ln k_0 - \frac{E_a}{R} \cdot T^{-1} \quad (6)$$

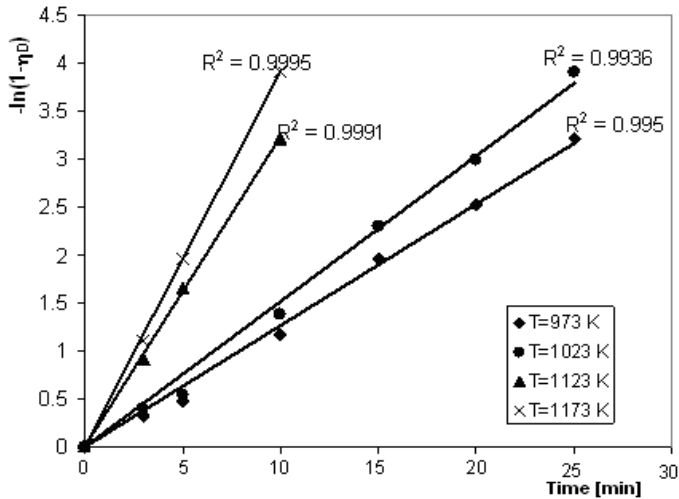


Figure 7. Determination of reaction rate constant at various temperature of PCC decomposition

The values of activation energy were estimated from the figure 8.

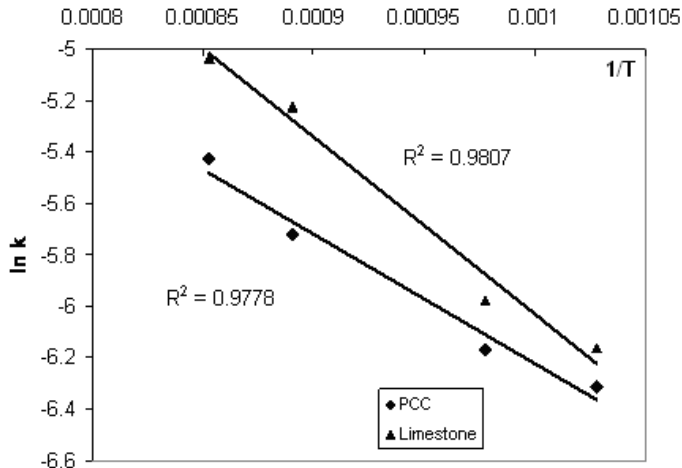


Figure 8. Dependence of reaction rate constant on temperature for granules with $d_p=0.063$ mm

The slope of the plotted graph in $\ln k$ versus $1/T$, indicates the activation energies E_a of the process. The values of E_a are 124,9 KJ/mol for PCC decomposition and 139,9 KJ/mol for limestone, in agreement with the values reported in the literature [7,8,14].

These values indicate that decomposition of precipitate calcium carbonate and Sandulesti limestone is generally kinetically controlled. At constant heating rate, activation energy is higher for limestone compared with PCC, thus the limestone consumed more energy to initiate the decomposition process.

CONCLUSIONS

The chemical composition of the two types of carbonate is very similar as they both have a content exceeding 96% CaCO_3 . IR analysis shows a very good analogy between the two sorts of carbonate. Chemical reactivity is the main parameter to validate or not to use the PCC in Ca-looping process for reducing CO_2 emissions.

The results obtained have indicated that the effect of temperature in the decomposition process of PCC and limestone is more significant than the grain size of the solid particles. Apparent activation energy obtained, $E_a=124,9$ KJ/mol for PCC decomposition and $E_a=139,9$ KJ/mol for limestone, suggested that the global process of decomposition is kinetically controlled. Activation energy is higher for limestone compared with PCC, thus the limestone consumed more energy to initiate the decomposition process. The results obtained during the decomposition process of precipitated calcium carbonate (waste) of NP fertilizer industry (PCC) and Sandulesti limestone showed that at temperature range studied followed a first order reaction.

The experimental research shows that the waste precipitate calcium carbonate (PCC) from NP fertilizers industry has a similar behavior in the decomposition process with natural limestone. PCC testing is recommended in the Ca-looping for CO_2 reduction in competition with limestone because both energy consumption for grinding and thermal decomposition process is less energy.

EXPERIMENTAL

In order to elucidate the effect of the temperature and grain size on the rate of the decomposition process, the isothermal gravimetric method was employed. The characterization of the two carbonate sources was carried out by crystallographic structure analysis. IR spectra were determined with a Digilab FTS 2000 spectrophotometer. The decomposition experiments were carried out isothermally on an experimental equipment presented in a previous paper [10]. The parameters of the system are shown in Table 3.

Table 3. Operate parameters of the system

Crt. Nr.	Parameter	Value
1	Calcination temperature	973 K, 1023 K, 1123 K, 1173 K
2	Heating rate	10°C/min
3	Calcination time	30 min
4	Pressure	1 atm.
5	Particle size of calcium carbonate	0,063 mm; 0,18 mm; 0.45 mm

ACKNOWLEDGEMENTS

The author would like to acknowledge the support from the Romanian National Authority for Scientific Research, CNCS-UEFISCDI, project ID PNII-CT-ERC-2012-1/2ERC:”Innovative systems for carbon dioxide capture applied to energy conversion processes.”

REFERENCES

1. C. Salvador, D. Lu, E.J. Anthony, J.C. Abanades, *Chemical Engineering Journal*, **2003**, 96, 187.
2. G.S. Grasa, J.C. Abanades, *Industrial and Engineering Chemistry Research*, **2006**, 45, 8846-8851.
3. J.C. Abanades, M. Alonso, N. Rodriguez, B. Gonzales, G. Grasa, R. Murillo, *Energy Procedia*, **2009**, 1, 1147.
4. J.D. Figueroa, T. Fout, S. Plasynski, H. Mcllvired, R. Srivastava, *International Journal of Greenhouse Gas Control*, **2008**, 2, 9.
5. M.C. Romano, *Chemical Engineering Science*, **2012**, 69, 257.
6. C. Chong, E. Specht, *Thermochimica Acta*, **2006**, 449 (1-2), 8.
7. I. Ar, G. Doğu, *Chemical Engineering Journal*, **2001**, 83, 131.
8. Al. Szép, Gh. Mihăilă, A.M. Busuioc, *Analele Științifice ale Universității „Al.I. Cuza” Iași, Seria Chimie, Tomul IX*, **2001**, 197.
9. S. Drăgan, M. Drăgan, *Studia UBB Chemia*, **2005**, 50(1), 89.
10. S. Drăgan, A. Ghirișan, *Studia UBB Chemia*, **2007**, 52(1),165.
11. B.R. Stanmore, P. Gilot, *Fuel Processing Technology*, **2005**, 86(16), 1707.
12. J.S. Dennis,R.Pacciani, *Chemical Engineering Science*, **2009**, 64(9), 2147.
13. O. Levenspiel, “Chemical reaction engineering”, 3rd Edition, John Wiley & Sons, New York **2006**, chapter 1.
14. M. Mustakimah, Y. Suzana, M. Saikat, *Journal of Engineering Science and Technology*, **2012**, 7, 1.

*Dedicated to Professor Liviu Literat
On the occasion of his 85th birthday*

SETTLING OF COAGULATED DILLUTED YEAST SUSPENSIONS

ADINA GHIRIŞAN^a

ABSTRACT. Specific settling tests have been made using diluted yeast suspensions coagulated/flocculated in the presence of FeCl_3 at constant pH of 4.0 in order to determine the flocs/aggregates size and gel solid concentration, parameters which are necessary in numerical simulation and characterization of sedimentation processes. The sizes of the incipient aggregates and the gel point show to be dependent on coagulant concentration. The size of aggregates and the gel point has increased with the increase of coagulant concentration.

Keywords: *settling tests, yeast coagulated suspensions, aggregate sizes, gel solid point.*

INTRODUCTION

Numerical simulation of sedimentation processes and design of specific apparatus are based on equations which contain characteristic parameters as settling rates (w), floc/aggregate sizes (d_A) and gel solid concentration (C_{Vg}) [1].

In the case of stable suspended solids as yeast suspension contains, the presence of coagulants/flocculants makes possible the change of solids structure with the formation of a connected aggregate or floc, which fall more quickly than the individual particles because of their larger mass to surface ratios.

The influence of FeCl_3 concentration used as coagulant on the settling rates, primary size of aggregates and on the suspension gel solid fraction is analyzed in this study.

^a *Universitatea Babeş-Bolyai, Facultatea de Chimie și Inginerie Chimică, Str. Kogălniceanu, Nr. 1, RO-400084 Cluj-Napoca, Romania, ghirisan@chem.ubbcluj.ro*

a. Settling rates and floc/aggregate sizes

In order to determine the floc/aggregate size, the group settling rate and the settling rate of an individual uniform and spherical particle can be connected by Richardson & Zaki equation [2]:

$$\mathbf{w} = \mathbf{w}_{St} \boldsymbol{\varepsilon}^{4.65} = \mathbf{w}_{St} (1 - C_V)^{4.65} \quad (1)$$

where: C_V is the particle volume fraction and w_{St} the Stokes' settling rate for the single uniform spherical particle, as equation (2) shows:

$$\mathbf{w}_{St} = \frac{1}{18} \cdot \frac{(\rho_A - \rho) \cdot d_A^2}{\eta} \cdot \mathbf{g} \quad (2)$$

In equation (2), ρ_A and ρ are the aggregate and the medium density, d_A is the average, (equivalent), aggregate/particle diameter, η is the medium viscosity, and g is the gravitational acceleration.

According to literature references, the aggregate diameter, d_A , can be considered independent of solid concentration over the "dilute" range, and so it does not change once the settling begun [3, 4].

From the material balance, the initial settling rate of aggregate can be considered as equation (3) shows [3]:

$$\mathbf{w}_0 = \frac{1}{18} \cdot \frac{(\rho_Y - \rho) \cdot d_A^2}{\eta C_{AY}} \cdot \mathbf{g} \cdot (1 - C_{AY} C_{VY})^{4.65} \quad (3)$$

where: ρ_Y is the yeast density and C_{AY} is the ratio:

$$C_{AY} = \frac{C_{VA}}{C_{VY}} = \frac{\text{volume of aggregate}}{\text{volume of yeast in aggregate}} .$$

Writing the equation (3) in the form:

$$\mathbf{w}_0^{1/4.65} = \left(\frac{1}{18} \cdot \frac{(\rho_Y - \rho_w) d_A^2}{\eta_w C_{AY}} \cdot \mathbf{g} \right)^{1/4.65} (1 - C_{AY} C_{VY}) \quad (4)$$

and plotting $w_0^{1/4.65}$ against the corresponding value of yeast volume fraction C_{VY} results a straight line, which gives us the possibility to estimate the aggregate size from the slope and intercept.

b. Gel point

The behavior of sedimentation process and the efficiency of solid-liquid separation in a sedimentation column depend on initial solid volume fraction, (C_{V0}) and volume solid fraction at gel point, (C_{Vg}). The critical volume fraction, C_{Vg} , called gel point is defined as the lowest concentration at which flocs are able to form a self-supporting network [5].

Determination of gel point, C_{Vg} , of flocculated suspensions in this study is based on equation (5) [1, 6]:

$$C_{Vg}(h_{\infty}) = \frac{d(C_{V0}h_0)}{dh_{\infty}} \quad (5)$$

where: C_{V0} and h_0 are the initial volume fraction of solids and initial height of suspension and h_{∞} is the equilibrium height of the sediment bed.

Following the work of Nasser and James, who studied the behavior of kaolin suspensions [1, 4]; synthetic baker's yeast suspensions in distilled water were used in the present work.

RESULTS AND DISCUSSION

a. Settling rates and floc/aggregate sizes

The initial settling rates for yeast suspensions with different concentrations are obtained by batch sedimentation tests, plotting the height of interface between slurry and the supernatant as a function of time. The settling curves obtained for different concentrations of coagulant $FeCl_3$ at pH 4 are shown in Figures 1 (a-d).

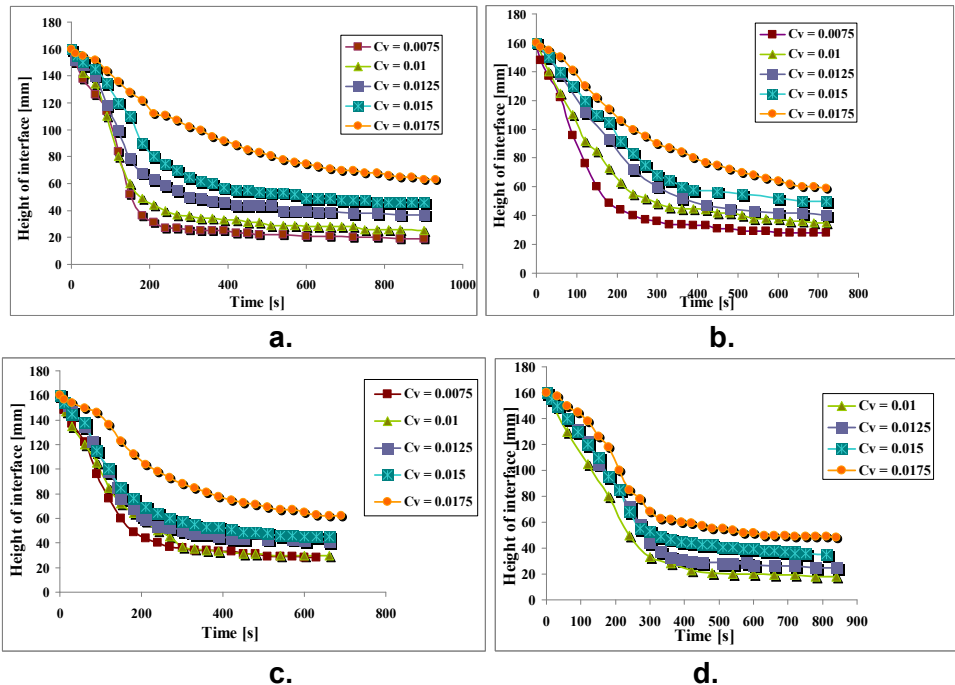


Figure 1. Sedimentation curves of yeast suspensions at the concentration of coagulant $FeCl_3$ of: $4.0 \cdot 10^{-4}$ M (a), $1.6 \cdot 10^{-3}$ M (b), $2.4 \cdot 10^{-3}$ M (c), $4.0 \cdot 10^{-3}$ M (d).

The yeast volume fraction of between 0.0075 and 0.0175 (m^3/m^3) was selected in order to have only "diluted" and highly flocculated suspensions for all concentration of FeCl_3 . The decrease in the sediment thickness with time indicates that flocs settle in flocculated form. Early work has shown that the optimal removal of yeast particles from suspension is obtained at pH value between 4 and 4.5 [7].

The initial settling rates can be now determined by tangent method, as the ratio between interface height and the corresponding time period of the linear part of each curve. The obtained values for different concentrations of FeCl_3 are shown in Table 1.

Table 1. Results obtained by settling tests

FeCl_3 concentration [M]	Volume yeast concentration C_{VY} [m^3/m^3]	Initial experimental settling rate $w_0 \cdot 10^3$ [m/s]	Average aggregate size d_A [μm]
$4.0 \cdot 10^{-4}$	0.0075	0.73	1000
	0.01	0.600	
	0.0125	0.400	
	0.015	0.333	
	0.0175	0.166	
$1.6 \cdot 10^{-3}$	0.0075	0.667	1018
	0.01	0.583	
	0.0125	0.367	
	0.015	0.222	
	0.0175	0.166	
$2.4 \cdot 10^{-3}$	0.0075	0.83	1120
	0.01	0.667	
	0.0125	0.416	
	0.015	0.366	
	0.0175	0.200	
$4.0 \cdot 10^{-3}$	0.01	0.500	1140
	0.0125	0.333	
	0.015	0.167	
	0.0175	0.133	

Typical linear curves result by plotting $w_0^{1/4.65}$ against the corresponding values of yeast concentration C_{VY} , (Figure 2, a-d). From the intercept and the slope of the each line it can be calculated the aggregate size. The average values of aggregates size obtained are shown in Table 1.

The values have shown the increase of the aggregates size from 1000 μm to 1140 μm with the increase of FeCl_3 concentration, from $4.0 \cdot 10^{-4}$ to $4.0 \cdot 10^{-3}$ M. The increase of the aggregate size has in the same time a positive effect in acceleration of the settling process.

The Stokes' settling rate for single aggregate is expressed by equation (6), when the yeast density ρ_Y is 1060 kg/m^3 , water density ρ is 997 kg/m^3 and water viscosity η is $0.9 \cdot 10^{-3} \text{ Pas}$ at the work temperature of 25°C :

$$w_{\text{St}} = 38150 \frac{d_A^2}{C_{\text{AY}}} \quad (6)$$

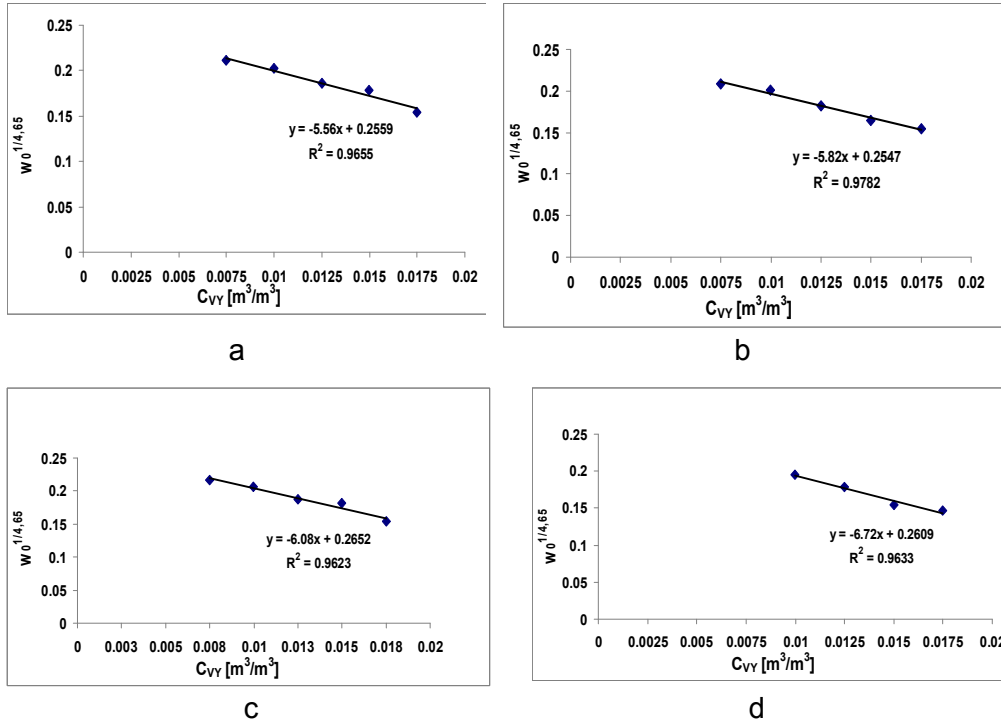


Figure 2. Correlation of settling rate and volume fraction of yeast using the FeCl_3 of: $4 \cdot 10^{-4} \text{ M}$ (a), $1.6 \cdot 10^{-3} \text{ M}$ (b), $2.4 \cdot 10^{-3} \text{ M}$ (c) and $4.0 \cdot 10^{-3} \text{ M}$ (d).

b. Gel point

In order to determine the gel point, the initial yeast volume fraction was chosen between 0.0025 and $0.0175 \text{ (m}^3/\text{m}^3)$, much lower than the volume fraction at which the gel point is expected to be found [1].

In the present work, the initial height of suspension, h_0 , is maintained constant and the initial concentration of yeast, C_{V0} , is varied. The product $C_{V0}h_0$ is plotted as a function of corresponding height equilibrium, h_∞ , obtained by settling tests (Figure 3, a-d). The gel point value determined from the slope of each line ($h_\infty \rightarrow 0$) is shown in Table 2.

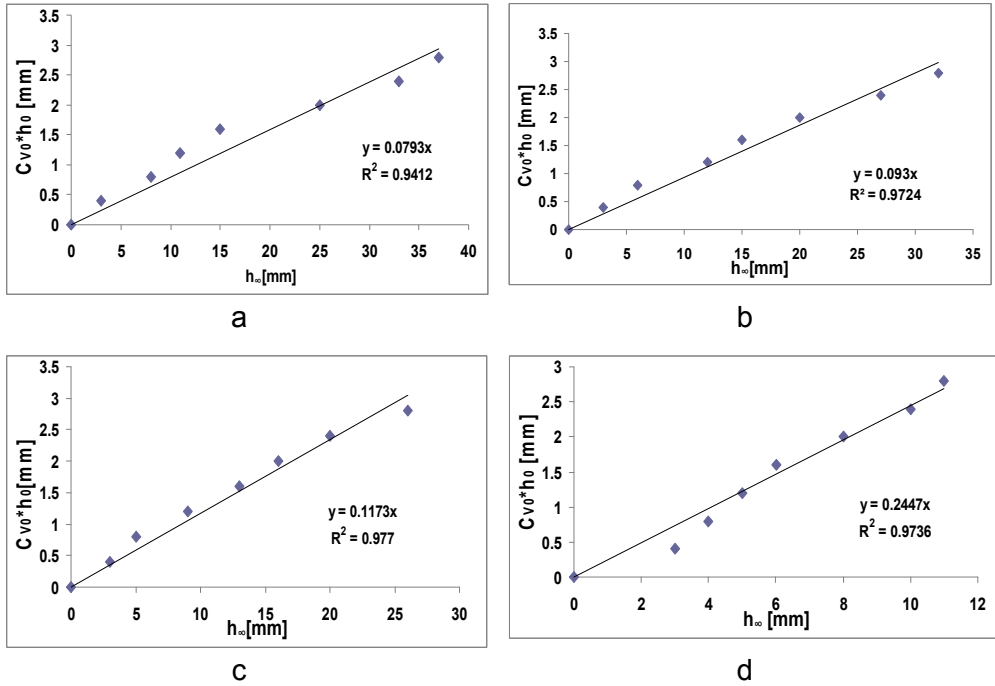


Figure 3. Gel point determination at different concentrations of $FeCl_3$: $4 \cdot 10^{-4}$ M (a), $1.6 \cdot 10^{-3}$ M (b), $3.0 \cdot 10^{-3}$ M (c), $6.5 \cdot 10^{-3}$ M (d).

As it can be seen, the gel point is sensitive to the coagulant concentration, the gel point concentration increases with the increase of coagulant concentration.

Table 2. Dependence of gel point on coagulant concentration

C_{FeCl_3} [M]	C_{Vg} [m ³ /m ³]
$4.0 \cdot 10^{-4}$	0.079
$1.6 \cdot 10^{-3}$	0.093
$3.0 \cdot 10^{-3}$	0.117
$6.5 \cdot 10^{-3}$	0.245

CONCLUSIONS

The experimental results obtained in this study have shown that the presence of FeCl_3 in diluted yeast suspensions made possible the settling tests with the determination of the aggregate sizes and gel point concentration.

The size of the incipient aggregates is found to be influenced by the coagulant concentration, an increase of aggregates size from $1000 \mu\text{m}$ to $1140 \mu\text{m}$ with the increase of FeCl_3 concentration from $4.0 \cdot 10^{-4}$ to $4.0 \cdot 10^{-3}$ M was obtained.

The gel point was influenced by the coagulant concentration too, the gel point concentration showing an increase of gel point with the increase of coagulant concentration.

The parameters determined in this study can be used with good agreement in numerical simulation and design of batch apparatus in settling processes.

EXPERIMENTAL SECTION

a. The aggregates/flocs size determination is based on settling tests. Suspensions with different volume fractions between 0.0075 and 0.0175 m^3/m^3 used in the experiments were prepared directly in 100 ml cylinders from dried Pakmaya yeast and distilled water. The pH of solution was maintained at constant value of 4, when the yeast suspensions are highly flocculated for all concentration of FeCl_3 , by using an appropriate amount of 0.1 HCl. The interface of slurry-supernatant position was recorded with settling time. Three replicate experiments were carried out for each set of experimental conditions.

b. The gel point, which is effectively the solids concentration at the surface of the sediment, was found from the initial slope ($h_\infty \rightarrow 0$) of the product $C_{V0}h_0$ as a function of h_∞ obtained from sequences of settling tests.

A series of 100 ml measuring cylinders were used for the gel point measurements and the initial volume fraction C_{V0} in range of 0.0025 and 0.0175 m^3/m^3 was varied. The FeCl_3 concentration was varied from $4 \cdot 10^{-4}$ to $6.5 \cdot 10^{-3}$ M and the pH was maintained at constant value of 4. The suspension was first homogenized and then left to settle. The h_∞ was recorded when it became constant.

REFERENCES

1. M.S. Nasser, A.E. James, *International J. Mineral Processing*, **2007**, 84, 144.
2. J.F. Richardson, W.N. Zaki, *Trans. Instn. Chem. Eng.*, **1954**, 32(1), 35.
3. A.S. Michaels, J.C. Bolger, *I & EC Fundamentals*, **1962**, 1(1), 24.
4. M.S. Nasser, A.E. James, *J. Eng. Science and Tech.*, **2009**, 4(4), 430.
5. K.A. Landman, L.R. White, R. Bucsall, *Advance in Colloidal and Interface Science*, **1994**, 51, 175.
6. R.G. de Kretser, D.V., Boger, P.J. Scales, *Rheology Reviews*, **2003**, 125.
7. A. Ghirișan, V. Miclăuș, *Chem. Bull. "Politehnica" Univ. Timișoara*, **2010**, 55(69), 68.

*Dedicated to Professor Liviu Literat
On the occasion of his 85th birthday*

SYNTHESIS AND CHARACTERIZATION OF CORDIERITE FOR DIESEL FILTERS

**MARIA GOREA^{a,*}, IOANA OLIVIA RUJONI^a,
NICOLAE HAR^b, MARCEL IOAN BENE^b**

ABSTRACT. Cordierite, $Mg_2Al_4Si_5O_{18}$, has a very low thermal expansion coefficient, thus a high resistance to thermal shocks as well as chemical stability at high temperatures. Accordingly, it is used in applications where high resistances to thermal shock are essential; such is the case of diesel particulate filters (DPF). This paper concerns the synthesis of cordierite by using the solid state reaction method starting from raw materials: kaolin, metakaolin and talc. The ceramics fired at 1300 °C and 1350 °C were submitted to chemical attack by an alkaline mixture (one mole Na_2CO_3 with 1.5 moles SiO_2) under so-called “less-severe” conditions, i.e., 900 °C and then under “severe” conditions at 1000 °C for 5 minutes. The SEM images evidence less corrosion in the first case, and slight corrosion features under the circumstance of the “severe” attack.

Keywords: *cordierite, ceramics, chemical attack*

INTRODUCTION

Cordierite ceramic has a high thermal shock resistance due to their low thermal expansion coefficient coupled with relatively high chemical and mechanical stability. These characteristics make it an important material for many applications such as heat exchangers for gas turbine engines, and honeycomb-shaped catalyst carriers in automobile exhaust systems. Because the natural mineral is not sufficiently pure, cordierite has to be synthesized. Cordierite powders can be prepared by the solid-state reaction, sol-gel technique,

^a Babeş-Bolyai University, Faculty of Chemistry and Chemical Engineering, 11 Arany Janos Str. RO-400028, Cluj-Napoca, Romania. * Corresponding author: mgorea@chem.ubbcluj.ro

^b Babeş-Bolyai University, Department of Mineralogy and Geology, 1 Kogălniceanu Str. RO-400084, Cluj-Napoca, Romania

sintering and crystallization from vitreous state or consolidation of raw structure with organic materials and subsequent calcinations for obtaining a porous cordierite ceramic.

The solid state reaction is the most used method for applications of cordierite as honeycomb carrier because this technique allows formation of the monolithic structure with optimum mechanical and thermal shock resistance. However, a disadvantage of cordierite ceramic compositions prepared by this method is the close fired temperature range to the different eutectic points.

The particle size distributions of the precursor's oxides facilitate cordierite synthesis and favors crystallization of mineral phases. [1] Evolution of the crystalline phases in the cordierite synthesis with temperature and time allows controlling chemical and structural characteristics of final ceramic supports. [2]

Kaolin-based cordierite ceramics prepared by solid state reaction and thermal treated at 1350 °C gave the pure cordierite phase, good compressive strength and low thermal expansion coefficient being the suitable for using as catalyst support. [3]

Heat resistant ceramic materials based on cordierite with various mineralizing additives for obtaining the crystalline phases that ensure low values of thermal expansion coefficient have been reported. [4]

The cordierite can be obtained directly from oxides as well from other raw materials whose chemical composition sums up to that of cordierite. For this purpose, it can be used like raw materials: elementary compounds (pure oxides, hydroxides, carbonates); double compounds (kaolins, clays, talc, steatite, sepiolite); triple compounds (chlorite). [5-8]

One of the most extended applications of cordierite is as ceramic monolithic honeycomb supports. This structure is increasingly used in many reactor applications, such as petrochemical industry selective reduction of nitrogen oxides, selective hydrogenation of alcohols, automobile emissions control and control of volatile organic compounds. [9-12]

Ceramic substrates have been employed as automobile catalyst supports to facilitate the conversion of CO and HC emissions to CO₂ and H₂O by redox reaction. Cordierite ceramic honeycombs are currently considered as leading candidates for trapping and oxidizing the carbonaceous particulate emission from automobiles.

The corrosion resistance of cordierite remains an important issue in studies on cordierite as a material for particulate filters. During use, a DPF collects soot, i.e. carbon based particles from diesel combustion, as well as small amounts of components other than carbon and organic matter. These typically include compounds containing Ca, Mg, Zn, P and S originating from fuel or lubricating oil, as well as metals or metal oxides from wear of the engine or the exhaust gas system. The mechanism of the corrosion of single crystal natural Cordierite by sodium silicate ash was analyzed. [13]

In our work [14] the chemical attack on ceramics from powders obtained by sol-gel method was studied. The alkaline corrosion attack tests showed no damages of ceramics in the case of milder conditions, at 900 °C, and evidenced corrosion when the temperature in the diesel filters exceeds 1000 °C.

The goal of this study was to analyze the corrosion of the ceramics obtained by conventional method, solid state reaction, to test for alkaline chemical attack under severe or less-severe experimental conditions. The influence of the cordierite synthesis parameters from kaolin, metakaolinite and talc for a complete reaction of reactants, the grain size and thermal behavior of raw mixture were determined. From powders, ceramic materials were obtained by applying thermal treatment at various temperatures on pressed pellets, which were characterized from physical-chemical point of view, and have been tested for alkaline chemical attack under severe or less-severe experimental conditions.

RESULTS AND DISCUSSIONS

Grain size distribution of the mixture

The grain size distribution of the raw mixtures obtained by using the solid state reaction method is illustrated in figure 1. The sample shows a grain size interval between 0.010 and 0.179 μm , with an average of 0.049 μm . The typical curve evidences one grain size interval with following particles ratio:

- 17 % particles between 0.097 μm and 0.179 μm ;
- 11 % particles between 0.010 μm and 0.028 μm ;
- 78 % particles between 0.028 μm and 0.097 μm .

The decrease of particle sizes determines a more completed reaction of the solid reactants, it is in favour of faster firing rate. The small particle size also reduces the risk of phase separation during preparation of the mixture.

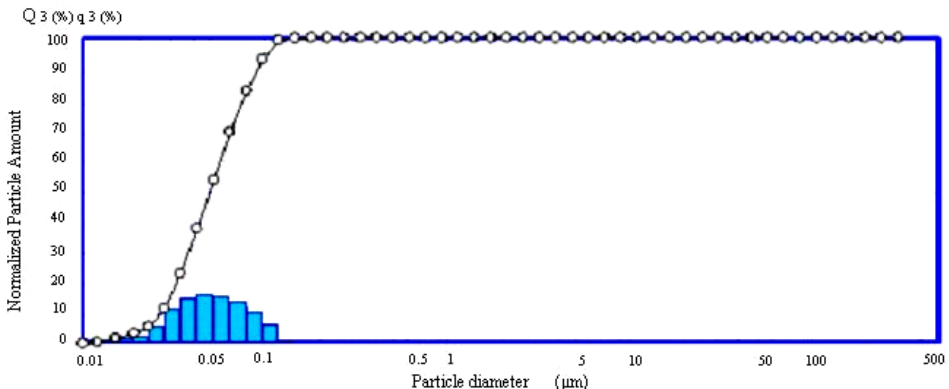


Figure 1. Particle size distribution of raw materials mixture

Thermal behaviour

Figure 2 shows the thermal differential (DTA) and weight loss (TG and DTG) curves for the raw materials mixture (kaolin, metacaolin and talc) until 1200 °C temperature under a heating rate of 10 °C/min.

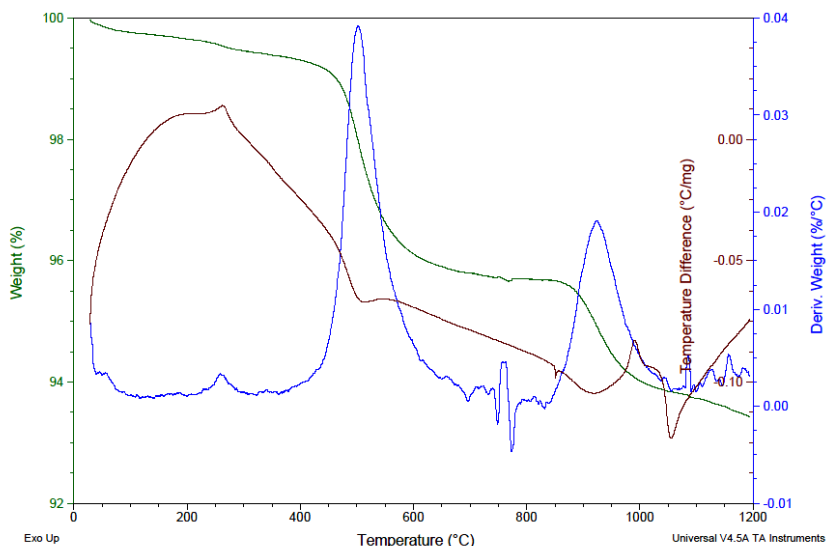


Figure 2. Thermal behaviour of raw materials mixture

The most important thermal effects evidenced in 20 °C – 1200 °C temperature interval are:

- In the 100-200 °C temperature range, an endothermic effect is due to elimination of the water adsorbed at the powder surfaces as a consequence of milling process;
- In the 200 – 300 °C temperature range, the sample shows a small exothermic effect accompanied by weight loss (about 0.5 %) as a result of oxidation of organic compounds;
- In the 400 – 600 °C temperature range the sample shows an endothermic effect accompanied by a weight loss (about 3 %) as a result of the dehydroxilation of kaolinite (transforming in metakaolinite at 450-500 °C) and elimination of OH⁻ groups from talc;
- In the 800-1200 °C temperature range the sample shows endothermic and exothermic effects as a result of decomposition of talc in magnesium metasilicate and silica oxide (at 600-1050°C temperature). Also the metakaolinite is transformed in spinel phase (at 900-1000 °C temperature), and after that in primary mullite. Talc is transformed in enstatite at about 1140 °C temperature. The weight loss in this interval is about 2 %.

X-ray diffraction

Figure 3 illustrates the X-ray diffraction of cordierite ceramic sample after thermal treatment at 1350 °C.

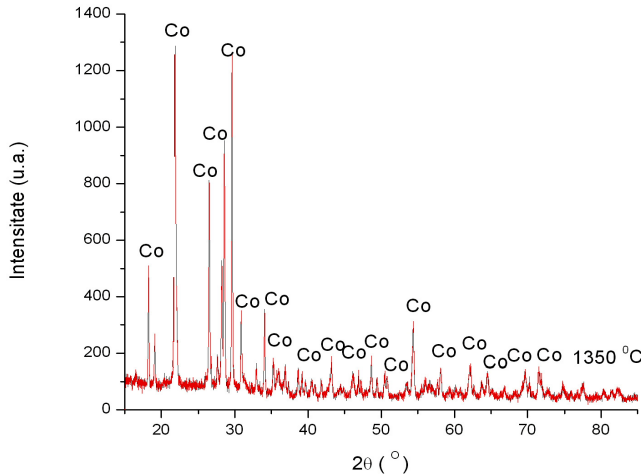


Figure 3. XRD pattern of ceramic sample fired at 1350 °C

The X-ray diffraction pattern of ceramic sample is dominated by the high temperature polymorph, α -cordierite. However, the relative lower intensity of the spinel and cristobalite index reflexes can be noticed. The presence of spinel and cristobalite might be explained as the result of an incomplete reaction the components in the system due to of an insufficient homogenization of raw materials. It is well known that the solid state reaction method has the disadvantage of an incomplete reaction between reactants. Thus, in final mineralogical composition can be found the intermediary compounds.

Compactness characteristics of ceramics

The compactness characteristics and relative size parameters in the case of the samples thermal treated at 1300 °C and 1350 °C, the heating rate being of 10 °C/min and maintaining 2 hours at maximum temperature are presented in Table 1.

Table 1. Compactness characteristics of ceramics

Sample	Firing temperature T_a [°C]	Water absorption a [%]	Apparent density ρ_a [g/cm ³]	Apparent porosity P_a [%]	Firing shrinkage C_a [%]
I	1300	0.417	1.993	0.831	3.49
II	1350	0.210	2.071	0.434	3.7

It can be observed that open porosity is small for both samples. An increasing of temperature with 50 °C determines a decreasing of apparent porosity, as it is expected.

For an efficient diesel particulate filter is necessary a porous material. The higher values for porosity were registered for the sample sintered at 1300 °C (0.831 %). The firing shrinkage does not vary significantly for the tested samples.

Thermal expansion

The thermal expansion coefficient of cordierite is low that recommend this material for various applications. This coefficient has been measured for ceramic samples sintered at 1300 °C and 1350 °C, the results being presented in Table 2.

Table 2. Thermal expansion coefficients for studied samples

Temperature [°C]	Ceramics sintered at	
	1300 °C	1350 °C
	$\alpha \text{ E}^{-6}/\text{K}$	$\alpha \text{ E}^{-6}/\text{K}$
200	9.1	3.0
300	9.6	6.2
400	8	5.7
600	6.3	5.3
1000	4.7	3.9

It can notice that the lowest value of thermal expansion coefficient is $3.9 \cdot 10^{-6}/\text{K}$ in the temperature interval of 20-1000 °C for the ceramic samples fired at 1350 °C. In the case of ceramics thermal treated at 1300 °C, the coefficient value in the same interval is higher ($4.7 \cdot 10^{-6}/\text{K}$) that can be explained by the compactness characteristics. The apparent porosity for samples fired at 1300 °C is higher than porosity for samples at 1350 °C.

The thermal expansion coefficient, in the 30-1000 °C range as imposed by the standards for cordierite ceramics has to fall in the 2-4.5 range for the ceramics with maximum 0.5 % apparent porosity.

In conclusion, the ceramics thermal treated at 1350 °C have the thermal expansion coefficient impose for cordierite ceramics and can be used in applications that require o high thermal shock resistance.

Resistance to corrosion of the cordierite ceramics

For testing the resistance to corrosion of the samples, a mixture of 1 mole Na_2CO_3 and 1.5 moles of SiO_2 was mixed that produced a reactive sodium silicate. The alkali-rich mixture was pressed as 6-mm pellets that were laid

on the cordierite ceramics' surface. The $\text{Na}_2\text{O-SiO}_2$ system phase diagram evidences the presence of one eutectic at temperature of $\sim 830^\circ\text{C}$ and an almost complete melting at $\sim 950^\circ\text{C}$. The sodium-rich melts are corrosive at temperatures significantly below 1000°C . Due to this fact, one would expect that the cordierite ceramics undergoes alkaline attack during its use as filter for Diesel engines if in contact with alkali-rich ashes.

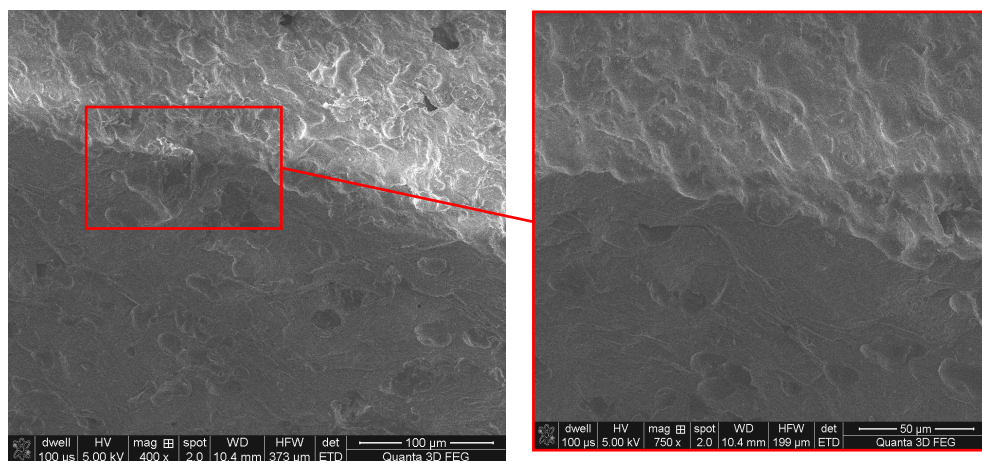


Figure 4. SEM image of the sample fired at 1350°C and corroded at 900°C

The tested cordierite ceramic was the sample sintered at 1350°C . It was topped by the pellets containing alkaline mixture and was submitted to two experimental corrosion sets-ups. The first set-up was considered the milder version, thus the ceramics with alkaline pellets were fired at 900°C for 5 minutes. For the second set-up, considered as intense chemical attack conditions, the samples were fired in a laboratory kiln at 1000°C , for 5 minutes. The effects of the chemical attack on the ceramics were evidenced by scanning electron microscopy (SEM) (Figs. 4 and 5).

In the case of the milder experimental conditions, at 900°C the ceramic obtained from solid state reaction powders, is easily attacked by sodium silicate ash. In the superior side it is showed the ash and in the inferior side, the ceramic. At 1000°C , the ceramic sample is corroded by sodium silicate ash. This corrosion is presented in the SEM image, figure 5 (left). The chemical attack is very well evidenced in figure 5 (right). Thus, if the temperature in the diesel filters exceeds 1000°C , corrosion of the cordierite ceramics occurs leading to increasing damage over time.

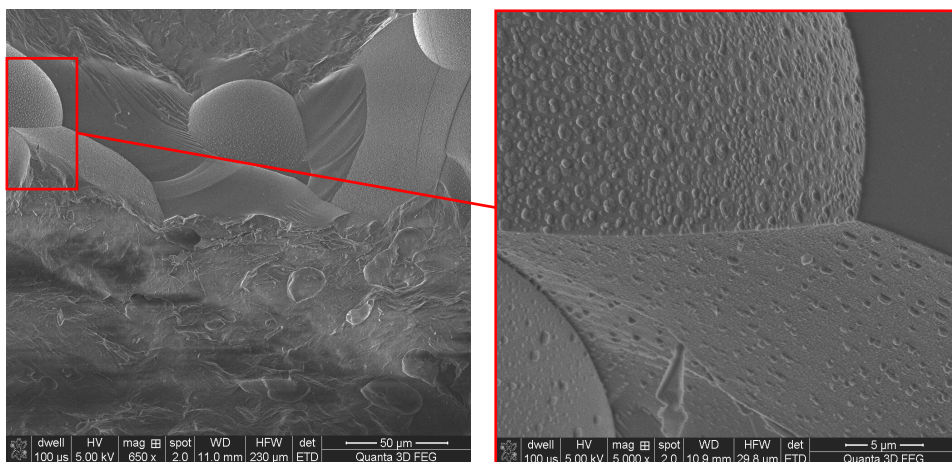


Figure 5. SEM image of the sample fired at 1350 °C and corroded at 1000 °C

CONCLUSIONS

The cordierite powders were synthesized by solid state reactions in the laboratory conditions. Cordierite ceramics were obtained by traditional route. Powders and cordierite ceramics were characterized.

The powders obtained by solid state method presents the nanometric particle sizes. The mean values for particle size of powders are 0.049 µm. The cordierite starts to crystallize after 1050 °C according to the thermal analysis. The firing shrinkage presents normal values, due to densification of the material during the sintering, and the dehydration compounds from kaolin and talc. The compactness characteristics (water absorption, apparent density, apparent porosity), are changed with the sintering temperature. For an efficient diesel particulate filter is necessary a porous material. The higher values for porosity were found for the sample sintered at 1300 °C. The thermal expansion coefficient presents lower values for the samples fired at 1350 °C In conclusion, to reach a low thermal expansion coefficient, high temperatures are necessary or a longer plateau at maximum temperature.

The SEM images show that the ceramics is easily attacked by the sodium silicate ash, under less severe conditions, at 900 °C. At 1000 °C, the samples are corroded by the sodium silicate ash.

The best properties are presented by the sample fired at 1350 °C, and corroded with sodium silicate ash at 900 °C. It presented nanometer particle size, the optim values for water absorption and porosity, low thermal expansion coefficient. In terms of corrosion, it is easily corroded by sodium silicate ash under less severe conditions.

EXPERIMENTAL

The raw materials used were kaolin, metakaolin (dehydroxylated at temperature 650 °C and time 5 h) and hydrated magnesium silicate (talc) [3MgO·4SiO₂·H₂O] (99.5%). Kaolin-based cordierite ceramics are prepared by the solid-state reaction by mixing a stoichiometric composition of kaolin, metakaolin and talc. The general processing diagram is presented in figure 6.

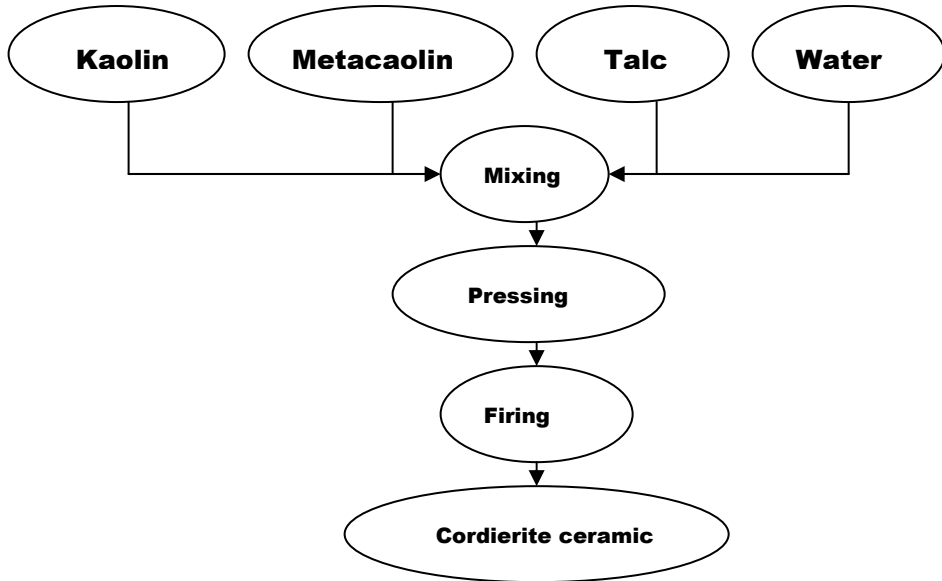


Figure 6. General processing diagram for obtaining cordierite ceramics

The raw materials are mixed in a ball mill at 200 rot/min for 4 h. The mixture is oven-dried at 115 °C for 12 h and then pre-fired at 300 °C for 3 h. The resulting powder was granulated and pressed as pellets with 28 mm in diameter and 2 mm thickness. The pellets were subsequently sintered at 1300 °C and 1350 °C with heating rate 10 °C/min and plateau at maximum temperature 2 h, in a Nabertherm-type laboratory kiln.

The grain size distribution of raw mixture has determined by using a Counter Coulter WING-SALD 7101 unit; the thermal behaviour by using a SDT Q 600-type apparatus, and the thermal expansion coefficient with a L75H1400 dilatometer. The mineralogical composition was established based on the XRD patterns measured on BRUKER D8 ADVANCE diffractometer with Cu K_{α1} ($\lambda_{Cu1} = 1.540598 \text{ \AA}$) radiation, Ni filter in order to eliminate the Cu K_β component, and Ge monochromator for eliminating the Cu K_{α2} component, on the 15–85° 2 θ interval.

REFERENCES

1. J.R. Gonzalez-Velasco, R. Ferret, R. Lopez-Fonseca, M.A. Gutierrez-Ortiz, *Powder Technology*, **2005**, 153, 34-42.
2. J.R. Gonzalez-Velasco, M.A. Gutierrez-Ortiz, R. Ferrt, A. Aranzabal, J.A. Botas, *Journal of Materials Science*, **1999**, 34, 1999-2002.
3. A. Yamuna, R. Johnson, Y.R. Mahajan, M. Lalithambika, *Journal of the European Ceramic Society*, **2004**, 24, 65.
4. E.M. Dyatlova, S.E. Barantseva, E.S. Kakoshko and V.M. Kononovich, *Glass and Ceramics*, **2005**, 62, 7.
5. J.B. Rodrigues Neto, R. Moreno, *Applied Clay Science*, **2007**, 37, 157.
6. M. Valaskova, G. Simha Martynkova, B. Smetana, S. Studentova, *Applied Clay Science*, **2009**, 46, 196.
7. J. Banjuraizah, H. Mohamed, Z.A. Ahmed, *Journal of Alloys and Compounds*, **2010**, 494, 256.
8. E.A. Cociș, A.F. Soporan, P. Ilea, F. Imre-Lucaci, B.M. Soporan, P. Bere, O. Nemeș, *Studia UBB Chemia*, **2012**, LVII(2), 147.
9. M. Fuji, Y. Shiroki, R.L. Menchavez, H. Takegami, M. Takahashi, H. Suzuki, S. Izuhara, T. Yokoyama, *Powder Technology*, **2007**, 172, 57.
10. Landong Li, Fuxiang Zhang, Naija Guan, *Catalysis Communications*, **2008**, 9, 409.
11. A. Schaefer-Sindlinger, I. Lappasa, C.D. Vogta, T. Itoa, H. Kurachib, M. Makinob, A. Takahashi, *Topics in Catalysis Vols.*, **2007**, 5, 42
12. P.I. Nemeș, N. Cotolan, L.M. Mureșan, *Studia UBB Chemia*, **2013**, LVIII(1), 81.
13. N. Maier, K.G. Nickel, C. Engel, A. Mattern, *Journal of the European Ceramic Society*, **2010**, 30, 1629.
14. M. Gorea, I.O. Rujoni, *Revista Romana de Materiale*, **2012**, 42(4), 415.

*Dedicated to Professor Liviu Literat
On the occasion of his 85th birthday*

ON THE OXIDATION OF GLUTATHIONE BY CHROMIUM (VI), IN AQUEOUS SOLUTIONS OF PERCHLORIC ACID

DANA-MARIA SABOU^{a,*} AND IOAN BÂLDEA^a

ABSTRACT. The oxidation of glutathione by chromium(VI) has been studied under pseudo-first order conditions at 293 K, in mildly acidic environment of controlled ionic strength (0.5 M, NaClO₄). The process was monitored spectrophotometrically and showed evidence of two stages. Both stages have been evaluated kinetically, the reaction orders were found and some of the rate constants were computed. The involvement of paramagnetic intermediates has been investigated. In agreement with the experimental findings, a reaction mechanism has been suggested, that showed changing features under the range of acidities employed.

Keywords: redox, chromium VI, glutathione, kinetics

INTRODUCTION

Chromium (VI) has been for a long time, and continues to be, widely used as a mild oxidant, for a variety of inorganic and organic substrates, not only in laboratories, but also at an industrial scale. The interest in clarifying the features of its reaction mechanisms is, therefore, understandable. A new boost has been given to the matter by the discovery of its ulcerating properties upon prolonged skin contact [1] and, more importantly, the carcinogenic effects of its dust upon inhalation, ultimately leading to lung cancers [2-4]. The toxicity of Cr(VI) contaminated water has also been periodically under assessment. While early results concluded it rather harmless, it has been recently proven positively carcinogenic upon either high dosage or long time ingestion [5]. It is believed that the responsibility lies with the mutagenic potential of the more active, lower valence states Cr(V) and Cr(IV) [6-8], formed during its

^a Babeş-Bolyai University, Faculty of Chemistry and Chemical Engineering, Str. Arany János, No. 11, RO-400028, Cluj-Napoca, Romania, * Corresponding author: dsabou@chem.ubbcluj.ro

reduction to Cr(III) by cellular constituents, amongst which ascorbic acid and glutathione are considered the most active ones [9, 10]. To this day, little has been established without doubt concerning the chemistry of the pathways leading to DNA alterations, and similar studies sometimes seem to have reached contradictory conclusions [11]. The outcome is that such findings have prompted re-examinations of the chemistry of chromium(VI) reduction by compounds containing alcoholic or thiolic moieties, in various environments. In this context, the reaction with glutathione received much attention, with most of the work focused on its behaviour in solutions of neutral (close to physiological) pH.

It is well known that in aqueous media, Cr(VI) is involved in a number of protolytic and hydrolytic equilibria [12, 13] that control its speciation. While at pH's of 7 and higher CrO_4^{2-} is the dominant species in the solution, in acidic environment this is protonated to HCrO_4^- and eventually to H_2CrO_4 , which becomes noticeable at pH's below 2 [13]. Also, in acidic medium, the condensation of two molecules of HCrO_4^- with the formation of the dimer $\text{Cr}_2\text{O}_7^{2-}$ becomes important at higher concentration of total Cr(VI) and increasing ionic strength. The dimer can also be involved in protolytic equilibria. However, it is possible to choose conditions so that the HCrO_4^- is the dominant species. Moreover, HCrO_4^- can undergo such condensation with virtually any partner able to provide an H^+ , making any acid a good candidate [14]. The further reactivity of the condensed species is dependent on the acid [15-17]. At lower total Cr(VI) concentrations, such condensations are much more likely to happen than the dimerization. The readiness with which the condensed species is formed and thus its amount, depends on the acid involved. Perchloric acid is considered to be the least prone to such condensation, thus, in diluted aqueous perchloric solutions, Cr(VI) exists as HCrO_4^- .

The wealth of work which has been done on the subject of chromium (VI) redox reactions in various media, with inorganic and organic substrates, including thiols, has been concluded in establishing a few features that are generally agreed upon. Their inner-sphere type mechanism is one such feature. They start with a reversible step in which the bonding of the thiol to chromium takes place, much like any other condensation with an acid. A condensation complex is formed, which subsequently decomposes by electron transfer. The number of the electrons simultaneously transferred in this step, the molecularity, the rate-determining stage of the whole process and sometimes the type of the reaction products, are features that differ from one reductant to another in similar environments. The same is valid for any individual reducing agent if the reaction conditions change.

This study deals with the reduction of Cr(VI) by glutathione in mildly acidic aqueous solutions of HClO_4 , providing both kinetic and extra kinetic data concerning the reaction. Thereby, it becomes possible to obtain more detailed insight on the reaction mechanism in this region of acidity.

RESULTS AND DISCUSSION

In this work, chromium (VI) was always used as the limiting reactant, while the glutathione and the hydrogen ion providing species were usually in large excess and the temperature and ionic strength were controlled (commonly 293 K and 0.5 M (NaClO₄) respectively). From literature data on the equilibrium constants, describing the speciation equilibria of Cr(VI) [12, 13, 18], it was computed that the dominant Cr(VI) species was always HCrO₄⁻ (in most cases around 98÷99 %, with ca. 86.8 % and 89 % as the lowest values, under the least favorable sets of conditions).

Stoichiometry

To determine the stoichiometry, three reaction mixtures containing glutathione (abbreviated as GSH) and Cr(VI) in an initial molar ratio of 20 to 1 were prepared and the reaction was allowed to finish. The remaining glutathione was titrated iodometrically. The results showed an average of 3.2 ± 0.2 moles of glutathione to be consumed for each mole of Cr(VI). Therefore, the reaction yields mainly the disulphide GSSG. This is in agreement with many literature data, concerning thiols in general [19-24] and glutathione in particular [25-29]. The reaction stoichiometry can be written as below:



Intermediates

UV-VIS Spectrophotometry

Upon mixing of the two reactants, a rapid change in colour of the solution can be observed within a time scale of seconds, followed by a much slower fading of this colour (tens to hundreds of minutes). This behaviour is explained by the occurrence of an intermediate [25, 28, 30-33]. McAuley and Olatunji [30] have calculated a spectrum showing a transient species with an absorption band in the region 375 ÷ 550 nm. We have also previously reported spectral evidence [14] for the formation, of a species with an absorption maximum at 435 nm, under conditions similar to those of this study. Such notable shift towards red, as compared to the 350 nm maximum of HCrO₄⁻, is consistent with the replacement of a Cr-O bond in HCrO₄⁻ by a Cr-S one, and supports the formation of a GS-Cr(VI) thioester. The binding of the glutathione to Cr(VI) through the cysteinyl thiolate group has been confirmed by Raman spectroscopy [34].

Some controversy existed in the literature about the assignment of the 400-500 nm absorption band to the GS-Cr(VI) thioester. This was sparked by the observation of an additional absorption band when working at pH 5.2÷5.9 [32], with a peak at 373 nm and higher molar absorptivity than that

of the CrO_4^{2-} (the dominant Cr(VI) species at this pH), with the maximum at 372 nm [35]. It was proposed that the thioester absorbed at 373 nm and some Cr(V) or Cr(IV) [28, 32] was responsible for the band at 400-500 nm. However, such a small shift (of only 1 nm) is uncharacteristic when sulphur replaces an oxygen in the chromium complex [14], but rather specific for the reactions of hydroxy compounds, which bind to Cr *via* the hydroxylic oxygen. In these, the bond type is not changed and only the charge distribution within the complex is affected. Moreover, under our conditions (pH 1-2) the 373 nm band is not present; on the contrary, a minimum of absorbance is noticed in that region [14]. Since HCrO_4^- , the dominant species in our case, is known to readily form condensation complexes, the species exhibiting the absorption band at 435 nm, that features in the spectra we recorded, should be the GS-Cr(VI) thioester. It is the band around 373 nm, occurring at the higher pH's, that should rather be attributed to a different kind of intermediate.

Combining absorption spectroscopy and EPR spectroscopy results, Lay and Levina [25] have later reported a spectrum for the thioester intermediate that was identical for pH's 2.9 and 7.4 and in perfect agreement with our spectral data. They attributed the high absorbance around 370 nm to a mixture of Cr(V) or potentially Cr(IV) intermediates and of CrO_4^{2-} (as one product of the Cr(V) disproportionation, at pH 8) [36].

ESR Spectroscopy

We made use of the ESR technique to observe the possible formation of Cr(V) species under the conditions of our study. For comparison with literature data, we worked at 277 K and spanned a larger range of pH's. Figure 1 A) shows comparatively the signals found in each case, two minutes after mixing the reactants, while B), C) and D) illustrate for some of them their time dependence.

It is evident that more than one type of Cr(V) intermediates may occur in the reaction mixture, and the extent to which each of them is formed, appears to be a pH-dependent feature. It could also be argued that after two minutes the reaction has reached different stages at the different acidities, hence some of the signals may have already vanished. However, the time evolution for each pH shows no growing signals, but only the decay of the already present ones.

While the recorded spectrum at pH 11 shows no notable features, for pH 8, two of the signals reported by Levina and Lay [36] with $g_{\text{iso}}=1.996$ and $g_{\text{iso}}=1.986$, are observable in figure 1 (A) and (D), with the latter being longer lived. Two signals similar to those reported earlier by Brauer and Wetterhahn ($g_{\text{iso}}=1.986$ and $g_{\text{iso}}=1.972$) [32] are seen at pH 5, and are quite stable (even at room temperature, where the measurement was repeated) but they almost vanish at pH 3. On the contrary, three signals (g_{iso} of 1.983,

1.980 and 1.978) comparatively weak at pH 5, and near-noise at pH 8 gain some importance at pH 3. At pH 1 no Cr(V) intermediate could be observed under the chosen settings and only a very broad Cr(III) signal was seen, indicating that the reaction had most likely already finished.

These findings show that there are several alternative pathways for the reaction, that proceed *via* Cr(V) intermediates. The differences in the Cr(V) species have to do with the involvement of hydrogen ions.

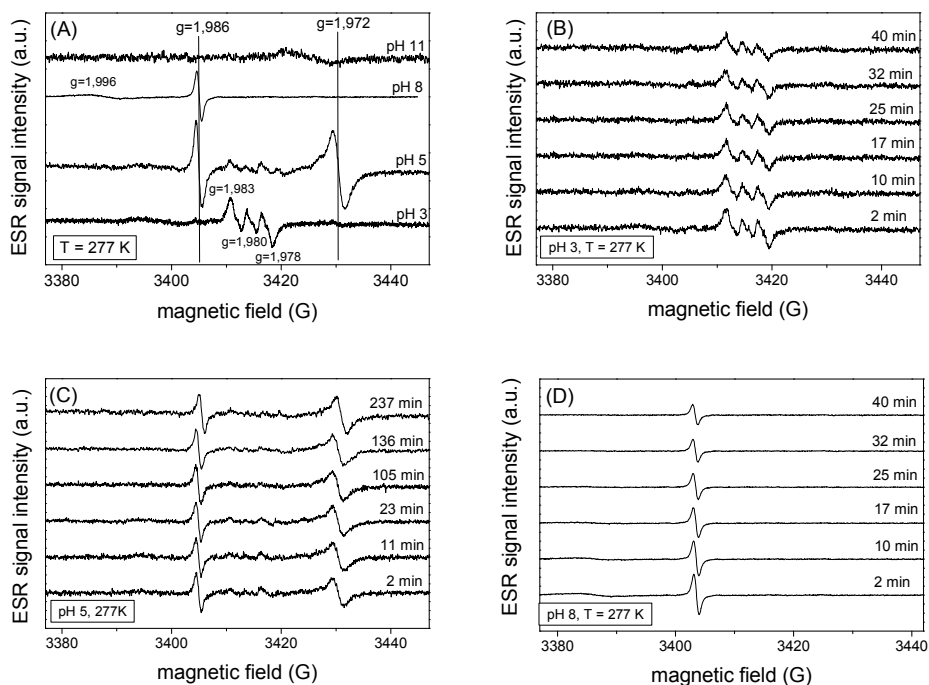


Figure 1. ESR spectral evidence for the formation of Cr(V)-glutathione complexes at various acidities during the oxidation of glutathione by chromium (VI).

Kinetics

At 435 nm, the shape of the kinetic curves clearly shows the two phases of the process, as illustrated in figure 2. The notable difference in their rates allowed us to further study them separately.

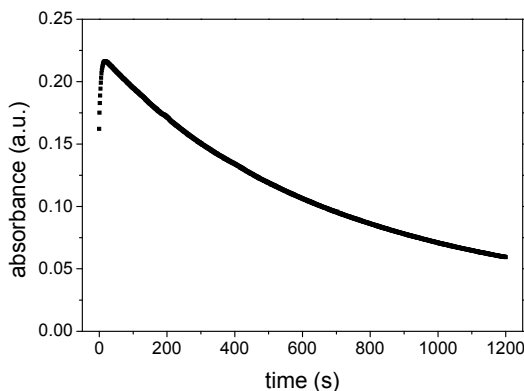


Figure 2. A kinetic curve at 435 nm for the reaction of Cr(VI) with glutathione in aqueous perchloric solution ($[\text{Cr(VI)}]_0 = 1.3 \cdot 10^{-4}$ M, $[\text{GSH}]_0 = 1.6 \cdot 10^{-2}$ M, $[\text{H}^+]_0 = 3.0 \cdot 10^{-2}$ M (HClO_4), $\mu = 0.5$ M (NaClO_4), $T = 293$ K)

The formation of the Cr(VI)-GSH intermediate complex

As indicated by the bathochromic shift in absorbance, the formation of the intermediate involves the binding of glutathione to the Cr(VI) *via* the thiolic moiety. This is a ligand substitution, hence a reversible step. In acidic environment, some involvement of the hydrogen ion can also be expected.

The reaction orders for the formation of the intermediate were determined using the initial rates method. A stopped-flow arrangement was used to monitor the beginning part of the reaction and the initial rates (expressed as dA/dt) were computed from the slopes of the curves absorbance-time for less than 0.1% total conversion (0.4 s or less). Three series of measurements were made. In each of them the concentration of only one species was varied while the others were kept constant. Table 1 lists the results obtained. (The errors, in the table 1 and throughout the paper, unless stated otherwise, are the standard errors of the parameter as determined from the linear regression.)

For such small conversions, the amount of intermediate formed is insignificant and the reverse reaction negligible. Therefore, the initial rate law can be written as:

$$\alpha \cdot r_{0,435} = \left. \frac{dA_{435}}{dt} \right|_{t \rightarrow 0} = \alpha \cdot k_1 \cdot [\text{GSH}]_0^a [\text{H}^+]_0^b [\text{HCrO}_4^-]_0^c \quad (2)$$

where $r_{0,435}$ and A_{435} are the initial rate and the absorbance at 435 nm, α is a constant containing the path length of the mixing chamber ($\ell = 0.336$ cm) and the molar absorptivity of HCrO_4^- at the used wavelength ($\epsilon_{435, \text{HCrO}_4^-}$), k_1 is the rate coefficient for the forward step, while a , b and c are the respective reaction orders for the three possible reactants.

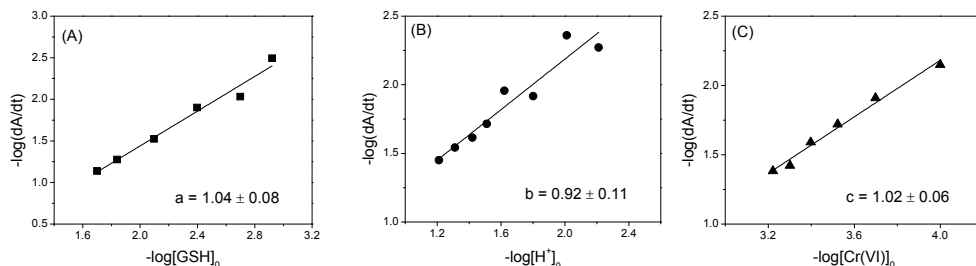
Table 1. Initial slopes dA/dt (directly proportional to the initial rates) computed from the experimental curves of absorbance vs. time ($\mu = 0.5 \text{ M (NaClO}_4\text{)}, T = 293 \text{ K}$)

$[\text{H}^+]_0$ (10^{-2} M)	$[\text{GSH}]_0$ (10^{-3} M)	$[\text{HCrO}_4^-]_0$ (10^{-3} M)	dA/dt (10^{-3} s^{-1})
2.6	1.2	0.40	3.2 ± 0.5
	2.0		9.3 ± 0.3
	4.0		12.5 ± 0.2
	8.0		30 ± 3
	15		53 ± 5
	20		70 ± 10
2.6	4.0	0.20	7.1 ± 0.3
		0.60	19.0 ± 0.3
		0.80	25.7 ± 0.3
		1.0	37.9 ± 0.3
		1.2	41.4 ± 0.3
6.2	4.0	0.40	35 ± 2
4.9			29 ± 1
3.8			24 ± 1
3.1			19 ± 1
2.4			11 ± 2
0.97			4.4 ± 0.4
0.62			5.4 ± 0.4

With each series of measurements, the reaction order with respect to the varied species can be determined from the slopes of the appropriate double logarithmic plot of equation 3, as it is shown by figure 3.

$$\log \frac{dA}{dt} = \log \alpha + a \cdot \log([\text{GSH}]_0) + b \cdot \log([\text{H}^+]_0) + c \cdot \log([\text{HCrO}_4^-]_0) \quad (3)$$

The three different plots are all linear and of slopes approximately unity.


Figure 3. Double-logarithmic plots for determining the three reaction orders (GSH: (A), H^+ : (B) and Cr(VI) : (C)) for the intermediate formation. Conditions like in table 1.

In mechanistic terms, this means that the intermediate has a 1:1 ratio GSH:Cr(VI) and its formation is catalyzed by one proton. Therefore, the step of forming the intermediate can be described by the equation 4:



where k_1 and k_{-1} stand for the reaction coefficients of the forward and reverse processes respectively. A simple third order rate law can be written for the build-up of the intermediate (the forward step):

$$r_1 = k_1[\text{GSH}][\text{H}^+][\text{HCrO}_4^-] \quad (5)$$

Furthermore, a value for the k_1 can be determined based on eq. 5, from the initial rates, which can be computed if the molar absorptivity of the reactant at 435 nm ($\epsilon_{435, \text{HCrO}_4^-}$) is known. To estimate the latter, we used the set of measurements where Cr(VI) was varied, to plot the initial absorbance values against the initial Cr(VI) concentration. We obtained a good line, with the slope $231 \pm 12 \text{ M}^{-1} \text{ cm}^{-1}$, equal to $\epsilon_{435, \text{HCrO}_4^-}$.

Using the data of all three sets of measurements, the plot of the initial reaction rates against the product of the three reactant concentrations was linear (figure 4), with a zero intercept within the error ($(3 \pm 10) \cdot 10^{-6} \text{ s}^{-1}$). The slope of the line was $(4.6 \pm 0.1) \cdot 10^3 \text{ M}^{-2} \text{ s}^{-1}$, and represents the third order rate constant k_1 at $T = 293 \text{ K}$ and $\mu = 0.5 \text{ M}$.

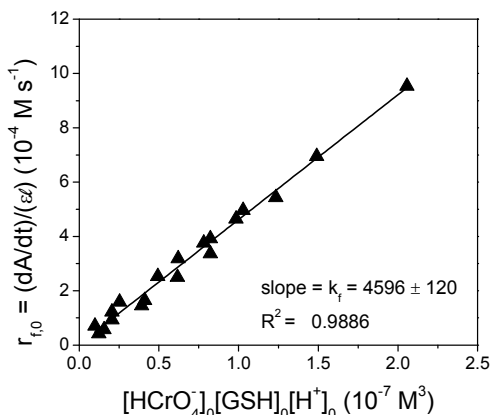


Figure 4. Dependence of the initial rate for the intermediate formation on the product of the three initial concentrations of the reactants ($T = 293 \text{ K}$, $\mu = 0.5 \text{ M}$).

Decay of the GS-Cr(VI) intermediate by electron transfer

As established, the decay of the intermediate is much slower than its formation. It is assumed that this process takes place with the transfer of one or more electrons and therefore is the slower step, as this usually involves more important rearrangements in the chromium complex.

Classical batch measurements were appropriate to monitor this stage of the process. In these, Cr(VI) was, once again, the limiting reactant and its concentration was always $1.33 \cdot 10^{-4}$ M. The concentrations of the glutathione and hydrogen ion were always in large enough excess to be considered practically constant throughout the reaction. The illustrative curve in figure 2 is part of this group of batch measurements.

Under the excess settings, the assumption of two consecutive pseudo-first order steps (where R stands for reactant, I for intermediate and P for a generic product) can be applied to the studied system (equation 6):



The observed first order for both steps is with respect to the Cr(VI) species (R or I) and the observed rate coefficients k_{1obs} and k_{2obs} are functions of the excess concentrations of the other reactants involved.

As already stated, much of the total absorbance at 435 nm appears to be brought about by the intermediate. However, some contribution from the weaker band of the HCrO_4^- in this region, or from the even weaker one of the Cr(III) product should be considered. Taking into account this and the rate law for the two steps first-order series (formation and decay of the intermediate), the following equation for the evolution of the absorbance in time is valid [19, 28]:

$$A - A_{\infty} = [R]_0 \ell \left\{ \varepsilon_R + \frac{k_{2obs} \varepsilon_P - k_{1obs} \varepsilon_I}{k_{1obs} - k_{2obs}} \right\} e^{-k_{1obs} t} + [R]_0 \ell \left\{ \frac{k_{1obs} (\varepsilon_I - \varepsilon_P)}{k_{1obs} - k_{2obs}} \right\} e^{-k_{2obs} t} \quad (7)$$

or its simpler form, obtained by combining all pre-exponential factors into some constants (γ_1 and γ_2):

$$A - A_{\infty} = \gamma_1 e^{-k_{1obs} t} + \gamma_2 e^{-k_{2obs} t} \quad (8)$$

If $k_{1obs} \gg k_{2obs}$, equation (8) reaches a limit form for late stages, where the first exponential vanishes, and γ_2 and k_{2obs} can be determined, respectively, based on equation (9):

$$\ln(A - A_{\infty}) = \ln \gamma_2 - k_{2obs} t \quad (9)$$

For the early stages of the process, equation (8) can be re-arranged into equation (10), to yield γ_1 and k_{1obs} :

$$\ln(A - A_{\infty} - \gamma_2 e^{-k_{2obs} t}) = \ln \gamma_1 - k_{1obs} t \quad (10)$$

Equation (9) was used to process our data. Indeed, for later stages, the plots $\ln(A - A_{\infty}) = f(t)$ became linear (R^2 between 0.9989 and 0.9999 at conversions higher than 70%, based on absorbance). The slopes of the linear parts represent k_{2obs} , and are given in table 2, for one series of measurements at constant acidity and varying the GSH concentration, and for three series where the H^+ was varied at constant GSH.

Table 2. Mean values (3-5 measurements) for the observed rate constants of the second stage in the reduction of Cr(VI) by glutathione, at T = 293 K, and $\mu = 0.5$ M, $[\text{Cr(VI)}]_0 = 1.33 \cdot 10^{-4}$ M. The listed errors are the standard errors of the means.

$[\text{GSH}]_0$ (10^{-3} M)	$[\text{H}^+]_0$ (M)	$[\text{GSH}]$ (M)			
	$3.0 \cdot 10^{-2}$	$6.7 \cdot 10^{-3}$	$3.3 \cdot 10^{-3}$	$1.3 \cdot 10^{-3}$	
	$k_{2\text{obs}}$ (10^{-4} s $^{-1}$)	$[\text{H}^+]$ (10^{-2} M)	$k_{2\text{obs}}$ (10^{-4} s $^{-1}$)	$k_{2\text{obs}}$ (10^{-4} s $^{-1}$)	$k_{2\text{obs}}$ (10^{-4} s $^{-1}$)
1.3	2.22 ± 0.02	9.9	18 ± 1	13.05 ± 0.02	9.1 ± 0.2
2.7	3.5 ± 0.1	8.0	14.2 ± 0.1	9.86 ± 0.03	6.8 ± 0.1
3.3	3.86 ± 0.07	6.3	11.6 ± 0.1	7.52 ± 0.01	4.95 ± 0.09
5.3	6.2 ± 0.1	5.0	9.6 ± 0.1	6.13 ± 0.02	3.85 ± 0.06
6.7	7.21 ± 0.05	3.9	8.20 ± 0.07	5.08 ± 0.02	2.83 ± 0.05
8.0	8.1 ± 0.3	3.0	7.21 ± 0.05	3.86 ± 0.07	2.22 ± 0.04
10	10.2 ± 0.1	1.6	6.34 ± 0.08	3.28 ± 0.02	1.56 ± 0.03
12	12.3 ± 0.3	0.51	5.80 ± 0.02	2.60 ± 0.03	0.96 ± 0.06
13	13.2 ± 0.2	0.30	5.9 ± 0.1	2.56 ± 0.07	0.85 ± 0.03
16	16.1 ± 0.7	0.13	6.0 ± 0.2	2.81 ± 0.08	0.83 ± 0.03

When a plot of the apparent first-order rate constants of the redox process against the varied concentration of GSH is made, it yields a good straight line, with a positive intercept and a slope as given in figure 5 A.

Moreover, if the rate of the decomposition is written as:

$$r_2 = k_2 [\text{GSH}]_0^{a'} [\text{H}^+]_0^{b'} [\text{GSCrO}_3^-] \quad (11)$$

$$\text{than } k_{2\text{obs}} = k_2 [\text{GSH}]_0^{a'} [\text{H}^+]_0^{b'} \quad (12)$$

and a plot of $\log(k_{2\text{obs}}) = f(\log[\text{GSH}]_0)$ is expected to be linear, with a slope equal to the order a' . In this way, $a' = 0.87 \pm 0.02$ was found (figure 5 B).

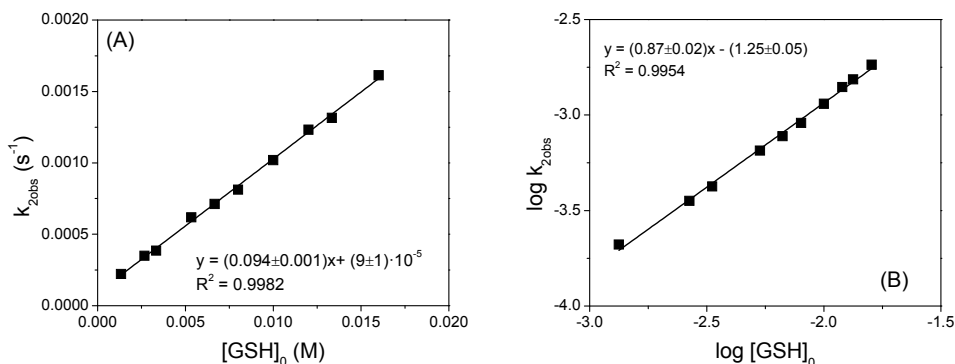


Figure 5. Dependence of the pseudo-first order constants $k_{2\text{obs}}$ for the decay of the intermediate on the glutathione concentration (A) and the double logarithmic plot to find the reaction order a' , based on equation 12 (B). Conditions like in table 2.

Combining the two observations, it can be assumed that two steps could be operative for the decomposition of the GSCrO_3^- complex: one being a monomolecular decomposition (order zero with GSH) and the other a bimolecular process in which a second molecule of GSH intervenes (order one with GSH).

Through similar treatment of the corresponding $k_{2\text{obs}}$ values at constant $[\text{GSH}]$ and variable $[\text{H}^+]$, dependences like those in figure 6 were found in the double logarithmic plot (A) and in the plot of $k_{2\text{obs}}$ against $[\text{H}^+]$ (B). Figure 6 (C) shows a comparative plot of $k_{2\text{obs}}$ against $[\text{H}^+]^2$.

Two patterns of behaviour can be identified.

a) The double logarithmic plot has a part of slope nearly zero, between pH 1.8 and 2.9. From table 2, if comparing the three $k_{2\text{obs}}$ values corresponding to the lowest acidities, for each set of data at constant glutathione concentration they can nearly be considered equal within the errors. This means that at low acidities, the hydrogen ion is not involved in the electron transfer decay of the intermediate. Bose et al. [28] have also noticed no significant pH dependence of the rate constants in the pH range 1.8÷3.3.

The non-zero intercepts in figure 6 (B) also support the existence of the H^+ independent path, which should, however, involve the glutathione, since the intercept values vary with the concentration of GSH used.

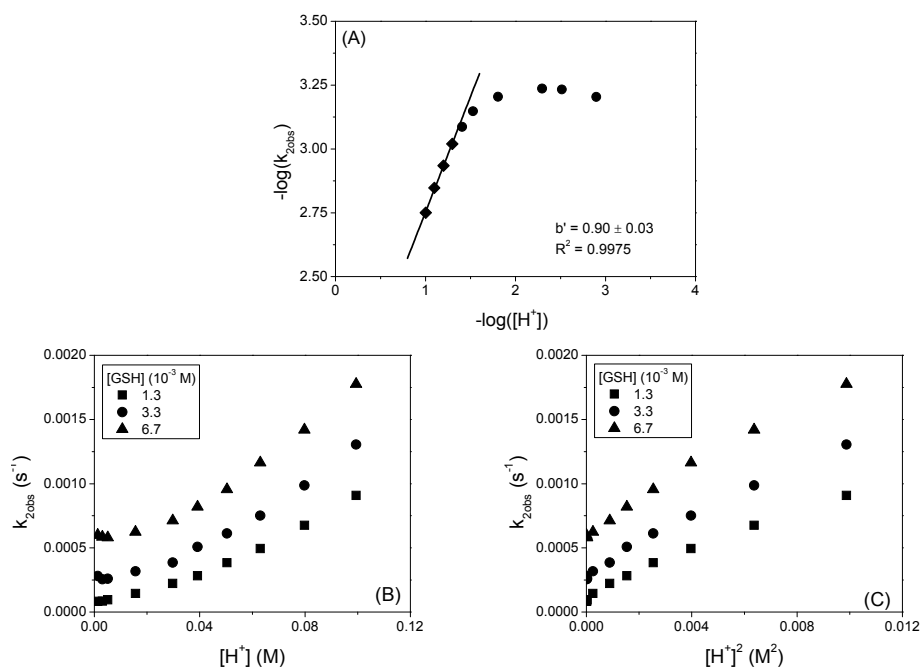


Figure 6. Example of a double logarithmic plot (A) and dependence of the pseudo-first order coefficients $k_{2\text{obs}}$ on the first (B) or second (C) power of the H^+ concentration.

b) Focusing on the region of the higher acidities, although the double logarithmic plot suggests a first order with H^+ , the curved dependence of k_{2obs} versus $[H^+]$ obtained (figure 6 B) indicates an order higher than first. However, a second-order representation as in figure 6 (C) does not result in a straight line either. This can only be reasoned by the occurrence of more parallel paths, which involve one or two protons respectively. Examining the three curves in figure 6 (B), they appear to increase with slightly different gradients, suggesting that at least one of the hydrogen ion assisted paths depends on the GSH concentration too.

To gain some more insight on the matter, more plots of the k_{2obs} values against the glutathione concentration were made, using the values in table 2 for the nine sets of three rate constants at different acidities, in comparison with those already shown in figure 5 A. They all gave straight lines (figure 7). The intercepts increased with the increase in acidity. At low acidity, the slopes were statistically equal, but progressing towards higher acidities ($3.9 \cdot 10^{-2} \div 9.9 \cdot 10^{-2} M$), they increased monotonously.

As expected, for the three lowest acidities, the points almost overlapped. They were used all together to compute a regression line ($R^2 = 0.9978$). The intercept was slightly negative, approximately zero within the error. Comparing this with the positive intercepts found for the lines at higher acidities, it follows that a monomolecular decomposition within the intermediate complex alone (zero order with both GSH and H^+) is not very likely; such a path requires hydrogen ion assistance and thus becomes important at higher acidities.

On the other hand, the slope of the line was $(9.4 \pm 0.2) \cdot 10^{-2} M^{-1}s^{-1}$. It represents the rate constant for the bimolecular decomposition of the intermediate, assisted by a second glutathione molecule, but not by the hydrogen ion (first order with the intermediate and glutathione, zero order with H^+). As it can be observed, the value is identical to the one obtained from the slope of the plot in figure 5 A, suggesting that at the acidity of $3.0 \cdot 10^{-2} M$ the GSH dependent path not involving hydrogen ions is still dominant. For even higher acidities, however, the increasing value of the slopes proves that some other GSH dependent paths, influenced by the H^+ , gain importance.

Regarding the GSH dependent and independent paths, it was of interest to figure out if any distinction could be made between the number of hydrogen ions involved in each of them. For this, we tried plots of the slopes and the intercepts respectively, against various powers of $[H^+]$. In both cases the best fit was obtained when plotting against a fractional order between one and two (straight lines, with $R^2 = 0.9909$ and 0.9987 respectively, when plotting against $[H^+]^{1.5}$). Also, in the case of the slopes, the plot had a positive intercept (statistically different from zero), showing that the bimolecular path of zero order in H^+ is still present. Therefore, no less than five parallel paths need to be considered at high acidities.

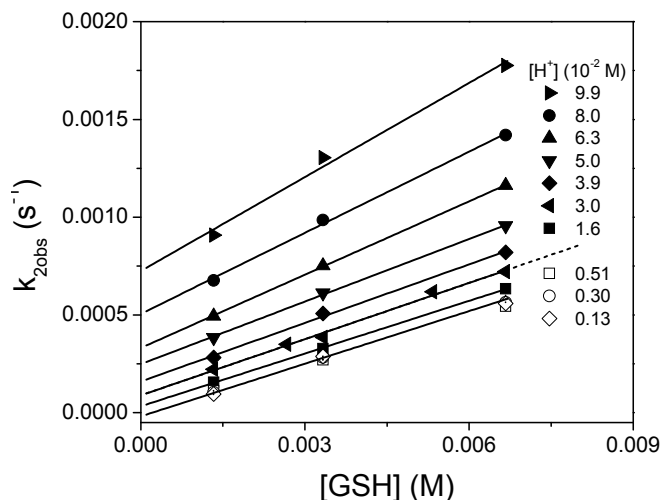


Figure 7. Plots of the k_{2obs} values against the glutathione concentration at various acidities. Conditions like in table 2.

Temperature and ionic strength effects on the decay of the intermediate

Measurements were made in order to determine the effects of the temperature and ionic strength on the electron transfer step. The pseudo-first order coefficients obtained are listed in table 3.

Table 3. Pseudo-first order rate constants k_{2obs} illustrating the effects of temperature (at $\mu=0.5$ M) and ionic strength (at $T = 293$ K) on the decay of the intermediate. ($[Cr(VI)]_0 = 1.3 \cdot 10^{-4}$ M; $[GSH]_0=6.7 \cdot 10^{-3}$ M; $[H^+]_0=3.0 \cdot 10^{-2}$ M)

T (K)	k_{2obs} (10^{-4} s $^{-1}$)	μ (M)	k_{2obs} (10^{-4} s $^{-1}$)
293	7.09	0.05	8.74 \pm 0.01
298	9.66	0.1	8.37 \pm 0.05
303	12.74	0.3	7.91 \pm 0.05
308	16.84	0.5	7.39 \pm 0.04
313	21.09	0.7	7.41 \pm 0.05
323	32.71	1.0	7.56 \pm 0.03

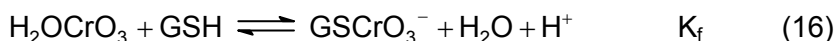
Given the many parallel pathways, it was not possible to determine each of their individual rate constants and only an apparent activation energy was found. The Arrhenius plot using the k_{2obs} values at the six different temperatures showed very good linearity and from the slope a value of $E_{a,obs} = 40.1 \pm 0.9$ kJ mole $^{-1}$ was computed.

The ionic strength effect was checked in the range 0.05 to 1 M. Some slight decrease of the pseudo-first order rate constant $k_{2\text{obs}}$ of the increase of the ionic strength was observable, suggesting that species with opposite charge are involved in the reaction.

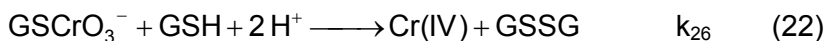
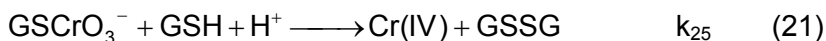
Reaction mechanism and rate law

The mechanism of the glutathione oxidation by Cr(VI) in acidic media is complex. Taking into account the features emerging from the interpretation of the kinetic and non-kinetic data, some considerations can be formulated.

The first step of the process is the reversible, hydrogen ion assisted formation of the 1:1 Cr(VI):GSH intermediate, described by the equation 4. This can be assumed to happen in two bi-molecular steps, with the first a rapid proton transfer to the leaving group in the Cr(VI) species.



The subsequent step is rate determining and consists on the decay of the intermediate by electron transfer. In theory, the alternative paths 17 to 22 are all possible.



However, from our results, step 17 seems to be the least likely and has been disregarded, while the others are of different importance, depending on the acidity.

A particular situation was found for the lower acidities within the investigated range ($1.58 \cdot 10^{-2} \div 0.13 \cdot 10^{-2}$ M), where the decay of the intermediate showed no dependence on the hydrogen ion concentration, and a first order dependence on the glutathione concentration.

Therefore, only the intermediate formation (equation 4), together with the bimolecular step (20) have to be considered for the rate law. The rate law for the second stage of the reaction can be written as:

$$r_2 = k_{24} [\text{GSH}] [\text{GSCrO}_3^-] \quad (23)$$

The shape of the kinetic curves suggests that the intermediate is formed in a fast pre-equilibrium, therefore its concentration can be expressed as:

$$[\text{GSCrO}_3^-] = K_{11}[\text{GSH}][\text{HCrO}_4^-] \quad (24)$$

where K_{11} is the equilibrium constant for the overall process of the intermediate formation ($K_{11} = k_1/k_{-1} = K_p \cdot K_f$). The hydrogen ion concentration does not appear in this equation, since it acts as a catalyst.

If the balance of all absorbing chromium (VI) species is taken into account, its total concentration ($[\text{Cr(VI)}]_t$) is given by equation 25:

$$[\text{Cr(VI)}]_t = [\text{HCrO}_4^-] + [\text{GSCrO}_3^-] \quad (25)$$

Substituting in equation 24, the concentration of the intermediate will be:

$$[\text{GSCrO}_3^-] = \frac{K_{11}[\text{GSH}]}{1 + K_{11}[\text{GSH}]} [\text{Cr(VI)}]_t \quad (26)$$

and the expression of rate law becomes:

$$r_2 = -\frac{d[\text{Cr(VI)}]_t}{dt} = k_{24} \frac{K_{11}[\text{GSH}]^2}{1 + K_{11}[\text{GSH}]} [\text{Cr(VI)}]_t = k_{2\text{obs}} [\text{Cr(VI)}]_t \quad (27)$$

This rate law is identical to the one found by Wetterhahn [26] at pH 7.4. Using the expression of $k_{2\text{obs}}$ in (27), a linear equation can be derived:

$$\frac{[\text{GSH}]^2}{k_{2\text{obs}}} = \frac{1}{k_{24}K_{11}} + \frac{1}{k_{24}} [\text{GSH}] \quad (28)$$

A plot of $[\text{GSH}]^2/k_{2\text{obs}}$ vs. $[\text{GSH}]$ using only the data at the low acidities is linear with the equation $[\text{GSH}]^2/k_{2\text{obs}} = 0.007 \pm 0.001 + (10.4 \pm 0.2)[\text{GSH}]$ ($R^2 = 0.9962$). From the slope, k_{24} can be computed, giving $(9.7 \pm 0.2) \cdot 10^{-2} \text{ M}^{-1} \text{ s}^{-1}$. (This is the same as found above $(9.4 \pm 0.2) \cdot 10^{-2} \text{ M}^{-1} \text{ s}^{-1}$ from the plots vs. $[\text{GSH}]$ of either the same $k_{2\text{obs}}$ values, or of those at $[\text{H}^+] = 3.0 \cdot 10^{-2} \text{ M}$). Combining the slope and the intercept, a value of $1526 \pm 275 \text{ M}^{-1}$ was computed for the equilibrium constant K_{11} . It fits well with the range of values characteristic for the formation of thioesters [14]. Although obtained from few data, this is close to the value of $1550 \pm 100 \text{ M}^{-1}$ found by McAuley and Olatunji [30], under similar conditions. From K_{11} , together with the value of k_1 determined earlier, a k_{-1} of $3.0 \pm 0.6 \text{ M}^{-1} \text{ s}^{-1}$ could be estimated.

At the higher acidities, our results show that an alternative, glutathione independent path becomes available for the decomposition of the intermediate. McAuley and Olatunji [27] suggested that two protons are assisting, and gave a mechanism composed of steps 4, 19 and 20. Their conclusions were

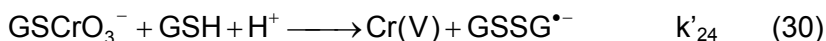
based on fewer measured points, therefore the curved rather than linear dependences of the $k_{2\text{obs}}$ on the $[\text{H}^+]^2$ might have been missed. It is reasonable to assume that the protons would also be involved in the bi-equivalent processes, as found for other systems [37, 38], and based on our observations such paths cannot be dismissed. Therefore, the sequence we propose is formed of steps (4) and (18) to (22), when the complex rate law takes the form:

$$-\frac{d[\text{Cr(VI)}]_t}{dt} = \left\{ k_{22}[\text{H}^+] + k_{23}[\text{H}^+]^2 + (k_{24} + k_{25}[\text{H}^+] + k_{26}[\text{H}^+]^2)[\text{GSH}] \right\} \cdot \frac{K_{11}[\text{GSH}]}{1 + K_{11}[\text{GSH}]} [\text{Cr(VI)}]_t \quad (29)$$

The paths (18), (19), (21) and (22) all involve some species of opposite charge. This in agreement with the effect of the ionic strength, which has been checked for one acidity within this range ($3.0 \cdot 10^{-2}$ M).

According to the stoichiometry, the final products of the reaction are Cr(III) and the disulphide. To complete the process, after the first electron transfer, Cr(V) or Cr(IV) intermediates react in further steps. Cr(V) could react with the excess GSH to form Cr(III) in a bi-equivalent step, or even with glutathyl radical to reduce to Cr(IV). Cr(IV) can also react with a glutathyl radical and reduce to Cr(III), or with another molecule of Cr(VI) to form Cr(V), although this is expected to be favoured when Cr(VI) is in excess. Two glutathyl radicals can readily combine in a rapid step to yield the glutathione-disulphide.

The Cr(V) complexes observed in the ESR spectra at low acidities can be the result of one such step. On the other hand, a bi-molecular one-equivalent path for the electron transfer decomposition of the intermediate can also be envisioned (equation 30), leading to the disulphide radical $\text{GSSG}^{\cdot-}$:



This would be kinetically indistinguishable, leading to the same rate law, and could also explain the formation of Cr(V) in neutral media. Disulphide radicals were proved to exist [39] and through molecular orbital calculations were found to be likely more stable than the thyl radicals.

CONCLUSIONS

The reaction between glutathione and chromium(VI) has been investigated under mildly acidic conditions. The process showed evidence of two distinct stages; a formation of an intermediate in a fast reversible step, followed by a much slower decay. A third order rate law was found for the intermediate formation, first order with both the main reactants and also the hydrogen ion. This step has been characterized by both rate constants and the equilibrium constant.

It was found that different mechanistic paths had to be considered for the decomposition of the intermediate, depending on the acidity. At low hydrogen ion concentrations ($\text{pH} > 1.8$), a bi-molecular and possibly bi-equivalent route involving a second molecule of glutathione was found to be dominant. For this, the value of the rate constant was computed.

At higher acidities, one-equivalent and bi-equivalent steps were proved to coexist, both of them involving either one or two hydrogen ions.

EXPERIMENTAL SECTION

The chemicals used were all of certified analytical reagent grade, purchased from commercial sources and used without further purification. The solutions were prepared in demineralized and tetra-distilled water. Stock solutions of HClO_4 and NaClO_4 were prepared and standardized by titration with NaOH solutions. Aliquots of the NaClO_4 solution were passed over the cationic resin Virolyte C-100 (Victoria, Romania) in the H-form, and subsequently the resulting acid was titrated. The solution of glutathione was freshly prepared and standardized iodometrically before each set of runs.

For the slow stage of the overall process, batch experiments were designed, in which the reaction was followed spectrophotometrically, at 435 nm. Glutathione was added in excess (10 to 120-fold), and also the hydrogen ion carrying species (10 to 750-fold). The ionic strength was adjusted by adding NaClO_4 . The apparatus used was a double-beam Jasco V-530 spectrophotometer interfaced with a DTK computer and equipped with a cell holder connected to a FALC SB15 digital thermostat, allowing the control of temperature within ± 0.1 degrees. A quartz cuvette with 5 cm path length was used. The reaction process was initiated by injecting thermostated chromic acid solution directly into the cell, over a mixture of the other reactants. The mixing time did not exceed 0.5 s.

To study the fast stage of the overall process (the formation of the intermediate), some other experiments were carried out, making use of the stopped-flow technique. A home-built stopped-flow apparatus with spectrophotometrical detection and oscillographic recording has been utilized. Again, Cr(VI) was the limiting reactant ($1 \cdot 10^{-4}$ to $6 \cdot 10^{-4} \text{M}$), with the glutathione ($8 \cdot 10^{-3}$ to $2.4 \cdot 10^{-2} \text{M}$) and hydrogen ion (0.01 to 0.1 M) in large excess. For each set of conditions four replicates were made using the same batches of solutions and the curves mediated, to minimize the noise.

ESR measurements were recorded using a Bruker ELEXSYS 500-Series spectrometer equipped with a Bruker liquid nitrogen temperature control system. The microwave frequency was 9.5 GHz (X-band) and the modulation frequency was 100 kHz. A modulation amplitude of 1 G was chosen in order to get the greatest possible signal intensity without suffering from overmodulation, which could otherwise have lead to distorted line shapes and positions. From

literature [32] a microwave power of 20mW and a temperature of 277 K were adopted. The remaining parameters were chosen according to the specifics of each individual sample.

ACKNOWLEDGMENTS

The authors would like to thank Prof. Dr. Günter Grampp, from the Institute of Physical and Theoretical Chemistry, Graz University of Technology, Austria, for providing the ESR and stopped-flow facilities and assistance with the ESR measurements.

REFERENCES

1. P. Sanz, J.L. Moline, D. Sole, J. Corbella, *Journal of Occupational Medicine*, **1989**, 31(12), 1013.
2. V. Bianchi, A.G. Lewis, *Toxicological and Environmental Chemistry*, **1987**, 15, 1.
3. M. Cieślac-Golonka, *Polyhedron*, **1996**, 15, 3667.
4. S.A. Katz, H. Salem, "The Biological and Environmental Chemistry of Chromium", VCH, New York, **1994**, p. 6.
5. N. McCarroll, N. Keshava, J. Chen, G. Akerman, A. Kligerman, E. Rinde, *Environmental and Molecular Mutagenesis*, **2010**, 51, 89.
6. S. Veritt, L.S. Levy, *Nature*, **1974**, 250, 493.
7. P.A. Lay, A. Levina, *Journal of the American Chemical Society*, **1998**, 120, 6704.
8. R. Codd, C.T. Dillon, A. Levina, P.A. Lay, *Coordination Chemistry Reviews*, **2001**, 216-217, 537.
9. P.H. Connett, K.E. Wetterhahn, *Structure and Bonding (Berlin)*, **1983**, 54, 93.
10. A.S. Standeven, K.E. Wetterhahn, *Journal of the American College of Toxicology*, **1989**, 8, 1275.
11. A.L. Holmes, S.S. Wise, J.P. Wise Sr., *Indian Journal of Medical Research*, **2008**, 128, 353.
12. N.N. Greenwood, A. Earnshaw, "Chemistry of the Elements", 2. Edition Butterworth-Heinemann, Oxford, **1997**, chapter 23.
13. J.D. Ramsey, L. Xia, M.W. Kendig, R.L. McCreery, *Corrosion Science*, **2001**, 43, 1557.
14. I. Bâldea, D.M. Sabou, *Studia UBB Chemia*, **2001**, 46(1-2), 17.
15. N. Cohen, F.H. Westheimer, *Journal of the American Chemical Society*, **1952**, 74, 4387.
16. U. Klaning, M.C.R. Symons, *Journal of the Chemical Society*, **1961**, 3204.
17. G.P. Haight Jr., D.C. Richardson, N.H. Coburn, *Inorganic Chemistry*, **1964**, 3, 1777.

18. J.D. Neuss, W. Rieman III, *Journal of the American Chemical Society*, **1934**, 56, 2238.
19. I. Bâldea, D.-M. Sabou, *Revue Roumaine de Chimie*, **2000**, 45, 537.
20. G. Niac, S. Schön, I. Bâldea, *Studia UBB Chemia*, **1986**, 31(2), 31.
21. I. Bâldea, G. Niac, *Studia UBB Chemia*, **1986**, 31(2), 41.
22. I. Bâldea, *Studia UBB Chemia*, **1987**, 32(2), 42.
23. I. Bâldea, *Studia UBB Chemia*, **1994**, 39(1-2), 138.
24. J.P. McCann, A. McAuley, *Journal of the Chemical Society, Dalton Transactions*, **1975**, 783.
25. A. Levina, P.A. Lay, *Inorganic Chemistry*, **2004**, 43, 324.
26. P.H. Connett, K.E. Wetterhahn, *Journal of the American Chemical Society*, **1985**, 107, 4282.
27. A. McAuley, M.A. Olatunji, *Canadian Journal of Chemistry*, **1977**, 55, 3335.
28. R.N. Bose, S. Moghaddas, E. Gelerinter, *Inorganic Chemistry*, **1992**, 31, 1987.
29. S. Moghaddas, E. Gelerinter, R.N. Bose, *Journal of Inorganic Biochemistry*, **1995**, 57, 135.
30. A. McAuley, M.A. Olatunji, *Canadian Journal of Chemistry*, **1977**, 55, 3328.
31. D.A. Dixon, T.P. Dasgupta, N.P. Sadler, *Journal of the Chemical Society Dalton Transactions*, **1995**, 13, 2267.
32. S.L. Brauer, K.E. Wetterhahn, *Journal of the American Chemical Society*, **1991**, 113, 3001.
33. J.F. Perez-Benito, D. Lamrhari, C. Arias, *Journal of Physical Chemistry*, **1994**, 98, 12621.
34. P.A. Meloni, R.S. Czernuszewicz, *Vibrational Spectroscopy*, **1993**, 5, 205.
35. N.E. Brasch, D.A. Buckingham, A.B. Evans, C.R. Clark, *Journal of the American Chemical Society*, **1996**, 118, 7969.
36. A. Levina, L. Zhang, P.A. Lay, *Inorganic Chemistry* **2003**, 42, 767.
37. I. Bâldea, D.-M. Sabou, A. Csavdari, *Studia UBB Chemia*, **2007**, 52(1), 1.
38. A. Csavdari, I. Bâldea, D.-M. Sabou, *Studia UBB Chemia*, **2007**, 52(3), 113.
39. Z.M. Hoffman, E. Hayon, *Journal of the American Chemical Society*, **1972**, 94(23), 7950.

*Dedicated to Professor Liviu Literat
On the occasion of his 85th birthday*

THERMODYNAMIC STUDY AND KINETIC MODELING OF BIOETHANOL STEAM REFORMING

ZSOLT TASNÁDI-ASZTALOS^{a,*}, ÁRPÁD IMRE-LUCACI^a, ANA-MARIA
CORMOȘ^a, MIHAELA DIANA LAZĂR^b, PAUL-ȘERBAN AGACHI^a

ABSTRACT. Reforming of bioethanol, mainly produced from biomass fermentation, provides a promising method for hydrogen production from renewable resources. This paper describes the research work carried out on the thermodynamic analysis and kinetic modeling of bioethanol steam reforming using Ni-Al₂O₃ 10% at the temperature 350°C. The thermodynamic analysis which takes into account the main chemical species involved in the reactions was performed at more H₂O/EtOH molar ratio. Following the thermodynamic study has resulted that the maximum concentration of H₂ was obtained at the molar ratio of H₂O/EtOH 3:1 temperature of 550°C and 1 bar pressure. The experimental measurements were performed at laboratory scale and were done in isothermal conditions. The Langmuir-Hinshelwood-Hougen-Watson model was used in the kinetic modeling. The experiments for kinetic modeling was conducted under conditions 350°C, 3 bar and at molar ration water/ethanol 24:1 and was observed that. High concentrations of hydrogen were obtained when low inert gas flow was used.

Keywords: *Bioethanol, Steam reforming, Thermodynamic analysis, Hydrogen production, Kinetic modeling*

INTRODUCTION

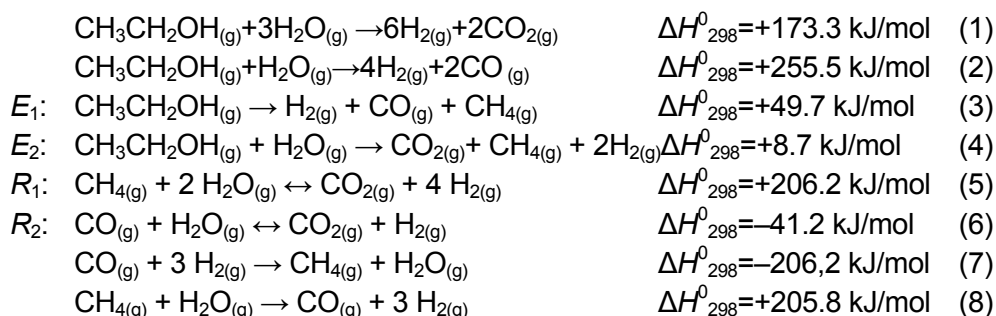
Over the last 10 years have become a certainty that fossil fuel resources are limited and CO₂ emissions cause global warming and severe climate change. To reduce dependence on fossil fuels and reduce CO₂ emission a

^a Babeș-Bolyai University of Cluj-Napoca, Faculty of Chemistry and Chemical Engineering, No. 11 Arany János Str., RO-40028 Cluj-Napoca, Romania, * tazsolt@chem.ubbcluj.ro

^b National Institute for Research and development of Isotopic and Molecular Technologies – INCDTIM, 65-103 Donath Street, RO-400293, Cluj-Napoca, Romania

lot of research work focuses in seeking new or alternative renewable sources of fuel and energy. Hydrogen is considered to be a clean energy carrier that will play an important role in the future global economy [1]. The demand for hydrogen is increasing in recent times because of its wide applications in areas such as: chemicals, crude oil refining, heavy oil, oil sands, metallurgy and aerospace propulsion upgrading and as fuel for the proton exchange membrane (PEM) fuel cell [2]. Hydrogen production is particularly attractive and interesting for fuel cell applications, which are regarded as having the potential to provide a source of clean energy for cars as an alternative to current fossil gasoline and diesel [1]. Biomass is recommended as an alternative for the production of hydrogen, because it is an abundant and renewable resource that does not contribute to net increase of CO₂ in the atmosphere.

The SRE (Steam Reforming of Ethanol) process involves the reaction between ethanol and water over a metal catalyst capable of breaking the C–C bond in the ethanol to produce a mixture of H₂ and CO₂ [1]. The main reaction is highly endothermic, ($\Delta H^0_{298}=+173.3$ kJ/mol) and occurs at relatively higher temperatures typically between 300 and 800°C. The literature proposes different chemical reactions to describe the SRE process. For this study the following reactions were chosen [1, 3-11]:



Although the stoichiometric molar ratio of steam/ethanol (H₂O/EtOH) should be 3:1 according to reaction (1), alcohol obtained by fermentation of biomass contains approx. 9 [% wt.] ethanol and 88 [% wt.] water, the remainder being impurities such as lactic acid and glycerol, equivalent to a molar ratio H₂O/EtOH ≈ 24, thus, using a large molar H₂O/EtOH is considered advantageous because it can eliminate the cost of ethanol distillation. However the excess water can promote the water gas shift (WGS) reaction to convert CO formed in the steam reforming reaction (2) and/or ethanol decomposition (3) [3].

Different kinetic models were proposed in literature to describe the SRE process. The Langmuir-Hinshelwood-Hougen-Watson (LHHW) model [12] was widely used and the main parameters of this model were determined based on experimental measurements.

Thermodynamic analysis

A thermodynamic analysis can be used to determine the favorable operating conditions in order to maximize the efficiency of the process. The most significant parameters influencing the process are: temperature T , pressure p and $\text{H}_2\text{O}/\text{EtOH}$ molar ratio r [12]. In this work, for the thermodynamic analysis, it has been considered for these three parameters a data range as follows: temperature between 300-800°C, pressure between 1 and 30 bar and the molar ratio of $\text{H}_2\text{O}/\text{EtOH}$ in the domain 3-25. These values were chosen so to cover a significant area of the possible operating conditions of the process.

The reaction main products was considered H_2 , and CO_2 . The following compounds were considered as potential reaction byproducts: CO , CH_4 , CH_3CHO , C_2H_4 and other, their initial concentrations are equal to 0. Concentrations of the reaction mixture were recalculated for dry mixture.

Steam reforming of ethanol leads to: H_2 , CO , CO_2 and CH_4 . The formation of CH_4 is predominant at low temperature (300-400°C) when the decomposition reaction is intensified, and at high temperature (650-800°C) production of H_2 is enhanced. CH_4 is an unwanted byproduct that radically reduces the amount of H_2 produced. In order to perform the thermodynamic study reactions 1 to 8 were considered [4-11].

Kinetic modeling

There are few papers in the literature on kinetic studies of ethanol steam reforming, because the system complexity. Ethanol was used as the representative component for bioethanol because of its much higher concentration compared to other components that are present in the bioethanol mixture.

Some published kinetic studies used power law, Eley Rideal (ER), Langmuir Hinshelwood (LH) and Langmuir-Hinshelwood-Hougen-Watson (LHHW) as kinetic expressions [2, 12-14]. Empirical and mechanistic rate models were developed to fit the experimental data as follows. Firstly, an empirical, irreversible fixed feed molar ratio power law rate model was developed as shown by the following equation [2]:

$$r_A = k_0 \cdot e^{\left(\frac{-E_0}{RT}\right)} \cdot N_A^n \quad (9)$$

Secondly, different mechanistic models were developed based on LHHW and ER mechanisms. Fundamentally, LHHW differs from the ER mechanism in that the former requires the adsorption of the two reactant species on the catalyst active site for any transformation to take place whereas the latter requires only one of the two reactants species to be adsorbed [2].

The criterion used in the selection of the kinetic model was the temperature range and the available kinetic data. Considering these aspects the LHHW kinetic model was selected and used in this work.

As it was established, the kinetic model consists only of 4 reactions: E_1 , E_2 , R_1 and R_2 - reactions (3-6) [12]. The reaction rates for these four reactions are [10-12, 15, 16]:

$$r_{E1} = \frac{K_{E1} \cdot Y_E \cdot Y_{CH4} \cdot Y_{H2}^{-\left(\frac{E}{2}\right)}}{DEN^2} \quad (10)$$

$$r_{E2} = \frac{K_{E2} \cdot Y_E \cdot Y_{CH4} \cdot Y_{H2} \cdot Y_{R1} \cdot Y_{R2}}{DEN^2} \quad (11)$$

$$r_{R1} = \frac{K_{R1} \cdot Y_{CH4} \cdot Y_{H2O} \cdot Y_{H2}^{-\left(\frac{E}{2}\right)} \cdot (1 - \beta_{R1})}{DEN^2} \quad (12)$$

$$r_{R2} = \frac{K_{R2} \cdot Y_{CO2} \cdot Y_{H2} \cdot (1 - \beta_{R2})}{DEN^2} \quad (13)$$

where the DEN term of these expressions is defined as:

$$DEN = 1 + K_{Et} \cdot Y_{Et} + K_{EtX} \cdot Y_{Et} \cdot Y_{H2}^{-(1/2)} + K_{Ac} \cdot Y_{Et} \cdot Y_{H2}^{-1} + K_{CHO} \cdot Y_{Et} \cdot Y_{CH4}^{-1} \cdot Y_{H2}^{-(1/2)} + K_{CH3} \cdot Y_{CH4} \cdot Y_{H2}^{-(1/2)} + K_{CH2} \cdot Y_{CH4} \cdot Y_{H2}^{-1} + K_{CH} \cdot Y_{CH4} \cdot Y_{H2}^{-(3/2)} + K_{H2O} \cdot Y_{H2O} + K_{OH} \cdot Y_{H2O} \cdot Y_{H2}^{-(1/2)} + K_{CH4} \cdot Y_{CH4} + K_{CO} \cdot Y_{CO} + K_{CO2} \cdot Y_{CO2} + K_{H2} \cdot Y_{H2}^{1/2} + K_{H2} \cdot Y_{H2} \quad (14)$$

The kinetic model parameters considered are presented in Table 1.

Table 1. Kinetic model parameters [9, 11, 12, 15]

$k_{i(T)} = k_{i(898.15K)} e^{-(E_{a,i}/R) \left(\frac{1}{T} - \frac{1}{898.15 K} \right)}$ [mol/min mg]	$E_{a,i}, \Delta H_i$ [kJ/mol]	
$K_{i(T)} = K_{i(898.15K)} e^{-(\Delta H_i/R) \left(\frac{1}{T} - \frac{1}{898.15 K} \right)}$ [dimensionless]		
$K_{E1(898.15K)}$	$1.13 \cdot 10^{-7}$	$E_{aE1} \quad 122.9$
$K_{E2(898.15K)}$	$3.06 \cdot 10^{-7}$	$E_{aE2} \quad 195.5$
$K_{R1(898.15K)}$	$2.48 \cdot 10^{-3}$	$E_{aR1} \quad 174.0$
$K_{R2(898.15K)}$	$9.12 \cdot 10^{-4}$	$E_{aR2} \quad 166.3$
$K_{Et(898.15K)}$	$8.76 \cdot 10^{-27}$	$\Delta H_{Et} \quad -601.4$
$K_{CHO(898.15K)}$	$2.10 \cdot 10^{-1}$	$\Delta H_{CHO} \quad -410.4$
$K_{CH2(898.15K)}$	$1.93 \cdot 10^{-22}$	$\Delta H_{CH2} \quad -118.4$
$K_{CH(898.15K)}$	$3.05 \cdot 10^{-1}$	$\Delta H_{CH} \quad -360.7$
$K_{CH3(898.15K)}$	$1.93 \cdot 10^{-22}$	$\Delta H_{CH3} \quad -126.8$
$K_{H2(898.15K)}$	$1.93 \cdot 10^{-22}$	$\Delta H_{H2O} \quad -83.1$
$K_{OH(898.15K)}$	$1.93 \cdot 10^{-22}$	$\Delta H_{OH} \quad -145.5$
$K_{CH4(898.15K)}$	$6.34 \cdot 10^{-18}$	$\Delta H_{CH4} \quad -86.1$
$K_{CO(898.15K)}$	$1.93 \cdot 10^{-22}$	$\Delta H_{CO} \quad -83.1$
$K_{H(898.15K)}$	$8.76 \cdot 10^{-27}$	$\Delta H_H \quad -247.4$
$K_{CO2(898.15K)}$	$1.93 \cdot 10^{-22}$	$\Delta H_{CO2} \quad -83.4$
$K_{H2(898.15K)}$	$1.93 \cdot 10^{-22}$	$\Delta H_{H2} \quad -931.2$

RESULTS AND DISCUSSION

Thermodynamic analysis

The goal of the thermodynamic analysis is to determine the conditions favorable to maximize the concentration of H₂ and to reduce to as low as possible the concentration of unwanted byproducts as: CH₄, CO₂ and CO. The thermodynamic study was performed using CHEMCAD process simulator. The equilibrium composition was determined for all possible combinations of the following values of parameters T , p and r .

- T : 300, 350, 400, 450, 500, 550, 600, 650, 700, 750 and 800°C;
- p : 1, 5, 9, 13, 17, 21, 25 and 30 bar;
- r : 3, 5, 7, 9, 11, 13, 15, 17, 19, 21, 23 and 25.

The thermodynamic analysis results are presented bellow. The variation of H₂, CH₄, CO and CO₂ concentration with temperature and pressure at the molar ratio of water/bioethanol, 7:1 is presented in Figure 1.

Figure 1.a shows that the maximum concentration of H₂ is reached at 1 bar in the temperature range of 550-600°C. At lower temperatures H₂ concentration is reduced because is favored CH₄ production. The maximum hydrogen concentration that was obtained is 45%. As shown in the Figure 1.b the maximum concentration of CH₄ (16-17%) is achieved at temperatures of 300°C and a pressure of 30 bar. At low temperatures the methane steam reforming reaction is favored. The maximum concentration of CO is achieved at temperatures of 800°C and 1 bar pressure (Figure 1.c). As shown in the Figure 1.d the maximum concentration of CO₂ (12%) is obtained in the temperature range of 550-600°C and pressure of 1 bar. The maximum concentration of CO is 8-8.5%. CO and CO₂ concentrations are strongly influenced by the WGS reaction.

Figure 2 presented variation of major components concentrations as a function of temperature and pressure variation, at molar ratio water/bioethanol is 7:1.

As shown in Figure 2.a the increasing of temperature increase the concentration of H₂ from 3% to 68% and the concentration of CH₄ decreases from 71% to 5%. The variation of CO and CO₂ concentration is insignificant until the temperature 550°C, after that the concentration of CO increases from 0.5% to 12% and the concentration of CO₂ decreases from 25% to 17%. Figure 2.b shows that the variation of major components concentration with pressure is insignificant for CO and CO₂, H₂ and CH₄ is significant.

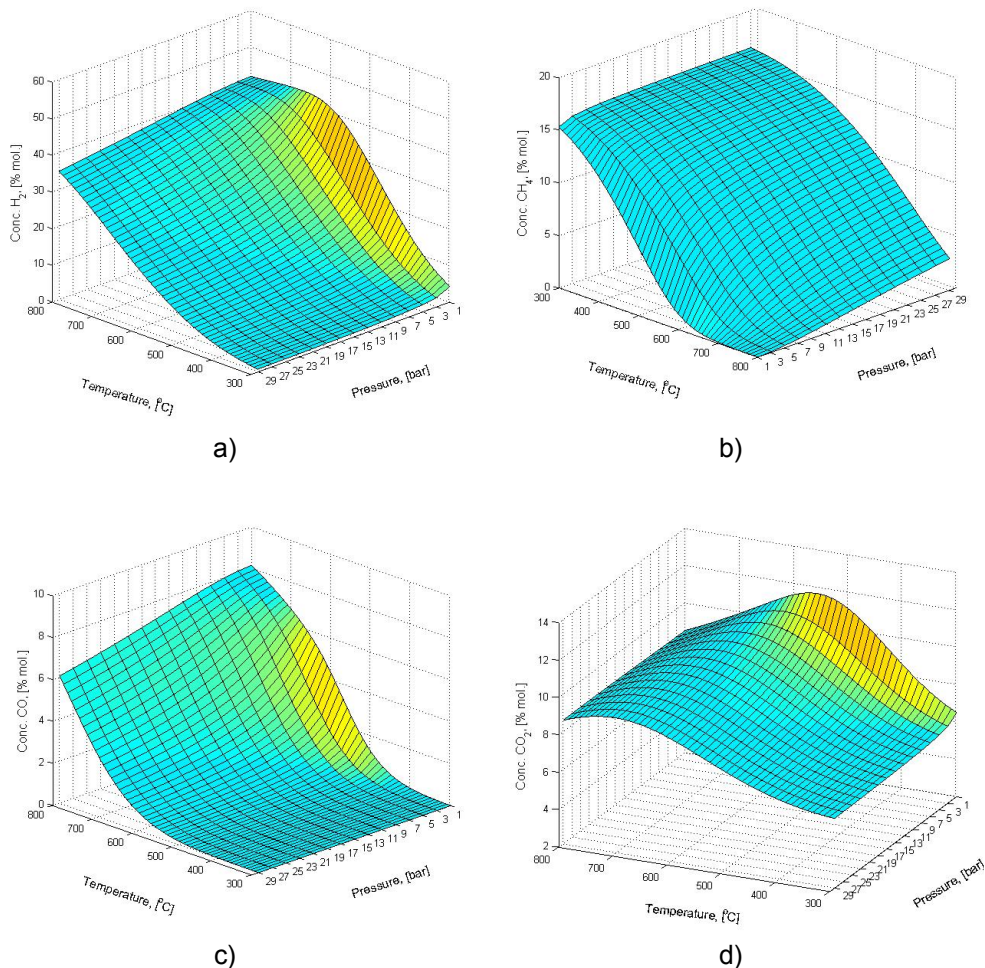


Figure 1. Variation of concentration of main products in the temperature and pressure at the molar ratio of water/bioethanol, 7:1.
 a) H₂, b) CH₄, c) CO, d) CO₂.

Figure 3 represents the variation of major products concentration as a function of water/ethanol molar ratio at the temperature of 800 °C and 30 bar. It can be observed that at high values of the water/ethanol molar ratio the mixture contains almost only H₂ and CO₂, while at low molar ratio values we have a significant concentration in all components (CH₄; CO and CO₂ each one's concentration is over 12%).

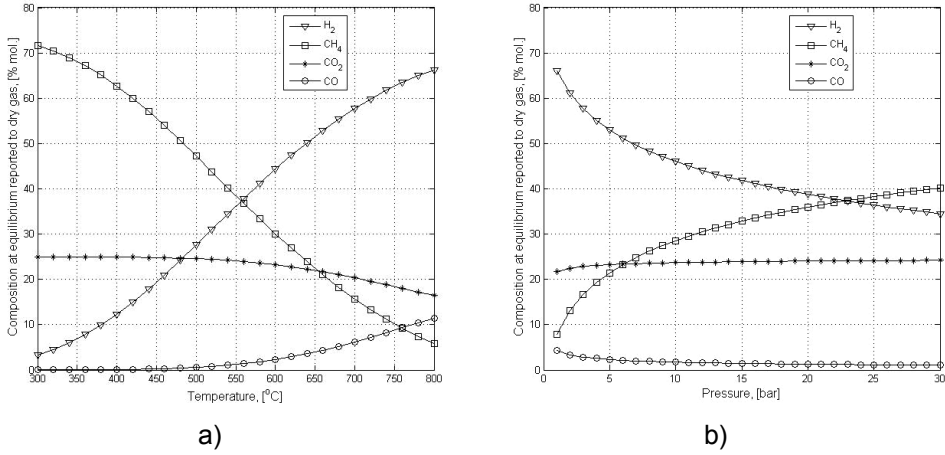


Figure 2. Variation of major components concentrations as a function of a) temperature at pressure 30 bar and b) pressure variation at 550°C, at molar ratio water/bioethanol 7:1.

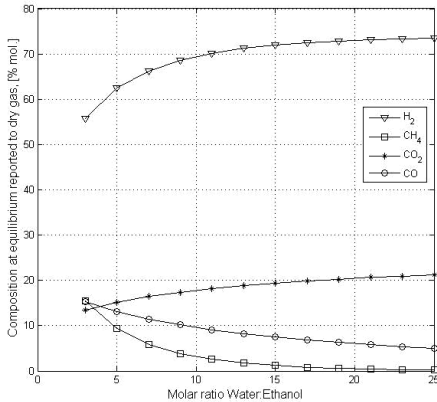


Figure 3. Variation of major products concentration as a function of molar ratio water/ethanol at the temperature of 800°C and 30 bar.

Kinetic model adjustment based on experimental data

As it was previously specified, based on the literature, LHHW kinetic model was considered in this work, but the main constants of the model need to be recalculated in order to assure the fitness of the model with available experimental data.

The experiments for kinetic model adjustment were performed at INCDTIM Cluj-Napoca. The laboratory plant for steam reforming of ethanol is composed of three main parts:

1. The feed part which in turn consists of two components:
 - a. the gaseous feeds (steam and carrier gas) is carried out by pressure regulators
 - b. the liquid feed (water/ethanol mixture) is done by using HPLC Shimadzu pump
2. The reactions take place in a stainless steel tubular reactor equipped with a stainless steel pill that catalyst ordering. The reactor is placed in a thermostatic enclosure with a maximum achievable temperature of 350 °C. The quantity of catalyst (10%Ni-Al₂O₃ was used) to be introduced is 1 g which is mixed with the same quantity of support material (Al₂O₃). In order to carry out the reaction, for each experimental run the catalyst is pre-treated 3 hours at 350°C in H₂.
3. Composition analysis part of the setup consists of two different chromatographs equipped with two detectors: one is TCD (thermal conductivity detector) and the other FID (flame ionization detector). The liquid products resulting from the reaction are analyzed by FID with a 5% Carbowax column 80/100 mesh length 1.5 m.

The experimental conditions are presented in Table 2.

Table 2. Main experimental parameters

Parameters	U.M.	Values
$F_{V,T}$	[mL/min]	10.1, 35.1, 133.1, 200.1, 300.1
$F_{V,dry}$	[mL/min]	0.1
W	[g]	1
T	[C]	350
$Time$	[h]	24
P	[bar]	3
D	[mm]	8
Dp	[μ m]	88

Argon was used as carrier gas. Experiments were performed at five different Ar flows (10, 35, 133, 200, 300 mL/min) in order to have a set of space time ($\theta_V = W/F_{V,T}$) values, a parameter that influences the reaction rate.

The kinetic model presented in literature [2, 12] was adapted to describe our system (10%Ni-Al₂O₃ catalyst working on 350 °C) by recalculation of the four kinetic constants of reactions (3-6), parameters considered the most important from the mathematical model point of view.

The four kinetic parameters were recalculated by minimizing the objective function that describes the relative deviations between experimental and calculated concentration data on the set of 5 different experimental sets as follows:

$$fob = \sum_{i=1}^{Exp} \left[\left(\frac{Y_{exp} - Y_{calc}}{Y_{calc}} \right)^2 \right]^{\frac{1}{2}} = \min \quad (16)$$

The calculated values of the four kinetic model parameters are presented in Table 3.

Table 3. Global kinetic constants of SRE

Parameter	Calculated values
k_{E1sim}	$3.64 \cdot 10^{-5}$
k_{E2sim}	$1.44 \cdot 10^{-5}$
k_{R1sim}	$0.55 \cdot 10^{-3}$
k_{R2sim}	$4.33 \cdot 10^{-2}$

Using these recalculated values, the variations of the main components concentrations obtained from the adjusted kinetic model are presented in Figure 4.

The kinetic model was implemented in MATLAB.

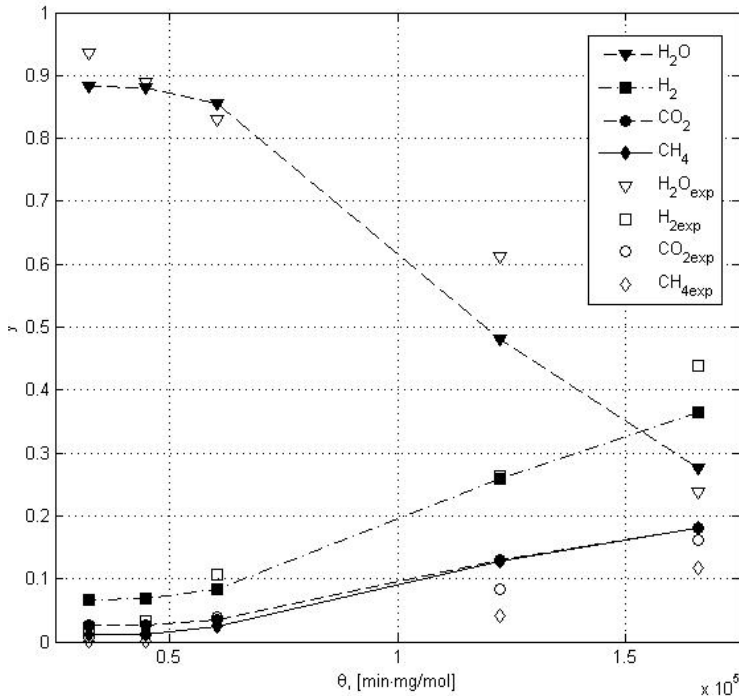


Figure 4. Measured and simulation data of steam reforming of bioethanol (with symbols are shown the experimental data and with lines and symbols the simulation results)

The results obtained by simulation compared with experimental data are presented in Table 4.

Table 4. Experimental and calculated values of components concentration

Comp.	Θ										$\bar{\varepsilon}_2$ %
	θ_1		θ_2		θ_3		θ_4		θ_5		
	Exp	Calc	Exp	Calc	Exp	Calc	Exp	Calc	Exp	Calc	
H ₂	0.02	0.07	0.03	0.07	0.10	0.08	0.26	0.26	0.44	0.36	35.2
H ₂ O	0.94	0.88	0.89	0.88	0.83	0.86	0.61	0.48	0.24	0.27	9.9
CO ₂	0.01	0.03	0.01	0.03	0.04	0.04	0.08	0.13	0.16	0.18	36.6
CH ₄	1·10 ⁻³	0.01	2·10 ⁻³	0.01	0.04	0.02	0.04	0.13	0.12	0.18	74.5
$\bar{\varepsilon}_1$ %	58.7		51.2		32.1		33.7		19.4		

The average errors $\bar{\varepsilon}_1$ and $\bar{\varepsilon}_2$ were calculated with the equations:

$$\bar{\varepsilon}_1 = \frac{1}{4} \sum_{comp} \left(\frac{y_{calc} - y_{exp}}{y_{calc}} \right) \cdot 100 \quad (17)$$

$$\bar{\varepsilon}_2 = \frac{1}{5} \sum_{\Theta} \left(\frac{y_{calc} - y_{exp}}{y_{calc}} \right) \cdot 100 \quad (18)$$

As it can be observed, the fitness of the adjusted model is not very good; the overall average error is 39 %. This was due mainly to the lack of sufficient experimental data. It is also necessary to include in the adjustment of the kinetic model, other parameters besides the kinetic constants considered in this work.

CONCLUSIONS

This paper describes the research work done on the thermodynamic analysis of the process of bioethanol steam reforming. Also, for a kinetic model reported in the literature, the kinetic constants were recalculated to adjust the model to the experimental data obtained by using 10%Ni-Al₂O₃ catalyst in isothermal conditions at 350°C. The thermodynamic analysis takes into account the main chemical species involved in the reactions (reactants as well as products). Following the thermodynamic study has resulted that the maximum concentration of H₂ was obtained at the molar ratio of water/ethanol 3:1, temperature of 550°C and 1 bar pressure.

The adjustment of the LHHW kinetic model based on the experimental data obtained in a laboratory plant succeeds to determine the kinetic constants of the process but the fitness of the model was rather poor. In order to improve the kinetic model accuracy, new experiments need to be considered and more parameters of the model have to be included in the adjustment process.

NOTATIONS:

D	reactor diameter [mm]
D_p	particle diameter [μm]
E_a	activation energy [kJ/mol]
$F_{V, dry}$	total dry gas flow [mL/min]
$F_{V, T}$	total flow [mL/min]
H	enthalpy [kJ/mol]
k_i	kinetic coefficient of i reaction [mol/min mg]
K_j	adsorption constant of j species [-]
p	pressure [bar]
R	gas constant
r_i	reaction rate of i reaction [mol/min mg]
T	temperature [K]
W	catalyst mass [mg]
y_{et}	ethanol molar fraction [-]
y_{H_2O}	water molar fraction [-]
y_j	molar fraction of the j species [-]
$y_{exp, i}$	molar fraction of the experimental values [-]
y_{calc}	molar fraction of the simulation values [-]
ΔH_i	reaction enthalpy of i reaction [kJ/mol]
ΔH_j	adsorption enthalpy of j species [kJ/mol]
θ_V	space time [min·mg/mL]
θ_i	space time for experiment i [min mg/mL]
$\bar{\varepsilon}_i$	average error [%]

ACKNOWLEDGEMENT

This work was supported by a grant of the Romanian National Authority for Scientific Research, CNCS – UEFISCDI, project ID PN-II-PT-PCCA-2011-3.2-0452: “Hydrogen production from hydroxylic compounds resulted as biomass processing wastes”.

REFERENCES

1. K. Liu, C. Song, V. Subramani, “Hydrogen and Syngas Production and Purification Technologies” A John Wiley & Sons, Inc., Publication **2010**.
2. E. Akpan, A. Akande, A. Aboudheir, H. Ibrahim, R. Idem, *Chemical Engineering Science*, **2007**, 62, 3112.
3. S. Tosti, A. Basile, R. Borelli, F. Borgognoni, S. Castelli, M. Fabbricino, F. Gallucci, C. Licusati, *International Journal of Hydrogen Energy*, **2009**, 34, 4747.

4. M. Ni, D.Y.C. Leung, M.K.H. Leung, *International Journal of Hydrogen Energy*, **2007**, 32, 3238.
5. M. Benito, J.L. Sanz, R. Isabel, R. Padilla, R. Arjona, L. Dazaa, *Journal of Power Sources*, **2005**, 151, 11.
6. L. Hernández, V. Kafarov, *Journal of Power Sources*, **2009**, 192, 195.
7. A. Iulianelli, A. Basile, *International Journal of Hydrogen Energy*, **2010**, 35, 3170.
8. M. Ni, D.Y.C. Leung, M.K.H. Leung, *International Journal of Hydrogen Energy*, **2007**, 32, 3238.
9. V. Mas, G. Baronetti, N. Amadeo, M. Laborde, *Chemical Engineering Journal*, **2008**, 138, 602.
10. P.D. Vaidya and A.E. Rodrigues, *Industrial & Engineering Chemistry Research*, **2006**, 45, 6614.
11. D.R. Sahoo, S. Vajpai, S. Patel, K.K. Pant, *Chemical Engineering Journal*, **2007**, 125, 139.
12. I. Llera, V. Mas, M.L. Bergamini, M. Laborde, N. Amadeo, Bio-ethanol steam reforming on Ni based catalyst. Kinetic study, *Chemical Engineering Science*, **2012**, 71, 356.
13. A. Akande, A. Aboudheir, R. Idem, A. Dalai, *International Journal of Hydrogen Energy*, **2006**, 31, 1707.
14. V. Mas, M.L. Bergamini, G. Baronetti, N. Amadeo, M. Laborde, *Top Catal*, **2008**, 51, 39.
15. A.G. Gayubo, A. Alonso, B. Valle, A.T. Aguayo, M. Olazar, J. Bilbao, *Chemical Engineering Journal*, **2011**, 167, 262.
16. O. Görke, P. Pfeifer, K. Schubert, *Applied Catalysis A: General*, **2009**, 360, 232.

*Dedicated to Professor Liviu Literat
On the occasion of his 85th birthday*

KINETICS OF CARBON DIOXIDE ABSORPTION INTO NEW AMINE SOLUTIONS

**RAMONA-ELENA TATARU-FARMUS^a, MIHAELA DRĂGAN^b,
SIMION DRĂGAN^b, ILIE SIMINICEANU^{a,*}**

ABSTRACT. The absorption of CO₂ into activated carbonate buffer solutions is the main process applied in the existing ammonia plants. The major drawback of this process is the high endothermicity of the regeneration step. Therefore, new chemical solvents must be introduced having not only high absorption rate and capacity but also low heat of regeneration. The objective of this work was to study the kinetics of CO₂ absorption into aqueous solutions of ethylenediamine (EDA). A thermo regulated constant interfacial area gas-liquid reactor has been used to measure the carbon dioxide absorption rates into this aqueous amine solution (3% mol) in the temperature range 298 – 333 K. The experimental results have been interpreted using the equations derived from the two film model. The enhancement factor was always greater than 3. The pseudo-first order rate constant derived from the experimental data was of the same order of magnitude as for absorption into mixtures of MEA and MDEA.

Keywords: carbon capture, ethylenediamine (EDA), Lewis absorber, rate constant, enhancement factor.

INTRODUCTION

Currently, fossil fuels fired power plants account for 80% of total energy production world wide and are the largest point sources of carbon dioxide emissions, accounting for roughly 40% of total carbon dioxide emissions [1]. A single such power station of 500 MW has emissions of 8,000 tones CO₂/ day.

^a *Universitatea Tehnica "Gheorghe Asachi", Departamentul de Inginerie Chimica, Bul. D. Mangeron 73, Iasi, * isiminic@yahoo.com*

^b *Universitatea Babeş Bolyai, Facultatea de Chimie si Inginerie Chimica, Arany Janos 11, Cluj-Napoca*

In Romania, the largest coal power station (in Turceni) had a generation capacity of 2,640 MW. For such giant flue gas flow rate sources, the chemical absorption is the best method to remove carbon dioxide [2, 3, 4]. The absorbent contains a substance which rapidly reacts with the dissolved carbon dioxide in the liquid phase. This reaction enhances/accelerates the overall mass transfer process. The substance is usually an alkali such potassium carbonate, sodium hydroxide, ammonia, amines. There is an important industrial experience with activated potassium carbonate solutions (Benfield, Carsol) used in ammonia plants to remove carbon dioxide from synthesis gas. A recent paper presents interesting results regarding the enhancement of the absorption using *arginine* as activator [6]. Chemical solvents such as alkanolamines are also commonly used to enhance carbon dioxide absorption rates and capacity and to improve selectivity. A wide variety of alkanolamines such as monoethanolamine (MEA), diethanolamine (DEA), di-isopropanolamine (DIPA), N- methyl-diethanolamine (MDEA) have been already used industrially [2, 3]. A recent advancement in gas treating is the absorption into blended amines. Blends of primary (MEA) and tertiary (MDEA) amines have been suggested for CO₂ removal [3]. Aqueous ammonia seems to be a practical solution for post- combustion carbon capture [4]. Which chemical solvent is the best? To answer this question, at least ten characteristics must be taken into account. A good chemical solvent for carbon dioxide capture has to meet the following requirements:

- (1) High solubility x (small Henry constant H , in: $p = H \cdot x$);
- (2) High selectivity for CO₂;
- (3) Low energy for solvent regeneration/ enthalpy of absorption;
- (4) High cyclic absorption capacity (mol CO₂ / mol solvent);
- (5) High absorption rate;
- (6) Thermal and chemical stability;
- (7) Low vapor pressure;
- (8) Low corrosivity;
- (9) Low toxicity for humans and environment;
- (10) Availability and low cost.

Our group published several papers on the characteristics of new solvents [6, 7, 8, 9, 10, 11] as well as on the absorption modeling and intensification [12, 13, 14, 15, 16, 17, 18, 19]. More recent papers published by other groups are concentrated on the optimization of the absorption into MEA solution [21]

The originality of the present work consists of two things: the system, and the apparatus. The system is a solvent which contains a primary amine (EDA). The results with EDA will be compared with TETA, with primary and secondary amine groups in the same molecule. Then TETA will be compared to the primary amine (EDA) and to the mixture EDA/TETA in aqueous solution.

RESULTS AND DISCUSSION

Table 1 gives the experimental results of the absorption of CO₂ into EDA solution (3 % mol) at three temperatures. R_C in the table is the loading ratio (moles of gas absorbed by one mole of amine).

Table 1. Experimental results for the absorption of CO₂ into EDA aqueous solutions (3%mol).

T/K	R _C , mol/mol	(P _T) ₀ , bar	P ^e _i , bar	β, s ⁻¹	Normal flux m/s
298.15	0.000	0.0687	0.0347	3.87E-02	6.30E-03
298.15	0.011	0.0673	0.0349	3.88E-02	6.32E-03
298.15	0.071	0.0672	0.0377	3.53E-02	5.77E-03
298.15	0.167	0.0649	0.0377	3.23E-02	5.30E-03
298.15	0.283	0.0677	0.0371	2.85E-02	4.69E-03
298.15	0.381	0.0693	0.0371	2.57E-02	4.25E-03
298.15	0.446	0.1294	0.0957	1.94E-02	3.21E-03
298.15	0.460	0.1219	0.0959	1.83E-02	3.04E-03
313.15	0.020	0.1038	0.0776	4.77E-02	1.05E-02
313.15	0.091	0.1039	0.0815	4.05E-02	8.97E-03
313.15	0.204	0.1054	0.0809	3.42E-02	7.61E-03
313.15	0.306	0.1088	0.0804	3.38E-02	7.55E-03
313.15	0.393	0.1110	0.0800	3.02E-02	6.77E-03
313.15	0.478	0.1677	0.1422	2.20E-02	4.95E-03
333.15	0.038	0.2237	0.1991	4.74E-02	1.44E-02
333.15	0.109	0.2311	0.2014	3.88E-02	1.18E-02
333.15	0.217	0.2309	0.2009	3.31E-02	1.02E-02
333.15	0.231	0.2269	0.2007	3.16E-02	9.68E-03
333.15	0.326	0.2306	0.2004	3.05E-02	9.38E-03
333.15	0.408	0.2366	0.2076	3.07E-02	9.48E-03
333.15	0.487	0.3026	0.2748	2.41E-02	7.49E-03

The rate of the chemical absorption of CO₂ (= i) is of the form [2]:

$$-\frac{dn_i}{A \cdot dt} = E \cdot k_L \cdot c_i^e \left[\frac{\text{mol}}{\text{m}^2 \cdot \text{s}} \right] \quad (1)$$

The gas phase is assumed ideal ($P_i \cdot V_g = n_i \cdot R \cdot T$). CO₂ is completely consumed by the reaction in the liquid film, and the CO₂ concentration at the interface is replaced by the Henry law ($c_i^e = P_i^e / H_i$).

The partial pressure of CO₂ is obtained by subtraction of vapor pressure of the solution (P_v) from the total measured pressure (P_T): $P_i = P_T - P_v$.

By integrating (1) under these assumptions, the equation (2) is derived:

$$\ln \frac{(P_T - P_v)_t}{(P_T - P_v)_{t_0}} = -\beta(t - t_0) \quad (2)$$

where:

$$\beta = \frac{E \cdot k_L \cdot A \cdot R \cdot T}{V_g \cdot H_i} \quad (3)$$

The enhancement factor E can be calculated for each experiment, using the equation (3).

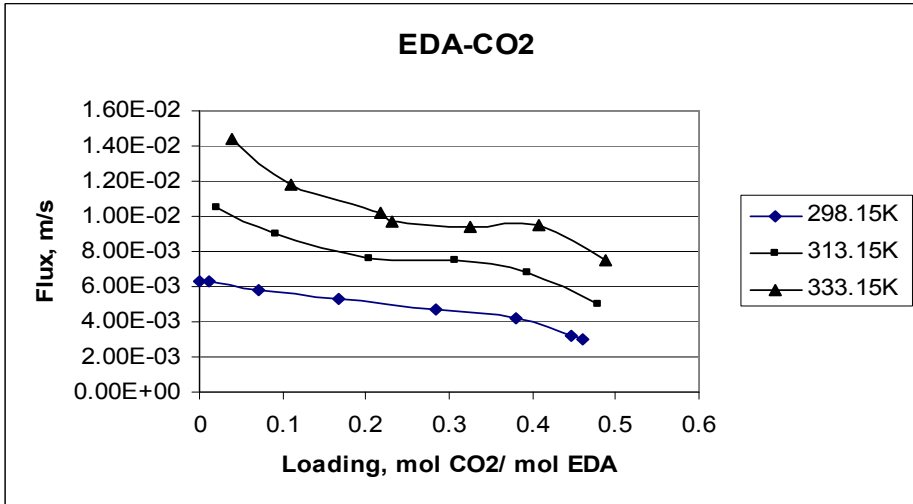


Figure 1. Experimental normal flux versus cell loading.

In order to compare our results with those for other solutions at the same temperature, the overall rate constant (k_{ov}) of the pseudo- first order reaction has been calculated for the fast reaction regime ($E = Ha > 3$):

$$k_{ov} = \frac{(k_L \cdot E)^2}{D_i} \quad (4)$$

E being calculated with the equation (3) using the experimental values of β from the tables 1. The results at 313.15 K are presented in the table 2.

Table 2.

The enhancement factor and the rate constant at 313.15 K for the EDA solution.
 ($k_L = 5 \times 10^{-4} \text{ m/s}$; $D_i = 1.6 \times 10^{-9} \text{ m}^2/\text{s}$; $Vg = 1.91875 \times 10^{-4} \text{ m}^3$; $A = 15.34 \times 10^{-4} \text{ m}^2$)

R_c	$\beta \times 10^2, \text{ s}^{-1}$	E	$k_{ov}, \text{ s}^{-1}$
0.020	4.77	11.51	20,700
0.091	4.05	9.77	14,900
0.204	3.42	8.25	10,600
0.306	3.38	8.15	10,400
0.393	3.02	7.29	8,300

Liao and *Li* [20] have obtained at the same temperature a k_{ov} of 195.4 s^{-1} for the absorption of CO_2 in a solution MEA- MDEA- H_2O with 0.1 mol/L MEA and 1.0 mol/L MDEA, and of 1703 s^{-1} by increasing the MEA concentration from 0.1 to 0.5 mol/L. Our values are superior of an order of magnitude for EDA solutions in other identical conditions. The results are promising taking into account that the system investigated by *Liao* and *Li* is considered the most effective from those studied till now.

CONCLUSIONS

Kinetics of CO_2 absorption into a new amine aqueous solution (EDA- H_2O) have been investigated at three temperatures (25°C , 40°C , and 60°C) on a laboratory Lewis type absorber with constant gas-liquid interface area. The enhancement factor and the pseudo-first order rate constant have been calculated on the basis of experimental data. The fast reaction regime was fulfilled at loadings less than 0.4 for all investigated systems. The rate constants were of the same order of magnitude as those obtained by *Liao* and *Li* [20] with some mixtures of MEA and MDEA. The investigation must be continued with EDA/TETA mixtures. Some properties of the solutions must be determined and correlated in order to improve the mathematical model.

EXPERIMENTAL SECTION

Experimental apparatus

The apparatus has been described in a previous paper [6]. It is a Lewis type absorber with a constant gas-liquid interface area of $(15.34 \pm 0.05) \times 10^{-4} \text{ m}^2$. The total volume available for gas and liquid phases is $(0.3504 \pm 0.0005) \times 10^{-4} \text{ m}^3$. The temperature is kept constant within 0.05 K by circulating a thermostatic fluid through the double glass jacket. The liquid phase is agitated by a six

bladed Rushton turbine (4.25×10^{-2} m diameter). The gas phase is agitated by 4×10^{-2} m diameter propeller. Both agitators are driven magnetically by a variable speed motor. The turbine speed is checked with a stroboscope.

The kinetics of gas absorption is measured by recording the absolute pressure drop through a SEDEME pressure transducer, working in the range $(0 \text{ to } 200) \times 10^3$ Pa. A microcomputer equipped with a data acquisition card is used to convert the pressure transducer signal directly into pressure P units, using calibration constant previously determined, and records it as function of time.

Experimental procedure

Water and EDA are degassed independently and aqueous solutions are prepared under a vacuum. The amounts of water and amine are determined by differential weightings to within $\pm 10^{-2}$ g. This uncertainty on weightings leads to uncertainties in concentrations of less than $\pm 0.05\%$.

The flask containing the degassed EDA aqueous solution is connected to the absorption cell by means of a needle introduced through the septum situated at the bottom of the cell. Weighing the flask with the tube and the needle before and after transfer allows the determination of the exact mass of solvent transferred into the cell.

Once the amine aqueous solution is loaded and the temperature equilibrated, the inert gas pressure P_i corresponding mainly to the solvent vapor pressure plus eventual residual inert gases is measured. The pure CO_2 is introduced over a very short time (about 2 seconds) in the upper part of the cell, the resulting pressure P_0 is between $(100\text{-}200) \times 10^3$ Pa. Then stirring is started and the pressure drop resulting from absorption is recorded.

MATERIALS

The main materials involved have been: water, carbon dioxide, ethylenediamine (EDA). Ordinary twice-distilled water was used. Carbon dioxide, purchased from *Air Liquid*, of 99.995% purity, was used as received. EDA from *Aldrich Chem.Co.* (Milwaukee WI, USA), material of state purity 99%, used as received.

NOTATION

- A, area of the gas- liquid interface, m^2 ;
- C_i , molar concentration, kmol/m^3 ;
- D_i , diffusion coefficient of i in solution, m^2/s ;
- E, enhancement factor of absorption by the chemical reaction;
- H_i , Henry constant, $\text{bar} \cdot \text{m}^3/\text{kmol}$;

Ha , Hatta number;
 k_L , liquid side mass transfer coefficient, m/s;
 k_{ov} , pseudo- first order reaction rate constant, s^{-1} ;
 n_i , number of moles of i ;
 P , total pressure, bar;
 P_v , vapor pressure of the solution, bar;
 R , gas constant ($0.082 \text{ bar m}^3/\text{ kmol K}$);
 T , temperature, K;
 t , time, s;
 V_g , gas phase volume, m^3 ;
 β , the slope in the equation (3), s^{-1} .

REFERENCES

1. B.P. Spigarelli, S.K. Kawatra, *Journal of CO₂ Utilization*, **2013**, 1(6), 69.
2. R.D. Noble, P.A. Terry, "Principles of Chemical Separations with Environmental Applications", Cambridge Univ. Press, Cambridge, **2004**, 312.
3. I. Siminiceanu, "Procese chimice gaz- lichid", Editura Tehnopres, Iasi, **2005**, 227.
4. B. Zhao, Y. Su, W. Tao, L. Li, Y. Peng, *International Journal of Greenhouse Gas Control*, **2012**, 9, 355.
5. P.M. Mathias, S. Reddy, A. Smith, K. Afshar, *Energy Procedia*, **2013**, 37, 1863.
6. R.E. Tataru-Farmus, I. Siminiceanu, *Bul. Inst. Polit. Iasi*, **2013**, LIX, 1, 87.
7. R.E. Tataru-Farmus, I. Siminiceanu, Ch. Bouallou, *Chemical Engineering Transactions*, **2007**, 12, 175.
8. R.E. Tataru-Farmus, I. Siminiceanu, Ch. Bouallou, *Annals of the Suceava University*, **2006**, 5(2), 16.
9. R.E. Tataru-Farmus, I. Siminiceanu, Ch. Bouallou, *En. Engineering and Management Journal*, **2007**, 6(5), 555.
10. I. Siminiceanu, R.E. Tataru-Farmus, Ch. Bouallou, *Bul. St. Univ. "Politehnica" Timisoara, s. Chim. Ing. Chim.*, **2008**, 53(1-2), 1.
11. I. Siminiceanu, R.E. Tataru-Farmus, Ch. Bouallou, *Rev. Chim. (Bucharest)*, **2009**, 60(2), 113.
12. I. Siminiceanu, *Studia UBB Chemia*, **1991**, 36(1-2), 71.
13. I. Siminiceanu, C. Gherman, M. Ivaniciuc, *Analele Univ. Craiova, s. Chim.*, **1995**, 2, 405.
14. I. Siminiceanu, C. Petrila, C. Gherman, *Rev. Chim. (Bucharest)*, **1996**, 47(3), 265.
15. I. Siminiceanu, M. Ivaniciuc, *Sci. Technol. Environ. Protection*, **1998**, 5(1), 25.

16. I. Siminiceanu, M. Dragan, A. Friedl, M. Harasek, S. Dragan, *Sci. Technol. Environ. Protection*, **1999**, 6(1), 31.
17. M. Dragan M., I. Siminiceanu, A. Friedl, M. Harasek, *Studia UBB Chemia*, **1999**, 44, 42.
18. M. Dragan, A. Friedl, M. Harasek, S. Dragan, I. Siminiceanu, *Ovidius Univ. Annals Chem.*, **2000**, 11, 123.
19. I. Siminiceanu, M. Dragan, *Analele Univ. Oradea*, **2004**, 7, 188.
20. C.H. Liao, M. H. Li, *Chemical Engineering Science*, **2002**, 57, 4569.
21. L. Tock, F. Marechal, *Computers & Chemical Engineering*, **2014**, 61, 51.

*Dedicated to Professor Liviu Literat
On the occasion of his 85th birthday*

ADSORPTIVE CHARACTERISTICS OF HISTOSOL MODIFIED BY SIMPLE CHEMICAL TREATMENTS FOR Ni(II) REMOVAL FROM AQUEOUS MEDIA

**DUMITRU BULGARIU^{a,b}, CONSTANTIN RUSU^{a,b},
LAURA BULGARIU^{c,*}**

ABSTRACT. The adsorptive characteristics of Ni(II) from aqueous media on histosol modified by simple chemical treatments was investigated. The chemical treatments have been achieved by mixing histosol with aqueous solution of common chemical reagents (HNO₃, NaCl and NaOH, respectively), without the addition of supplementary additives. The influence of initial Ni(II) concentration and equilibrium contact time was studied in a series of batch experiments, in comparison with untreated histosol. An increase of adsorption capacity of histosol in case of treatments with NaCl and NaOH (15.58 % and 24.19 %, respectively) was obtained, and this is mainly attributed to the increase of functional groups availability from adsorbent surface. In addition a significant decrease of equilibrium contact time in case of modified histosol was also found. The experimental data were analyzed using two isotherm models (Langmuir and Freundlich) and three kinetics models (pseudo-first order, pseudo-second order and intra-particle diffusion model). The Langmuir model provides best correlation of equilibrium experimental data, and the pseudo-second order describes well the adsorption kinetics of Ni(II) on untreated and modified histosol. The histosol modified by considered simple chemical treatments has potential for serving as Ni(II) adsorbent, and the cost of these treatments is very low.

Keywords: *adsorption, Ni(II) ions, histosol, chemical treatment, kinetics, isotherm*

^a *Universitatea "Al. I. Cuza" din Iași, Facultatea de Geografie și Geologie, Bld. Carol I, Nr. 20A, RO-700506, Iași, România*

^b *Academia Română, Filiala din Iași, Colectivul de Geografie, Bld. Carol I, Nr. 18A, RO-700506, Iași, România*

^c *Universitatea Tehnică "Gheorghe Asachi" din Iași, Facultatea de Inginerie Chimică și Protecția Mediului, Bld. D. Mangeron, Nr. 71A, RO-700050 Iași, România, * ibulg@ch.tuiasi.ro*

INTRODUCTION

Unlike organic pollutants that are susceptible to biological degradation once they are discharged into environment, the heavy metals cannot be degraded into harmless end products. In addition, due to their toxicity, mobility and accumulating tendency, the contamination of aqueous environment with heavy metals is an important source of pollution with serious human health consequences [1,2]. Consequently, heavy metals should be eliminated or at least reduced from industrial wastewater before discharge into environment.

Nickel is one the common heavy metals that is present into environment mostly due to the industrial activities. Thus, many industries (such as: metal plating, mining, tanneries, etc.) produce large quantities of waste stream containing nickel along with other metal ions from process. In most of cases, Ni(II) ions are added to waste stream at a much higher concentration that the permissible limits, leading to health hazard and environment degradation [3,4].

Several methods can be employed to remove Ni(II) ions from industrial wastewater, including chemical precipitation, flotation, ion exchange, membrane-related processes, biological techniques [5-9]. Unfortunately, in many cases the applicability of these methods is limited because are expensive, have low selectivity, high energy consumption or generate large amounts of sludge that are also difficult to treat [10].

Adsorption provide potential alternative to overcome the disadvantages of conventional methods for wastewater treatment containing heavy metals. Well-design adsorption process has high efficiency and lead to getting a high-quality effluent that can be recycled. In addition, if the adsorbents have a low-cost or the adsorbents regeneration is feasible, then the adsorption process is inexpensive and accessible [11]. The natural materials or waste products from industrial or agricultural activities, which are available in large quantities, may have potential as low-cost adsorbents in the control of environmental pollution [12,13].

The histosol could be especially useful because this material is fairly abundant in many regions of the world, has a greatly metal removal potential and large surface area [14,15]. The excellent binding capacity of histosol is determined by the presence of various functional groups of lignin, cellulose and humic substances on they structure [16,17], but also to the small and uniform distribution of binding sites [18].

Nevertheless, there are still many aspects that need to be solved before that the histosol to be used in real applications in wastewater treatment. The most important is the fact that the adsorption capacity of histosol should be improved, mainly because low adsorption capacity may cause large amounts of wastes loaded with heavy metals, which are also a source of environmental pollution [19]. The studies from literature show that the adsorption capacities of histosol for different heavy metals do not exceed 2.5 mmol/g, which are significant lower that those obtained for commercial adsorbents, such as

activated carbon. In consequence, new preparation methods of adsorbents derived from histosol should be developed, and the cost of preparation should be kept low. In order to improved the adsorption characteristics of histosol for Ni(II) ions, several simple chemical treatments were used. These treatments suppose the mixing of histosol with aqueous solution of several common chemical reagents (HNO₃, NaCl and NaOH), and the main advantage of these procedures is that the enhancement of adsorption characteristics of histosol is done without adding expensive additives, and thus the cost of adsorbent preparation remains low.

In this study, the adsorptive characteristics of Ni(II) from aqueous media on histosol modified by simple chemical treatments was examined, at laboratory scale. The influence of initial Ni(II) ions concentration and equilibrium contact time was studied at room temperature (25 ± 0.5 °C) in batch experiments, in comparison with untreated histosol. Two isotherm models (Langmuir and Freundlich) and three kinetics models (pseudo-first order, pseudo-second order and intra-particle diffusion model) were used for the mathematical description of experimental data, and various model parameters have been calculated in each case.

RESULTS AND DISCUSSION

The histosol is usually considered as a complex material, which contains organic matter in various decomposition stages [20,21]. The major constituents (lignin, cellulose and humic substances) contains in their structure various functional groups (-OH, -COOH, -C=O, -NH₂, etc.), that can be involved in specific chemical interactions (ion-exchange or complexation) with metal ions from aqueous solution, during the adsorption.

FT-IR spectrum (Figure 1) was used to characterize the histosol. Several important peaks, at 3452, 2920, 1728, 1633, 1514, 1381 and 1037-1058 cm⁻¹ are observed in the spectrum of histosol used as adsorbent in this study.

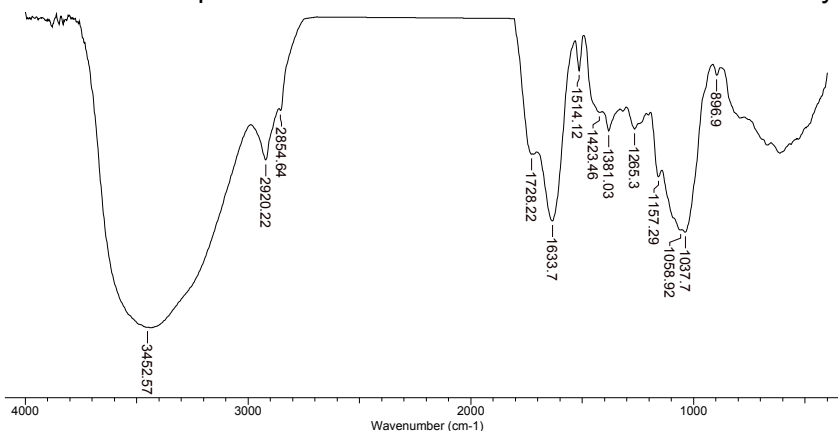


Figure 1. FT-IR spectrum of histosol used as adsorbent in this study.

The broad and strong band from 3452 cm^{-1} is attributed to the overlapping of O–H and N–H stretching vibrations. Peak at 2920 cm^{-1} is the C–H stretching vibration. The peaks at 1728 and 1633 cm^{-1} can be assigned to C=O stretching vibrations. Thus, the absorption band from 1633 cm^{-1} corresponding to carbonyl bond from carboxylic groups ($-\text{COO}^-$), while the band from 1728 cm^{-1} corresponds to the carbonyl bond from esters and carboxylic acid compounds. The peak at 1514 cm^{-1} is assigned to N–H vibrations. The peak at 1381 cm^{-1} is O–H bending vibration in alcohols. The strong band at $1058\text{--}1037\text{ cm}^{-1}$ indicates the presence of organic compounds with two or more hydroxyl groups. On the basis of these observations, it can be concluded that in the structure of histosol numerous functional groups (hydroxyl, amine, carbonyl, carboxylic groups, etc.) are present, and these can interact with Ni(II) ions during the adsorption process.

In consequence, it is expected that the efficiency of adsorption process to depend both on the affinity of metal ions for the superficial functional groups of histosol, and on the availability of these groups to interact with metal ions from aqueous solution. In case of a given metal ion, the increase of adsorption efficiency can be achieved by increasing of the availability of superficial functional groups of histosol, using specific treatments.

Starting from these observations, for the treatment of histosol three common chemical reagents (HNO_3 , NaCl and NaOH), have been selected because: (i) a strong mineral acid can remove the metal ions that are already bonded on superficial functional groups of histosol, and thus these become free; (ii) a neutral salt with high mobile cation, can replace the low mobile metal ions already bonded on superficial functional groups; and (iii) a strong base that will increase the dissociation degree of the functional superficial groups from adsorbent surface, without the histosol structure to be significant affected.

In order to evaluate the performances of histosol modified by these treatments on Ni(II) adsorption efficiency, the influence of initial metal ion concentration and equilibrium contact time was studied in comparison with untreated histosol, under optimum experimental conditions ($\text{pH} = 6.0$ (acetate buffer), $5\text{ g adsorbent/dm}^3$), established previously [22].

Effect of initial Ni(II) concentration

The influence of initial Ni(II) concentration on its adsorption efficiency on untreated histosol and modified histosol was studied in the $24.45\text{--}244.52\text{ mg/dm}^3$ concentration range. The experimental results, presented in Figure 2, shows that the amount of metal ion retained on mass unit of adsorbent (q , mg/g) increase with increasing of initial Ni(II) concentration from aqueous solution, in all cases.

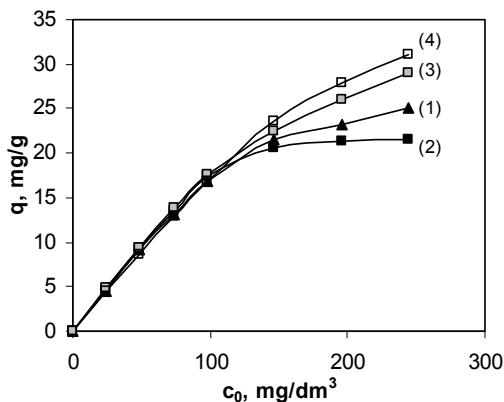


Figure 2. Influence of initial Ni(II) concentration on its removal on: (1) untreated histosol; (2) histosol treated with HNO₃; (3) histosol treated with NaCl; (4) histosol treated with NaOH (pH = 6.0 (acetate buffer); 5 g adsorbent/dm³).

It can also be observed from Figure 2 that in the studied Ni(II) concentration range the adsorption efficiency depends by the type of treatment used for histosol modification, and follows the order: histosol treated with NaOH ($q = 31.11$ mg/g) > histosol treated with NaCl ($q = 28.95$ mg/g) > untreated histosol ($q = 25.04$ mg/g) > histosol treated with HNO₃ ($q = 21.49$ mg/g), for an initial concentration of 244.51 mg/dm³.

The obtained experimental results suggest that the adsorption of Ni(II) from aqueous solution on untreated histosol and modified histosol occurs predominantly by electrostatic (ion-exchange) interactions, and the efficiency of adsorption process depends by the availability and dissociation degree of functional groups from adsorbent surface. Thus, when the histosol is treated with NaCl or NaOH, some functional groups, which are not active in the metal-binding process become available, and so the adsorption capacity increase. The change in availability of superficial functional groups of histosol by these simple chemical treatments determined an enhancement of adsorption capacity with 15.58 % in case of histosol treated with NaCl, and with 24.19 % in case of histosol treated with NaOH, respectively.

In case of histosol treated with HNO₃, even if the number of free functional groups is increased, most of these are un-dissociated. This makes that the number of electrostatic interactions with Ni(II) ions from aqueous solution to be low, and in consequence a decrease of adsorption capacity with 14.21 % in comparison with untreated histosol was obtained.

Equilibrium modelling

The adsorption isotherms of Ni(II) on untreated histosol and modified histosol, used for equilibrium modelling are presented in Figure 3.

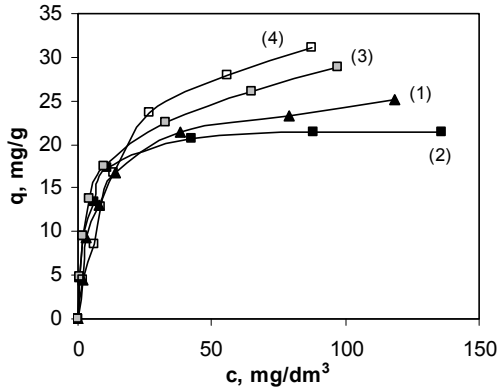


Figure 3. Adsorption isotherms of Ni(II) onto: (1) untreated histosol; (2) histosol treated with HNO₃; (3) histosol treated with NaCl; (4) histosol treated with NaOH (pH = 6.0 (acetate buffer); 5 g adsorbent/dm³).

The adsorption isotherm represents the equilibrium distribution of the Ni(II) ions between phases of solid adsorbent and aqueous solution, and are characterized by definite parameters, whose values express the surface properties and affinity of adsorbent for metal ions. In this study, two isotherm models were selected to fit the experimental data, namely Langmuir and Freundlich models.

The Langmuir isotherm model is based on the assumption that the adsorption occurs at specific homogeneous sites on the adsorbent surface, by adsorption forces similar to the forces on chemical interactions [23,24], and is used to estimate the maximum adsorption capacity (q_{max} , mg/g) corresponding to the adsorbent surface saturation. The linear form of the Langmuir isotherm model can be expressed by:

$$\frac{1}{q} = \frac{1}{q_{max}} + \frac{1}{q_{max} \cdot K_L} \cdot \frac{1}{c} \quad (1)$$

where: q_{max} is the maximum adsorption capacity (mg/g), corresponding to the complete monolayer coverage of surface, c is the Ni(II) concentration at equilibrium (mg/dm³) and K_L is the Langmuir constant, related to the adsorption / desorption energy (dm³/g).

The Freundlich isotherm model is derived from multilayer adsorption and adsorption on heterogeneous surface [24,25], and was chosen to estimate the adsorption intensity of Ni(II) ions on untreated histosol and modified histosol. The linear form of this model is:

$$\lg q = \lg K_F + \frac{1}{n} \lg c \quad (2)$$

where: K_F is the Freundlich constant and represent an indicator of adsorption capacity ($\text{mg}\cdot\text{dm}^{3/n}/\text{g}\cdot\text{mg}^{1/n}$) and n is a constant that characterized the surface heterogeneity. The $1/n$ value between 0 and 1 indicate that the adsorption process is favourable under studied experimental conditions [24].

The obtained values of Langmuir and Freundlich isotherm parameters, evaluated from the slope and intercept of the corresponding plots ($1/q$ vs. $1/c$, and $\lg q$ vs. $\lg c$, respectively) are summarized in Table 1, together with the linear regression coefficients (R^2), which were used to settle the best fit isotherm model.

Table 1. Isotherm parameters for the adsorption of Ni(II) on untreated histosol and modified histosol

Langmuir isotherm model			
Adsorbent	R^2	q_{\max} , mg/g	K_L , dm^3/g
Untreated histosol	0.9992	25.4451	0.1832
Histosol treated with HNO_3	0.9991	21.9784	0.3315
Histosol treated with NaCl	0.9929	29.4126	0.1873
Histosol treated with NaOH	0.9975	36.6303	0.0625
Freundlich isotherm model			
Adsorbent	R^2	$1/n$	K_F , $\text{mg}\cdot\text{dm}^{3/n}/\text{g}\cdot\text{mg}^{1/n}$
Untreated histosol	0.9246	0.4437	5.2612
Histosol treated with HNO_3	0.8945	0.1881	9.4363
Histosol treated with NaCl	0.9798	0.2604	9.0095
Histosol treated with NaOH	0.9334	0.4472	4.6968

The values of correlation coefficients (R^2) show that the adsorption isotherm data are very well represented by the Langmuir model, indicating the formation of monolayer coverage of Ni(II) ions on the other surface of adsorbent. The maximum adsorption capacity, which is a measure of the adsorption capacity to form a monolayer is higher in case of Ni(II) adsorption on histosol treated with NaCl and NaOH respectively, and lower in case of Ni(II) adsorption on histosol treated with HNO_3 , than those obtained by using untreated histosol as adsorbent. The increase of the maximum adsorption capacity, calculated according with equation (4) was by 15.59 % in case of histosol treated with NaCl and by 43.96 % in case of histosol treated with NaOH, while in case of histosol treated with HNO_3 a decrease with 13.62 % was obtained. This is another argument that sustain the hypothesis that after treating the histosol with NaCl and NaOH respectively, more many superficial functional groups from histosol surface become available for interactions with Ni(II) ions, therefore which make that the amount of metal ions required to form a complete monolayer on such modified histosol is higher. In addition,

the K_L values follows the same order, and indicate that between functional groups of adsorbent surface and Ni(II) ions from aqueous solution strong interactions occurs.

The fractional values of $1/n$ constant from Freundlich isotherm model (Table 1) suggests that untreated histosol and histosol modified by considered chemical treatments have an heterogeneous surface, but the adsorption process of Ni(II) ions on these adsorbents is a favorable process.

Effect of equilibrium contact time

The effect of equilibrium contact time between adsorbent (untreated histosol and modified histosol) and Ni(II) aqueous solution with an initial concentration of 48.90 mg/dm^3 , at $\text{pH} = 6.0$ (acetate buffer) is presented in Figure 4.

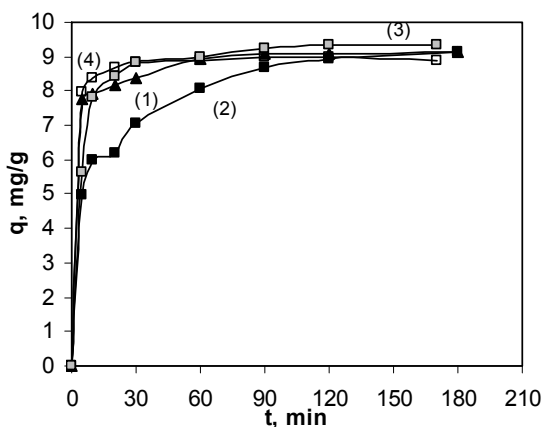


Figure 4. Effect of equilibrium contact time on Ni(II) adsorption onto: (1) untreated histosol; (2) histosol treated with HNO_3 ; (3) histosol treated with NaCl ; (4) histosol treated with NaOH ($\text{pH} = 6.0$ (acetate buffer); $5 \text{ g adsorbent/dm}^3$).

It can be observed that in all the cases the amount of Ni(II) ions retained on mass unit of adsorbent increase with increasing of contact time. The adsorption process is very fast during of initial stage, when in the first 20 min around of 80 % of Ni(II) is retained (84.54 % in case of untreated histosol, 63.74 % in case of histosol treated with HNO_3 , 86.63 % in case of histosol treated with NaCl and 89.71 % in case of histosol treated with NaOH , respectively). After this initial step, the rate of adsorption process become slower, near to equilibrium, which is practically obtained after 60 min in case of untreated histosol, 90 min in case of histosol treated with HNO_3 , 25 min in case of histosol treated with NaCl and 20 min in case of histosol treated with NaOH , respectively. These results show that in case of histosol treated with

NaCl and NaOH respectively, the required time for to attain the equilibrium of adsorption process is lower than case of untreated histosol. This is because after these treatments, most of functional groups from histosol surface become dissociated, and the electrostatic interactions with Ni(II) ions from aqueous solution occurs more easily. The fast adsorption on histosol treated with NaCl and NaOH respectively, makes these adsorbents suitable for continuous flow rate treatment systems.

Kinetics modelling

The kinetics modeling is important in the design of wastewater treatment system, and allows the selection of optimum conditions for operating in full scale process, as it provide valuable insights into the process pathways and adsorption mechanism. In order to analyze the adsorption kinetics of Ni(II) on untreated histosol and modified histosol, three kinetics models (pseudo-first order, pseudo-second order and intra-particle diffusion model) were tested to fit the experimental data. The linear expressions of the pseudo-first order (Eq. (3)) and pseudo-second order (Eq. (4)) kinetics models can be written as [26,27]:

$$\lg(q_e - q_t) = \lg q_e - \frac{k_1}{2.303} \cdot t \quad (3)$$

$$\frac{t}{q_t} = \frac{1}{k_2 \cdot q_e^2} + \frac{t}{q_e} \quad (4)$$

where: q_e and q_t are the amounts of Ni(II) retained on mass unit of adsorbent at equilibrium and at time t respectively, (mg/g), k_1 is the rate constant of pseudo-first order kinetic model (1/min), and k_2 is the rate constant of the pseudo-second order kinetic model (g/mg·min).

The kinetics parameters of the pseudo-first order and pseudo-second order kinetics models, calculated from the linear dependences $\lg(q_e - q_t)$ vs. t and t/q_t vs. t respectively, together with the corresponding correlation coefficients (R^2) are summarized in Table 2.

The obtained results showed that the adsorption capacities (q_e , mg/g), calculated from the pseudo-first order equation, are very different from the experimental values (q_e^{exp} , mg/g) in all cases. This means that the pseudo-first kinetic model is not adequate to describe the kinetics data of Ni(II) adsorption on untreated histosol and modified histosol.

The experimental data were further fitted to the pseudo-second order kinetic model, when a better fitting was obtained with high correlation coefficients ($R^2 > 0.999$), in all cases. Also, the adsorption capacity values, calculated from the pseudo-second order kinetic model (q_e , mg/g) have similar values with those obtained experimentally (Table 2).

Table 2. Kinetics parameters for the adsorption of Ni(II) on untreated histosol and modified histosol

Pseudo-first kinetic model				
Adsorbent	q_e^{exp} , mg/g	R^2	q_e , mg/g	k_1 , 1/min
Untreated histosol	9.1424	0.9701	1.6462	$3.11 \cdot 10^{-2}$
Histosol treated with HNO ₃	9.1350	0.9942	4.6676	$1.15 \cdot 10^{-2}$
Histosol treated with NaCl	9.3412	0.9094	2.4294	$1.57 \cdot 10^{-2}$
Histosol treated with NaOH	9.8631	0.9201	3.0904	$2.15 \cdot 10^{-2}$
Pseudo-second kinetic model				
Adsorbent	q_e^{exp} , mg/g	R^2	q_e , mg/g	k_2 , g/mg.min
Untreated histosol	9.1424	0.9995	9.2421	$3.40 \cdot 10^{-2}$
Histosol treated with HNO ₃	9.1350	0.9996	9.0551	$1.29 \cdot 10^{-2}$
Histosol treated with NaCl	9.3412	0.9999	9.4971	$3.93 \cdot 10^{-1}$
Histosol treated with NaOH	9.8631	0.9999	9.8431	$2.12 \cdot 10^{-1}$

The pseudo-second kinetics model is based on the assumption that the rate controlling step in the adsorption process is the chemical interaction between metal ions from aqueous solution and superficial functional groups of adsorbent [27]. The good fitting of experimental data by this model indicate that in case of untreated histosol and modified histosol, the rate of adsorption process depends by the availability of Ni(II) ions and superficial functional groups to interact. If the availability of functional groups is higher, the rate of adsorption process is also higher. Thus when the histosol is treated with NaCl or NaOH respectively, the availability of superficial functional groups is increased (mainly due to the increase of dissociation degree of these), and the obtained values of rate constants are higher even with one order of magnitude than in case of untreated histosol. Contrary, by treating the histosol with HNO₃ solution, the availability of superficial functional groups to interact with Ni(II) ions from aqueous solution decrease (due to the decrease of dissociation degree of functional groups) and the obtained values of rate constant is lower than in case of untreated histosol.

The intra-particle diffusion model was used to determine the participation of diffusion process in the adsorption of Ni(II) on untreated histosol and modified histosol. The mathematical equation of the intra-diffusion model can be expressed as [28]:

$$q_t = k_{\text{diff}} t^{1/2} + c \quad (5)$$

where: k_{diff} is the intra-particle diffusion rate constant ($\text{mg/g} \cdot \text{min}^{1/2}$) and c is the concentration of Ni(II) ions solution at equilibrium (mg/dm^3).

According with the intra-particle model, if the diffusion process is the rate controlling step, the graphical representation of q_t vs. $t^{1/2}$ should yield a straight line, passing through the origin. The experimental results have show

that in case of Ni(II) adsorption on untreated histosol and modified histosol, the plots q_t vs. $t^{1/2}$ (Figure 5) does not go through the origin and two separated regions exists in all cases.

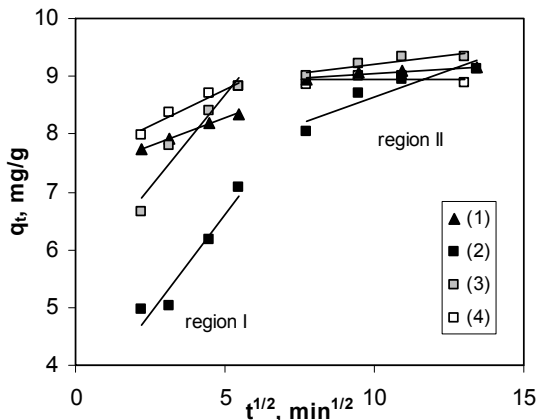


Figure 5. The plots of intra-particle diffusion model for the adsorption of Ni(II) onto: (1) untreated histosol; (2) histosol treated with HNO₃; (3) histosol treated with NaCl; (4) histosol treated with NaOH (pH = 6.0 (acetate buffer); 5 g adsorbent/dm³).

The parameters of intra-particle diffusion model (k_{diff} and c), calculated for each region from the slopes and intercepts of the linear portions of the plots, are summarized in Table 3.

The deviation of the straight line from the origin indicate that the intra-particle diffusion process is not the rate controlling step [29], and the boundary layer diffusion controls the adsorption to some degree, in all cases. In addition, the higher values of the rate constants obtained from this model sustain the hypothesis that the intra-particle diffusion does not limit the rate of adsorption process of Ni(II) on untreated histosol and modified histosol. The first region (region I from Figure 5) is attributed to mass transfer of Ni(II) from the bulk solution to adsorbent surface, while the second region (region II from Figure 5) indicated the intra-particle diffusion.

The significant differences between these two regions is given by the slope, thus in all cases the first region has a pronounced slope, while the slope of second region is much lower. This indicate that the binding sites are located on adsorbent surface of the at external intra-layer surface, and are readily accessible from Ni(II) ions from aqueous solution.

The obtained experimental data have show a limited contribution of mass transfer and boundary layer diffusion in the adsorption process of Ni(II) on untreated histosol and histosol modified by considered chemical treatments, and that the intra-particle diffusion influenced the adsorption process in a certain degree.

Table 3. Intra-particle model parameters for the adsorption of Ni(II) on untreated histosol and modified histosol

Region I			
Adsorbent	R ²	c, mg/dm ³	k _{diff} ^I , mg/g.min ^{1/2}
Untreated histosol	0.9980	7.3215	0.1903
Histosol treated with HNO ₃	0.9037	3.8499	0.5751
Histosol treated with NaCl	0.8281	4.1943	0.9049
Histosol treated with NaOH	0.9572	7.4981	0.2531
Region II			
Adsorbent	R ²	c, mg/dm ³	k _{diff} ^{II} , mg/g.min ^{1/2}
Untreated histosol	0.8633	8.7269	0.0322
Histosol treated with HNO ₃	0.8682	6.7886	0.1844
Histosol treated with NaCl	0.7706	8.5965	0.0608
Histosol treated with NaOH	0.9006	8.9278	0.0181

CONCLUSIONS

In this study, the adsorptive characteristics of histosol modified by several simple chemical treatments have been investigated for the removal of Ni(II) ions from aqueous media, in comparison with untreated histosol. The chemical treatments imply the mixing of histosol with 0.2 mol/dm³ aqueous solution of common chemical reagents (HNO₃, NaCl and NaOH, respectively), without the addition of supplementary additives, and thus the cost of adsorbent preparation remains low.

In order to estimate the adsorptive characteristics of modified histosol in the adsorption process of Ni(II) ions from aqueous solution, the influence of initial metal ion concentration and equilibrium contact time were studied, in optimum experimental conditions (pH = 6.0 (acetate buffer), 5 g adsorbent/dm³), in comparison with untreated histosol. The experimental results have show that in case of treatments with NaCl and NaOH respectively, an increase of the adsorption capacity of histosol with 15.58 % and 24.19 % was obtained, while in case of treatment with HNO₃, the adsorption capacity decrease with 14.21 %, towards untreated histosol. Another important advantage of using modified is that the required time for Ni(II) ions adsorption is shorter.

The experimental data were best correlated with the Langmuir isotherm model. The maximum adsorption capacity was higher with 15.59 % in case of histosol treated with NaCl, with 43.96 % in case of histosol treated with NaOH, while in case of histosol treated with HNO₃ a decrease of this parameter with 13.62 % was obtained, in comparison with untreated histosol. The pseudo-second order model best describe the adsorption process of Ni(II) on untreated histosol and modified histosol. This model is based on the assumption that the rate controlling step is the chemical interaction between

metal ions from aqueous solution and functional groups from adsorbent surface. The calculated values of model parameters indicate that the rate of adsorption process is limited by the availability of superficial functional groups to interact. Thus, when the availability of superficial functional groups is higher (in case of histosol treated with NaCl and NaOH, respectively), the rate of adsorption is also higher.

The results of this study show that the chemically modified histosol can have better adsorptive characteristics than untreated histosol, and could be employed as an efficient adsorbent for the removal of Ni(II) ions from aqueous media.

EXPERIMENTAL SECTION

Materials

In this study, histosol samples from Poiana Stampei (Romania) at depth below 0.5 m was used as adsorbent. Before use, the raw material was dried in air for 24 hours at room temperature (25 ± 0.5 °C), and then grounded and sieved until the particles had the granulation less than 1-2 mm. The chemical composition and some physical-chemical characteristics of this adsorbent have been presented in a previous study [30].

The chemical treatments were done by mixing histosol samples with aqueous solution of chemical reagents. Thus, 2.0 g of histosol was mechanically shaken with 100 cm³ of 0.2 mol/dm³ solution of HNO₃, NaCl and NaOH respectively, for 30 min. After 24 hours of stand-by the modified histosol samples were filtrated, washed with distilled water until a neutral pH, dried in air and then mortared.

Reagents

All chemical reagents (HNO₃, NaCl and NaOH) were of analytical degree and were used without further purifications. In all experiments, distilled water obtained from a commercial distillation system, was utilized for the preparation of solution. The stock solution of nickel, containing 611.29 mg Ni(II)/dm³, was prepared by dissolving nickel nitrate (purchased from Reactivul Bucharest) in distilled water. Fresh dilution were prepared and used for each experiment. The initial pH value of working solutions was obtained using acetate buffer (CH₃COOH / CH₃COONa) with pH = 6.0.

Adsorption experiments

The adsorption experiments were performed by batch technique, at room temperature (25 ± 0.5 °C), mixing 0.125 g sample of untreated histosol and modified histosol with volume of 25 cm³ solution of known concentration

(24.45 – 244.51 mg/dm³), in 150 cm³ conical flasks, with intermittent stirring. All experiments were run in optimum experimental conditions (pH = 6.0 (acetate buffer), adsorbent dose = 5 g/dm³) previously established [22]. In case of kinetics experiments, a constant amount of untreated histosol and histosol modified by considered chemical treatments (5 g/dm³) was mixed with 25 cm³ of 48.90 mg/dm³ Ni(II) solution, at various time intervals between 5 and 180 min. At the end of adsorption procedure, the phases were separated by filtration and the Ni(II) concentration in filtrate was determined using the spectrophotometric method (Digital Spectrophotometer S 104 D, rubeanic acid, $\lambda = 600$ nm, 1 cm glass cell) [31], using a prepared calibration graph.

Data evaluation

The adsorption efficiency of Ni(II) on untreated histosol and histosol modified by considered chemical treatments was quantitatively evaluated from experimental results using amount of Ni(II) retained on mass unit of adsorbent (q , mg/g), calculated from the mass balance expression:

$$q = \frac{(c_0 - c) \cdot (V / 1000)}{m} \quad (3)$$

where: c_0 is the initial Ni(II) concentration (mg/dm³), c is the equilibrium concentration (mg/dm³), V is the volume of solution (cm³) and m is the adsorbent mass (g).

The difference between adsorption capacity of untreated histosol and histosol modified by considered chemical treatments was calculated according to the relation:

$$\Delta q = \frac{q_{\text{modified}} - q_{\text{untreated}}}{q_{\text{untreated}}} \cdot 100 \quad (4)$$

where: q_{modified} , $q_{\text{untreated}}$ are the amounts of Ni(II) retained on mass unit of modified histosol and untreated histosol, respectively (mg/g).

ACKNOWLEDGMENTS

This paper was supported by Project No. 3 / theme 1 / 2013 financed by the Romanian Academy, Iași Branch.

REFERENCES

1. O.M.M. Freitas, R.J.E. Martins, C.M. Delerue-Matos, R.A.R. Boaventura, *Journal of Hazardous Materials*, **2008**, 153, 493.
2. A.H. Sulaymon, A.A. Mohammed, T.J. Al-Musawi, *Desalination and Water Treatment*, **2013**, 51, 4424.

3. O. Aksakal, H. Uçun, Y. Kaya, *Environmental Engineering and Management Journal*, **2008**, 7, 359.
4. P.R. Gogate, A.B. Pandit, *Advanced Environmental Research*, **2004**, 8, 553.
5. A. Mudhoo, V.K. Garg, S. Wang, *Environmental Chemistry Letters*, **2012**, 10, 109.
6. J.C. Igwe, A.A. Abia, *African Journal of Biotechnology*, **2006**, 5, 1167.
7. E.F. Covelo, F.A. Vega, M.L. Andrade, *Journal of Hazardous Materials*, **2008**, 159, 342.
8. S.M. Shaheem, C.D. Tsadilas, T. Mitsibonas, M. Tzouvalekas, *Communications in Soil Science and Plant Analysis*, **2009**, 40, 214.
9. A. Dabrowski, Z. Hubicki, P. Podkoscielny, E. Robens, *Chemosphere*, **2004**, 56, 91.
10. V.O. Arief, K. Trilestari, J. Sunarso, N. Indraswati, S. Ismadji, *CLEAN – Soil, Air, Water*, **2008**, 36, 937.
11. T.A. Kurniawan, G.Y.S. Chan, W. Lo, S. Babel, *Science of the Total Environment*, **2006**, 366, 409.
12. S. Babel, T.A. Krniavan, *Journal of Hazardous Materials*, **2003**, B97, 219.
13. P.S. Kumar, S. Ramalingam, R.V. Abhinaya, S.D. Kirupha, A. Murugesan, S. Sivanesan, *CLEAN – Soil, Air, Water*, **2012**, 40, 188.
14. T. Malterer, B. McCarthy, R. Adams, *Mining Engineering*, **1996**, 48, 53.
15. B. Coupal, A.I. Spiff, *Water Research*, **1999**, 33, 1071.
16. P.A. Brown, S.A. Gill, S.J. Allen, *Water Research*, **2000**, 34, 3907.
17. S.E. Bailey, T.J. Olin, M.R. Bricka, D.D. Adrian, *Water Research*, **1999**, 33, 2469.
18. L. Bulgariu, M. Ratoi, D. Bulgariu, M. Macoveanu, *Environmental Engineering and Management Journal*, **2008**, 5, 211.
19. J.L. Hu, X.W. He, C.R. Wang, J.W. Li, C.H. Zhang, *Bioresource Technology*, **2012**, 121, 25.
20. C.C. Liu, M.K. Wang and Y.S. Li, *Industrial Engineering Chemical Research*, **2005**, 44, 1438.
21. E.L. Cochrane, S. Lu, S.W. Gibb, I. Villaescusa, *Journal of Hazardous Materials*, **2006**, B137, 198.
22. L. Bulgariu, D. Bulgariu, M. Macoveanu, *Environmental Engineering and Management Journal*, **2010**, 9, 667.
23. K.H. Chong, B. Volesky, *Biotechnology and Bioengineering*, **1995**, 47, 451.
24. Y.S. Ho, J.F. Porter, G. McKay, *Water, Air Soil Poll.* **2002**, 141, 1.
25. J. Febrianto, A.N. Kosasih, J. Sunarso, Y.H. Ju, N. Indrawati, S. Ismadji, *Journal of Hazardous Materials*, **2009**, 162, 616.
26. Y.S. Ho, G. McKay, *Water Research*, **2000**, 34, 735.
27. C. Gerente, V.K.C. Lee, P. Lee, G. McKay, *Critical Review in Environmental Science and Technology*, **2007**, 37, 41.
28. Y. Wu, S. Zhang, X. Guo, H. Huang, *Bioresource Technology*, **2008**, 99, 7709.
29. I.D. Mall, V.C. Srivastava, N.K. Agarwal, *Dyes and Pigments*, **2006**, 69, 210.

30. L. Bulgariu, M. Ratoi, D. Bulgariu, M. Macoveanu, *Journal of Environmental Science and Health Part A*, **2009**, *44*, 700.
31. A.H. Flaska, A.J. Barnard, "Chelates in Analytical Chemistry", Marcel Dekker, Inc., New York, **1967**, 231.

*Dedicated to Professor Liviu Literat
On the occasion of his 85th birthday*

INFLUENCE OF THE CITRIC ACID ON THE CERIUM SUBSTITUTED HYDROXYAPATITE MORPHOLOGY

**ANA MARIA BARGAN^a, GABRIELA CIOBANU^{a,*},
CONSTANTIN LUCA^a, EUGEN HOROBA^a**

ABSTRACT. In the present study the obtaining of the simple and substituted hydroxyapatite with cerium ions (Ce^{4+}) in presence of citric acid was studied. The hydroxyapatite samples were prepared by wet coprecipitation method. The structural properties of hydroxyapatite powders were characterized by scanning electron microscopy (SEM) coupled with X-ray analysis (EDX), X-ray powder diffraction (XRD) and Fourier Transform Infrared spectroscopy (FTIR). Like organic modifier, the citric acid has an influence on the morphology and particle size of hydroxyapatite as shown by XRD and SEM-EDX analysis. The results obtained indicated that cerium ions were incorporated into hydroxyapatite structure and the presence of citric acid was useful on the average crystallite size reduction of the samples obtained.

Keywords: *hydroxyapatite, citric acid, cerium*

INTRODUCTION

The bone mineral is described as a poorly crystalline non-stoichiometric apatite (biological apatite) with chemical composition of calcium phosphate [1]. Biological apatites are rarely stoichiometric, usually being calcium-deficient containing a wide variety of relatively small amounts of other substituted atoms. The major cause of nonstoichiometry is the incorporation of some impurities like cations or anions which may substitute calcium ions, phosphate and hydroxyl groups [2].

^a "Gheorghe Asachi" Technical University of Iasi, Faculty of Chemical Engineering and Environmental Protection, Prof. dr. docent Dimitrie Mangeron Rd., no. 73, 700050, Iasi, Romania. * Corresponding author: gciobanu03@yahoo.co.uk

The calcium phosphate group is a part of the bioceramics family being the most important inorganic hard tissues constituents of the bones and dentine material in the vertebrate species [3].

The calcium phosphates have been classified in to three major structural types [2,4]:

- 1) the apatite type $\text{Ca}_{10}(\text{PO}_4)_6\text{X}_2$ (X = OH or F in hydroxyapatite or fluorapatite) and those related to apatite-type structures such as octacalcium phosphate (OCP) $\text{Ca}_8(\text{HPO}_4)_2(\text{PO}_4)_4 \cdot 5\text{H}_2\text{O}$ and tetracalcium phosphate (TTCP) $\text{Ca}_4(\text{PO}_4)_2\text{O}$;

- 2) the glaserite type which include polymorph forms of tricalcium phosphates (TCP) $\text{Ca}_3(\text{PO}_4)_2$ and

- 3) the CaPO_4 based compounds such as dicalcium phosphate dihydrate (DCPD) $\text{CaHPO}_4 \cdot 2\text{H}_2\text{O}$, dicalcium phosphate anhydrous (DCPA) CaHPO_4 and monocalcium phosphates $\text{Ca}(\text{H}_2\text{PO}_4)_2 \cdot \text{H}_2\text{O}$ and $\text{Ca}(\text{H}_2\text{PO}_4)_2$.

The synthetic hydroxyapatite, $\text{Ca}_{10}(\text{PO}_4)_6(\text{OH})_2$ (HA), is one of the most well-known phosphates that can be used in bone reconstruction for the implants fabrication with many biomedical applications. The hydroxyapatite bioceramics as bone substitute materials have more advantages such as: abundant supply, non-toxic, more biocompatible with an organism than other implanted materials and low cost. The hydroxyapatite is also being tested as an absorbent for organic molecules that exist inside the human body [5].

It is well known that the organic modifiers are used in the synthesis of the hydroxyapatite in order to control the morphology and size of the crystals [6]. Examples of such organic modifiers are: ethylene glycol, trisodium citrate, citric acid, polyethylene glycol, Tween20, D-sorbitol, sodium dodecyl sulphate, sodium dodecylbenzene sulphonate and polyoxyethylene [7].

In the past few years the scientists have been studied the substitution of the hydroxyapatite with rare earth elements and due to greater charge-to-volume ratios and despite their different valences, the Lanthanides readily displace calcium from biological apatite [8].

Discovered in 1803, cerium (^{58}Ce) is a trivalent atom although unique among the Lanthanides, it also has a quaternary valence (Ce^{4+}) [8]. Cerium is one of the cheapest and most abundant rare earths. However, high purity is usually required for its utilization in industry like sulphur control in steels, pyrophoric alloys, ceramic, catalyst support, polishing powders, phosphors luminescence, etc. [9].

The exchange of calcium ions in hydroxyapatite with cerium ions is an interesting subject in medical, catalysis and environmental sciences. In general, the compounds containing cerium ions have been used in medicine for a long time as antibacterial agents. Therefore, the incorporation of Ce ions into the hydroxyapatite lattice is important for the developing of artificial bones.

In this work we have studied the effect of citric acid like a chelating reagent during the precipitation process on the formation of simple and cerium substituted hydroxyapatite. The morphology and crystal structure of samples were characterized by SEM (scanning electron microscopy), EDX (Energy Dispersive X-ray spectroscopy), XRD (X-ray diffraction analyses) and FTIR (Fourier Transform Infrared spectroscopy) analyses.

RESULTS AND DISCUSSION

The properties of the hydroxyapatite can be improved by anion/cation substitutions in its network. Anion substitution reaction of PO_4^{3-} groups by HPO_4^{2-} and CO_3^{2-} and OH^- by F^- can modify the surface properties and the thermal stability of the material [10]. The substitution of Ca^{2+} with divalent cations (Sr^{2+} , Mg^{2+} , Cd^{2+} , Zn^{2+} , Pb^{2+} , Ba^{2+} , etc.) [11, 12, 13, 14], trivalent cations (Cr^{3+} , Al^{3+} and Fe^{3+}) and lately with rare earth cations [15], affects important characteristics of hydroxyapatite such as crystallinity, solubility, thermal stability, metabolizability, etc. [16].

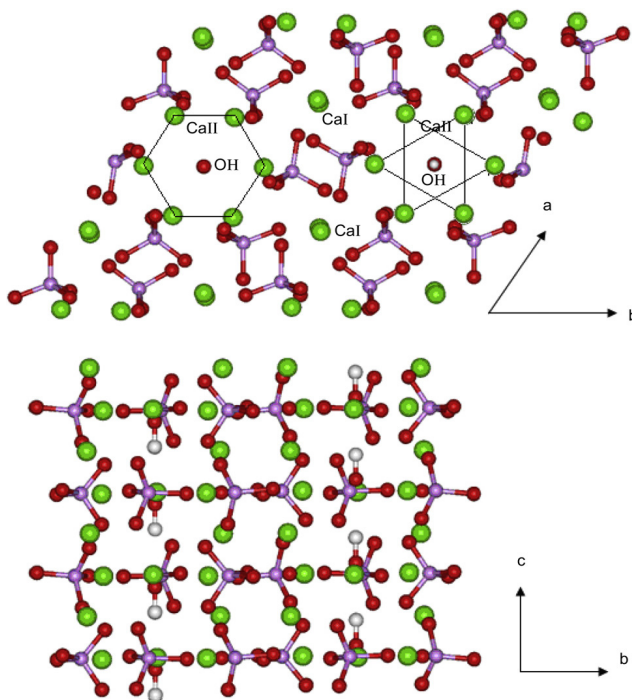


Figure 1. Representation of the hydroxyapatite structure perpendicular to the crystallographic c and a axes, showing the OH^- channels and the different types of Ca ions [18]

As illustrated in Figure 1, there are two crystallographically calcium sites in the hydroxyapatite unit cell: Ca (I) and Ca (II). Each Ca(I) is coordinated to nine O atoms belonging to six different PO_4^{3-} anions. The Ca(II) cations have a less regular seven-fold coordination: they are bound to six O atoms belonging to five different phosphates and to one hydroxyl group.

The incorporation of rare earth (lanthanide series) ions in the hydroxyapatite structure are favorable when there is a small difference in ionic radii which minimizes the difference in bond strength when one Ca^{2+} ion is substituted for another ion. Substitution in a crystal is expected to be common when there is an ionic radii difference of less than 15% [17]. With quite comparable dimensions, the Ce^{4+} ions (radius of 0.97 Å) can substitute Ca^{2+} ions (radius of 1.00 Å) during the synthesis process. The minimal difference (3%) in ionic radius between Ce^{4+} and Ca^{2+} contributes to the calcium replace.

In this research, in order to understand how the incorporation of a large cation like Ce^{4+} in the hydroxyapatite lattice and influence of citric acid can affect the cation and anion environment, the SEM, EDX, XRD and FTIR studies were carried out.

The SEM and EDX methods were performed in order to determine the surface elemental composition of the hydroxyapatite and cerium-substituted hydroxyapatite samples. Figure 2 shows the SEM micrographs of the calcinated samples. The samples without citric acid (HA and HA-Ce samples) consist of needle-like particles. Instead, the samples which content citric acid (HA-CitA and HA-CitA-Ce samples) consist of big aggregates of small particles due to the presence of calcium citrate complexes. These results indicate that citrate absorbs on the calcium phosphate nuclei, inhibits their growth and finally leading to the formation of a large number of small particles which contribute to a higher surface area, in agreement with literature data [19].

The EDX analysis (figures not shown) of the samples confirms the presence of the calcium, cerium, phosphorous, oxygen and carbon elements in certain proportions; no other elements are detected in the samples. The C signal in HA-CitA and HA-CitA-Ce samples is probably due to the traces of the uncalcined citric acid used as organic modifier in hydroxyapatite synthesis (due perhaps to the incomplete calcination of the samples). Using EDX method, the mass fractions of different elements in the hydroxyapatite and cerium-substituted hydroxyapatite samples were obtained and the atomic ratios were calculated, as presented in Table 1. The results confirm that cerium ions have been incorporated into the hydroxyapatite nanocrystals and the (Ce+Ca)/P atomic ratio in these powders is around 1.6.

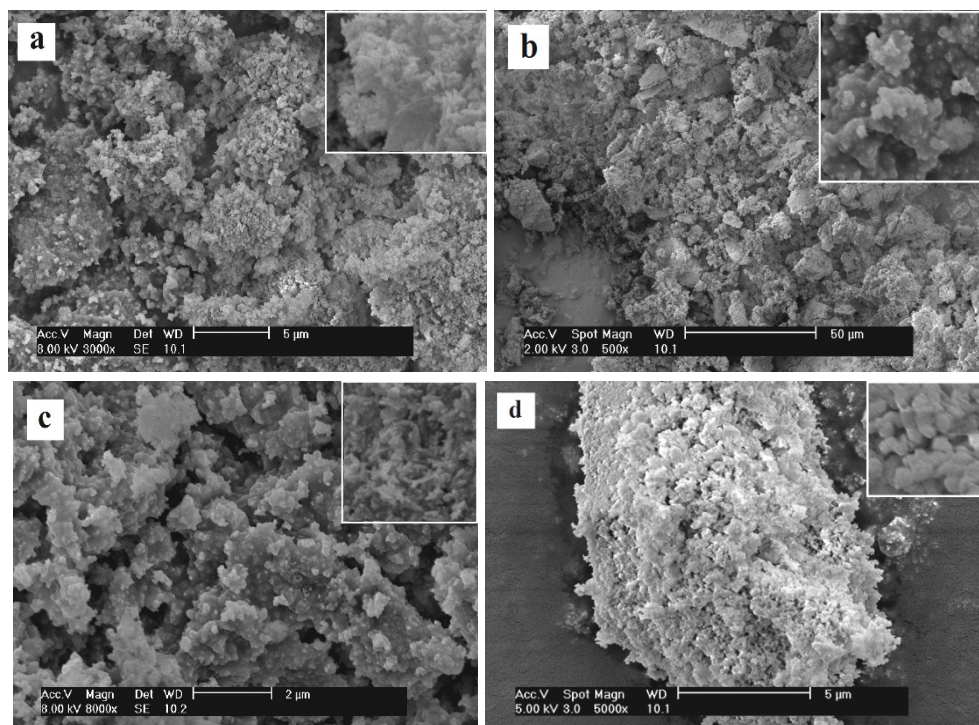


Figure 2. SEM images of the calcinated samples: (a) HA, (b) HA-CitA, (c) HA-Ce and (d) HA-CitA-Ce

Table 1. The elemental composition (% mass) and atomic ratio in the final products calcined in air at 850 °C

Sample	Ca (%)	P (%)	O (%)	C (%)	Ce (%)	(Ca+Ce)/P
HA	41.61	19.28	39.08	0	0	1.673
HA-Ce	40.5	19.91	32.08	0	7.51	1.660
HA-CitA	40.12	18.91	31.32	9.65	0	1.644
HA-CitA-Ce	39.07	18.98	29.32	5.35	7.28	1.680

The phase composition, lattice parameters, degree of crystallinity and size of the hydroxyapatite crystallites were determined by X-ray diffraction analysis. In the figure 3 it can see the patterns of the HA, HA-CitA and HA-CitA-Ce samples. All XRD patterns show the diffraction lines characteristic of hydroxyapatite, both present in standards and in literature. The major phase is hydroxyapatite which is confirmed by comparing data obtained with the JCPDS Data Card 09-0432 (for hydroxyapatite). The pattern of the sample

containing Ce (HA-CitA-Ce) exhibit similar but broader diffraction peaks, in agreement with a reduced degree of crystallinity of the cerium-substituted hydroxyapatite sample [15].

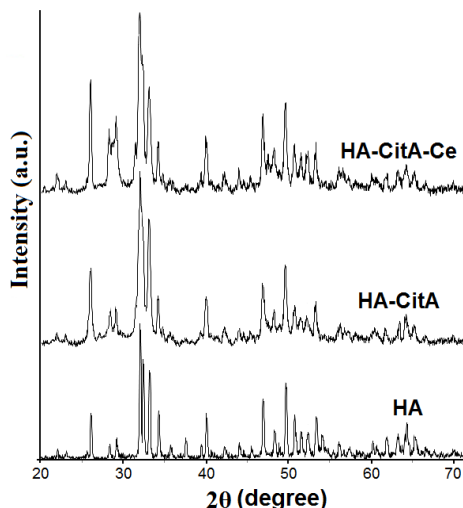


Figure 3. XRD patterns of the HA, HA-CitA and HA-CitA-Ce calcined samples

The average crystallite size (D) of the hydroxyapatite powders was calculated from XRD data using the Scherrer equation. The average crystallite size of the HA and HA-CitA hydroxyapatite powders were 59 and 54 nm, respectively. For the HA-Ce and HA-CitA-Ce cerium-substituted hydroxyapatite powders the average crystallite size were 47 and 43 nm, respectively. For samples doped with cerium, a small decrease in crystallite size was observed.

The FTIR spectra obtained from hydroxyapatite samples were given in Figure 4. The FTIR spectra of samples analysed provides information on the existing groups in the structure of hydroxyapatite, such as phosphate (PO_4^{3-}), hydroxyl (OH^-) and possibly carbonate (CO_3^{2-}) groups.

In Figure 4, the phosphate characteristic bands were observed at 472, 564, 602, 962, 1044, and 1092 cm^{-1} . These bands indicate the arrangement of the polyhedrons of PO_4^{3-} in the hydroxyapatite structure. The broader band between 3200 and 3500 cm^{-1} was produced by the water molecule adsorbed on the surface of hydroxyapatite and the stretching and vibration of O-H bonds on the surface of hydroxyapatite were located at 3590-3560 cm^{-1} . The entire FTIR spectrum shows the presence of an important peak in the range 1400-1500 cm^{-1} indicating the formation of calcium carbonate or calcium oxide in the apatite layer.

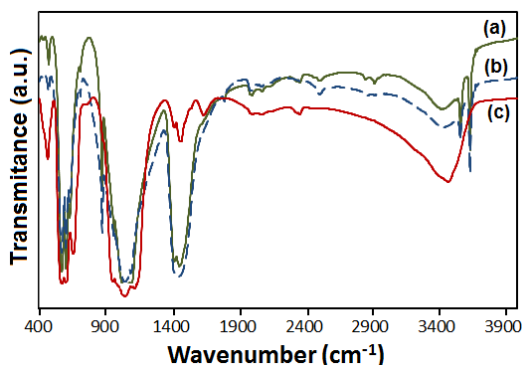


Figure 4. FTIR spectra of the calcined samples: (a) HA, (b) HA-CitA and (c) HA-CitA-Ce

The precipitation of calcium phosphate is inhibited in the presence of the citric acid, but in the small degree; this can be confirmed by the FTIR spectroscopy, in the figure 4, by the fact that the carboxyl group is identified in the spectra of sample HA-CitA at 1096 cm^{-1} for C-O stretch and at 2530 cm^{-1} and 2892 cm^{-1} for O-H bends. The intensity of the peaks is weak.

Compared to the spectrum of HA, no significant shift either to lower or higher wave number is observed upon doping with cerium ion. However, the intensity of all bands is weakened upon adding of Ce. The weakening of OH^- bands may be resulted from the breakage of balance of electric charge in hydroxyapatite; this is due perhaps to the substitution of Ca^{2+} with Ce^{4+} . In order to compensate these positive charges, OH^- may transform to O^{2-} , as suggested by Serret et al. [20]. The weakening of PO_4^{3-} bands may arise from the introduction of Ce^{4+} and subsequent alteration of the bonding force between ions, which lead to the weakening of the vibration of P-O and O-P-O.

EXPERIMENTAL SECTION

Hydroxyapatite powders can be synthesized by several methods, using a range of different reactants. The main processing techniques include wet chemical methods (precipitation), hydrothermal techniques, sol-gel methods, biomimetic deposition technique, electrodeposition [8], microemulsion [9] and spray drying method [10].

In this work hydroxyapatite simple and substituted with cerium ions were synthesized by coprecipitation method, as described elsewhere [21,22]. Reagent grade calcium hydroxide ($\text{Ca}(\text{OH})_2$), phosphoric acid (H_3PO_4), ceric sulphate pentahydrate ($\text{Ce}(\text{SO}_4)_2 \cdot 4\text{H}_2\text{O}$), citric acid ($\text{C}_6\text{H}_8\text{O}_7$) and sodium hydroxide (NaOH) used in this investigation were purchased from Sigma-Aldrich.

Calcium phosphate powders were prepared by neutralising a solution of $\text{Ca}(\text{OH})_2$ 0.01M with a solution of H_3PO_4 0.01M. We have made two solutions denoted A and B. The solution A (H_3PO_4 and distilled water) is added in the solution B ($\text{Ca}(\text{OH})_2$, $\text{C}_6\text{H}_8\text{O}_7$ and water) by dipping at 70°C and pH was adjusted at 11 with NaOH solution. The reaction was carried out at 70°C for 1 hour and then the slurry was aged for 48 h at room temperature, decanted and vacuum filtered. The obtained powder was dried at 110°C for 3 hours and calcined at 850°C during 3 hours.

For the cerium substituted hydroxyapatite preparation, $\text{Ce}(\text{SO}_4)_2$, $\text{Ca}(\text{OH})_2$ and $\text{C}_6\text{H}_8\text{O}_7$ were dissolved in water and then added to a solution of H_3PO_4 to attain the $(\text{Ca} + \text{Ce})/\text{P}$ mass ratio between 1,5 - 1,8. The pH was maintained at 10 - 11 with NaOH 10 M. The suspension was matured for 3 hours at approximately 70°C under magnetic stirring. After that, the powder was removed from the solution, washed with deionized water and dried at 60°C for 24 hours. The powder obtained was calcinated in an electrically heated furnace at a temperature of 850°C for 3 hours, in order to increase their crystallinity. In this study, all samples have denotes as follows: **HA** (simple hydroxyapatite), **HA-CitA** (hydroxyapatite with citric acid), **HA-Ce** (hydroxyapatite substituted with cerium) and **HA-CitA-Ce** (hydroxyapatite with citric acid and substituted with cerium).

The phase composition, crystal structure and morphology of the as obtained hydroxyapatite powders were analysed by scanning electron microscopy coupled with energy dispersive X-ray spectroscopy (SEM-EDX) (QUANTA 200 3D microscope), X-ray diffraction (XRD) (X'PERT PRO MRD diffractometer, using $\text{CuK}\alpha$ radiation $\lambda = 0.15418$ nm) and Fourier Transform Infrared spectroscopy (FTIR) (SPECTRUM BX II / PerkinElmer spectrophotometer).

CONCLUSIONS

The cerium-substituted hydroxyapatite powders were produced by coprecipitation reactions, using citric acid as organic modifier. The hydroxyapatite samples obtained have maintained the apatite structure. The Ce^{4+} ions were entered in the apatite crystal lattice by Ca^{2+} ions substitution. After substitution the crystallinity and the IR wave numbers of bonds in the HA-CitA-Ce sample decreased with the doping of cerium ion and the morphology of the nanoparticles changed from the rod-shaped (HA sample) to the needle-shaped (HA-Ce sample). The XRD pattern of the HA and HA-CitA samples display well-defined and sharp peaks in agreement with a high degree of crystallinity, with no visible modifications. The pattern of the sample containing Ce (HA-CitA-Ce) exhibit broader diffraction peaks, in agreement with a reduced degree of crystallinity of the cerium-substituted hydroxyapatite sample. The results obtained indicated that cerium ions were incorporated into hydroxyapatite structure and the presence of citric acid was useful on the average crystallite size reduction of the samples obtained.

REFERENCES

1. H. Yuan, K. de Groot, *Learning from Nature How to Design New Implantable Biomaterials*, **2004**, 37-57.
2. M. Mathew, S. Takagi, *Journal of Research of NIST*, **2001**, 106, 1035.
3. S. Pramanik, A.K. Agarwal, K.N. Rai, A. Garg, *Ceramics International*, **2007**, 33, 419.
4. W.J.E.M. Habraken, J.G.C. Wolke, J.A. Jansen, *Advanced Drug Delivery Reviews*, **2007**, 59, 234.
5. M. Jarcho, *Clinical Orthopedics and Related Research*, **1981**, 157, 259.
6. D.N. Misra, *Journal of Dental Research*, **1996**, 75, 1418.
7. A. Wang, H. Yin, D. Liu, H. Wu, Y. Wada, M. Ren, Y. Xu, T. Jiang, X. Cheng, *Materials Science and Engineering: C*, **2007**, 27(4), 865.
8. J.P. Garner, P.S.J. Heppell, *Burns*, **2005**, 31, 539.
9. Ş. Sert, C. Kütahyalı, S. İnan, Z. Talip, B. Çetinkaya, M. Eral, *Hydrometallurgy*, **2008**, 90, 13.
10. S. Shimoda, T. Aoba, E. Morenoe, Y. Miake, *Journal of Dental Research*, **1990**, 69, 173.
11. M.D. O'Donnell, Y. Fredholm, A. De Rouffignac, R.G. Hill, *Acta Biomaterialia*, **2008**, 4(5), 1455.
12. G. Qi, S. Zhang, K.A. Khor, S.W. Lye, X. Zeng, W. Weng, C. Liu, S.S. Venkatraman, L.L. Ma, *Applied Surface Science*, **2008**, 255, 304.
13. T. Tamm, M. Peld, *Journal of Solid State Chemistry*, **2006**, 179, 1581.
14. A. Yasukawa, K. Gotoh, H. Tanaka, K. Kandori, *Colloids and Surfaces A: Physico-chemical and Engineering Aspects*, **2012**, 393, 53.
15. Z. Feng, Y. Liao, M. Ye, *Journal of Materials Science: Materials in Medicine*, **2005**, 16, 417.
16. N.S. Resende, M. Nele, V.M.M. Salim, *Thermochimica Acta*, **2006**, 451, 16.
17. R.D. Shannon, *Acta Crystallographica*, **1976**, A32, 751.
18. D. Laurencin, N. Almora-Barrios, N.H. de Leeuw, C. Gervais, C. Bonhomme, F. Mauri, W. Chrzanowski, J.C. Knowles, R.J. Newport, A. Wong, Z. Gan, M.E. Smith, *Biomaterials*, **2011**, 32, 1826.
19. K.S. Tenhuisen, P.W. Brown, *Journal of Materials Science: Materials in Medicine*, **1994**, 5, 291.
20. A. Serret, M.V. Cabanas, M. Vallet-Regi, *Chemistry of Materials*, **2000**, 12, 3836.
21. G. Ciobanu, D. Ignat, G. Carja, C. Luca, *Environmental Engineering and Management Journal*, **2009**, 8, 1347.
22. G. Ciobanu, S. Ilisei, M. Harja, C. Luca, *Science of Advanced Materials*, **2013**, 5(8), 1090.

*Dedicated to Professor Liviu Literat
On the occasion of his 85th birthday*

MINERALOGICAL AND PHYSICAL CHARACTERISTICS OF ROMAN CERAMICS FROM HISTRIA, *BASILICA EXTRA MUROS* SECTOR, WEST-EAST SECTION (ROMANIA)

**MARCEL BENE^{a,*}, RAMONA IENCIU^b,
VIORICA RUSU-BOLINDEȚ^c**

ABSTRACT. The paper presents the results of the mineralogical and physical investigation performed on 10 fragments of Roman ceramics (oil lamps, bowls, plates) out of the 20 samples collected from the west-east Section of the *Basilica extra muros* Sector, Histria (Constanța County, Romania). Our goal was to define the physiographical features: structure, texture and firing parameters for this group of ceramic objects. The original 20 archaeological objects are represented by oil lamps (4), plates (8), bowls (6), one jug, and one terracotta – all in the form of fragments. From the technical realisation point of view, 13 objects were pressed in moulds, while the rest (7) were formed on the potter's wheel. Excepting three objects that lack decoration, the rest show various decorations: in relief, incised or printed.

The 10 ceramic fragments we have investigated are representative for the original group of 20 samples. They were investigated macroscopically, microscopically, by X-ray diffraction (XRD), and for their compaction characteristics: water adsorption, density and apparent density.

Based on their macroscopic and physical features, as well as on the mineral composition by XRD, we could separate two categories of ceramics fired at different temperature ranges: (1) 800°-900°C (6 samples), and (2) 900°-950°C (4 samples).

Keywords: *Roman ceramics, mineralogical and physical analysis, Histria Romania*

^a Babeș-Bolyai University, Faculty of Biology and Geology, Department of Geology, 1, Kogălniceanu str., RO-400084 Cluj-Napoca, Romania, * marcel.benea@ubbcluj.ro

^b S.C. Geosearch S.R.L., 103, Calea Mănăștur, RO-400663 Cluj-Napoca, Romania

^c National History Museum of Transylvania, 2, Constantin Daicoviciu str., RO-400020 Cluj-Napoca, Romania

INTRODUCTION

Ceramic production started in prehistory. The discovery that firing modelled clay turns into ceramics represented a turning point in the development of humankind. When one studies ceramics for its historical signification, understanding the fabrication technology, the firing parameters and, in a limited measure, the raw materials as provenance area are important. They can be deduced based on the ceramics structure, texture, or mineralogical composition [1, 2, 3, 4].

Histria was a Greek colony founded in Dobrogea, near the Black Sea coast (nowadays on the border of Sinoe Lake) towards the middle of the 7th century B.C.. It lasted for 13 centuries, till the 7th century A.D.. Histria is the oldest Greek colony on the western shore of the Pontus Euxinus and one of the first ones build around this sea. At the same time, it represents the first town officially attested in the present-day territory of Romania [5, 6]. Archaeological investigations in the Greek-Roman fortified town started in 1914, coordinated by Prof. V. Pârvan. Ever since, generations of researchers, historians and archaeologists have dedicated their efforts in studying the Milesian settlement. This makes Histria one of the most well-studied and known colonies around the Pontus Euxinus. Currently, 15 monographic volumes are published; besides, numerous studies illustrate various archaeological finds, as well as a wide insight into the political, economic, social and cultural life of this key Greek-Roman town (see series *Histria*¹, volumes I-XV, of which *Histria V* is dedicated to the ceramic workshops).

The paper presents the result of the mineralogical and physical investigation on 10 Roman ceramic fragments (oil lamps, bowls and plates) carefully selected from the total of 20 samples collected from the west-east section, *Basilica extra muros* Sector from Histria. The ceramic objects illustrate a wide range of usages, from luxury objects to the daily use ones, including lightning purposes. They were unearthed during the 2002-2004 archaeological campaign (for the archaeological overall results, see [6, 7, 8, 9]).

Our goal was to establish the ceramics physiographical characteristics: structure, texture and firing parameters. We also included a brief presentation of the geology of Central and South Dobrogea, as background information on the potential local sources of clay raw materials. All the original 20 samples have been macroscopically characterized; based on these features we have selected the 10 fragments for further investigation.

¹ http://www.cimec.ro/Arheologie/web-histria/6bibliografie/bibliografie_eng.htm

RESULTS AND DISCUSSION

Macroscopic characterisation

The categories of objects identified in the archaeological site are oil lamps (4), plates (8), bowls (6), one jug and one terracotta figurine; all are present as fragments. From the technical realisation point of view, 13 objects were pressed in moulds, while the rest (7) were formed on the potter's wheel. Excepting three objects that lack decoration, the rest show various decorations: in relief, incised, printed or just coloured stripes on the outer side.

In general, the ceramic paste has a homogeneous colour varying from various red hues to reddish brown [10], suggesting oxidizing firing regime. Only samples 13 and 14 (Figs. 1 and 3) show areas with distinctive colorations: within the light red paste, there are different coloured layers towards the inner, and respectively the outer surfaces. The matrix is also relatively homogenous, while no clast aggregates were noticed. The matrix (structural/grain-size) fineness varies from fine to semifine. The clasts are angular to rounded and show various sizes (up to 2 mm). Macroscopically, we noticed quartz grain and muscovite lamellae as mineral components. Porosity varies in limited range; both mainly elongated primary pores lined parallel to the surfaces, and secondary pores with circular or irregular outlines generate it. The pore sizes range between 0.5 x 1.5 and 1.5 x 2.0 mm.

The archaeological information and the macroscopic characteristics of the samples selected for further study among the original set are presented in Tables 1 and 2.

Table 1. Archaeological information on the studied ceramic fragments

Sample no.	Inventory no. / Archaeological source	Object type / Observations
1	52/2004 S I, square 4, -2.20-2.30 m depth, infilling of oven no. 5	Oil lamp; imported product
2	35/2003 S I, square 8, -1.10 m depth, southern profile, at the level of the phase II B floor	Oil lamp; local product (?)
4	31/2004 S I, square 1, -1.70 m depth, in the area of oven no. 1	Oil lamp; imported product
5	6/2003 S I, square 3, -1.64 m depth, underneath the wall foundation in room A (phase II B)	<i>terra sigillata</i> plate; imported product
11	9/2003 S I, square 5, -0.73 m depth, in the filling layer between phases IV A and II B	Bowl Drag. 24; <i>Eastern sigillata C</i> ; imported product
12	53/2003 S I, square 9, -1.45 m depth, from the demolition layer of the room with mortar-bound wall and wood wall, phase I C	Plate; local product

Sample no.	Inventory no. / Archaeological source	Object type / Observations
13	14/2002 S I, square 5, -1.60-1.70 m depth, at the level of the smith workshop	Bowl; local product; traces of secondary firing on the outer surface
14	40/2003 S I, square 7-8, -1.46 m depth, from the yellow loam floor, phase II A	Bowl; local product, possibly a refuse; <i>graffiti</i> in Greek on the bowl's body surface
16	79/2004 S I, square 5, -2.60 m depth, from the infilling of oven no. 8	Bowl; local product (?)
20	8/2003 S I, square 4, -1.50-1.70 m depth, from the ditch underneath the organisational level of phase IV A	<i>terra sigillata</i> plate; local product (?)

Table 2. Macroscopic characteristics of the studied ceramic fragments

Sample no.	Paste (quality, Munsell colour, components)	Engobe	Decoration
1	- fine, reddish-brown (2,5YR, 7/8), with iron oxides and fine muscovite lamellae	Red shiny engobe, with golden metallic lustre at the outside	The lid shows a relief decoration with vine leaf and tendril
2	- fine, light red (10R, 7/8), with fine fragments of quartz and muscovite lamellae	Red engobe at the outside	The lid is shell-like with relief leaves on the lateral side
4	- fine, light red (10R, 6/8), with fine fragments of quartz and muscovite lamellae	Red shiny engobe of extremely high quality at the outside	Half-oval printed decoration on the side, incised decoration in the central area of the lid
5	- fine, reddish brown (2,5YR, 7/6), with fragments of quartz and muscovite	Red shiny engobe with metallic lustre, of extremely high quality	Incised decoration on the side, in relief on the handle (of vegetal inspiration?); three flutings in relief marking the transition from the plate's rim to the body
11	- fine, light red (10R, 4/8); with fine muscovite lamellae	Dark red engobe of extremely high quality	Incised decoration
12	- fine, light red (10R, 4/8), with fine muscovite lamellae	Brown reddish engobe on $\frac{3}{4}$ of the outer surface; inside, only on the rim	Not decorated
13	- semifine, light red (10R, 4/8), with grey stripe in the middle (10R, 6/1, reddish grey) as a	-	Decoration represented by flutes in the upper part of the body

Sample no.	Paste (quality, Munsell colour, components)	Engobe	Decoration
	result of incomplete firing; quartz grains of variable sizes		
14	- semifine, light red (10R, 6/8), with lighter stripe at the exterior (7.5YR, 8/4, pink); with quartz fragments	Various hues of brown reddish engobe at the outer surface	Not decorated
16	- fine, reddish brown (2,5YR, 4/4), with quartz and muscovite fragments	Dark brown engobe, shiny on both sides	Fine flutes below the rim and above the maximum diameter
20	- fine, reddish brown (2,5YR, 7/8), with fine fragments of quartz	Engobe of the same colour as the paste	Decoration in relief: a. hunting scene; b. animals (goats) in motion; c. male mask, left side profile, with frontal caduceus



Figure 1. Sample 14 - bowl



Figure 2. Sample 20a – plate



Figure 3. Sample 13 - bowl



Figure 4. Sample 2 - oil lamp



Figure 5. Sample 1 - oil lamp



Figure 6. Sample 12 – plate

Optical microscopy

We have used transmitted light optical microscopy for completing the information on the mineral components of the matrix and the flux, for identifying the thermal transformations thus defining the firing temperature, and for assessing the fineness, *i.e.*, the fabric of the studied ceramics.

The matrix consists of thermally affected clay minerals and, to a lesser extent, of quartz, feldspars and micas. In parallel polarized light, one nicol, it is light brown-yellowish gradually passing into reddish brown, dark brown or even black (sample 13 – Figure 9) as a function of increasing firing temperatures. Similarly, under crossed nicols, the matrix displays birefringence with intensities decreasing with increase of firing temperature. In addition, we noticed transition areas from the inner to the outer surface of the ceramic fragment marked by darker coloration (sample 12 - Figure 12).

Grain size measurements on thin sections allowed us to separate two categories of ceramics: semifine (lutitic-siltic-arenitic type) and fine (lutitic-siltic type) (lutite < 0.004 mm, silt = 0.004-0.063 mm; arenite = 0.063-2 mm) [11, 12, 13]. Based on the ratio of crystalline components vs. amorphous phases in the ceramic matrix, we separated three fabric types: microcrystalline (samples 2, 4, 5, 14, and 20), microcrystalline-amorphous (samples 1, 11, 12, and 16) and amorphous-microcrystalline to amorphous, in only one sample (13).

The primary elongated pores are dominant (2–3 %, in samples 1, and 13) and do not exceed 0.55 x 1.50 mm. Reinforcing the preferential orientation of the mica lamellae, the orientation of the primary pores ensures a flow texture that is obvious in most of the ceramic samples.

The crystalloclasts reflect the mineralogical and petrographical diversity of the raw and the flux materials. Quartz crystalloclasts are ubiquitous (up to 3–5 %, maximum sizes of 0.35 x 0.70 mm); they are subangular to rounded, and sometimes display undulatory extinction and a variable degree of inner fissuring due to firing. Twinned plagioclase feldspars are present in subordinate amounts; they are sometimes sericitized and kaolinitized, with maximum sizes

of 0.10 x 0.15 mm. Fine mica (muscovite and rarer biotite) lamellae, as a rule with relatively high birefringence pointing to firing temperatures below 800 - 850°C, were also noticed. Besides, iron oxi-hydroxides aggregates (mainly hematite grains of up to 0.03 x 0.08 mm), spinel fragments (up to 0.1 x 0.15 mm) and in sample 13 small zircon grains (0.08 x 0.10 mm) are present. The identification of calcite films (up to 0.17 x 0.30 mm in size) in sample 12 suggests relatively low firing temperatures (~ 800°C).

Among the lithoclasts, only quartzite fragments were identified, with maximum sizes of 0.80 x 1.05 mm representing not more than 2 % of the material (samples 13 and 14). In some cases, we could notice undulatory extinction of quartz grains.

Ceramoclasts vary from zero (or sizes below the microscopic range) in samples 1, 5, 11, 13, and 16 to up to 3 % of the mass in the rest of them, with maximum sizes of 0.87 x 1.87 mm (sample 14).

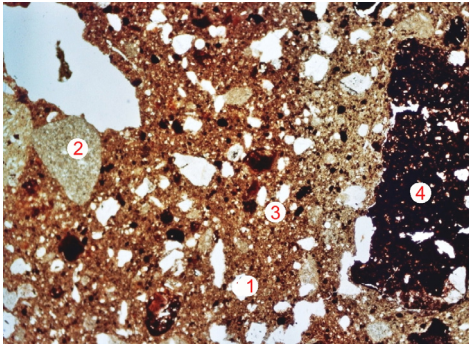


Figure 7. Sample 14 – semifine ceramics with microcrystalline matrix, with large pores; 1 quartz, 2 quartzite, 3 micas, 4 ceramoclast, 5 feldspar; 1N, 35x

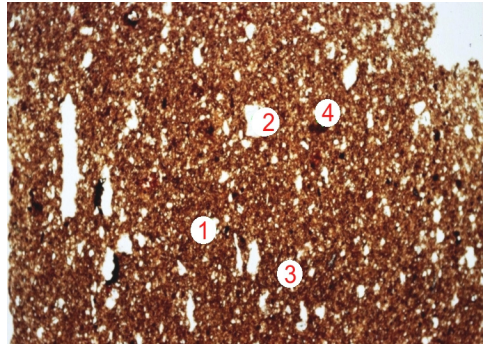


Figure 8. Sample 20 – fine ceramics with microcrystalline matrix, and elongated pores oriented parallel to the object's surface; 1 quartz, 2 quartzite, 3 micas, 4 ceramoclast; 1N, 35x

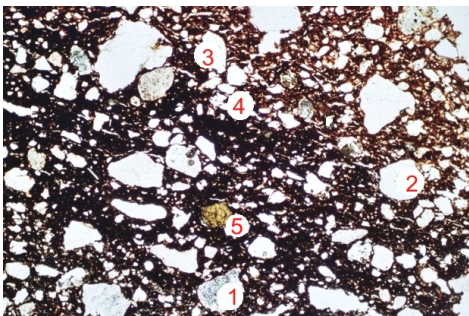


Figure 9. Sample 13 – semifine ceramics with amorphous-microcrystalline to amorphous matrix, and elongated pores; 1 quartzite, 2 quartz, 3 feldspar, sericitized and kaolinized, 4 micas, 5 spinel; 1N, 35x

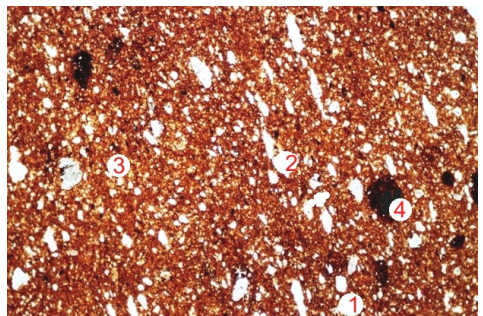


Figure 10. Sample 2 – fine ceramics with microcrystalline matrix, and elongated pores; 1 quartz, 2 quartzite, 3 micas, 4 ceramoclast; 1N, 35x

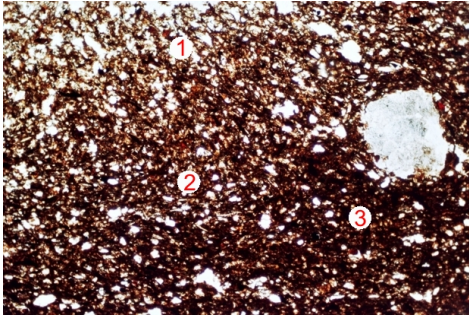


Figure 11. Sample 1 – fine ceramics with microcrystalline-amorphous matrix, and elongated pores oriented parallel to the object's surface; 1 quartz, 2 micas, 3 iron oxy-hydroxides aggregates; 1N, 35x

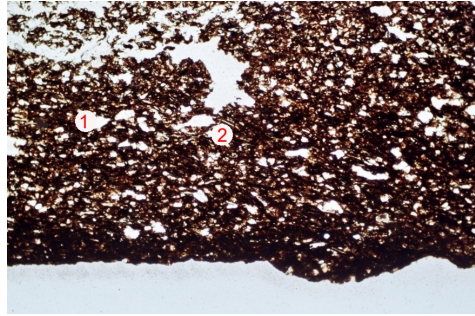


Figure 12. Sample 12 – fine ceramics with microcrystalline-amorphous matrix, and numerous elongated pores oriented parallel to the object's surface; 1 quartz, 2 micas; 1N, 35x

X-ray diffraction

The XRD patterns evidence a relatively simple mineralogical composition (Figs. 13 and 14). The main minerals, identified in all the studied samples, are quartz and Ca-Na feldspars (albite–anorthite). Clay minerals have been

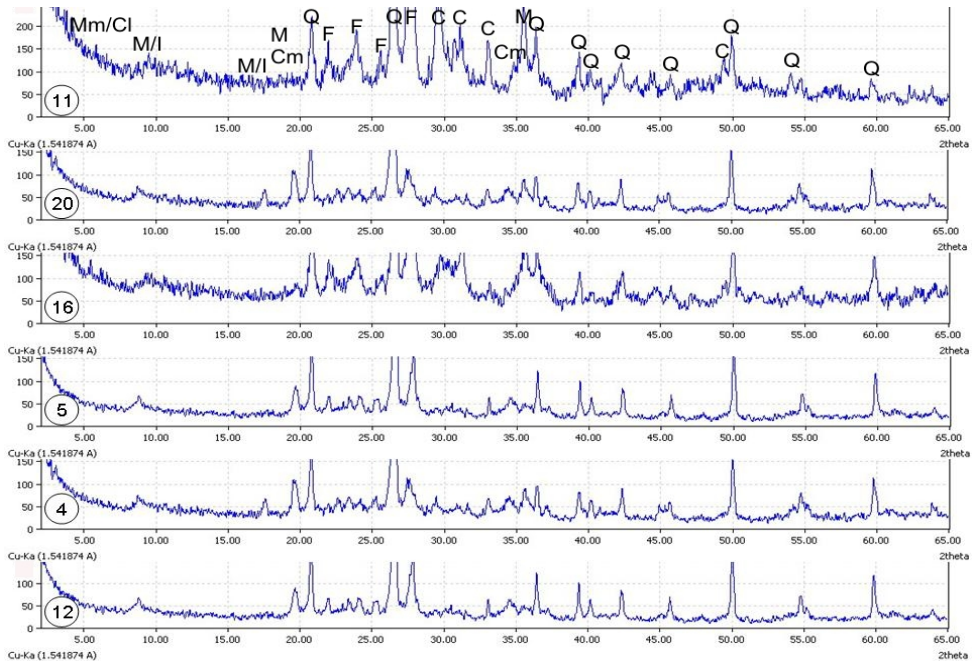


Figure 13. XRD patterns of the low firing temperature group of studied ceramic fragments; Q – quartz, F – feldspars (Ca-Na), C – carbonates (calcite), M/I – muscovite/illite, M – micas, Mm/Cl – montmorillonite/chlorite, Cm – clay minerals; firing temperatures between 800–900°C; sample no. is indicated in the lower left corner.

thermally affected; they are illustrated only by the diffraction lines at 4.5 Å and 2.6 Å. Exceptionally, samples 1, 2, 13 and 14 lack the lines corresponding to micas and clay minerals, but show the XRD contribution of iron oxihydroxides (hematite/goethite). Carbonates (calcite) and micas (muscovite, muscovite / illite) have been identified in samples 4, 5, 11, 12, 16 and 20. We have assigned the 14 Å lines in sample 16 to montmorillonite–chlorite mixed-layers.

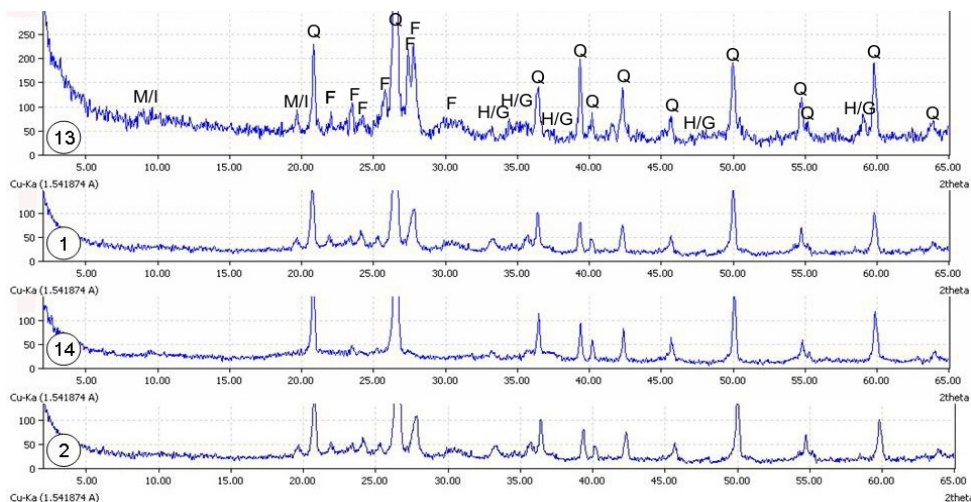


Figure 14. XRD patterns of the high firing temperature group of studied ceramic fragments; Q – quartz, F – feldspars (Ca-Na), H/G – hematite/goethite, M/I – muscovite/illite; firing temperatures between 900–950°C; sample no. is indicated in the lower left corner.

Physical characteristics

From every ceramic sample under study, we have collected three fragments for physical characterization. The fragments were preserved in vacuum for 30 min, then dried in an oven and weighted. Then, they were placed in water for 2 hours and weighted afterwards again.

Table 3 summarizes the compaction characteristics of the ceramic samples, i.e., water adsorption, apparent density and porosity. The values vary to a little extent in the studied material, except for sample 1 that shows maximum values for water adsorption and porosity, and sample 2 that shows the minimum water adsorption value.

Table 3. Compaction characteristics of the studied ceramic samples

Sample no.	Water adsorption [%]	Apparent density [g/cm ³]	Apparent porosity [%]
1	22.944	1.605	36.825
2	9.959	2.019	20.104
4	18.363	1.700	31.217

Sample no.	Water adsorption [%]	Apparent density [g/cm ³]	Apparent porosity [%]
5	19.200	1.685	32.355
11	20.906	1.699	35.513
12	10.201	2.029	20.688
13	10.827	1.907	20.647
14	14.358	1.901	27.289
16	18.005	1.769	31.842
20	18.504	1.736	32.121

Based on the range of data obtained, we could group the samples into three groups:

Samples 4, 5, 11, 16, and 20 – with water adsorption values between 18.005 % and 20.906 %

Samples 2, 12, 13, and 14 (water adsorption between 9.959 % and 14.358 %)

Sample 1 (water absorption is 22.944 %).

The explanation for these distinctive behaviours resides in the macroscopic and microscopic features. Thus, sample 1 showing the higher water adsorption has a heterogeneous colouring pattern with darker colour towards the outer surface of the ceramic body, and numerous pores oriented parallel to it.

CONCLUSIONS

Among the 20 studied archaeological objects, there were 4 oil lamps, 8 plates, 6 bowls, one jug and a terracotta figurine, all present as fragments. 13 objects were pressed into moulds, while 7 were formed on the potter's wheel. Except for three non-decorated objects, the rest show various types of decorations (in relief, incised, printed or with stripes of various colours on the outer surface).

Macroscopically, the ceramic fragments are homogeneously coloured, slightly varying from red to reddish brown, involving oxidizing firing regimes. Only samples 13 and 14 show distinctively coloured areas, as light red paste with layers of different colours towards both inner and outer surfaces.

The fineness (by structure/grain size) of the matrix varies from fine to semifine. The clasts are angular to rounded or irregular; their maximum sizes are below 2 mm. At macroscopic scale, we could identify only quartz grains and muscovite lamella as mineral components.

The microscopic investigation evidenced the presence of a matrix consisting of thermally affected clay minerals and crystalloclasts: quartz, plagioclase feldspars, micas, magnetite, hematite, calcite, zircon, and spinel. Quartz crystals are mainly angular; they sometimes show undulatory extinction. Feldspars are often sericitized, kaolinized and polysynthetically twinned.

Carbonate films noticed in thin sections were also confirmed by the XRD patterns of samples 4, 5, 11, 12, 16, and 20. Lithoclasts are exclusively represented by quartzites, while ceramoclasts are present in almost all the samples. The grain size measurements performed under the microscope allowed the separation of two categories within our ceramic samples: fine (lutitic-siltic) and semifine (lutitic-siltic-arenitic). Based on the ratio between the crystalline components vs. the amorphous phases, we have separated three fabric types: microcrystalline, microcrystalline-amorphous and, in only one sample (13), amorphous-microcrystalline to amorphous.

A much darker matrix in some areas of the ceramic body reflects relatively higher local temperatures in the oven, leading to the transformation of the iron oxi-hydroxides.

Porosity varies to limited extent, between 1 to 5 %. It is represented by mainly elongated primary pores oriented parallel to the surface of the ceramic body, and by rounded or irregular secondary pores. Compaction, as evidenced by water adsorption values, ranges from 9.59 % and 27.65 %.

The mineralogical transformations at microscopic scale, such as fissures forming in the quartz grains, presence of iron oxi-hydroxides, matrix isotropization, presence of secondary pores, variable amounts of micas, and presence/absence of carbonates have allowed us to estimate the firing temperatures for the studied ceramics.

Thus, based on the microscopic observations and the XRD mineralogical composition, we could group our samples into two categories with distinctive firing temperatures: (1) 800°-900°C for samples 4, 5, 11, 12, 16, and 20; (2) 900°-950°C for samples 1, 2, 13, and 14.

Concerning the local raw materials, clays are frequent in Dobrogea. The Central Dobrogean Massif is a distinctive compartment tectonically lifted between the Capidavia-Ovidiu and Peceneaga-Camena faults. Its basement consists of a slightly metamorphosed sedimentary series, known as „the green schists series”, and a mezometamorphic crystalline schists series [14, 15]. Locally, a slightly folded unconformable sedimentary cover consisting of Jurassic, Cretaceous and Tertiary epicontinental deposits (limestones, dolomites, conglomerates, sandstones, glauconitic sands, clays, and marls) overlies the basement. Clay occurrences possible use in ceramic industry outcrop in the neighbourhoods of Histria, Saele, Cogeaalac, and Sinoe localities.

In Central and South Dobrogea, thick deposits of loam of red-brownish clay formed on the top of the pre-Quaternary deposits. In the base of this succession, red and red-yellowish clays are known, frequently containing calcareous and Fe-Mn concretions, gypsum crystals and fragments of pre-Dobrogea rocks [16]. Complex studies on obtaining industrial ceramics were performed also by using the clays from Cobadin quarry (Constanța County) [17].

EXPERIMENTAL SECTION

- the macroscopic investigation was performed by using a Nikon SMZ 645 binocular.

- the XRD patterns were obtained with a Shimadzu XRD6000 (Bragg-Brentano geometry) diffractometer, with Cu anticathode (Cu-K_α, λ_{Cu} = 1.541874 Å), 40kV, 30 mA, in the 2°–65° 2Theta interval, Δ2θ = 0.02°.

- the microscopic study was performed on thin sections (< 25 μm) in polarized light by using a Nikon Eclipse E200 microscope. The microphotographs were taken with a NIKON FDX-35 camera.

- the physical characteristics (apparent density, water adsorption, apparent porosity) were determined based on the Law of Archimedes, by saturation in water and boiling of the ceramic fragments.

ACKNOWLEDGEMENTS

The study was supported by PN-II-ID-PCE-2011-3-0881 project funds (UEFISCDI-CNCS/Romanian Ministry of Education). Many thanks are due to Dr. Dana Pop for the English translation.

REFERENCES

1. W. Noll, "Alte Keramiken und ihre Pigmente. Studien zu Material und Technologie", E. Schweitzerbart'sche Verlagsbuchhandlung, Stuttgart, **1991**, 334 p.
2. V. Rusu-Bolindeț, "Ceramica romană de la Napoca. Contribuții la studiul ceramicii din Dacia romană," Bibliotheca Musei Napocensis, XXV, Ed. Mega, Cluj-Napoca, **2007**, 681 p.
3. M. Benea, M. Gorea, N. Har, . *Rom. J. Materials*, **2007**, 37(3), 219.
4. M. Gorea, R. Creț, F. Kristaly, *Studia UBB Chemia*, **2011**, LVI (4), 97.
5. Al. Suceveanu, Zur Entstehung der regio Histriae, *Dacoromania. Jahrbuch für ostliche Latinität*, **1986**, 113.
6. V. Rusu-Bolindeț, Al. Bădescu, *Studii și cercetări de istorie veche și arheologie*, (2003-2005) **2006**, 54-56, 103.
7. Al. Suceveanu, K. von der Lohe, V. Rusu-Bolindeț, Al. Bădescu, Istria, Sector: *Basilica extra muros*, Cronica cercetărilor arheologice din România. Campania 2001, București, **2002**, 168-170.
8. Al. Suceveanu, V. Rusu-Bolindeț, Al. Bădescu, Istria, Sector: *Basilica extra muros*, Cronica cercetărilor arheologice din România. Campania 2002, București, **2003**, 163-165.
9. Al. Suceveanu, V. Rusu-Bolindeț, Al. Bădescu, Istria, Sector: *Basilica extra muros*, Cronica cercetărilor arheologice din România. Campania 2003, București, **2004**, 156.

10. Munsell Color Chart, http://irtel.uni-mannheim.de/colsys/Munsell_A0.pdf
11. C. Ionescu, L. Ghergari, Mic glosar de termeni geologici utilizați în studiul ceramicii arheologice, *Cercetări arheologice*, **2006**, *XIII*, 451-460.
12. C. Ionescu, L. Ghergari, O. Țentea, *Cercetări arheologice*, **2006**, *XIII*, 413-436.
13. C. Ionescu, L. Ghergari, Caracteristici mineralogice și petrografice ale ceramicii romane din Napoca. In: V. Rusu-Bolindeț, "Ceramica romană de la Napoca. Contribuții la studiul ceramicii din Dacia romană," Bibliotheca Musei Napocensis, XXV, Editura Mega, Cluj-Napoca, **2007**, 434-462.
14. V. Mutihac, M.I. Stratulat, R.M. Fechet, "Geologia României", Ed. Did. Și Ped., București, **2007**, 249 p.
15. C.P. Răcățianu, R. Koch, P. Brandlein, M. Benea, P.I. Răcățianu, "Romanian natural building stones: geology, rock types, quarries, companies and products. Vol. II: Dobrogea and Transylvania Regions", Erlangen, Friedrich-Alexander-Universität; ARGONAUT, Cluj-Napoca, **2009**, 228 p.
16. A. Conea, "Formațiuni cuaternare în Dobrogea: loessuri și paleosoluri", Ed. Academiei RSR, București, **1970**, 234 p.
17. V. Burghilea, A.I. Ignat, A. Cociș, *Rom. J. Materials*, **2007**, 37 (4), 307

*Dedicated to Professor Liviu Literat
On the occasion of his 85th birthday*

SCIENTIFIC INVESTIGATION OF PIGMENTS EMPLOYED FOR „CRUCIFIXION” PROCESSIONAL FLAG PAINTING FROM THE ETHNOGRAPHIC MUSEUM OF TRANSYLVANIA HERITAGE

**CONSTANTIN MĂRUȚOIU^a, LAURA TROȘAN^b,
VASILICA-DANIELA TOADER^b, ZAHARIE MOLDOVAN^c,
ALEXANDRU I. TURZA^c, CLAUDIU TANASELIA^d AND IOAN BRATU^{c,*}**

ABSTRACT. The processional flag is a cult object belonging to the churches. Nowadays, as well as it was in the past, the flag is carried by people, preceding the religious processions; it is used on the occasion of bringing icons and holy relics from one place to another; the flag is also used at different ceremonial moments and at funerals. The Ethnographic Museum of Transylvania owns 10 processional flags in various conservation stages. Pigment samples were taken and we present the result of the samples expertise achieved by using the FTIR spectrometry, X-Ray diffraction, X-ray fluorescence and gas chromatography-mass spectrometry for the processional flag with the inventory number 8254. The results will be used to recommend several correct conservation and preservation methods.

Keywords: *processional flag, painting materials, XRF, XRD, FTIR, GC-MS*

INTRODUCTION

Inside the Romanian space the flag had different hypostases: in military and political life, as well as the state flag and banner for the fight; in traditional manifestations, as the wedding, and symbol of the groups of male slime; in religious life that processional flag [1].

^a Babeș-Bolyai University, Faculty of Orthodox Theology, 18 Avram Iancu Sq., Cluj-Napoca, Romania

^b Ethnographic Museum of Transylvania, 21 Memorandumului Str., 400114, Cluj-Napoca, Romania

^c National Institute for R&D of Isotopic and Molecular Technologies, 65-103 Donath Str., 400293, Cluj-Napoca, Romania

^d INCDO-INOE 2000 Research Institute for Analytical Instrumentation, 67 Donath Str., 400293 Cluj-Napoca, Romania. * Corresponding author: ibratu@itim-cj.ro

The processional flag is an object of worship kept in churches and used in religious processions, solemn moments and at funeral. His successor Byzantine battle flags, wearing on him the crucifix or representations of religious themes, is a symbol of the fight against sin, against the known and unknown enemies and also a triumph of Christianity [2].

The processional flags are encountered since the IVth century and after Eusebiu Cezarea description's it had the following form: a long spearhead with gold-plated trims intersect with a stick of wood, forming a cross; in the top was placed a crown and trim of gold and precious stones. Horizontal arm of the cross was hanging a flag or a square red canvas, decorated with precious stones and sewn with gold yarn [3].

The processional church, as an object of worship, is a result of association of Roman Legions symbols with Christian icons [1].

At present, processional flag is made from a piece of canvas approximately 1(one) meter long and 60 cm wide or larger dimensions, fixed on a wooden support, an T form stick, which had a cross on the top. On this canvas are painted both sides icons representing: Saints, Christ, Virgin Mary, the Saint protector of the Church and religious themes.

As to the existence of processional flags in the Romanian world, with its poor little churches, it seems they were missing from the majority of Orthodox communities up to the middle of the 18-th century. We could encounter it only in cathedrals and big and wealthy monasteries.

The conservation of processional flags has to be made taking into account the diversity of materials of which they are composed and their functions well defined. Without an adequate scientific method, based on the principles and rules for conservation [4], we will not be able to stop processes of degradation and parts with great historic value will disappear.

Processional flags may be made of two woven fabrics removable, painted separately, or from a single fabric painted on both sides. It is important to study both structure of fabrics from which it was carried out the flag, as well as the technical execution, because during the years the painted fabric had different reactions to the environmental factor, physical-chemical and mechanical.

The support that has to be painted can be made of cotton, line, natural silk, wool or synthetic fabrics. It is necessary to determine the exact material of support because each of this materials had his own methods and rules of conservation.

The primer, next layer, made from binder and filler material is thin, transparent and irregular. Primer composition helps us in the choice of methods of restoration. Analysis of the primer and its components is usually reduced to determining the chemical composition and microscopic cross-sectional research. In the primer, animal or plant glue, plaster and powdered chalk can be found.

Color layer is homogeneous and thin, in terms of composition, being made up of mineral origin or pigments and organic binder. A layer is made up of two or more color grains. The glue is organic and can be of vegetable or animal origin. The binder is made from egg yolk and egg white, sometimes mixed with resins in tempera paintings or vegetable glues and resins in oil paintings.

The color painted layer is the most important part of the processional flag because it is determining the historical-documentary and artistic value. That is why most of the physical, chemical and physical-chemical research studies with priority the color layer, in order to determine its composition and physical properties.

The protective layer, lacquer, applied for protecting the painting, is prepared in the past from natural resins, which until the late 16th century, were blended with vegetable glues. Starting with 17th century it was used the topal lacquer and in the 19th century, dammar lacquer [5].

Ethnographic Museum of Transylvania, Cluj-Napoca owns 10 processional flags in different conservation states. Within the project "Modern Methods of Investigation, Authentication and Storage of Icons of the Ethnographic Museum of Transylvania's heritage", developed in collaboration with the Faculty of Orthodox Theology and National Institute for R&D of Isotopic and Molecular Technologies, Cluj-Napoca, different methods have been used for separation, identification and analysis of pigments, support layer and primer layer of processional flags.

The color layer samples for analysis of pigments processional flag inventory no.8254 were taken in the Restoration and Conservation Laboratory of the Ethnographic Museum of Transylvania, in accordance with the rules of restoration and conservation [6].

The investigation of patrimony objects can be performed with mechanical, thermal, optical, spectroscopic, magnetic, X-ray (diffraction and fluorescence) methods, etc. One can identify the metal, mineral, pigments, dyes [7], binders, nature [8-12], etc. With modern methods are clarified the structure of layers and materials composition of the ethnographic pieces, thus discovering the way in which they were made, the initial mode of preparation and technologies used for obtaining this objects. The spectroscopic methods can be useful in identifying substances or their mixtures, purity degree and the impurity nature. The microscopic methods allow in several cases the determination of the nature and the origin of the materials. The thermal methods can characterize the durability, fragility, fluidity and plasticity of materials [13]. These methods allow the identification and the study of various ethnographic materials.



Figure 1a. Front 1 of Processional flag inventory no. 8254



Figure 1b. Front 2 one sequence of Processional flag inventory no. 8254
(St. Arch. Michael only)

The processional flag painted on both sides was analyzed, inventory no. 8254 (Figs. 1a and 1b). Front 1 painting: The Crucifixion with the Evangelists Mark and Matthew on the sides, and below with five Prophets, two partially present and one missing. Front 2 (verso) painting: St. Arch. Michael with Evangelists John and Luke on the sides and below five Prophets only four visible. The processional flag was purchased by Ethnographic Museum of Transylvania in 1939 from the Turda area. The object has a width in the upper part of 94 cm and a maximum length of 108 cm.

The investigation process of a processional flag, must be carried out by analyzing the multilayers structure; the fabric support, primer, painted layer and protective layer being the main elements and the paper aim.

RESULTS AND DISCUSSION

FTIR spectroscopy

FTIR spectra recorded in different spectral domains for all collected samples are presented in Figs. 3-5.

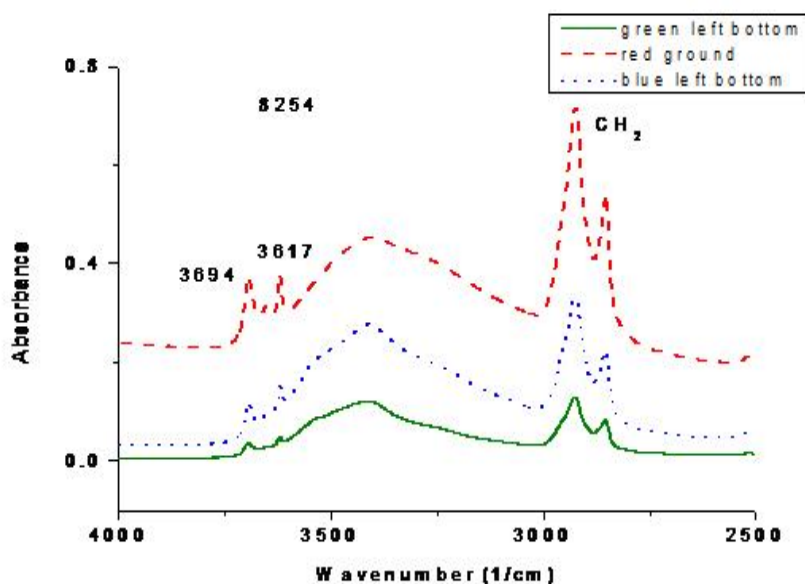


Figure 3. FTIR spectra for samples 1-3 of painted flag on both sides (8254), 4000–2500 cm^{-1} spectral domain. Legend: 1-middle; 2-top; 3-bottom

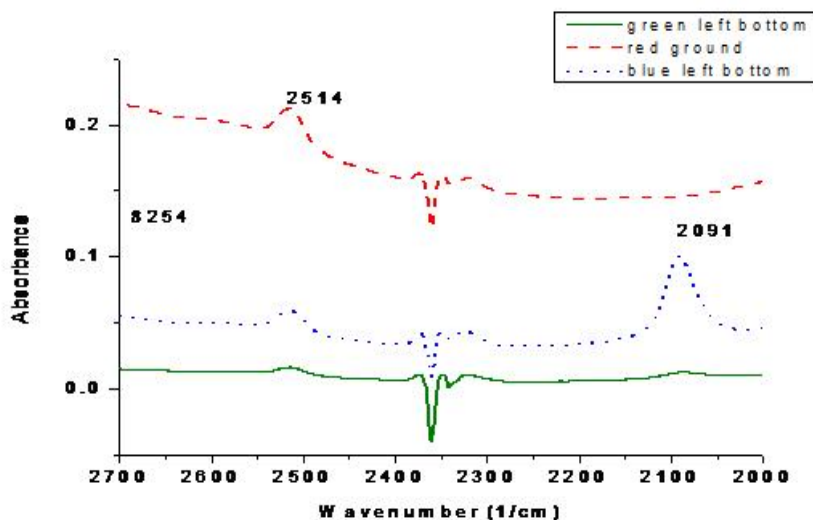


Figure 4. FTIR spectra for samples 1-3 of painted flag on both sides (8254), 2700-2000 cm^{-1} spectral domain. Legend: 1-middle; 2-top; 3-bottom

Identified compounds: derivatives containing SH group (2514 cm^{-1}), CN group (2091 cm^{-1}), probably Prussian blue - $\text{Fe}_4[\text{Fe}(\text{CN})_6]_3$.

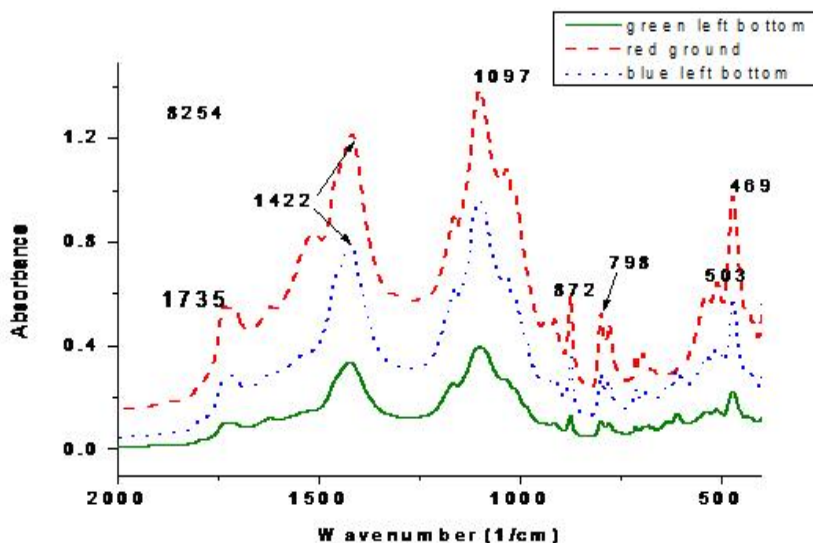


Figure 5. FTIR spectra for samples 1-3 of painted flag on both sides (8254), 2000-400 cm^{-1} spectral domain. Legend: 1-middle; 2-top; 3-bottom

Identified compounds [14], see Figs. 3-5: free OH groups (3697 and 3617 cm^{-1} , probably gypsum bands $\text{CaSO}_4 \cdot 2\text{H}_2\text{O}$), CH_2 groups (aliphatic compounds), esters (1735 cm^{-1} , of line oil), PbCO_3 absorbtions at ~ 1422 and 870 cm^{-1} , 1097 cm^{-1} (BaSO_4 and possible some contribution of Si-O-Si band), SiO_2 (quartz- 798 cm^{-1}), Pb_3O_4 (469 and 530 cm^{-1}). In line oil a sicative agent (lead minium), litharge or ceruse is added. Lead minium (Pb_3O_4) was found in all coloured samples. During the time, derivatives that contain SH group appear (absorption at $\sim 2514\text{ cm}^{-1}$). For green painting material malachite ($\text{CaSO}_4 \cdot 2\text{H}_2\text{O}$, 1097 cm^{-1}) was proposed, containing white pigment (carbonate) as diluant, also.

X-ray fluorescence

Red painting material: Hg (HgS) and Pb also (probably red lead), as major cations employed also for the ground of the processional flag. For the book contour one can identify Hg as major cation (cinnabar).

Blue painting material: major cations Cu (azurite, $2\text{CuCO}_3 \cdot \text{Cu}(\text{OH})_2$) and Fe (Prussian blue), mixed in order to obtain a dark blue touches.

For the greenish dress, Cu was identified as major element: malachite can be the green pigment.

Lead was identified in all samples and in oil also as lead minium employed as sicative agent.

The halo contains a lot of As, so one can speak about auripigment (As_2S_3). The ground could contain a mixture of gypsum, barite and Ca carbonate for color "dilution".

X-ray diffraction

The identification of pigments was as follows:

- for red pigment, see Fig.6, HgS (cinnabar) was the major component but PbO , PbO_2 and Pb_3O_4 were identified also;
- as concerned blue pigment, azurite and Prussian blue were identified, see Fig. 7.

The crystallinity of the processional flag texture was: 31.4% , 34% for blue painted processional flag and 43.5% for red-painted processional flag. The higher crystallinity for the processional flag painted texture can be due to the crystalline status of the employed pigments.

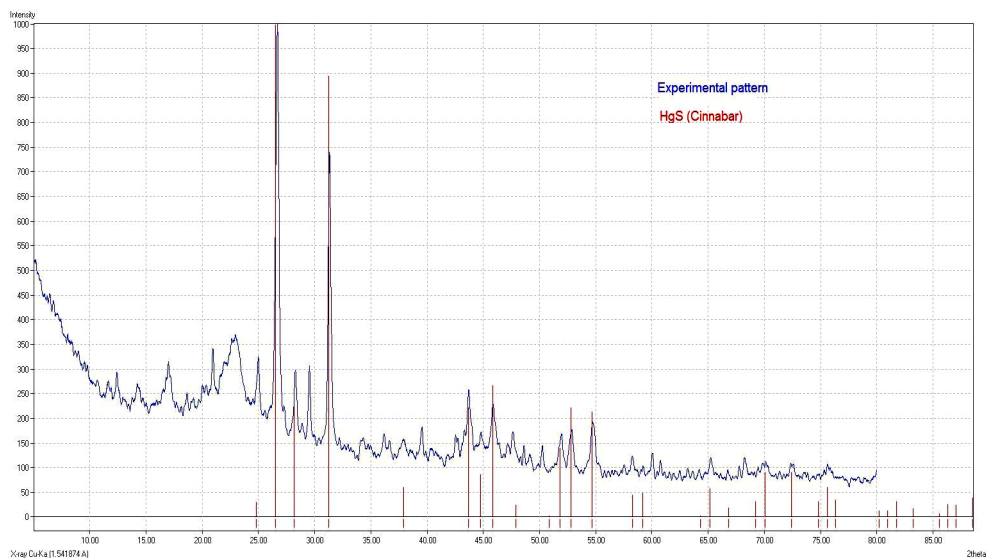


Figure 6. XRD pattern of red painting material as compared to HgS pattern from PDF-2 database.

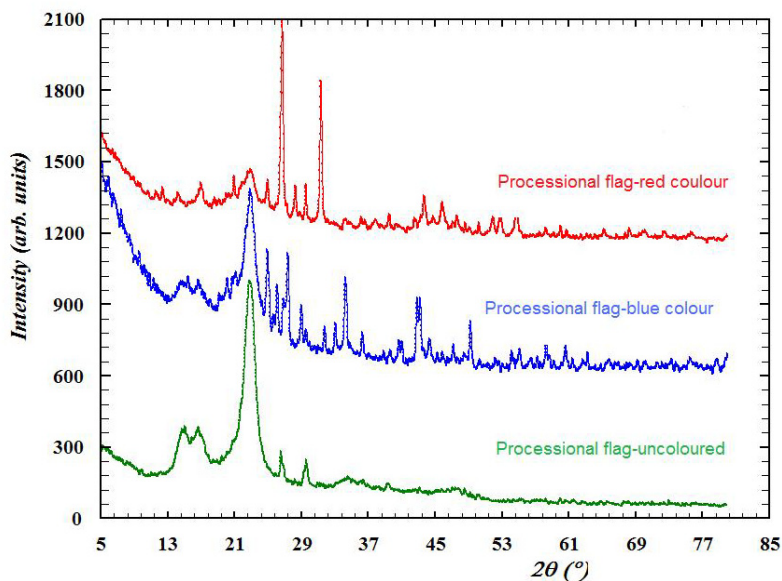


Figure 7. XRD patterns of Processional flag support and of painting materials.

Mass spectrometry*Red pigment*

The analysis by mass spectrometry of the collected sample near red pigment zone indicates the presence of vegetal oil (taking into account the compounds ratio, one establish the presence of line oil). For temperatures higher than 250 °C are identified the following molecular ions corresponding to peaks at m/z 64, 101 and 202 that are specific to red pigment HgS (cinnaber or vermilion). These peaks are due of to S_2^+ , Hg^{++} and Hg^+ , respectively being produced from HgS by electron impact.

Blue pigment

The ions attributed to fatty acids having the carbon atom number between 9 and 18 were identified. The intensities ratio of palmitic and stearic acids confirmed the use of line oil as painting material. The maximal intensity is due to palmitic acid followed by stearic one, their sum represents 60 % relative to all acids. There were also identified the molecular ions corresponding to $M = 172, 186, 200, 214, 228, 242, 256, 270$ and 284 that are molecular ions of C_{10} - C_{16} and C_{18} acids. One can mention that the peaks corresponding to fatty acids with even molecular masses are more abundant relative to those with odd molecular masses. The used pigment looks to be Prussian blue, confirmed also by FTIR band corresponding to CN group belonging to $[Fe(CN)_6]_3Fe_4$ compound.

Green pigment

In the case of sample collected from the green pigment zone the ions similar to those of blue pigment were identified. One can therefore confirm the use of line oil and the pigment was a combination of blue and yellow pigments, the last one being inorganic, impossible to be detected by mass spectrometry with electronic impact.

CONCLUSIONS

As a result of the previous analyses, one can establish that the processional flag was painted with pigments based on line oil and the employed pigments were Prussian blue, red Cinnaber or Vermilion, green malachite, red lead and other lead oxides. These results will help in conservation and a future restoration of this processional flag.

EXPERIMENTAL SECTION

The following samples, see Figures 8a and 8b, were collected from the processional flag: red pigment (background verso), green pigment (left down verso) and blue pigment (left down, front). The quantities taken were of the order micrograms. Sampling was carried out in sterile plastic mini tubes with lid. Each tube was numbered.



Figure. 8a Front 1 of Processional flag inventory no. 8254:
the place of blue sampling



Figure. 8 b. Front 2 one sequence of Processional flag inventory no. 8254:
the places of red and green samplings

The collected samples were investigated by FTIR spectroscopy, X-ray fluorescence, X-ray diffraction and mass spectrometry.

FTIR measurements were performed with a JASCO 6100 spectrometer in the 4000–400 cm^{-1} spectral domain and a resolution of 4 cm^{-1} employing KBr pellete technique.

X ray fluorescence measurements were performed using an INNOV-X Alpha-6500 portable instrument. All colours on both sides of the processional flag- red, green, blue, black and aura were analysed.

The diffraction data were collected in the $2\theta = 3-85^\circ$ angular domain with a Bruker D8 Advance diffractometer, using $\text{Cu K}\alpha_1$ radiation ($\lambda = 1.5406 \text{ \AA}$) (40 kV; 40 mA). In order to increase the resolution, a Ge 111 monochromator was used to eliminate the $\text{K}\alpha_2$ radiation. Data collection was performed at room temperature with the programs package DIFFRAC plus XRD Commander. The pigment identification was made by comparing the obtained patterns with PDF-2 database. The amorphous/crystalline ratio was calculated by using Material Studio software.

Mass spectrometry measurements were done with a coupled GC-MS system. Mass spectrometer with ionic trap Polaris Q, gas chromatograph Trace GC Ultra and Autosampler AS2000 (ThermoFinnigan San Jose, USA)

REFERENCES

1. J. Chevalier, A. Gheerbrant, “Dicționar de simboluri”, volumul 3, P-Z; Editura Artemis, București, **1995**.
2. I. Evseev, “Enciclopedia semnelor și simbolurilor culturale”; Editura Amacord, Timișoara, **1999**.
3. E. Murray, “Politica și utilizarea simbolurilor”, Editura Polirom, Iași, **1999**.
4. ***, “Norme de conservare a bunurilor care fac parte din patrimoniul cultural”, Editura Museion, București, **1993**.
5. S. Macri, “Cercetări de conservare și restaurare a patrimoniului muzeal”, Muzeul Național de Istorie, vol. 1, „Metodologia restaurării steagurilor pictate”, București, **1981**, p. 91-98.
6. I. Sandu, M. Mustață, “Știința, Tehnica și Arta Conservării și Restaurării Patrimoniului Cultural”, Editura Universității “Al. I. Cuza”, vol. I, Iași, **1997**.
7. Z. Sofransky, “Paleta culorilor populare”, Editura Etnologica, București, **2006**.
8. A. Baciuc, Z. Moldovan, I. Bratu, O.F. Măruțoiu, I. Kacsó, I. Glăjar, A. Hernanz, C. Măruțoiu, *Curr. Anal. Chem.* **2010**, 6, 53.
9. I. Bratu, Z. Moldovan, I. Kacsó, C. Măruțoiu, L. Troșan, V.C. Măruțoiu, *Revista de Chimie*, **2013**, 64 (5), 542.

10. A.R.Trifa, C.Măruțoiu, Gh.Santa, I.Bratu, V.C.Măruțoiu, *European Journal of Science and Theology*, **2013**, 9(2), 169.
11. A. Hernanz, I. Bratu, O. F. Măruțoiu, C. Măruțoiu, J. M. Gavira-Vallejo, H. G. M. Edwards, *Anal Bioanal Chem.*, **2008**, 392, 263.
12. C. Marutoiu, S. P. Grapini, A. Baciuc, M. Miclaus, V.C.Marutoiu, S. Dreve, I. Kacso, I. Bratu, *Intern. J. Spectrosc.*, **2013**, <http://dx.doi.org/10.1155/2013/957456>.
13. Th. Bechtold, R. Mussak (eds.), „Handbook of Natural Colorants”, John Wiley & Sons, Chichester, **2009**.
14. Peter J. Larkin, “IR and Raman Spectroscopy. Principles and Spectral Interpretation”, Elsevier, Amsterdam, **2011**.

*Dedicated to Professor Liviu Literat
On the occasion of his 85th birthday*

PROTECTION OF ARTISTIC BRONZES BY ARTIFICIAL PATINA AND WAX

JULIETA DANIELA CHELARU^a, LUCIAN BARBU-TUDORAN^b,
LIANA MARIA MUREȘAN^{a,*}

ABSTRACT. The artificial patina is important to the restoration of historical objects or creation of bronze artworks. The main objective of this paper was to study the protective effect of one type of deliberately produced artificial patina on a bronze surface, in presence / absence of wax. Corrosion tests were carried out in a 0.2 g / L Na₂SO₄ + 0.2 g / L NaHCO₃ (pH = 5) solution simulating an acid rain. The protective effect of artificial patina with / without wax was comparatively investigated by electrochemical and non - electrochemical methods. The microscopic structure study of the bronze surface with / without artificial patina was conducted through optical and electronic microscopy. The chemical composition and the morphology of the corrosion products layer, formed on the bronze / artificial patina surface were determined by SEM - EDX.

Key words: *bronze, corrosion, artificial patina, polarization curve, wax*

INTRODUCTION

On a bronze sculpture, the patina has the capacity to enrich its aesthetic aspect. Patination art can be defined as a coloring of metal surface by oxidation or by prolonged exposure to the surrounding atmosphere [1 - 4]. That can be the definition of both categories of patina existing in the case of bronze: *natural* and *artificial*.

The natural patina can be observed especially in museums, or on outdoor sculptures and its color is green, yellow or black. As stated by Mattsson [5], "*the atmospheric exposure of copper has generally no detrimental effect, but rather a beneficial one; it develops an interesting and pleasing play of colours on the metal surface excellent for architectural purposes*".

^a Department of Chemical Engineering, "Babes-Bolyai" University, 11 Arany Janos St., 400028 Cluj-Napoca, Romania. * Corresponding author: limur@chem.ubbcluj.ro

^b Biology and Geology Department, "Babes-Bolyai" University, Piata Unirii 31, 400098 Cluj-Napoca, Romania

Because the formation of natural patina requires a long period of time, it is possible to create artificial patina. Production of artificial patina is an important step in the restoration of historical objects and creation of art works of bronze. Artificial patina is obtained by specific treatments (chemical or electrochemical) applied to the surface [1, 6 - 8]. There is a variety of chemicals that can confer a wide palette of colors to the resulting patina [1, 6 - 9]. For additional protection, after application of artificial patina, the surfaces are polished with wax [7, 9]. Nevertheless, the protective properties and the corrosion resistance of different types of artificial patina are insufficiently studied until now, and there are only few papers on this topic [4, 7 - 11].

In this context, the main objective of this paper is to study the protective effect of a green artificial patina, chemically produced on bronze by using sodium thiosulfate and ferric nitrate, in the absence or in the presence of wax. The corrosion behavior of the bronze samples was investigated under conditions that simulated acid rain (0.2 g / L Na_2SO_4 + 0.2 g / L NaHCO_3 , pH = 5 solution).

RESULTS AND DISCUSSION

Microscopic structure

To conduct the studies, a contemporary bronze whose chemical composition, displayed in Table 1, is close to the bronze used by sculptors in the early 20th century [12] was selected.

Table 1. The chemical composition of the investigated bronze

Alloy	Cu [%]	Sn [%]	Impurities, [%] max								
			Zn	Pb	Sb	Fe	Al	S	As	Mn	Ni
CuSn8	rest	7-9	0.8	1.0	0.1	0.2	0.02	0.1	0.15	0.2	1.0

Figure 1 presents the microscopic structures of bare bronze electrodes, magnified at x100, x200, x500, which were subsequently subjected to accelerated corrosion in an environment that simulated an acid rain.

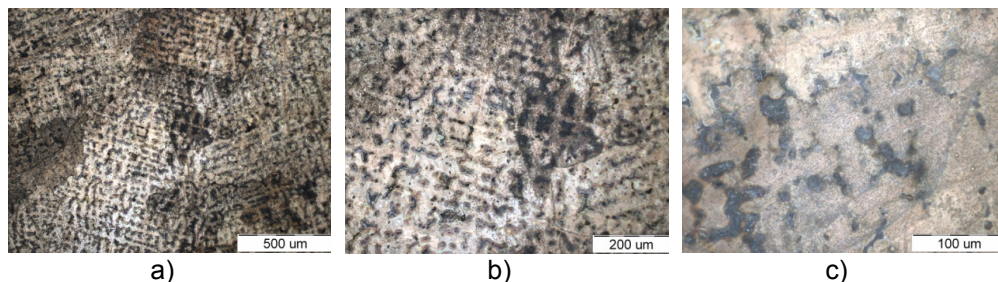


Figure 1. Microscopic structure of bronze used for electrochemical studies: a) x100; b) x200; c) x500

As it can be observed, the images illustrate the dendritic segregation of the α solid solution and interdendritic segregations of eutectoid $\alpha + \delta$ in small quantities. Additionally, the images obtained by scanning electron microscopy (Figure 2) show that the cross-sectional appearance of the bronze samples is homogeneous, without stratifications, slag inclusions or foreign material.

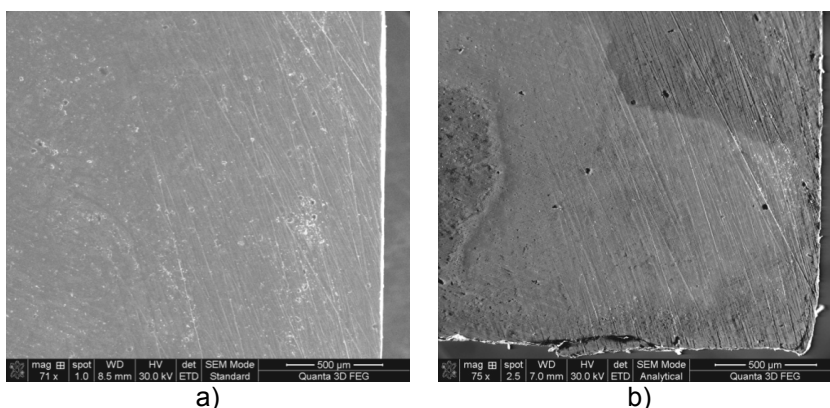


Figure 2. Images SEM, for the bronze used in the present work: a) x71, b) x75

The optical micrograph images of the artificially patinated bronze (Figure 3) show a discontinuous layer of corrosion products (artificial patina) reproducing the dendritic microstructure of the substrate [13].

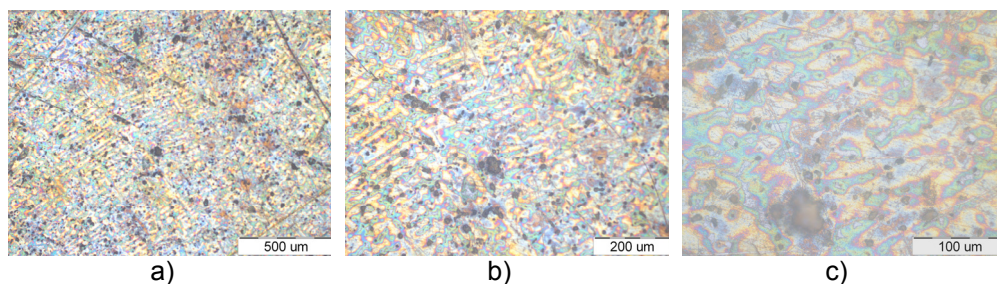


Figure 3. Microscopic structure of bronze used for electrochemical studies covered with artificial patina: a) x100; b) x200; c) x500

Morphological characterization of the corrosion products by SEM - EDX

In order to determine the morphology and the chemical composition of the patina layer formed on the bronze surface, SEM - EDX analysis was performed at different points of the electrode's surface and some results are presented in Figure 4 and Table 2.

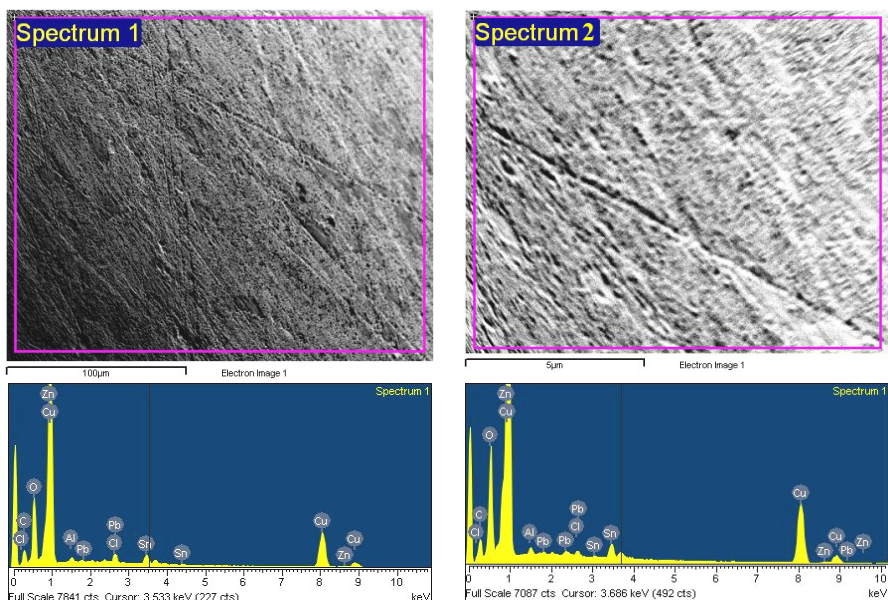


Figure 4. SEM/EDX results obtained on surface of bare bronze after corrosion tests

As can be seen from Table 2, the distribution of the chemical elements is relatively homogenous. The EDX analysis in different points indicated the presence of copper, oxygen, carbon, zinc and tin, whereas aluminum and lead were present as minor elements.

Table 2. Elemental composition [%] of the corrosion products formed at different points of the bronze electrodes, determined by EDX analysis

		C	O	Al	Zn	Pb	Fe	Sb	Sn	Cu
		[%]	[%]	[%]	[%]	[%]	[%]	[%]	[%]	[%]
Bare bronze		9.42	15.27	0.51	4.24	0.97	-	-	4.02	65.57
Bronze covered with patina	surface	7.82	15.09	0.60	3.79	0.90	-	-	3.71	68.09
	cross section	32.46	17.88	4.61	2.27	1.32	2.91	-	2.15	36.40
	cross section	30.08	9.35	0.82	3.19	1.11	1.22	-	2.82	51.41
	cross section	7.47	1.76	-	3.82	-	-	-	8.04	78.91
	cross section	11.78	1.79	0.33	2.44	1.05	0.85	0.91	11.84	69.01

The presence of zinc in the corrosion products layer in higher concentration than in the bronze substrate could be the sign of dezincification, which is a form of selective corrosion, where one of the components of the alloy is removed or leached out. Previously reported experiments showed that a high content of Sn protects the alloy from Zn loss (dezincification) [14]. On

the other hand, the copper content in the corrosion products layer is the result of copper selective dissolution from the alloy (decuprification) [15]. In general, zinc dissolves preferentially, but the zinc / copper ratio is not constant during the dissolution process. Thus, at the beginning, copper and zinc display an analogous trend of dissolution, but afterwards copper remains nearly constant with increasing exposure time [16]. This could be probably due to the set-in of equilibrium between the copper dissolving in the solution and the metal precipitating as corrosion product on the surface.

The presence of C in the corrosion products layer can be explained by the fact that this element enters in the composition of the electrolyte used in the electrochemical tests. The higher Al content than that identified in the composition of the alloy can be explained by the use of aluminum oxide (Al_2O_3) for the samples polishing. It can be also noticed the presence of oxygen in the analyzed corrosion products layer, presuming the formation of copper oxides (cuprite, Cu_2O) on the bronze surface [7].

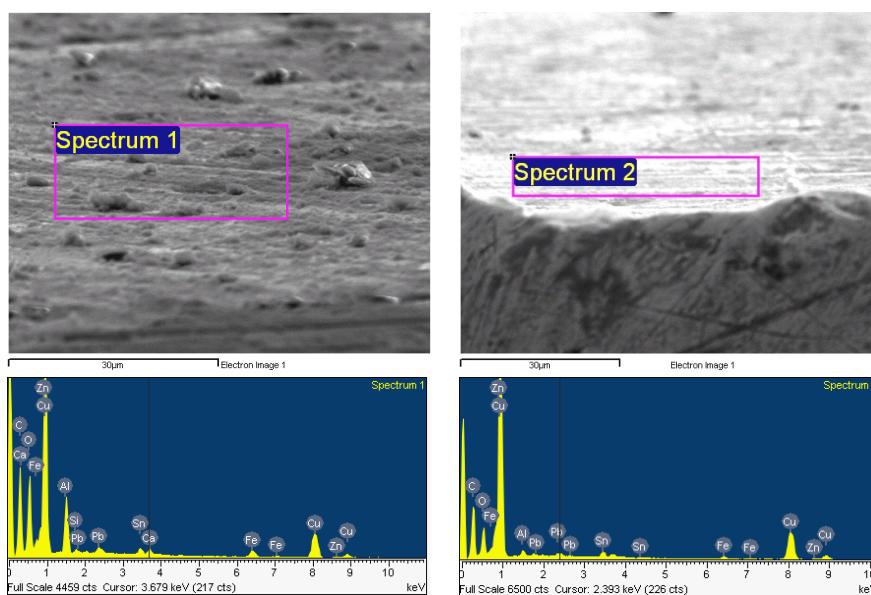


Figure 5. SEM/EDX results obtained on surface of bronze electrode covered with green artificial patina, after corrosion tests

In order to determine the morphology and the chemical composition of the patina layer formed on the surface of bronze covered with green artificial patina, SEM-EDX analysis was performed at different points of the electrode's surface and some results are presented in Figure 5 and Table 2.

In this case the EDX analysis at different points indicated the presence of copper, oxygen, carbon, zinc and tin whereas iron, aluminum and lead were present as minor elements.

The patina was analyzed also in cross-section (Figure 5 and Table 2).

Analyzing the SEM images from Figure 5 it can be noticed that the original surface is well preserved and no porosities are observed at the alloy / patina interface. As can be seen from Table 2, the EDX analysis at two different points on cross-section of bronze electrode covered with green artificial patina, indicated the presence of oxygen, in smaller quantities than on its surface (1.76 – 1.79 %). This can presume an internal oxidation, possibly with formation of tin species, which stabilize the patina layer [17]. As it can be observed, the elemental composition of the patina is relatively the same at the surface and in depth (cross-section) of the layer covering the bronze surface. Nevertheless, the Cu and the Sn content is higher in the depth of the patina layer, due to the proximity of the bronze substrate.

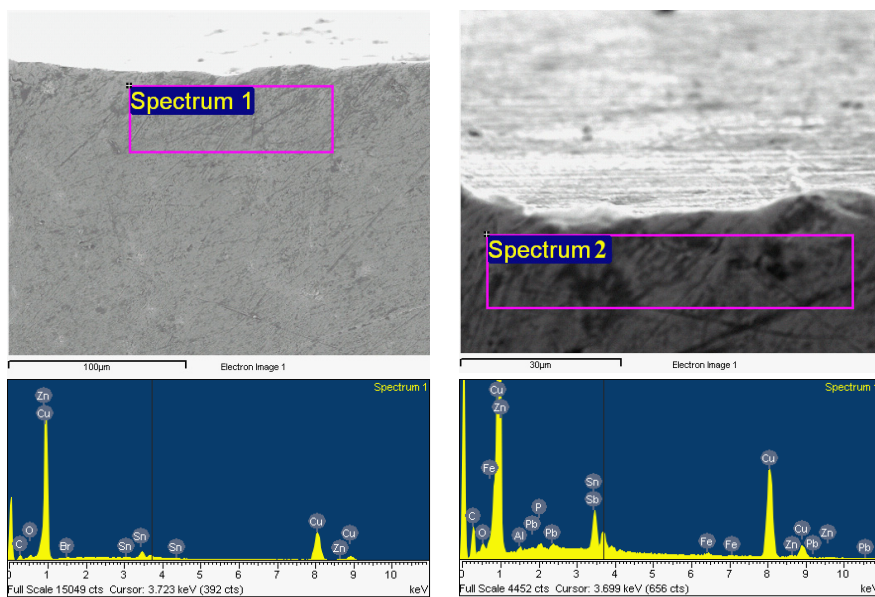


Figure 5. SEM/EDX results obtained on cross-section of bronze electrode covered with green artificial patina.

Polarization measurements

In order to characterize the protective effect of the green patina, electrochemical corrosion measurements were carried out.

The experiments started with measuring the open circuit potential (OCP) of the bare bronze and of electrodes covered with green artificial patina, in the absence or in the presence of wax, during 3600 s. The OCP for all studied electrodes increased in the first minutes of immersion in the corrosive solution, reaching a stationary value after approx. 25 minutes. These values were 51 mV / SCE for bare bronze, 15 mV / SCE for bronze covered with green artificial patina and 41 mV / SCE for electrodes covered with green artificial patina polished with wax, respectively. This behavior can be attributed to the chemisorption of oxygen on the surface of the dissolved bronze, along with the formation of surface oxide layers, hydrosulphate and / or hydroxycarbonate [18].

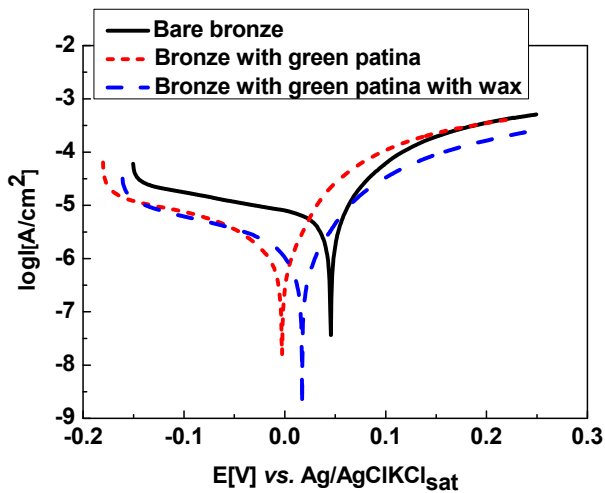


Figure 6. The polarization curves (± 200 mV vs. OCP) for the studied electrodes immersed in 0.2 g / L Na_2SO_4 + 0.2 g / L NaHCO_3 (pH = 5); scan rate, 10 mV / min.

To determine the kinetic parameters of the corrosion process, polarization curves were recorded in the potential range of ± 200 mV vs. OCP (Figure 6). The Tafel interpretation of the polarization curves led to the results presented in Table 3.

Table 3. Corrosion process parameters for the examined samples

Electrode	E_{corr} [mV vs SCE]	i_{corr} [$\mu\text{A}/\text{cm}^2$]	β_a [mV]	$-\beta_c$ [mV]	R_p [$\text{k}\Omega\text{cm}^2$]
Bare bronze	62	0.71	44	162	2.98
Bronze with green patina	-3	0.68	33	73	4.48
Bronze with green patina and wax	17	0.45	56	35	5.58

β_a and β_c are the Tafel coefficients [mV]

The analysis of the data from Table 3 reveals that the highest corrosion resistance is exhibited by the electrode covered with green artificial patina in presence of wax ($R_p=5.58$ [$k\Omega cm^2$], $i_{corr}=0.45$ [$\mu A/cm^2$]), followed by the bronze with green patina.

The corrosion current density calculated from Tafel representation and the polarization resistance was used to evaluate the efficiency of wax used for the protection of bronze. The protection efficiencies (PE) conferred by green artificial patina in the absence or in the presence of wax were determined using the equation 1.

$$PE[\%] = \frac{R_{p \text{ patina/wax}} - R_{p \text{ without patina/wax}}}{R_{p \text{ patina/wax}}} \times 100 \quad (1)$$

The best results were obtained, as expected, in the case of bronze covered with patina in the presence of wax (approximately 50%).

CONCLUSIONS

The corrosion behavior of an artistic bronze was investigated in the presence of chemically formed patina and wax.

Based on the SEM / EDX analysis of bronze surface it can be concluded that the green patina deliberately formed on bronze has a moderate protective effect.

The tests carried out in an environment that simulated acid rain on bronze showed that the best protection efficiency was exerted by green patina with wax (approximately 50 %).

EXPERIMENTAL

The working electrodes made of bronze CuSn8, cylindrical shaped, were placed in a PVC tube, while the sealing was assured with epoxy resin. In this way, the surface of the electrode exposed to the solution was disk - shaped, with a surface $S = 2.00$ cm^2 . For electrical contact a metal rod was attached (Figure 7).



Figure 7. The electrodes used during the experiments

For the microscopic study, the electrodes were polished on the sample polishing machine with alumina paste, after which the surface was washed with ammoniacal cupric chloride. The study of the surface was conducted through optical microscopy (OLIMPUS GS 51) and electronic microscopy (electron microscope FEI Quanta 3D)

SEM studies were performed with a Scanning Jeol JEM5510LV (Japan) coupled with Oxford Instruments EDX Analysis System Inca 300 (UK) at 15kV and spot size 39 μm .

The electrochemical corrosion measurements were performed on a PC – controlled electrochemical analyzer AUTOLAB - PGSTAT 10 (Eco Chemie BV, Utrecht, The Netherlands) using a three electrodes cell containing a working electrode (bronze), an Ag/AgCl electrode as reference electrode and a platinum counter electrode. Anodic and cathodic polarization curves were recorded in a potential range of ± 20 mV and of ± 200 mV vs. the value of the open circuit potential, with a scan rate of 10 mV / min, after 1 hour immersion in corrosive solution.


The electrolyte solution for corrosion measurements contained 0.2 g / L Na_2SO_4 + 0.2 g / L NaHCO_3 (pH = 5).

Artificial patina

Green artificial patina was prepared on the polished bronze surface in several steps, using the solutions mentioned in Table 3.

The stages in the patination process were: polishing the surface; maintaining in solution (T, t) until the patina layer is formed; neutralization with distilled water; drying with ethyl alcohol; applying of a protective solution containing wax (1 part) and anticorrosive oil (3 parts).

Table 3. Substances used to create artificial patina

Color	Chemical composition of the solution	Chemical formula	Quantity [g/L]	Duration of imersion / temperature	The working electrode
Green patina	Sodium thiosulfate	$\text{Na}_2\text{S}_2\text{O}_3$	45	3 - 5 minutes / 70 °C	
	Ferric nitrate	$\text{Fe}(\text{NO}_3)_3$	78		

REFERENCES

1. P. Kipper, Patina for Silicon Bronze, Regal Printing, Hong Kong, **2003**.
2. B. Rosales, R. Vera, G. Moriena, *Corrosion Science*, **1999**, *41*, 625.
3. S. Varvara, L.M. Muresan, K. Rahmouni, H. Takenouti, *Corrosion Science*, **2008**, *50*, 2596.
4. D. De la Fuente, J. Simancas, M. Morcillo, *Corrosion Science*, **2008**, *50*, 268.
5. E. Mattsson, R. Holm, ASTM STP 435, United States, **1968**, 197.
6. I.Z. Balta, S. Pederzoli, E. Iacob, M. Bersani, *Applied Surface Science*, **2009**, *255*, 6378.
7. H. Otmačić-Ćurković, T. Kosec, K. Marušić, A. Legat, *Electrochimica Acta*, **2012**, *83*, 28.
8. K. Marušić, H. Otmačić-Ćurković, Š. Horvat-Kurbegović, H. Takenouti, E. Stupnišek-Lisac, *Electrochimica Acta*, **2009**, *52*, 7106.
9. T. Kosec, H. Otmačić-Ćurković, A. Legat, *Electrochimica Acta*, **2010**, *56*, 722.
10. T. Kosec, A. Legat, I. Milosev, *Progress in Organic Coating*, **2010**, *69*, 199.
11. J.D. Chelaru, L.M. Mureșan, V.F. Soporan, O. Nemeș, T. Kolozsi, *International Journal of Conservation Science*, **2011**, *2*, 109.
12. M.L. Young., S. Schnepf, F. Casadio, A. Lins, M. Meighan, J.B. Lambert, D.C. Dunand, *Anal Bioanal Chem*, **2009**, *395*, 172.
13. L. Guadagnini, C. Chiavari, C. Martini, E. Bernardi, L. Morselli, D. Tonelli, *Electrochimica Acta*, **2011**, *56*, 6598.
14. L. Campanella, O. Colacicchi Alessandri, M. Ferretti, S.H. Plattner, *Corrosion science*, **2009**, *51*, 2183.
15. L. Robbiola, J.M. Blengino, C. Fiaud, *Corrosion Science*, **1998**, *40*, 2083.
16. E. Bernardi, C. Chiavari, C. Martini, L. Morselli, *Applied physics a: materials science & processing*, **2008**, *92*, 83.
17. L. Robbiola, R. Portier, *Journal of Cultural Heritage*, **2006**, *7*, 1.
18. N. Souissi, L. Bousselmi, S. Khosrof, E. Triki, *Material and Corrsion*, **2003**, *54*, 318.

*Dedicated to Professor Liviu Literat
On the occasion of his 85th birthday*

COUPLED VOLTAMMETRIC AND ELECTROGRAVIMETIC INVESTIGATION OF COPPER BEHAVIOR IN CARBONATE- BICARBONATE SOLUTIONS

FLORIN HANC-SCHERER^a, ADRIAN NICOARĂ^{a,*}

ABSTRACT. Among other alternatives, CO₂ electroreduction on copper electrodes exhibits formation of desirable reduction products with reasonable high yield. However, passivation of the electrocatalyst prevents a long time operation, limiting the economical efficient applicability. Aiming an investigation of the occurring phenomena, a coupled voltammetric and electrogravimetric investigation is further presented.

Keywords: CO₂ electroreduction, copper, voltammetry, electrogravimetry.

INTRODUCTION

Known as global warming gas, carbon dioxide can be reduced by electrochemical methods because of two main reasons: (1) selectivity towards formation of convenient gaseous or liquid products on employed cathode materials and (2) the experimental equipment required is rather inexpensive because neither high vacuum nor high reaction temperatures are needed. In this way, CO₂ have been converted into potential energy sources such as CH₄, C₂H₄, HCOOH, CH₃OH, etc. [1,2]. Products distribution and yield of the CO₂ electroreduction process is strongly influenced by the nature of employed cathode material. Formation of CO and HCOOH is preferential on Ti cathode, with additional formation of H₂ on Ag, Au and Sn [3]. On Cu-Ag alloys, high yield formation of C₂ compounds (especially C₂H₄, C₂H₅OH, and CH₃CHO) [4] while on Cu, CO and hydrocarbons (CH₄ and C₂H₄) were mainly obtained [5-8].

^a *Universitatea Babeș-Bolyai, Facultatea de Chimie și Inginerie Chimică, Str. Kogălniceanu, Nr. 1, RO-400084 Cluj-Napoca, Romania, * anicoara@chem.ubbcluj.ro*

Among the above-mentioned cathode materials, copper and its alloys are important alternative for CO₂ electroreduction because of their cost, reasonable corrosion resistance and important yield towards formation of valuable products. However, influenced by the nature of solvent and employed electrolyte, a passivation phenomenon decreases significantly the catalytic activity [9,10]. The present work aims investigation of charge and mass changes on copper/carbonate aqueous solution in the conditions identical to those employed during CO₂ electroreduction.

In this work, the electrolyte solution was chosen a mixture between sodium carbonate and bicarbonate, acting as precursor for CO₂ reduction and with significant supporting electrolyte contribution, using water as solvent. Avoiding the use of a high pressure experimental setup, this electrolyte solution is commonly reported.

The determination of electric charge is a common issue in electrochemical measurements, achievable either instrumentally, by chronocoulometry, or computationally, by integrating the current in potentiostatic and galvanostatic techniques, solely the methodology of the determination of mass change will be discussed further in detail [11].

The resonance frequency of the quartz resonator depends on its mass and the mechanical forces applied upon. By choosing conditions in which the latter are invariable, the resonance frequency will be influenced mainly by the mass addition or removal from the resonator. By construction, the resonator has two conductive electrodes, one functioning as working electrode, being immersed into solution, as the second remains in air. In this way the mass changes (Δm) of the electrode immersed into solution can be correlated to the frequency variation (Δf) of copper coated quartz resonator by using the Sauerbrey equation [9]:

$$\Delta f = -2f_0^2 \Delta m / A(\mu_q \rho_q)^{1/2} = -C_f \Delta m \quad (1)$$

where f_0 is the fundamental (in air) resonant frequency (9 MHz) of the quartz resonator, A is the geometric area (0.196 cm²) of the metallic plate, μ_q is the quartz shear modulus (2.947 10¹¹ g cm⁻¹ s⁻²), and ρ_q is the quartz density (2.648 g cm⁻³). For the used resonator the theoretical value of the Sauerbrey constant (C_f) is 945.6 Hz μg^{-1} whereas the calibration that uses copper electrodeposition from Oettel solution (see [12] for details) give an experimental value of 943.7 \pm 1.2 Hz μg^{-1} . As the validity of Sauerbrey equation is restricted to relative small frequency variation ($\Delta f/f_0 < 0.01$), the chosen thickness (150nm) of electrodeposited copper layer assures the operation well inside the validity domain ($\Delta f/f_0 = 0.0028$) allowing a significant margin to a potential formation of a film during investigation.

For describing the electrochemical processes at the electrode surface, the primary Δf vs. potential (E) electrochemical quartz crystal microbalance data

can be treated in different ways. In this paper was used a straight-to-forward method, based on a Q vs Δm correlation. Using Faraday's law it is possible to calculate the parameter $\Delta M/n$:

$$\Delta M / n = F \Delta m / |Q| \quad (2)$$

where ΔM is the stoichiometric molecular (or atomic) mass variation of the solid phase species involved in reaction, n the number of exchanged electrons, Q the charge consumed by the reaction and F the Faraday constant (96,485.31 C mol⁻¹). Usually, the $\Delta M/n$ parameter is specific for a given reaction. By comparing these values with the experimental found ones, it is possible to identify the reactions taking place at the electrode.

RESULTS AND DISCUSSION

The measurements were carried out with a mixture of carbonate and bicarbonate in order to modify the pH while keeping the sum of the two mentioned CO₂ precursors concentration constant. In that way, a more mechanistic approach is allowed for the study, since allows discrimination between pH-independent and dependent elementary reaction steps.

All the measurements were carried out using relative small scan rate of electrode potential, between 2 and 10mVs⁻¹, in order to decrease the influence of double layer capacitance charge on measured current and occurring electrocapillary forces on quartz resonance.

As can be seen in Fig. 1, for pH=10.51, the voltammograms present a single cathodic peak, at potentials between -0.5 and -0.55V, and two consecutive anodic peaks at approx. -0.15 and -0.025V, respectively. Only the last anodic peak exhibits an approx. proportionality between the peak current and square root of the scan rate, which is an indication of involvement of diffusion of reactants. On the contrary, for the other two peaks the slopes of I_p vs v plots in logarithmic coordinates are bigger than 1/2 as expected for processes involving diffusion of electroactive species, but less than one as expected for processes involving adsorbed electroactive species; this suggest that the formation of the first two peaks is the result of some complex charge transfer processes involving both soluble and adsorbed (or at least immobilized on the electrode) reactants.

Conversely, the frequency shift of quartz crystal resonator has a more complicated behavior. During the initial reduction scan there is a frequency decrease even in the potential range when a noticeable current peak is not present. As indicated by the Sauerbrey equation, the decrease of the frequency denotes an increase of the mass of the electrode. Further, on the potential range where the first voltammetric cathodic peak is present, there is an important mass loss. During the initial stages of oxidation scan a small mass increase is

noticeable in a potential domain in which any voltammetric peak is absent, but the first anodic peak takes place with a more important mass increase, while the second anodic peak takes place with a very important mass loss, process that continues during the initial stages of the final reductive scan. Similar behaviour can be noticed at all the investigated pH values, see Fig. 2.

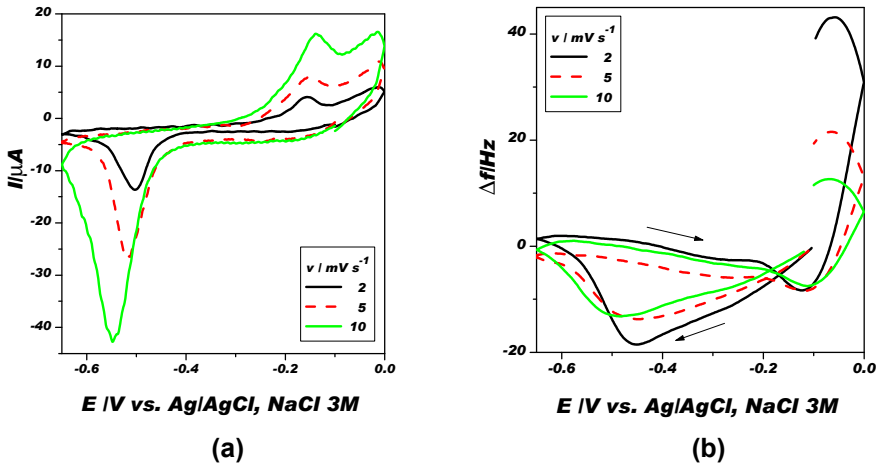


Figure 1. Influence of scan rate on current intensity (a) and resonance frequency shift (b) for pH=10.51.

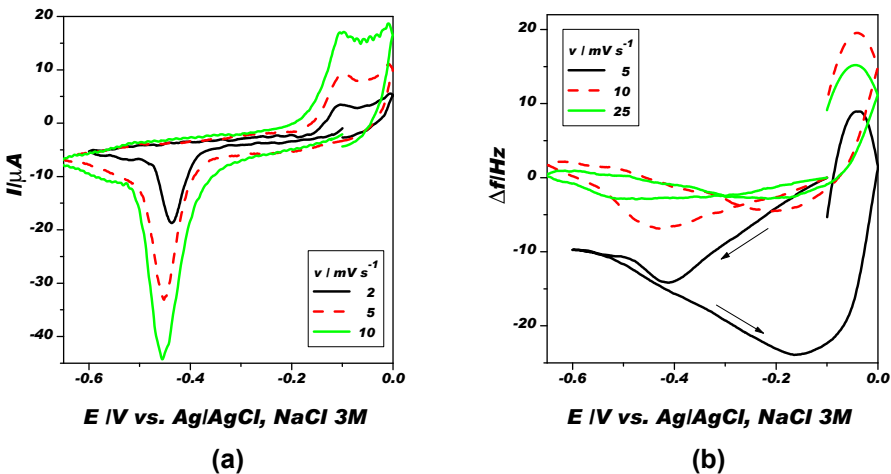


Figure 2. Influence of scan rate on current intensity (a) and resonance frequency shift (b) for pH=8.89.

Qualitative analysis is further completed by describing the influence of pH of the solution on measurements, as indicated by Fig. 3. As evidenced in Fig. 3a, the increase of pH reduces the cathodic current peak and shifts the potential peak towards more negative values. This indicates that the reaction responsible for this voltammetric peak has at least one of the reactants with the concentration influenced by the pH; it can be a species with decreasing concentration upon alkalinification – like H^+ , HCO_3^- or CO_2 – and exclude as reactants the species of those concentration increases upon alkanification, like OH^- or carbonate ions. In addition, it is also possible the involvement of an electroactive species in large excess to those of which the decrease of interfacial concentration causes the formation of the voltammetric peak; in this case, H^+ could be a reactant or OH^- , a product. The involvement of an electroactive species in large excess causes a peak potential shift without influencing the peak current.

The influence of pH on the first anodic peak is more complex without a clear dependence, while the second anodic peak is not always present. These suggest that the peaks are not correlated, namely are evidence of some chemically irreversible charge transfer processes.

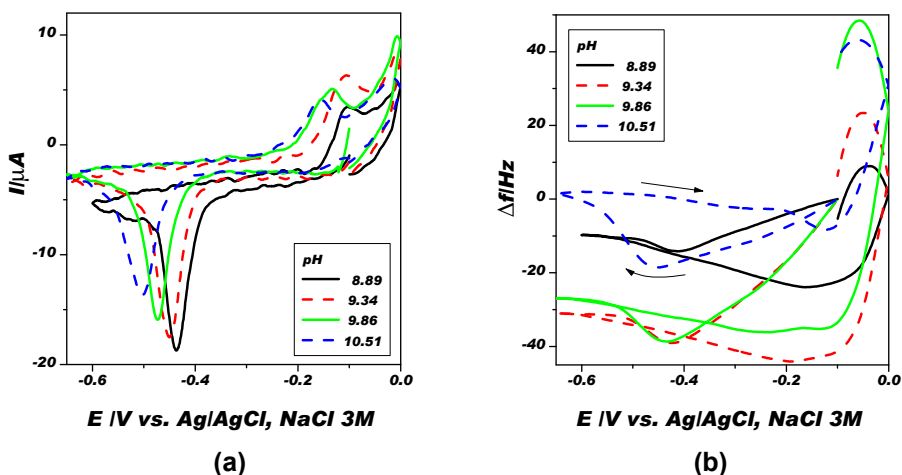


Figure 3. Influence of pH on current intensity (a) and resonance frequency shift (b) for $2mV s^{-1}$ scan rate.

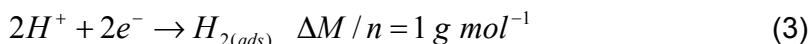
The influence of pH on the mass changes of the electrode is more complex as the mass changes at intermediate pH values are larger than those at extreme pH values. However, there are correlations between the mass decreases and mass increases on every pH values.

In order to attempt a quantitative evaluation, the scanned potential range was divided in several potential windows in which a possible individual process takes place. These potential windows are presented in Tab. 1 alongside the charge calculated by integration of voltammograms in the given potential window, the mass changes, and the calculated parameter $\Delta M/n$.

Table 1. Electrogravimetric parametres for pH=8.89 and $v=2\text{mV s}^{-1}$ scan rate.

Zone	Potential window / V	$\Delta Q / \mu\text{C}$	$\Delta m / \mu\text{g}$	$\Delta M/n / \text{g mol}^{-1}$
C1	-0.1 to -0.3	-340	9.73	2.7
Cp	-0.42 to -0.5	-438	-3.72	-0.8
C3	-0.6 to -0.16	-767	14.9	1.9
Ap1	-0.16 to -0.06	81.9	-4.09	-4.8
Ap2	-0.06 to 0 to -0.04	34.4	-22.70	-62.8
C0	-0.04 to -0.1	-28.7	15.09	50.7

The zone **C1**, in which the charge is transferred without formation of an voltammetric peak, could easily be confused with a capacitive zone. But the important mass increase is a strong indication that a faradaic process occurs. More likely is the underpotential hydrogen formation, a process in which the hydrogen obtained remains adsorbed as a monolayer on the interface:

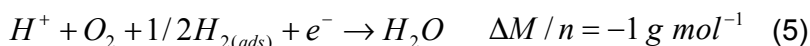


Common hydrogen evolution, where the hydrogen is desorbed and released as bubbles, is not thermodynamically possible in this potential range, and would have $\Delta M/n = 0 \text{ g mol}^{-1}$; this process was reported only at potentials more negative than about -0.9V [13]. It is possible that a parallel reduction, with higher $\Delta M/n$, is the cause for the discrepancy between the experimental and theoretical values.

The zone **Cp** includes the cathodic peak and takes place with a very modest mass decrease. Due to the difficult kinetics, it is unlikely that hydrogen evolution would take place at potentials larger than -0.5V. More reasonable is to assume the oxygen reduction:



or oxygen reduction with some involvement of adsorbed hydrogen obtained in zone **C1**, like:

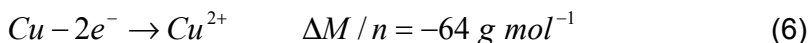


Only these two reactions predict correctly the influence of pH on the cathodic peak parameters.

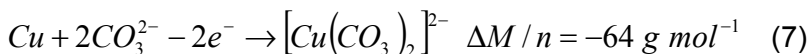
The zone **C3** does not contain a voltammetric peak but the mass increase is yet important. The reaction (3), compensating the vacancies from the hydrogen monolayer generated by reaction (5), can be responsible only partial for the behavior as the charge involved in **C3** is more than twice that of **C1**. More likely another reduction process with higher $\Delta M/n$ is also involved, but the obtained experimental data make difficult a complete identification.

The zone **Ap1** includes the first anodic peak and takes place with significant mass decrease. Even more important mass decrease takes place in zone **Ap2**, zone that includes the second anodic peak.

Such important anodic mass decreases can be only asserted taking into consideration copper oxidation as:

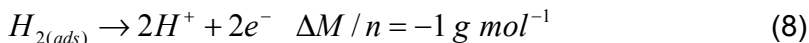


or oxidation with formation of a soluble copper complex, like



Regardless the nature of the formed soluble copper products, these reactions could explain the behaviour in zone **Ap2**.

The lower value of $\Delta M/n$ in zone **Ap1** as compared to this of **Ap2** suggests additional processes. The oxidation of adsorbed hydrogen:

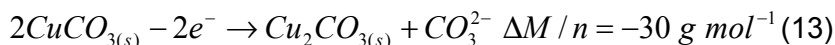
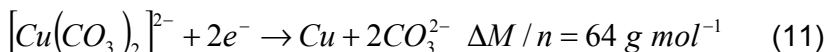
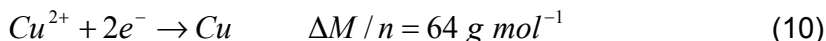


and copper oxidation leading to insoluble products, like:



could contribute to the lowering of founded value of $\Delta M/n$ as compared with theoretical ones of reactions (6) and (7).

Finally, the last cathodic zone, **C0**, takes place with important mass increase. Combination of following reductions could be assigned:



in which reactions (10) or (11) have the most important contribution.

CONCLUSIONS

The present study attempted the investigation of the phenomena occurring during reduction on copper of a carbonate solution. The evidence for the blocking of the electrode with insoluble or adsorbed species and the evidence of CO_2 reduction would have provide some insights about this important process.

Unfortunately, no direct evidence for CO₂ reduction was observed in the investigated potential window. The only potential window in which this process could have been present is that of the investigated more negative values. As already mentioned, in zone **C3** a process with $\Delta M/n$ higher to those evidenced in **C1** and **Cp** could be related also to some kind of CO₂ reduction. In this potential window, and also at more negative potentials, further studies should be carried out.

It is favourable to mention that between a large number of potentially solid state copper compounds, which could caused passivation towards CO₂ reduction by covering the copper electrode, neither was has significant contribution to the electrochemical behaviour of the system. The only species found to cover significantly the copper electrode is a monolayer of hydrogen which, due to its reactive state, could even participate as a mediator in homogenous reduction reactions.

EXPERIMENTAL

The measurements were carried out using a computer controlled potentiostat (PARStat 2273, Princeton Applied Research, USA) and a quartz crystal microbalance (QCM922, Princeton Applied Research, USA). The resonator allowing the monitoring of mass changes was a 9 MHz quartz crystal (QA-A9M-AU), inserted into a well cell resonator holder (QA-CL4, Princeton Applied Research, USA).

The measurements were performed in a conventional single compartment cell, equipped with three electrodes: the working electrode (WE) consisted of the exposed face of the resonator ($A=0.196 \text{ cm}^2$); the auxiliary electrode was a Pt wire; and Ag/AgCl, NaCl_{sat} was used as reference electrode.

The working electrode was obtained by the electrodeposition of a thin film of Cu from an Oettlel solution (CuSO₄ 125 g L⁻¹, C₂H₅OH 50 g L⁻¹, H₂SO₄ 50 g L⁻¹, all Reactivil, Bucharest, Romania) onto one of the gold faces of the quartz crystal. The electrodeposition was performed galvanostatically by applying a current density of 20 mA cm⁻² for 20 s, conditions allowing the obtaining of a 150 nm thick copper film.

The four investigated electrolyte solutions contained Na₂CO₃ (0.01, 0.03, 0.06 and 0.09M), NaHCO₃ (0.09, 0.07, 0.04 and 0.01M, respectively) and 0.5M Na₂SO₄ as supporting electrolyte. The measured pH values were 8.89, 9.34, 9.86 and 10.51, respectively.

Prior to any measurement, the electrode was conditioned at -0.1V for 30s. The scans use a four potential scheme, when a initial reduction scan, from -0.1 to -0.65V, is followed by an oxidation scan, to 0V, and the cycle is completed by a reduction scan to the initial -0.1V value.

Electrolyte solution were prepared by dissolving Na₂CO₃ (Reactivul, Bucharest, Romania), NaHCO₃ (Chimopar, Bucharest, Romania) and Na₂SO₄ (Reactivul, Bucharest, Romania) in distilled water. All measurements were performed at room temperature (23 ± 1 °C).

ACKNOWLEDGMENTS

FHS thanks for the financial support received from “The Sectorial Operational Program for Human Resources Development 2007-2013, co-financed by the European Social Fund, under the project number POSDRU/107/1.5/S/76841 with the title “Modern Doctoral Studies: Internationalization and Interdisciplinarity”.

REFERENCES

1. B.P. Sullivan, K. Krist, H.E. Guard, “Electrochemical and Electrocatalytic Reactions of Carbon Dioxide”, Elsevier, Amsterdam, **1993**.
2. K. Hara, A. Kudo, T. Sakata, *J. Electroanal. Chem.*, **1995**, 391, 141.
3. K. Christmann, *Surf. Sci. Ref.*, **1988**, 9, 163.
4. S. Ishimaru, R. Shiratsuchi, G. Nogami, *J. Electrochem. Soc.*, **2000**, 147, 1864.
5. Y. Hori, O. Koga, H. Yamazaki, T. Matsuo, *Electrochim. Acta*, **1995**, 40, 2617.
6. T. Mizuno, A. Naitoh, K. Ohta, *J. Electroanal. Chem.*, **1995**, 391, 199.
7. S. Kaneco, H. Katsumata, T. Suzuki, K. Ohta, *Electrochim. Acta*, **2006**, 51, 3316.
8. M.R. Gonçalves, A. Gomes, J. Condeço, T.R.C. Fernandes, T. Pardala, C.A.C. Sequeira, J.B. Branco, *Electrochim. Acta*, **2013**, 102, 388.
9. J.J. Kim, D.P. Summers, K.W. Frese Jr., *J. Electroanal. Chem.*, **1998**, 24, 233.
10. R.L. Cook, R.C. MacDuff, A.F. Sammells, *J. Electrochem. Soc.*, **1989**, 136, 1982.
11. A.J. Bard, L.R. Faulkner, “Electrochemical Methods: Fundamentals and Applications”, Wiley, New York, **1980**, chapter 17.5.
12. A. Nicoară, *Studia UBB Chem.*, **2004**, 49, 65-76.
13. Y. Hori, A. Murata, R. Takahashi, *J. Chem. Soc. Faraday Trans.*, **1989**, 185, 2309.

*Dedicated to Professor Liviu Literat
On the occasion of his 85th birthday*

ELECTROCHEMICAL STUDY OF ISOPRENALINE AND EPINEPHRINE AT PLATINUM-NANOPARTICLES-CHITOSAN MODIFIED GRAPHITE ELECTRODE

**IOANA FORT^a, ILEANA ELISABETA SILAI^a,
DORINA CASONI^b, GRAZIELLA L. TURDEAN^{a,*}**

ABSTRACT. Two catecholamines (epinephrine and isoprenaline) were studied by cyclic (CV) and square-wave voltammetry (SWV) at bare graphite (G) and Pt nanoparticles (Pt-NP) - chitosan modified graphite electrodes (G/Pt-NP-Chitosan). The obtained results shown similarly redox behavior for both investigated compounds by mentioned electrochemical techniques at the investigated electrodes, consisting in two pairs of peaks (peak I and II) corresponding to a quasi-reversible processes. The difference between the structures of compounds doesn't influence the electrochemical parameters values. As expected, the presence of the Pt nanoparticles acts as a diffusion barrier on the electrode surface leading to a decrease of the current intensities values, when electrodes were investigated by CV and SWV. The G/Pt-NP-Chitosan nanocomposites matrix can be satisfactorily used for detecting catecholamines.

Keywords: *catecholamines, Pt nanoparticles, chitosan, cyclic voltammetry, square wave voltammetry.*

INTRODUCTION

Catecholamines are produced by sympathetic nervous system activation and act as hormones and neurotransmitters to monitor heart rate, brain muscles activity, glycogenolysis, fatty acid mobilization and body temperature [1]. Epinephrine and isoprenaline are two important catecholamines having similar structures.

^a "Babeş-Bolyai" University, Faculty of Chemistry and Chemical Engineering, Chemical Engineering Department, 11 Arany Janos Street, 400028 Cluj-Napoca, Romania, *gturdean@chem.ubbcluj.ro

^b Chemistry Department, Babeş-Bolyai University, Faculty of Chemistry and Chemical Engineering, 11 Arany Janos Street, 400028 Cluj-Napoca, Romania

Epinephrine (often called adrenaline) is an important catecholamine neurotransmitter in mammalian central nervous system and biological body fluids. It has been used for the treatment of myocardial infarction, hypertension, bronchial asthma, cardiac arrest, and cardiac surgery in clinics. Studies show that many physiological phenomena are correlated to the changes of its concentration in the body fluids [2-3].

Isoprenaline (or isoproterenol) is a catecholamine drug that affects the heart by increasing inotropic and chronotropic activity. This sympathomimetic beta-receptor stimulant was used for the treatment of bradycardia (slow heart rate), heart block and rarely for asthma. The cardiovascular effects of isoprenaline are compared with the epinephrine, which can relax almost every kind of the smooth musculature that receives adrenergic nervous, but this effect is pronounced in the musculature of bronchus and also in the gastrointestinal tract [4-5].

Therefore, quantitative determination of these compounds in biological fluids and/or pharmaceutical preparations is very important. In the literature, a great number of methods have been presented, such as: chromatography (high performance liquid- or gas-), capillary electrophoresis, flow injection, chemiluminescence, fluorimetry, spectrophotometry and electrochemical methods [4, 6].

Among these methods, the electrochemical techniques and mainly the applications of chemical modified electrodes have increased enormously, because of their simplicity, rapidity, high selectivity and sensitivity. Thus, modified electrodes with various nanomaterials having unique electronic and catalytic properties were used in electrochemical studies of some catecholamine compounds [5].

The main purpose of the paper is to investigate the electrochemical behaviour of two catecholamines (epinephrine and isoprenaline) having similar structures, at a new prepared Pt nanoparticles-chitosan modified graphite electrodes, by cyclic and square-wave voltammetry.

RESULTS AND DISCUSSION

Electrochemical behavior of catecholamines by cyclic voltammetry

Figure 1 presents the cyclic voltammograms of the studied catecholamines recorded on G and G/Pt-NP-Chitosan electrodes. Within the studied potential window, the supporting electrolyte shows no characteristic peaks, besides the charging of the electrical double layer (thin lines in figures 1A, B), while the studied catecholamines shown two pairs of peaks (abbreviated I, II) on both G and G/Pt-NP-chitosan investigated electrodes.

It is worth to mention, that the whole mechanism reaction consisting by chemical (C) and electrochemical (E) steps, involves different forms of epinephrine (scheme 1) and was detailed in literature. Briefly, it consists by the succession of ECCCEE steps, where the first E is assigned to IIa peak, followed by deprotonation (first C), cyclization (second C), and disproportionation (third C), and then again E (for Ic peak), and finally E (for Ia peak) [1, 7-9].

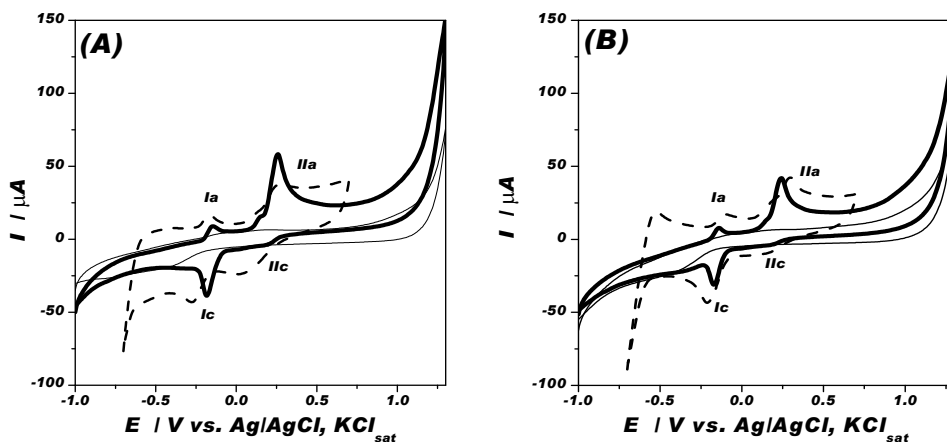
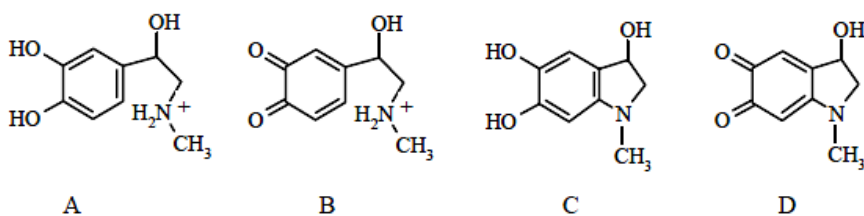
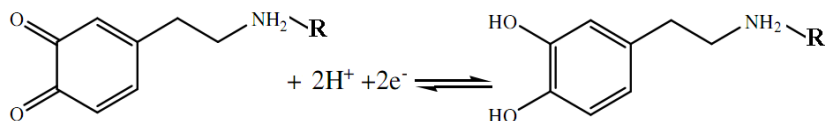


Figure 1. Cyclic voltammograms of 10^{-3} M isoprenaline (A) and 10^{-3} M epinephrine (B) at G (thick solid line) and G/Pt-NP-chitosan (dash thick line) electrode. Experimental conditions: electrolyte, 0.1 M phosphate buffer, pH 7 (thin solid line); scan rate, 50 mV/s; starting potential, -1 or 0.75 V vs. Ag/AgCl, KCl_{sat} .



Scheme 1. Structures of different forms of protonated epinephrine (A), protonated epinephrinequinone (B), leucoadrenochrome (C) and adrenochrome (D).

At pH 7, regardless the type of used working electrode, the total redox process consists in the oxidation (two protons, two-electron) of epinephrine or isoprenaline to its corresponding open chain quinone epinephrinequinone or isoprenalinequinone following the reaction depicted in scheme 2:



Scheme 2. Redox process at pH 7 for epinephrine (R = -CH₃) or isoprenaline (R = -CH(CH₃)₂)

The electrochemical parameters describing the redox behavior of the investigated compounds are synthesized in table 1.

Table 1. Electrochemical parameters of 10⁻³ M epinephrine and 10⁻³ M isoprenaline investigated by cyclic voltammetry. Experimental conditions: see figure 1.

Parameters	$E_{pa}/$	$I_{pa}/$	$E_{pc}/$	$I_{pc}/$	$\Delta E/$	$E^0/$	I_{pa}/I_{pc}	
Electrode	Peak	V/ER	A	V/ER	A	V	V/ER	
epinephrine								
G	I	-0.146	1.22 10 ⁻⁵	-0.185	-2.99 10 ⁻⁵	0.039	-0.166	0.41
	II	0.230	4.05 10 ⁻⁵	0.162	-2.63 10 ⁻⁶	0.068	0.196	15.4
G/NP-Pt-chitosan	I	-0.104	6,25 10 ⁻⁶	-0.212	-2.68 10 ⁻⁵	0.108	-0.158	0.23
	II	0.296	2.07 10 ⁻⁵	0.164	-4,27 10 ⁻⁶	0.132	0.230	4.84
isoprenaline								
G	I	-0.150	8.10 10 ⁻⁶	-0.185	-2.74 10 ⁻⁵	0.035	-0.168	0.29
	II	0.255	4.65 10 ⁻⁵	0.186	-2.93 10 ⁻⁶	0.069	0.220	15.9
G/NP-Pt-chitosan	I	-0.168	7.48 10 ⁻⁶	-0.270	-1.47 10 ⁻⁵	0.102	-0.219	0.51
	II	0.257	1.46 10 ⁻⁵	0.062	-1.04 10 ⁻⁵	0.195	0.160	1.4

where: ER is the reference electrode; $\Delta E_p = E_{p,a} - E_{p,c}$ is the peak potentials separation; $E^0 = (E_{pa} + E_{pc})/2$ is the formal standard potential; E_{pa} and E_{pc} are the anodic and cathodic peak potentials, respectively.

As it can be seen, the electrochemical behavior of isoprenaline is similar with the redox behavior of epinephrine due to their analogous structure. A shift towards positive (peak II at G) or negative (peak I and II at G/Pt-NP-chitosan) directions of peak potentials of isoprenaline comparing to epinephrine is visible. If the difference between the E^0 of isoprenaline and epinephrine is of + 24 mV (peak II) at G electrode, the presence of Pt-NP lead to a difference of - 61 mV (peak I) and -70 mV (peak II), the two compounds becoming better separated.

Also, the variation of the current intensities of either the Ia, or the IIc peaks which are much smaller than the mirror corresponding one (I_{pa}/I_{pc} much greater/smaller than 1), and additionally with the variation of the peak potentials separation values ($\Delta E_p = E_{p,a} - E_{p,c} = 0.035 \div 0.195$ V, at 50 mV/s), confirms that the redox behaviour of isoprenaline and epinephrine correspond to a quasi-reversible process at both type of investigated electrodes. However, because peak IIc is hardly visible, it can be considered that the process II corresponds to an irreversible oxidation of epinephrine or isoprenaline, at pH 7.

With increasing of the scan rate, the peak current intensity is increasing and the corresponding peak potentials of Ia, IIa and Ic are shifting towards positive and negative values, respectively (results not shown). The plots of $\log(I_p) - \log(v)$ for each peaks currents (I and II) are linear with a slope close to 0.5 (see Table 2), proving that the adsorption of studied compounds is very weak at G/Pt-NP-chitosan and bare G electrodes, at pH 7.

Table 2. Parameters of the linear regression for the $\log(I_p/\mu\text{A}) - \log(v/(V*s^{-1}))$ dependence. Experimental conditions: see figure 2.

Electrode	Slope R/n			
	Peak Ia	Peak Ic	Peak IIa	Peak IIc
G	-	isoprenaline		
		0.732 ± 0.019	0.306 ± 0.024	0.257 ± 0.055
G/NP-Pt-chitosan	0.599 ± 0.116 0.9025/8	0.411 ± 0.055	0.269 ± 0.027	0.263 ± 0.032
		$0.9654/6$	$0.9800/6$	$0.9711/6$
G	-	epinephrine		
		0.760 ± 0.015	0.476 ± 0.040	-
G/NP-Pt-chitosan	0.473 ± 0.059 0.9551/8	0.434 ± 0.058	0.342 ± 0.076	0.291 ± 0.025
		$0.9497/8$	$0.9142/6$	$0.9852/6$

As consequence the epinephrine or isoprenaline redox electrode process can be considered to take place under diffusion control [10]. Also, the plot I versus $v^{1/2}$ is linear (see Figure 2), as expected the current intensities at G/Pt-NP-chitosan electrode being smaller than at bare G electrode.

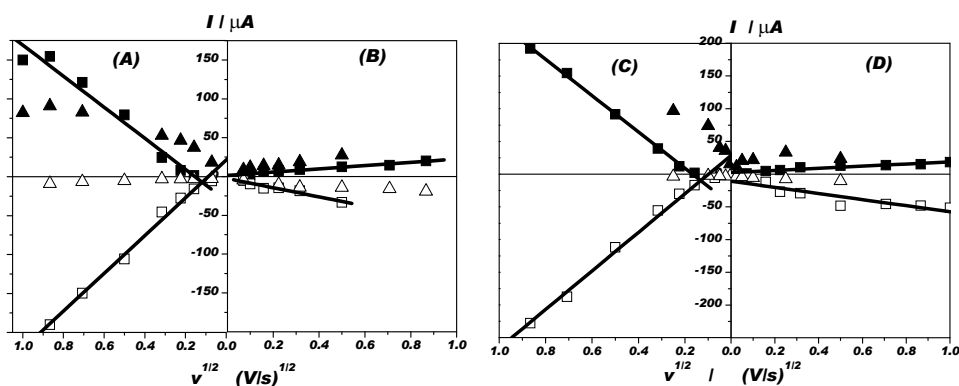


Figure 2. Influence of the scan rate on the current intensity of peak I (■, □) and peak II (▲, △) of 10^{-3} M isoprenaline (A, B) and 10^{-3} M epinephrine (C, D) at G (A, C) and G/Pt-NP-chitosan (B, D) electrode. Experimental conditions: see figure 1.

For a reversible process, using the Randles-Sevcik equation (1) the diffusion coefficients of catecholamines could be calculated.

$$I_{p,a} = 2.69 \cdot 10^{-5} n^{3/2} A D_0^{1/2} v^{1/2} c_{ox}^* \quad (1)$$

where: $I_{p,a}$ (A) refers to the anodic peak current, n is the number of transferred electron, A (cm^2) is the area of the electrode, D_0 ($\text{cm}^2 \text{s}^{-1}$) is the diffusion coefficient, c_{ox}^* (mol cm^{-3}) is the catecholamine concentration and v (V s^{-1}) is the scan rate.

From the slope of I_{pa} versus $v^{1/2}$ plots, and presuming the surface area of graphite electrode being 0.071 cm^2 , for a 10^{-3} M catecholamine concentration, the diffusion coefficients were $D_0 = 5.8 \cdot 10^{-5} \text{ cm}^2 \text{ s}^{-1}$ for epinephrine and $D_0 = 0.3 \cdot 10^{-5} \text{ cm}^2 \text{ s}^{-1}$ for isoprenaline at G electrodes, values which are in accordance with literature data (i.e., for epinephrine $D = 4.2 \cdot 10^{-5} \text{ cm}^2 \text{ s}^{-1}$ at CPE [11] or $1.4 \cdot 10^{-4} \text{ cm}^2 \text{ s}^{-1}$ at poly(*p*-xylenolsulfonephthalein) glassy carbon modified electrode [3]).

Electrochemical behavior of catecholamines by square-wave voltammetry

The square-wave voltammetry investigation technique was chosen for the study of the catecholamines because it is the most advanced and most sophisticated method from the pulse voltammetric techniques and exhibits the advantages of a large speed and high sensitivity [1, 12].

In Figure 3A are shown the SW voltammograms obtained for the epinephrine and isoprenaline at different electrodes. As expected, the current intensities obtained at G/Pt-NP-chitosan electrodes comparing with those at bare G are smaller, confirm that the Pt-NP-chitosan matrix act as diffusion barrier for epinephrine or isoprenaline towards electrode interface. At both investigated electrodes, the peak potentials have close values ($E_{a,I} = -0.160 \text{ V}$; -0.200 V and $E_{a,II} = 0.210 \text{ V}$; 0.185 V for epinephrine and isoprenaline at G electrode, respectively; $E_{a,I} = -0.150 \text{ V}$; -0.200 V and $E_{a,II} = 0.240 \text{ V}$; 0.200 V for epinephrine and isoprenaline at G/Pt-NP-chitosan electrode, respectively) than in CV technique.

According to the theoretical model proposed by Mirceski and co-workers for SWV, a dependence of $I_p f^{1/2}$ vs. $f^{1/2}$ associated with a well-developed maximum corresponds to a quasi-reversible electrode reactions [13] and an exponential dependence indicate a diffusion-controlled electrode process [14]. Note that the ratio $I_p f^{1/2}$ corresponds to the dimensionless net-peak current (Φ) and the $f^{1/2}$ to the resistance parameter (q), where: $\Phi = I_p(nFS c_{ox}^*)^{-1}(Df)^{-1/2}$, $q = R_\Omega(n^2F^2/RT)S c_{ox}^*(Df)^{1/2}$, n is the number of electrons, F is the Faraday

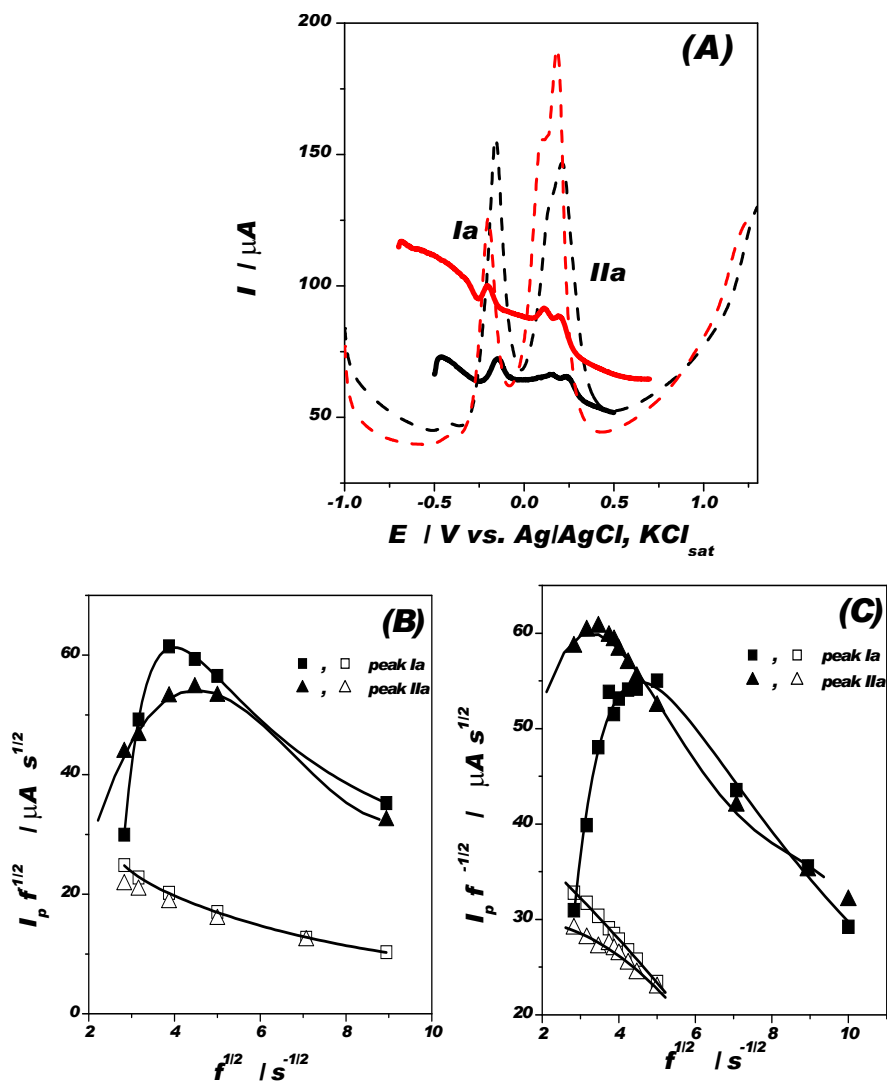


Figure 3. (A) Square-wave voltammograms of 10^{-3} M isoprenaline (red solid or dash line) and 10^{-3} M epinephrine (black solid or dash line) at G electrode (dash lines) and G/Pt-NP-chitosan (solid lines). Influence of SW frequency on the ratio of the SW peak current and the square root of the frequency for the oxidation of 10^{-3} M epinephrine (B) and 10^{-3} M isoprenaline (C) at graphite electrode (■, ▲) and G/NP-Pt-chitosan (□, △) electrode. Experimental conditions: electrolyte, 0.1 M phosphate buffer (pH 7); interval time, 0.1 s; initial potential, -1 V vs. $\text{Ag/AgCl, KCl}_{\text{sat}}$; step potential, 0.00195 V; amplitude, 50 mV; frequency, 10 s^{-1} .

constant, S is the electrode surface area, c_{OX}^* is the bulk concentration of the reactant Ox, R_{Ω} is the resistance of a thin film, f is the SW frequency and D is the diffusion coefficient.

Figures 3B and 3C show the dependence of the ratio $I_p f^{-1/2}$ on $f^{1/2}$ for the oxidation of 10^{-3} M isoprenaline and epinephrine, respectively. For both peak pairs, the maximum of the mentioned dependence at G electrode proves the existence of a quasi-reversible electrode process and the exponential decrease at G/Pt-NP-chitosan prove the diffusion-controlled oxidation process, as observed in the CV experiments. Also, the results are in good qualitative agreement with the theoretical variation predicted for an EC type mechanism [15].

CONCLUSIONS

A new modified electrode consisting by Pt nanoparticles immobilized in a biocompatible chitosan matrix on graphite surface was prepared employing a simple and general methodology.

At G and G/Pt-NP-Chitosan electrodes, epinephrine and isoprenaline having similar structures, cyclic voltammograms showed two pairs of peaks (peaks I and II), corresponding to a quasi-reversible redox processes. As expected, the presence of the Pt nanoparticles acts as a diffusion barrier on the electrode surface leading (i) to a decrease of the peak current intensities values, when electrodes were investigated by CV or SWV and (ii) to a negative shift of the redox formal potential of isoprenaline comparing to the epinephrine, when CV was used as investigation method.

The easy and low cost modified electrode containing Pt nanoparticles seems to be of great utility for making a voltammetric sensor for the detection of epinephrine and isoprenaline using cyclic or square wave voltammetry.

EXPERIMENTAL SECTION

Reagents

The p.a. quality of 4-[1-hidroxi-2-(izopropilamino)etil]benzen-1,2-diol (isoprenaline), (*R*)-4-(1-hidroxi-2-(metilamino)etil)benzen-1,2-diol (epinephrine) and chitosan were supplied by Sigma–Aldrich GmbH. The corresponding 10^{-3} M solutions of catecholamines were prepared in 0.1 M phosphate buffer solution (pH 7). The appropriate amounts of Na_2HPO_4 , NaH_2PO_4 , supplied also by Sigma, were used for preparing the 0.1 M phosphate buffer solution. Nanoparticles of Pt stabilised on graphite powder (Pt-NP) were a kindly gift from dr. Dan Goia (Clarkson University, Potsdam, USA) and is greatly acknowledged here. Acetic acid was purchased from Reactivul-Bucuresti.

Equipments

In order to investigate the electrochemical behavior of the compounds cyclic voltammetry (CV) and square-wave voltammetry (SWV) methods were used, employing a computer controlled - Autolab analytical unit (PGStat10, EcoChemie, Holland). For electrochemical measurements an undivided cell was used, equipped with the following three-electrodes: a modified graphite working electrode (Ringsdorff-Werke GmbH, Bonn-Bad Godesberg, Germany) (diameter 0.3 cm), an Ag/AgCl, KCl_{sat} reference electrode (Radiometer, France) and a Pt wire counter electrode. For comparison, all experiments were, also carried out on unmodified graphite. Before each experiment, the bare graphite was mirror-polished with different grit emery papers.

G/Pt-NP-Chitosan electrode modification

Chitosan (10 mg) was dissolved in 10 ml acetic acid 0.1 M. A suspension of 1 mg of Pt-nanoparticles in 500 μ L chitosan solution was strongly mixed by sonication, for 10 min. A volume of 5 μ L of the suspension was deposited on the bare freshly polished graphite electrode. The obtained G/Pt-NP-Chitosan electrodes were used after solvent evaporation.

ACKNOWLEDGEMENTS

G.L. Turdean acknowledges the financial support from PN-II-ID-PCE-2011-3-0366 grant.

REFERENCES

- [1] R.N. Goyal, S. Bishnoi, *Talanta*, **2011**, *84*, 78.
- [2] Y. Zeng, J. Yang, K. Wu, *Electrochimica Acta*, **2008**, *53*, 4615.
- [3] A. Ensafi, M. Taei, T. Khayamian, *Colloids and Surfaces B: Biointerfaces*, **2010**, *79*, 480.
- [4] A. Ensafi, E. Khoddami, H. Karimi-Maleh, *International Journal of Electrochemical Science*, **2011**, *6*, 2596.
- [5] M. Chen, X. Ma, X. Li, *Journal of Solid State Electrochemistry*, **2012**, 10.1007/s10008-012-1770-z].
- [6] X. Liu, D. Ye, L. Luo, Y. Ding, Y. Wang, Y. Chu, *Journal of Electroanalytical Chemistry*, **2012**, *665*, 1.
- [7] A. Cristian, A. Dobre, I. Sandu, A. Lungu, C. Mihailciuc, *Revue Roumaine de Chimie*, **2010**, *55*, 249.

- [8] S.-M. Chen, J.-Y. Chen, V. S. Vasantha, *Electrochimica Acta*, **2006**, 52, 455.
- [9] Y. Zeng, J. Yang, K. Wu, *Electrochimica Acta*, **2008**, 53, 4615.
- [10] J. Huo, J. Li, Q. Li, *Materials Science and Engineering C*, **2013**, 33, 507.
- [11] M. Mazloum-Ardakani, Z. Taleat, H. Beitollahi, H. Naeimi, *Chinese Chemical Letters*, **2011**, 22, 705.
- [12] Y. Li, X. Liu, W. Wei, *Electroanalysis*, **2011**, 23, 2832.
- [13] V. Mirceski, R. Gulaboski, F. Scholz, *Journal of Electroanalytical Chemistry*, **2004**, 566, 351.
- [14] V. Mirceski, A. Bobrowski, J. Zarebski, F. Spasovski, *Electrochimica Acta*, **2010**, 55, 8696.
- [15] F.J. Arévalo, P.G. Molina, M.A. Zón, H. Fernández, *Journal of Electroanalytical Chemistry*, **2008**, 619-620, 46.

*Dedicated to Professor Liviu Literat
On the occasion of his 85th birthday*

ELECTROCHEMICAL BEHAVIOR OF SOME CATECHOLAMINES INVESTIGATED BY CYCLIC AND SQUARE-WAVE VOLTAMMETRY

**ILEANA ELISABETA SILAI^a, GRAZIELLA LIANA TURDEAN^{a,*},
DORINA CASONI^b**

ABSTRACT. Electrochemical measurements of the oxidation of organic compounds can be helpful to understand how these compounds are metabolized by living organisms. Cyclic and square-wave voltammetry were used in view to estimate the electrochemical parameters of redox processes involving catecholamines compounds (isoprenaline, epinephrine, levonordefrin, norepinephrine, dopamine, d-DOPA and carbidopa). Redox processes related to catecholamines are quasi-reversible diffusion controlled reactions at a graphite electrode. According to the decreasing of the oxidation potential, the capacity to act as antioxidant of different catecholamines increases in the order: norepinephrine < levonordefrin < epinephrine < isoprenaline or carbidopa < d-DOPA < dopamine. Both series are influenced by the position of –OH and –NH₂ in *para*-alkyl substituents.

Keywords: *catecholamine, cyclic voltammetry, square wave voltammetry, antioxidant capacity.*

INTRODUCTION

Free radicals are highly reactive molecules generated by redox reactions in food, chemicals and even in living systems. Highly reactive free radicals and reactive oxygen species (ROS) present in biological systems can (i) oxidize nucleic acids, proteins and lipids, as a part of normal cell metabolism or (ii)

^a *Chemical Engineering Department, Babeş-Bolyai University, Faculty of Chemistry and Chemical Engineering, 11 Arany Janos Street, 400028 Cluj-Napoca, Romania, *gturdean@chem.ubbcluj.ro*

^b *Chemistry Department, Babeş-Bolyai University, Faculty of Chemistry and Chemical Engineering, 11 Arany Janos Street, 400028 Cluj-Napoca, Romania*

act in the course of free-radical-mediated diseases such as: *Diabetes mellitus*, cancer, rheumatoid arthritis, renal, cardiovascular, inflammatory, infectious and neurological diseases [1]. Biologically important ROS (including superoxide anion ($O_2^{\bullet-}$), singlet oxygen (O_2^1), hydrogen peroxide (H_2O_2), hypochlorous acid (HOCl), hydroxyl radical (OH^{\bullet}), peroxynitrite ($ONOO^-$), peroxy (ROO^{\bullet}) and alkoxy (RO^{\bullet})) represent the most important class of free radicals generated in living system. These compounds are eliminated from the body by their interaction with antioxidants. Antioxidants significantly delay or avoid the oxidation of easy oxidable substrates.

The antioxidants are classified in (i) low-molecular weight compounds (e.g. vitamins E and C, β -carotene, glutathione, uric acid, bilirubin etc.) and (ii) high-molecular weight compounds (e.g. protein albumin, ceruloplasmin, ferritin, superoxide dismutase, glutathione peroxidase, catalase etc.).

The total antioxidant capacity (TAC) is the expression of the overall activity of antioxidants and antioxidant enzymes. The determination of antioxidant capacity has been widely investigated by traditional analytical techniques, such as: spectrophotometry, fluorescence or chromatography. In the last years, electrochemical methods have opened new possibilities to investigate the antioxidant capacity.

According to their polyphenolic nature, and due to the presence of conjugate benzene rings and hydroxyl groups, catecholamines are a group of compounds exhibiting good natural antioxidant properties, by reacting rapidly with ROS. [2]. Compounds having antioxidant capacity are helpful in reducing and preventing damage from free radical reactions because of their ability to donate electrons which neutralize the radical without forming another [3]. Thus, it is performed the decrease of ROS toxic action and is prevented the chain reactions involving free radicals in organism.

The aim of this work was to establish a relationship between chemical structure, electrochemical parameters (formal standard potential) and antioxidant activity of catecholamines (isoprenaline, epinephrine, levonordefrin, norepinephrine, dopamine, d-DOPA and carbidopa) using different electrochemical techniques (cyclic voltammetry and square-wave voltammetry). The influence of the experimental conditions (scan rate and frequency) on the electrochemical behavior of the investigated compounds on graphite electrode allowed to understand the kinetics of the involved redox process.

RESULTS AND DISCUSSION

Electrochemical behavior of catecholamines

The electrochemical redox reactions of catecholamines at the graphite electrode were studied by both cyclic voltammetry (CV) and square-wave voltammetry (SWV). Selected cyclic voltammograms recorded in the 10^{-3} M

solution of catecholamines in the supporting electrolyte are presented in figures 1 A, B.

Within the potential range where the redox behavior of catecholamines is visible, the supporting electrolyte shows no characteristic peaks, besides charging the electrical double layer (thin lines in figures 1A, B).

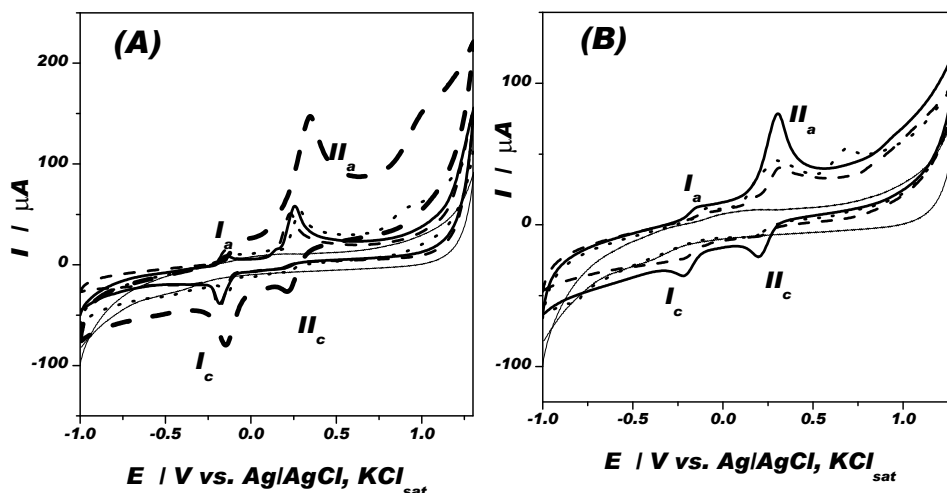


Figure 1. Cyclic voltammograms of 10^{-3} M isoprenaline (solid thick line), epinephrine (dash line), levonordeprine (dot line), norepinephrine (thick dash line) (A) and dopamine (solid thick line), d-DOPA (dash line), carbidopa (dot line) (B) at graphite electrode. Experimental conditions: electrolyte, 0.1 M phosphate buffer solution (pH 7) (solid thin lines); starting potential, -1 V vs. Ag/AgCl, KCl_{sat} ; scan rate, 50 mV/s.

Cyclic voltammograms recorded in the catecholamines solutions (Figures 1A, B) show two pairs of peaks which characterize a global redox process of these compounds involving two protons, two-electron, as described by the typical reaction (1) for dopamine [4, 5].

It is worth to mention, that although, the current intensity of either the first, or the second anodic or cathodic peak is much smaller than the mirror corresponding one, this behavior proves a quasi-reversible redox behavior of the investigated catecholamine compounds.

The SWV investigation technique was chosen for the study of the catecholamines because it is the most advanced and most sophisticated method from the pulse voltammetric techniques and exhibits the advantages of a large speed and high sensitivity [6].

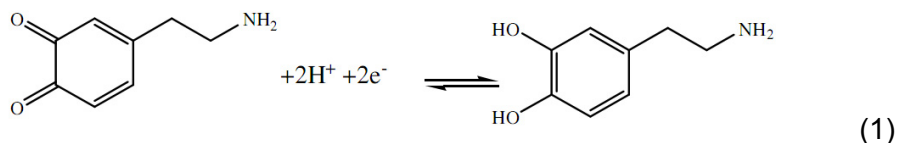


Figure 2 summarize the SW voltammograms obtained for the different catecholamines.

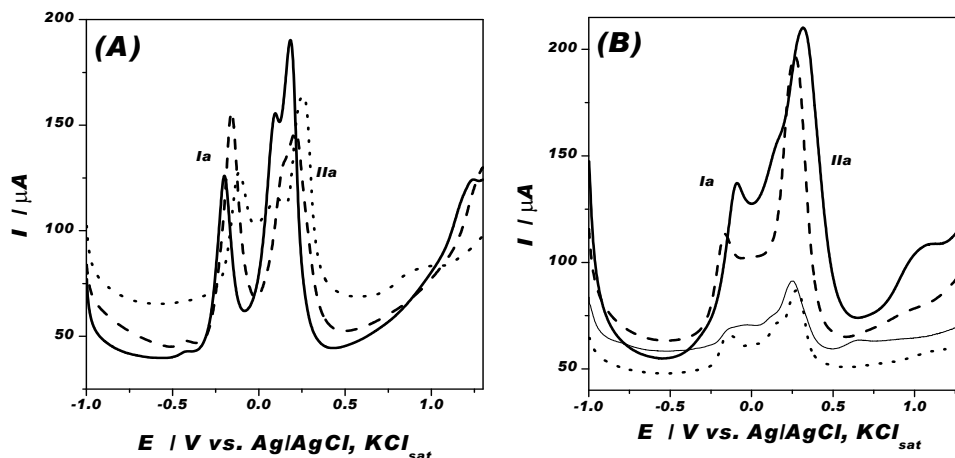


Figure 2. Square-wave voltammograms of 10^{-3} M isoprenaline (solid thick line), epinephrine (dash line), levonordefrine (dot line) (A) and norepinephrine (solid thick line), dopamine (dash line), d-DOPA (dot line) and carbidopa (solid thin line) (B) at graphite electrode. Experimental conditions: electrolyte, 0.1 M phosphate buffer (pH 7); initial potential, -1 V vs. Ag/AgCl, KCl_{sat}; step potential, 0.002 V; amplitude, 50 mV; frequency 10 s^{-1} .

The oxidation potentials (E_{pa}) and the estimated formal standard potential ($E^{0'}$) of the first and second anodic peaks for the studied catecholamines, by both SWV and CV techniques, are reported comparatively in table 1. The data of the table shows that in all cases, the peak potential for the anodic peak I or II is shifted to negative values with at least 50 mV in the SWV, than in the CV technique, because of the different experimental conditions.

Also, it is well-known that lower oxidation potentials correspond to a higher ability of a compound to donate an electron and therefore to act as an antioxidant. It is important to underline that the oxidation potential, because of its thermodynamic nature, does not give any information about the reaction rate. Although the oxidation process takes place at the two -OH groups linked to the benzene ring as described in the above reaction, it is probably that the presence of -OH, = O or -CH₃ groups on the ramification branch promotes or not this process.

Table 1. Electrochemical parameters for the studied catechoamines.
Experimental conditions: see figures 1 and 2.

Catechoaminic compounds	CV, $v = 50 \text{ mV/s}$				SWV, $f = 10 \text{ s}^{-1}$	
	Peak Ia		Peak IIa		Peak Ia	Peak IIa
	$E_{pa} /$	$E^{0'} /$	$E_{pa} /$	$E^{0'} /$	$E_{pa} /$	$E_{pa} /$
	V vs. ER					
isoprenaline	-0.150	-0.168	0.255	0.220	-0.201	0.184
epinephrine	-0.146	-0.166	0.230	0.196	-0.159	0.212
levonordefrin	-0.097	-0.119	0.289	0.255	-0.117	0.254
norepinephrine	-0.067	-0.107	0.343	0.285	-0.098	0.315
dopamine	-0.141	-0.178	0.284	0.243	-0.171	0.266
d-DOPA	-0.107	-0.161	0.313	0.260	-0.140	0.275
carbidopa	0.289	0.231	0.685	-	-0.131	0.254

$E^{0'}$ is the mean value of anodic peak potential (E_{pa}) and cathodic peak potential (E_{pc}).

The catecholamine derivatives with electron-donating *para*-alkyl substituents were oxidized more easily depending on the position of the $-\text{OH}$ and $-\text{NH}_2$ groups on the ramification branch. The effect of a conjugated double bond ($=\text{O}$) was, moreover, well evidenced, by the lowest oxidation potentials of d-DOPA and carbidopa comparing with dopamine [7].

Analyzing the influence of the intensity of the inductive/electromeric effect of substituents on the N atom in position 1 of the branches of the benzenic ring it can be concluded:

- For levonordefrin and norepinephrine, the substituent H does not induce any inductive effect and consequently the antioxidant behavior is similarly, confirmed by the quasi - identical values of the standard formal potential ($E^{0'}_{\text{levonordefrin}} = -0.119 \text{ V}$ and $E^{0'}_{\text{norepinephrine}} = -0.107 \text{ V}$).

- For epinephrine and isoprenaline the $-\text{CH}_3$ (methyl) and $-\text{CH}(\text{CH}_3)_2$ (isopropyl) groups induce a positive inductive effect (+ I) increasing in the order methyl < isopropyl, which is neglected for antioxidant capacity because of the similitude of the standard formal potential values ($E^{0'}_{\text{epinephrine}} = -0.166 \text{ V}$ and $E^{0'}_{\text{isoprenaline}} = -0.168 \text{ V}$), probably because is too far away from the oxidation site.

- Although the difference between dopamine and d-DOPA is the presence of a $-\text{COOH}$ group which induces an electromeric effect overlapped on the inductive one (due to $-\text{NH}_2$ group), their antioxidant capacity were not significantly different (close $E^{0'}$ values, $E^{0'}_{\text{dopamine}} = -0.178 \text{ V}$, $E^{0'}_{\text{d-dopa}} = -0.161 \text{ V}$).

- Significant difference is observed between the antioxidant capacity of d-DOPA and carbidopa ($E^{0'}_{\text{d-dopa}} = -0.161 \text{ V}$ and $E^{0'}_{\text{carbidopa}} = 0.231 \text{ V}$). The presence of C-NH-NH₂ having electromeric effect (+ E) lower than that of the $-\text{COOH}$ group of carbidopa could be considered negligible in relation to the electromeric effect of $-\text{COOH}$ group of d-DOPA.

Influence of scan rate and frequency

In order to establish the type of control corresponding to the studied redox reactions, cyclic voltammetry experiments were carried out at various scan rates. At pH 7, from cyclic voltammograms of different catecholamines, the peak current intensities of peak I depend linearly on the square root of the scan rate (figure 3), how it was expected for diffusion controlled redox process.

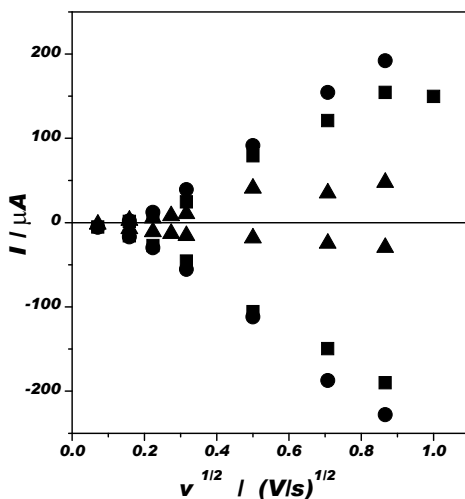


Figure 3. Influence of the scan rate on the peak current intensity of peak I for 10^{-3} M isoprenaline (■) epinephrine (●) and levonordefrin (▲). Experimental conditions: see figure 1.

This behavior is associated especially with a fast electron transfer in studied catecholamines. Also, from figure 3 could be seen, the ratio of both anodic and cathodic peak current is constant at different scan rates, confirming the quasi-reversible redox electrode process [4].

Figure 4 shows the dependence of the ratio $I_p f^{1/2}$ on $f^{1/2}$ for the oxidation of 10^{-3} M isoprenaline at graphite electrode. Note that the ratio $I_p f^{1/2}$ corresponds to the dimensionless net-peak current Φ ($\Phi = I_p(nFS c_{OX}^*)^{-1}(Df)^{-1/2}$) and the $f^{1/2}$ to the resistance parameter q ($q = R_{\Omega}(n^2F^2/RT)S c_{OX}^*(Df)^{1/2}$, (where n is the number of electrons, F is the Faraday constant, S is the electrode surface area, c_{OX}^* is the bulk concentration of the reactant Ox , R_{Ω} is the resistance of a thin film, f is the SW frequency and D is the diffusion coefficient).

For both peaks, the dependence $I_p f^{1/2}$ vs. $f^{1/2}$ is associated with a well-developed maximum corresponding to reversible electrode reactions [8, 9].

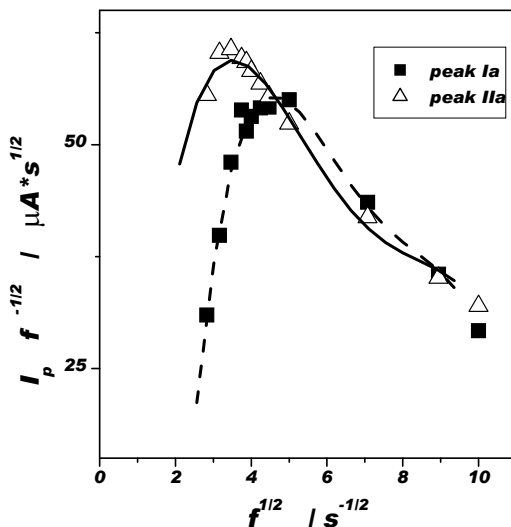


Figure 4. The influence of the SW frequency on the ratio of the SW peak current and the square root of the frequency for the oxidation of 10^{-3} M isoprenaline at graphite electrode. Experimental conditions: see figure 2.

CONCLUSIONS

Although based on different approaches, the use of both cyclic and square-wave voltammetry investigation techniques showed the effect of the -OH and -NH₂ groups of *para*-alkyl substituents on the antioxidant capacity of the studied catecholamine compounds. It is well-known that the antioxidant capacity increases with the decrease of the oxidation potential. Thus, for the studied catecholamines the antioxidant capacity increase in the following order: norepinephrine < levonordefrin < epinephrine < isoprenaline or carbidopa < d-DOPA < dopamine.

Based on the importance of the intermediate oxidation products and the ability to control the redox process by electrochemical and selective methods (e.g., under potentiostatic conditions), further study of these compounds is required to fully achieve their potential applicability in both ageing and therapeutic processes.

EXPERIMENTAL SECTION

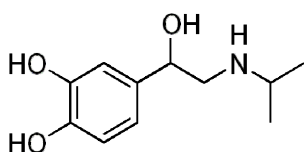
Reagents

The following compounds, with different number of -OH and -NH₂ groups, were used:

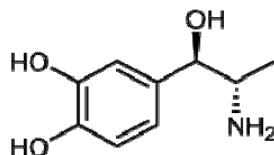
- 4-[1-hidroxi-2-(izopropilamino)etil]benzen-1,2-diol (isoprenaline),
- (*R*)-4-(1-hidroxi-2-(metilamino)etil)benzen-1,2-diol (epinephrine),
- 4-[(1*R*,2*S*)-2-amino-1-hidroxypropyl]benzene-1,2-diol (levonordefrin),
- 4-[(1*R*)-2-amino-1-hidroxyetil]benzene-1,2-diol (norepinephrine),
- 4-(2-aminoetil)benzen-1,2-diol (dopamine) and
- (*R*)-2-Amino-3-(3,4-dihidroxyfenil)propanoic acid (d-DOPA)
- (2*S*)-3-(3,4-dihidroxyfenil)-2-hidrazino-2-metilpropanoic acid (carbidopa)

These p.a. quality compounds were supplied by Sigma–Aldrich GmbH and the corresponding 10^{-3} M solutions were prepared in 0.1M phosphate buffer solution (pH 7). The structures of the studied compounds are shown in figure 5.

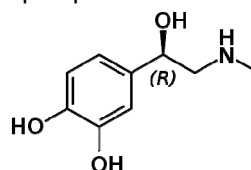
Isoprenaline



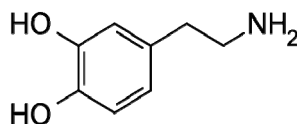
Levonordefrin



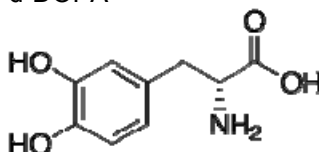
Epinephrine



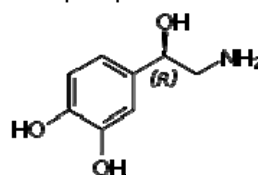
Dopamine



d-DOPA



Norepinephrine



carbidopa

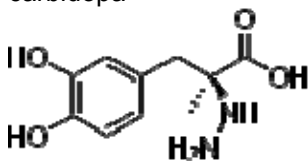


Figure 5. Structures of studied catecholaminic compounds.

The appropriate amounts of Na_2HPO_4 , NaH_2PO_4 , supplied also by Sigma, were used for preparing the 0.1M phosphate buffer solution.

Equipments

In order to assess the electrochemical behavior of the investigated compounds cyclic voltammetry (CV) and square-wave voltammetry (SWV) methods were used, employing a computer controlled - Autolab analytical

unit (PGStat10, EcoChemie, Holland). For measurements was used an undivided cell equipped with following three-electrodes: a graphite working electrode (Ringsdorff, Germany) (diameter 0.3 cm), an Ag/AgCl, KCl_{sat} reference electrode (Radiometer, France) and a Pt wire counter electrode. The working electrode was mirror-polished with graded alumina powder prior to each experiment.

ACKNOWLEDGEMENTS

The authors acknowledge the financial support from PN-II-ID-PCE-2011-3-0366 grant.

REFERENCES

- [1] J. Psotova, J. Zahalkova, J. Hrbac, V. Simanek, J. Bartek, *Biomedical Papers*, **2001**, *145*, 81.
- [2] E.I. Korotkova, O.A. Voronova, E.V. Dorozhko, *Journal of Solid State Electrochemistry*, **2012**, *16*, 2435.
- [3] A. Masek, M. Zaborski, E. Chrzescijanska, *Food Chemistry*, **2011**, *127*, 699.
- [4] H. Mohammad-Shiri, M. Ghaemi, S. Riahi, A. Akbari-Sehat, *International Journal of Electrochemical Science*, **2011**, *6*, 317.
- [5] S.-M. Chen, J.-Y. Chen, V. S. Vasantha, *Electrochimica Acta*, **2006**, *52*, 455.
- [6] Y. Li, X. Liu, W. Wei, *Electroanalysis*, **2011**, *23*, 2832.
- [7] R. Bortolomeazzi, N. Sebastianutto, R. Toniolo, A. Pizzariello, *Food Chemistry*, **2007**, *100*, 1481.
- [8] V. Mirceski, R. Gulaboski, F. Scholz, *Journal of Electroanalytical Chemistry*, **2004**, *566*, 351.
- [9] V. Mirceski, A. Bobrowski, J. Zarebski, F. Spasovski, *Electrochimica Acta*, **2010**, *55*, 8696.

*Dedicated to Professor Liviu Literat
On the occasion of his 85th birthday*

RECYCLING SOLID WASTES AS POLYMER COMPOSITES

**ION ROPOTA^a, MIHAI BRATU^b, DRAGA DRAGNEA^c,
OVIDIU DUMITRESCU^{c,*}, OVIDIU MUNTEAN^c, MARCELA MUNTEAN^c**

ABSTRACT. Recycling and / or reuse of by-products (waste) is a goal to be achieved under the current economic and ecological crisis. The reuse of waste leads to saving energy and raw materials reduces environmental pollution and risk factors for public health and so on. The solid organic or inorganic wastes have been immobilized in polymer resins used as a binder matrix. All obtained composites present very good physical-mechanical properties: high hardness, good strengths at abrasion and the compressive strengths are all above 90 MPa. They also have good thermal stability at high temperature variation and high stability in different aggressive media. Some of such polymeric composites have good sound absorption capacity depending on the proportion and nature of the waste used.

Keywords: *Solid wastes recycling, polymer composites, noise attenuation, organic wastes; inorganic wastes*

INTRODUCTION

Composites are materials made by the association of at least two components whose properties complement each other, thus results a material with properties superior to either component alone.

^a Plastic Art College "Dimitru Paciurea", Str. Baiculești 29, Bucharest, Romania

^b National Research & Development Institute for Industrial Ecology - ECOIND, Str. Panduri 90-92, Bucharest, Romania

^c University "POLITEHNICA" Bucharest, Dep. Oxide Materials Science & Engineering, Str. Polizu 1-7, Bucharest, Romania

* Corresponding author: ovidiu_d_dumitrescu@yahoo.fr ; Phone: +40.722430189

A special class is represented by the polymer composites [1]. Of all composites, the metal ones occupy 10 ÷ 15%, the ceramic composites 15 ÷ 20% and the polymer composites represent 70 ÷ 75%.

The polymer composites have expanded because they have a number of technological advantages compared to ceramics and metals: do not require high temperature, long period of times and complicated processes for obtaining and finishing. They can be easily processed at low temperatures, with no danger of destruction of reinforcement materials.

Solid wastes recovery in various types of composite materials has many environmental impacts and represents an economic advantage. Every type of solid waste results from processes which requires significant quantities of resources, primarily fossil fuels, both as a raw material and as a source of energy for the manufacturing process. Therefore, their recovery in such special composite with high durability involves significant economic and ecological effects.

Recycling and/or reuse of by-products (waste) is a goal to be achieved under the current economic and ecological crisis. Ecosystem problems are acute problems in the current context of sustainable development. The reuse of waste leads to important savings of raw materials and energy. Also reduces pollution of the environment factors and decrease risk factors for public health.

To date, the purpose of the composite materials technology is to recover wastes and other recycled substances and to obtain new and performing materials with long life cycle [1-3].

The fields of application of polymer composites can be enlarged depending upon the properties of composite materials [1,2,4-6]. For example, dense materials can be obtained very resistant with high durability in an epoxy polymer matrix or unsaturated polyester type resin, but also, some porous composites polyester or formaldehyde resins can be obtained with good sound absorption capacity.

The waste composition is influenced by many factors [7] as: the level of economic development, the cultural norms, the geographical location, energy sources, climate and others.

Global composition of wastes in 2009 [7] is illustrated in Figure 1:

Table 1. Types of waste and their sources [7]

Type	Sources
Organic	Food scraps, yard waste, wood, process residue
Paper	Paper scraps, cardboard, newspapers, magazines, bags, boxes, wrapping paper, telephone books, shredded paper, paper beverage cups.
Plastic	Bottles, packaging, containers, bags, lids, cups

RECYCLING SOLID WASTES AS POLYMER COMPOSITES

Type	Sources
Glass	Bottles, broken glassware, light bulbs, coloured glass
Metal	Cans, foil, tins, non-hazardous cans, appliances, railings, bicycles
Other	Textiles, leather, rubber, multilaminates, appliances, ash, other inert materials

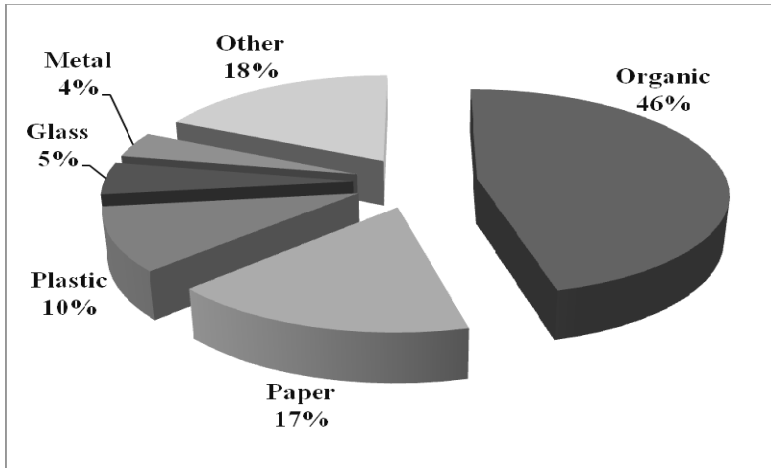


Figure 1. Global waste composition.

Table 2 shows the countries that produce the most trash in the world [8].

Table 2. The countries that produce the most trash in the world [8].

No.	Country	Quantity of trash/year, [million tons]
1	China	300
2	United States	236
3	Russia	200
4	Japan	52.36
5	Germany	48.84
6	United Kingdom	34.85
7	Mexico	32.17
8	France	32.17
9	Italy	29.74
10	Spain	26.34
11	Turkey	25.99

According to European Trade Association for Plastic Manufacturers, 265 millions tones of plastic are produced globally each year. The impacts of plastic waste on our health and the environment are only just becoming apparent. Most of our knowledge is around plastic waste in the marine

environment and once the plastic waste enters the oceans it is influenced by global currents that distribute it around the world [9]. Some researches indicate that plastic waste in landfill and in badly managed recycling systems also could have an impact, mainly from the chemicals contained in plastic. Other important wastes are wood chips and rubber powder. The wood chips waste is generated by constructions, commercial and industrial works, including furniture manufacture, and municipal wood waste. The used tires are in large quantities and are extremely cheap for the production of rubber powder [10,11]. Therefore, the immobilization of these wastes using fastest and cheapest methods is a current challenge.

EXPERIMENTAL SECTION

To obtain polymer composite materials the solid wastes of organic or inorganic nature were mixed with a polymer matrix, as a binder system, that. Four classes of resins with different behaviour at hardening were used: epoxy and unsaturated polyester resins which are hardened at room temperature and polyester or formaldehyde resins which are hardened following some thermal treatment. In what follows the resins are depicted as:

- Epoxy (E), in which the corresponding hardening component was tetra-triethylentetramine;
- Unsaturated polyester resin: isophthalic (IPh), orthophthalic (OPh) and orthophthalic with additive (OPha) with peroxide methyl cetone as the hardening component;
- Polyester (Pe) resins;
- Formaldehyde (F) resins: phenol-formaldehyde (PhF), urea-formaldehyde (UF) and melamine-formaldehyde (MF) resins.

The resins characteristics are presented in detail in the PhD thesis [1,6]. Because the resins are hydrophobic it is absolutely necessary to make a dry preparation of solid wastes composite. The presence of water determines a decrease of the mechanical properties.

Both unsaturated polyester and epoxy resins were hardened in presence of hardening component (tetra-triethylentetramine for epoxy and peroxide methylcetone for polyester) at room temperature, while the formaldehyde and saturated polyester resins were hardened at thermal curing at 80-120°C.

As reinforcement materials were used inorganic and organic solid wastes.

Organic wastes: polyethylene terephthalate (PET) flakes and granules, polypropylene (PP) / polystyrene (PS) granules, rubber powder and wood chips.

Inorganic wastes: silica sand, cullet and glass fiber, furnace slag from thermal power stations, steel slag, fly ash and burned husks ash.

The granulometry of the reinforcing agent was chosen depending on the properties that one wants to achieve for the composite material. Generally, the maximum dimension of solid waste used as reinforcement materials of polymer matrix was 3 mm. Only the size of wood chips was up to 5 mm. Granulometric spectrum of each type of waste used was carefully controlled.

Thus, all inorganic wastes were characterized by the same size distribution. For example, the sand, slag and cullet granulometry was quite similar: the fraction $0 \div 0.3$ mm represents 48-50%, that of $0.3 \div 1$ mm is 40 \div 42% and the higher fraction $1.00 \div 3.00$ mm is only 9 \div 10% mass. Other solid wastes, such as fly ash and husk ash, are characterized by very fine particles: the particles under 100 μm was 85% by mass.

Organic wastes as (PET) flakes and granules, (PP)/(PS) granules, rubber powder and wood chips were very different in size. As example, rubber powder was very fine, more than 96% of mass was under 1 mm, while the wood chips have dimensions between $0.1 \div 5$ mm.

For all type of resins and reinforcement agent the flow chart of polymer composites preparation, in laboratory, is very similar - Figure 2. The reinforcement agent, the resin and the hardening component (as applicable) are dosed with an accuracy of $\pm 0.01 \div 0.03$ g for a batch of 100 g. The mass ratio between solid waste and resin was $(73 \div 85) / (15 \div 27)$ that to obtain a good viscosity, and therefore a good workability for the composite samples. The homogenization was performed very intensive in a shock resistant container. The mixture was then cast in properly cleaned and lubricated forms.

As mentioned, the hardening of composite material takes place as follows: 5 hours at room temperature in the presence of hardening component or by heating at 120°C for 4 hours followed by cooling at room temperature.

The resulted composites have been tested for mechanical properties (compressive and flexural strength), density, water adsorption–open porosity, resistance to freezing, chemical stability in water at 100°C and in aggressive media solutions. For composite samples with controlled porosity the capacity of sound absorption has been determined. The composites structure has been examined by SEM and by selection the elemental chemical analysis at the interface was evidenced.

RESULTS AND DISCUSSION

The physical and mechanical properties of synthesized composites depend both on the nature and the characteristics of reinforcement agent, and on the nature of polymer matrix. From this point of view the epoxy composites

with inorganic wastes reinforcement have the best behaviour – see Figure 3 and 4.

After 4 curing days a remarkable compressive strengths have the epoxy composites with sand, steel slag, cullet and flay ash ($R_c = 114 \div 129$ MPa). Such values are superior even to those of special high-strength concretes.

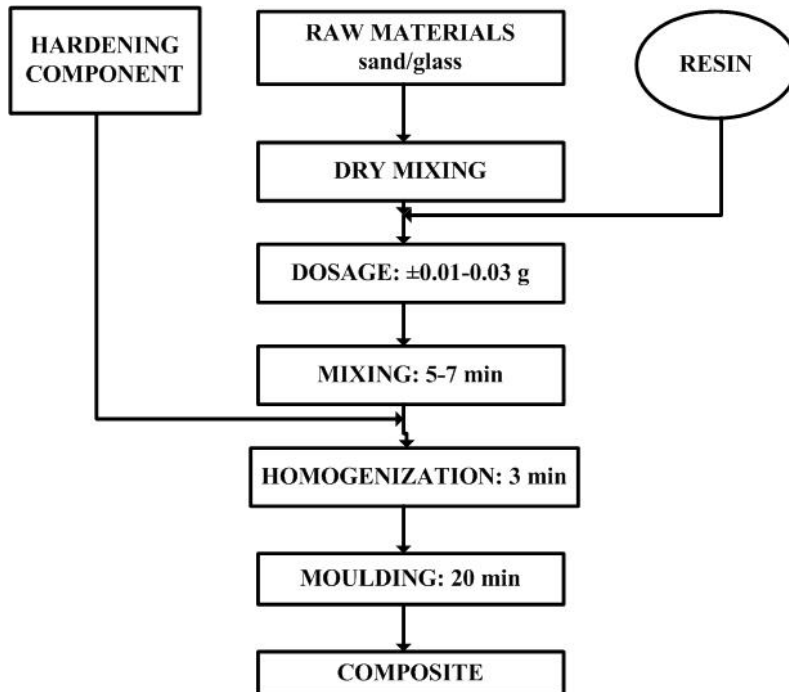


Figure 2. Flow diagram of laboratory polymer composites preparation

The composites with husks ash, PET granules or flakes, PP/PS granules and wood chips have less compressive strength ($R_c = 77 \div 89$ MPa) and those with rubber powder have rather small resistances to compression ($R_c = 43$ MPa).

A direct dependence between the density and the compressive strength was evidenced. The density of the polymer composites for the same resin is directly affected by the nature of reinforcement materials, respectively their density.

In terms of flexural strength, things are a little different. Thus, one finds the best flexural behaviour of reinforced polymer composite with wood chips ($R_i = 41$ MPa). This decreases in the series:

Wood chips (41) > rubber powder (38) > PET granules (32) > PP/PS granules (31) > PET flakes (30)

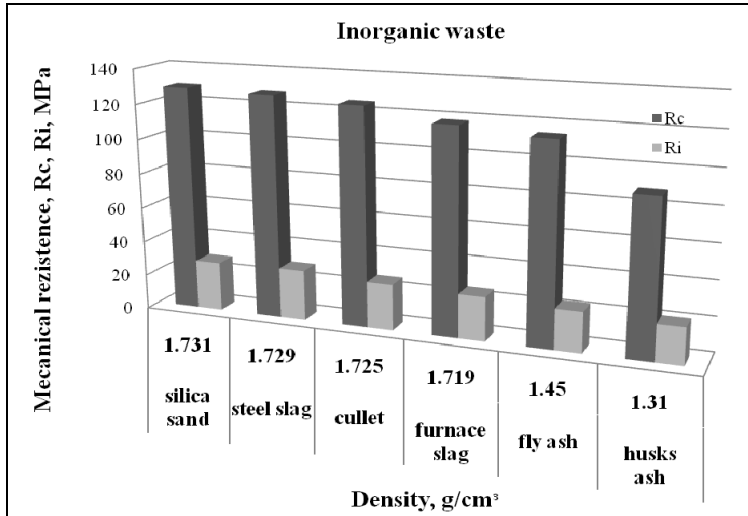


Figure 3. Compressive and flexural strength (MPa) vs. density (g/cm³) for some inorganic wastes.

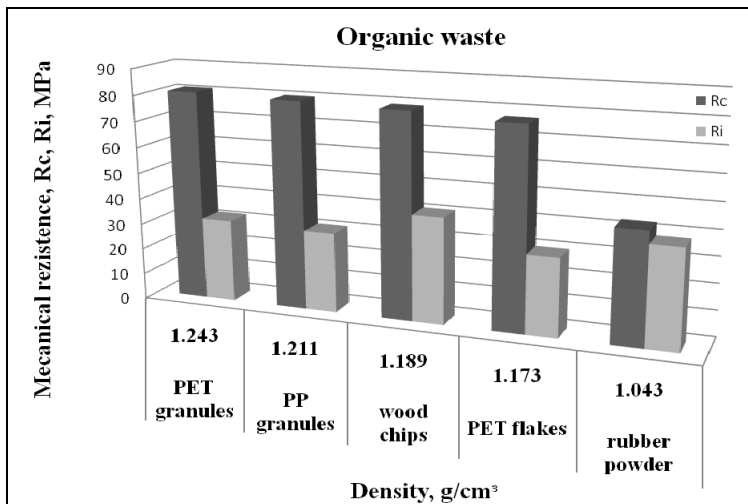


Figure 4. Compressive and flexural strength (MPa) vs. density (g/cm³) for some organic wastes.

The flexural strength for polymer reinforced with inorganic wastes decreases reaching 21 MPa when husks ash was used as reinforcement agent.

All this can be explained by structural changes of the polymer composite in presence of different reinforcement materials. When dense wastes as reinforcing agent in the polymer structure are used successive layers of resin occur on the surface of reinforcing grains, resulting a compact material, with good mechanical properties - Figures 5, 6. Between epoxy matrix and inorganic wastes there is a very good compatibility. Also, a good compatibility exists between epoxy resin and PET granules (Figure 7) or PET flakes (Figure 8).

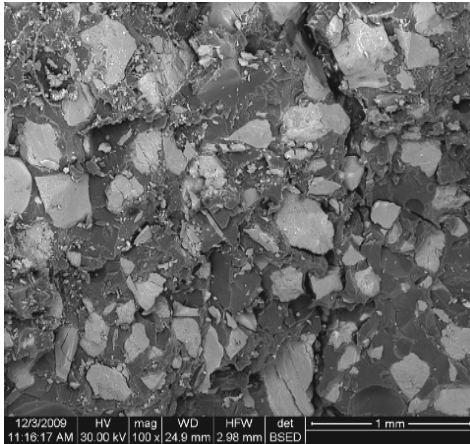


Figure 5. Composite with silica sand

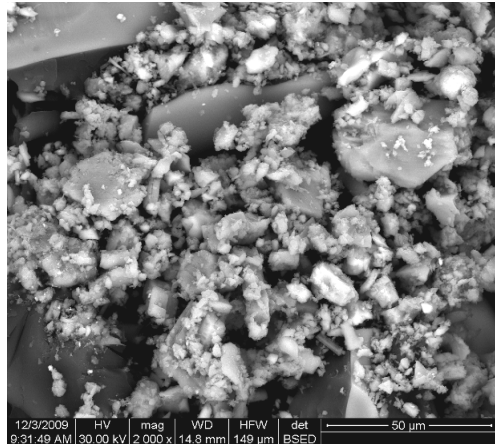


Figure 6. Composite with cullet

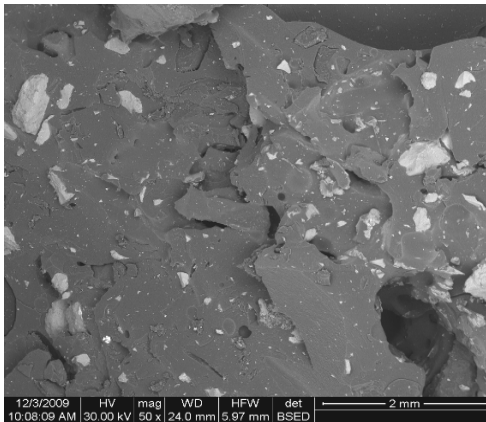


Figure 7. Composite with PET granules

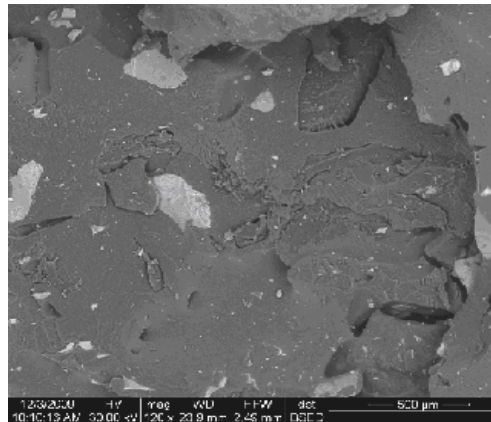


Figure 8. Composite with PET flakes

If the rubber powder was used as reinforcement agent in the epoxy composite often occur some areas not covered completely with resin and there are numerous pores in the structure, which explains the poor behaviour

in compression of the samples - Figure 9 and 10. However, due to the elastic nature of the rubber powder, the flexural strength is good in comparison with other reinforcing agents.

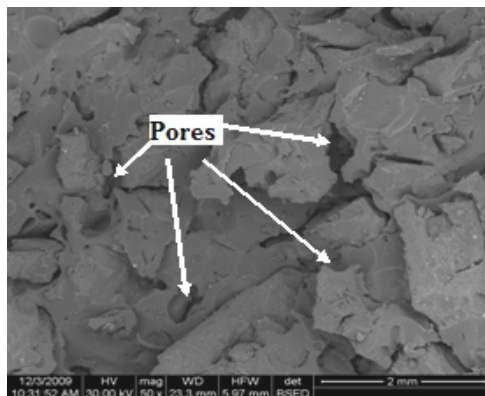


Figure 9. Composite with rubber powder

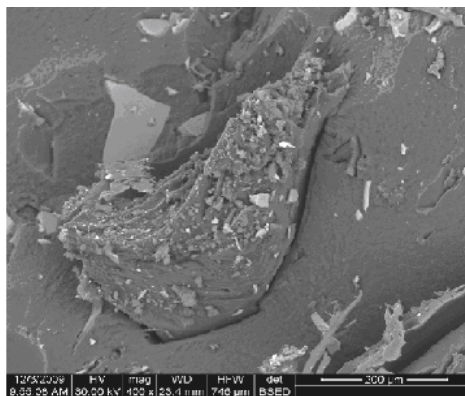


Figure 10. Composite with cullet and rubber powder

Thus, depending on the property that one wishes to improve, for example, the compression or the flexural strengths suitable mixtures of the reinforcing agents could be used. When the same reinforcement agent was used it was important to choose the matching resin. As expected, the resin type, together with the aggregate type are those which determine the polymer composite properties.

In all cases, for every type of solid waste used as reinforced material, the epoxy resin composites showed higher mechanical properties in comparison with other resins. Thus, from the three unsaturated polyester resins categories, only isophthalic, resin shows a good behaviour of composite samples from mechanical point of view - Figure 11.

The other two, orthophthalic (OPh) and orthophthalic with additive (OPha) resins generated porous polymer composites with a structure more heterogeneous in comparison with epoxy or isophthalic mass matrix (see Figure 11 and Figure 12-15).

In this case, the use of rubber powder as reinforcement leads to a heterogeneous structures (Figure 12 compared to composites made from the same resin (isophthalic) but with glass aggregate (Figure 13), sand (Figure 14) or PET (Figure 15). As can be seen from Figure 11, the polyester and the formaldehyde resins (PhF, UF and MF) also form weaker matrix of polymer composites.

It should be noted that, although the rubber powder has an advanced fine (more than 96% of the mass was under 1 mm), its embedding in resin has been developed with difficulty regardless of the type of resin used. It is necessary to use a filler to improve the adhesion.

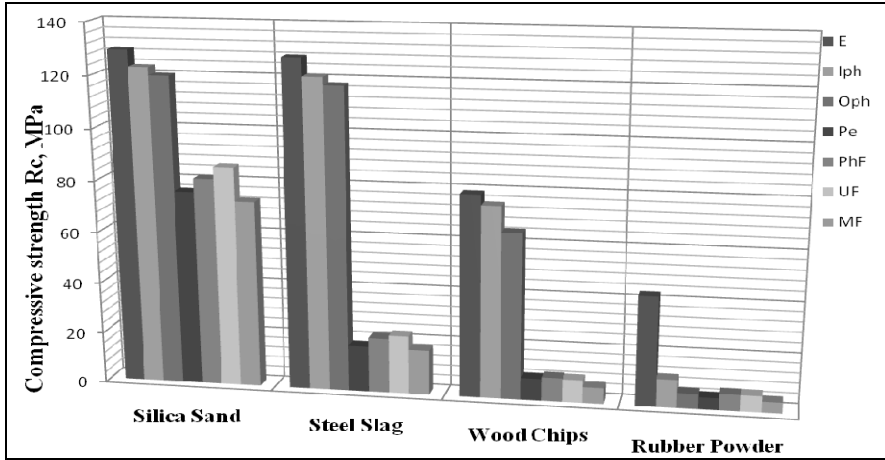


Figure 11. Compressive strength for different resins

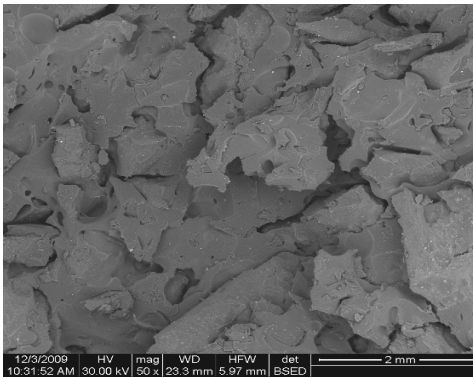


Figure 12. Rubber powder polyester composite (Iph)

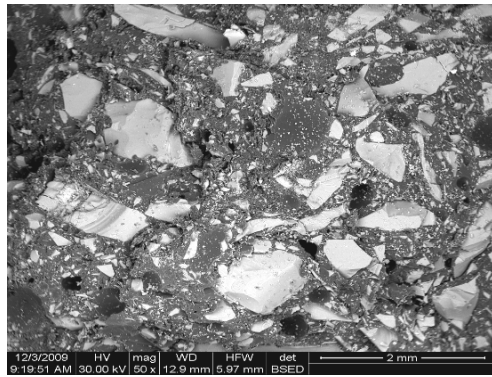


Figure 13. Glass polyester composite (Iph)

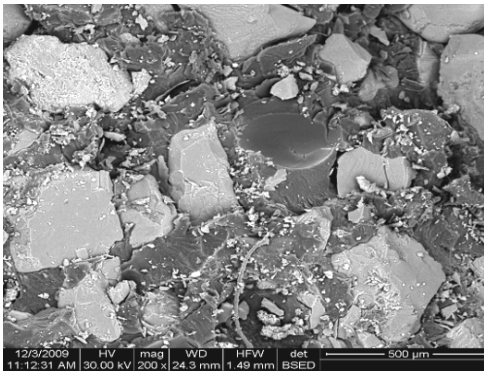


Figure 14. Sand polyester composite (Iph)

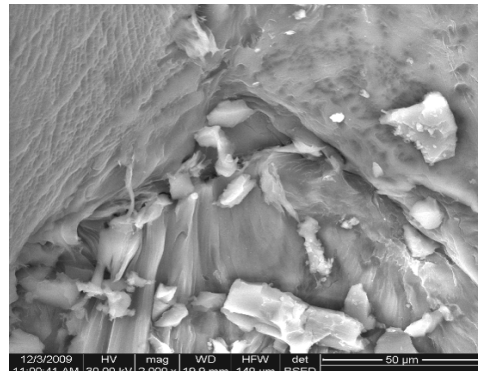


Figure 15. PET flakes polyester composite (Iph)

The compact structure of epoxy and the isophthalic composites which have practically zero porosity give their high stability [12]. There were no observed losses of mass or decreases in mechanical properties at freeze-thaw, or when they were kept in the hot water at 100°C or other aggressive media at ambient temperature [12]. These composites can be used in construction for pedestrian walkways, floors in areas subject to corrosion or other aggressive environmental actions, rehabilitation of buildings in earthquake zones, seal tanks, reservoirs, swimming pools etc. They also have good thermal stability and high stability in different aggressive media.

As has been mentioned above, the composites which have as organic matrix polyester and formaldehyde resins (PhF, UF and MF) led to more diverse structural composite materials with high porosity, often more than 10-12% and inhomogeneities in the structure.

Thus, polymer composites reinforced with wood chips (Figure 16) or steel slag (Figure 17), with high porosity, above 25 – 46 % have a high capacity for noise absorption [6]. Although, they do not have very high mechanical strength (35÷48 MPa), however, one can obtain composite panels used as noise protection materials. SEM analyses show very clear an inhomogeneous structure with large pores with various dimensions. In the same time, the elemental analysis of the interface between reinforced aggregate and resin evidences a good interaction between the composite phases.

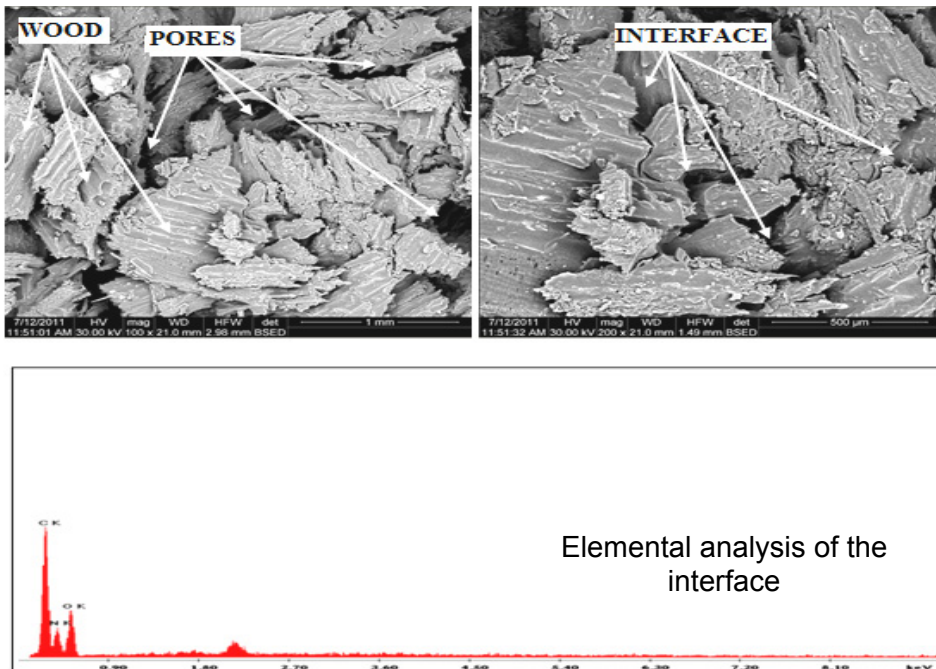
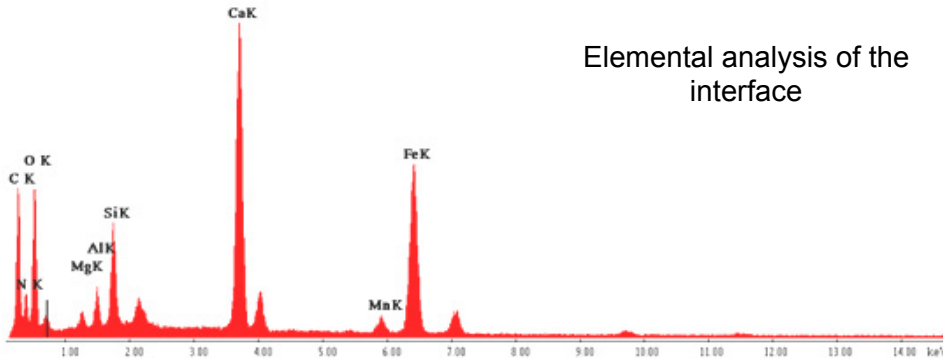
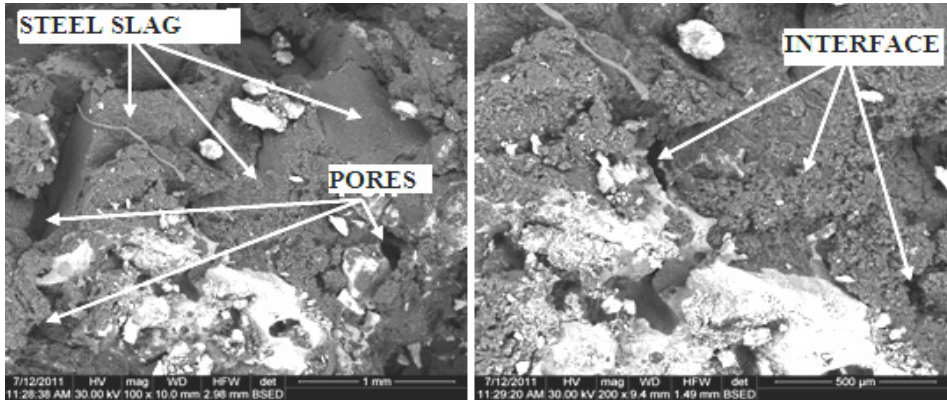


Figure 16. Wood chips formaldehyde composite (PhF), ≥ 25 - 46 %



Elemental analysis of the interface

Figure 17. Steel slag formaldehyde composite (PhF), porosity $\geq 42\%$

Both materials were characterized by a good sound absorption coefficient (class A and class B) [5,6] and can be used to manufacture absorbent panels to be used in industry, transport, road rails or air.

CONCLUSIONS

From the above results the main conclusions are:

One can obtain polymer composites with various solid wastes as reinforcing agent and different type of resins as organic matrix;

Some composites evidenced excellent physical and mechanical properties especially when epoxy or isophthalic resins were used;

Porous polymer composites based on phenol-formaldehyde resin and wood waste or steel slag were obtained with good sound absorption capacity.

REFERENCES

1. I. Ropota, "Polymeric Composites with Special Purpose", PhD Thesis, University Politehnica of Bucharest, **2010**.
2. I. Ropota, E. Zamfirache, M. Muntean, *Environmental Engineering and Management Journal*, **2009**, 8(4), 931.
3. K.A. Hossain, F.I. Khan., K. Hawboldt, *Journal of Hazardous Materials*, **2008**, 150, 4.
4. I. Ropotă, O. Dumitrescu, M. Muntean, *International Review of Chemical Engineering (I.RE.CH.E.)*, **2010**, 2(3), 430.
5. M. Bratu, I. Ropota, O. Vasile, O. Dumitrescu, M. Muntean, *Romanian Journal of Materials*, **2011**, 41(2), 147.
6. M. Bratu, "Ecological composite materials for noise reduction", PhD Thesis, University Politehnica of Bucharest, **2012**.
7. Information on <http://siteresources.worldbank.org/INTURBANDEVELOPMENT/Resources/336387-1334852610766/Chap5.pdf> (last citation February **2013**)
8. Information on <http://greenanswers.com/q/63410/recycling-waste/garbage/what-countries-produce-most-trash> (last citation March **2013**).
9. Information on <http://www.plasticoceans.net/the-facts/a-global-issue/>
10. Information on <http://www.guardian.co.uk/environment/2011/dec/29/plastic-packaging-waste-solution> (last citation March **2013**).
11. Information on <http://www.wealthywaste.com/rubber-powder-from-waste-tyres-an-approach-to-tyre-recycling> (last citation February **2013**).
- 12.***, SR EN 12720/2004, "Resistance to different aggressive media", **2004**.

*Dedicated to Professor Liviu Literat
On the occasion of his 85th birthday*

AN ANALYSIS OF THE STABILIZATION MECHANISM OF REVERSE FLOW REACTORS WITH APPLICATION IN CATALYTIC VOC COMBUSTION

IOANA STOICA^a, IONUȚ BANU^{a,*}, GRIGORE BOZGA^a

ABSTRACT. The aim of the work is a thorough theoretical analysis regarding the time evolutions of state variables during the stabilization of temperature and composition profiles, for a fixed catalytic bed reactor, operated in forced unsteady state regime by periodically changing the flow direction. The decontamination of lean waste gases by VOC combustion over a commercial Pt/alumina catalyst with non-uniform distribution of Pt is considered as a case study. The process is mathematically described by a heterogeneous one-dimensional model. The simulation results evidence that the stabilized (pseudo-steady) state regime is achieved when the amount of heat generated during a cycle equals the amount of heat withdrawn from the bed by gaseous mixture.

Keywords: *packed bed, reverse flow, unsteady-state, process simulation, sensitivity analysis*

INTRODUCTION

The reverse flow reactor (RFR) is a gas-solid catalytic packed or monolith bed reactor operated in forced unsteady-state regime by periodical change of feed flow direction. The main advantage in this technique consists in the possibility to realize the autothermal operation, even at low volatile organic compounds (VOC) concentrations, by achieving appropriate temperature profiles along the bed. One of the important applications suitable for this apparatus is the VOC elimination from lean gaseous mixtures by catalytic combustion [1-5].

^a *University Politehnica of Bucharest, Faculty of Applied Chemistry and Material Science, Department of Chemical and Biochemical Engineering, Bucharest, Romania.*

* *Corresponding author: Ionut Banu, University Politehnica of Bucharest, Faculty of Applied Chemistry and Material Science, Department of Chemical and Biochemical Engineering, 313-Spl. Independentei, sect. 6, 060042 Bucharest, Romania, Tel: +021 4023938, Email: i_banu@chim.upb.ro*

Kolios [6] referred to the RFR as a multi-functional apparatus, as it is embodying in a single device the functions of reactor and heat exchanger.

Generally, the mechanisms of unsteady processes are more complex, as compared with processes occurring at steady state. In the development of their mathematical models, particular unsteady state correlations should be used for calculation of the kinetics of chemical and physical process steps. However, in the absence of such data, analysis and design calculations for unsteady processes are usually based on correlations based on steady state data.

This paper aims to highlight the features of auto-thermal operated reverse flow packed bed reactors, in VOCs catalytic combustion applications. There are emphasized the interplay of the physical and chemical process steps, as well as the conditions that ensure the time stabilization (achievement of pseudo-steady state).

The principle of RFR operation consists in feeding the gaseous reactants mixture, usually at room temperature, over the hot catalytic bed, the gas pre-heating to the reaction temperature being assured by the entry zone of the packed bed, which is progressively cooled. Thus, it appears a cooled zone of the bed, which is slowly moving in the direction of the gas flow. If the direction of gas flow in the reactor is reversed with an adequate frequency, after a sufficient number of reversals, a succession of axial temperature profiles, insuring the consumption of reactant, are achieved and stabilized inside the bed. A sketch of the reactor connections needed for reactants supply and products removal for reverse flow operation are shown in Figure 1. The reaction mixture can be fed either from the left to the right (when the valves 1 and 4 are open, and 2 and 3 closed) or from the right to the left (2 and 3 are open, 1 and 4 are closed). In the case of irreversible reactions, the extreme zones of reactor bed (I and III in Figure 1) have roles only in heat accumulation and its transfer to the gas phase, the chemical reaction taking place in the central zone (II). Consequently, in the zones I and III it can be used an inert solid (non-catalytic material), preferentially having a high specific heat capacity. This is also the bed structure considered in the present study [1, 2].

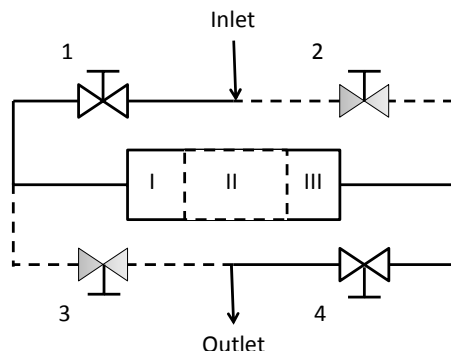


Figure 1. Connection scheme of a reverse flow operated packed bed reactor

MATHEMATICAL MODEL AND NUMERICAL METHOD

The present theoretical analysis is based on process description by a heterogeneous, one-dimensional axial dispersion model, considering, in addition to convective transport in the gas phase, a mechanism of mass and heat dispersion in axial direction. The model neglects the contribution of the metallic wall in the axial heat transport (the heat transferred from the packed bed to the wall, and then through the wall in the axial direction is not taken into account). In addition, the thermal regime is adiabatic, the gas phase behavior is ideal, the pressure drop in the packed bed is neglected and the chemical reactions are considered only on the surface of the catalyst.

The mass and heat balances in the gaseous and solid phases of the bed are expressed by equations (1) to (4). They apply for both catalyst and inert zones of the packed bed, for the latter canceling the terms which represent the contributions of the chemical reaction ($r_A = 0$).

$$\varepsilon \frac{\partial Y_{AG}}{\partial t} = \varepsilon D_L \frac{\partial^2 Y_{AG}}{\partial z^2} - u \frac{\partial Y_{AG}}{\partial z} - k_G a_v C_t (Y_{AG} - Y_{AS}) \quad (1)$$

$$k_G a_v C_t (Y_{AG} - Y_{AS}) = \rho_{cat} \eta_i \cdot r_A(Y_{AS}, T_S) \quad (2)$$

$$\varepsilon \rho_G c_{pG} \frac{\partial T_G}{\partial t} = \varepsilon \lambda_L \frac{\partial^2 T_G}{\partial z^2} - u \rho_G c_{pG} \frac{\partial T_G}{\partial z} + \alpha a_v (T_S - T_G) \quad (3)$$

$$\rho_S (1 - \varepsilon) c_{pS} \frac{\partial T_S}{\partial t} = (1 - \varepsilon) \lambda_S \frac{\partial^2 T_S}{\partial z^2} + (-\Delta H_{RA}) \rho_{cat} \eta_i r_A(Y_{AS}, T_S) + \alpha a_v (T_S - T_G) \quad (4)$$

Initial conditions: $t = 0$, $0 \leq z \leq L$, $Y_{AG} = Y_{Ai}(z)$;

$$T_G = T_{Gi}(z);$$

$$T_S = T_{Si}(z); \quad (5)$$

Boundary conditions (Danckwerts type):

$$z = 0, t > 0 \quad u_0 \cdot (Y_{A0} - Y_{AG}) = -\varepsilon D_L \frac{\partial Y_{AG}}{\partial z} \quad (6)$$

$$\rho_G \cdot u_0 \cdot c_{pG} (T_{G0} - T_G) = -\varepsilon \lambda_{LS} \frac{\partial T_G}{\partial z} \quad (7)$$

$$\frac{\partial T_S}{\partial z} = 0 \quad (8)$$

$$z = L, t > 0 \quad \frac{\partial Y_{AG}}{\partial z} = \frac{\partial T_G}{\partial z} = \frac{\partial T_S}{\partial z} = 0 \quad (9)$$

In the above equations: Y_A - molar fraction of hydrocarbon; C_t - molar density of the gas (total molar concentration); T - temperature; r_A - VOC consumption rate; η_i – internal effectiveness factor; u – superficial velocity of the gas; ρ_{cat} , ρ_S , ρ_G – catalyst density, solid density and gas density; k_G , α - mass and heat gas-solid transfer coefficients; a_v – specific interfacial surface area; ε - void fraction of the bed; c_{pG} , c_{ps} – specific heats of gas and solid; D_L , λ_L – effective gas phase transport coefficients by axial dispersion; λ_s – effective thermal conductivity of packed bed; ΔH_{RA} - reaction enthalpy; the indices G and S refer to the gaseous and solid phase values, whereas the index 0 for the values at the inlet of the packed bed.

The duration between two successive flow reversals instants is called semi-cycle or half-cycle (t_{sc}) and its twofold value is called cycle or period ($t_c=2 \cdot t_{sc}$). At the initial moment of the first semi-cycle, the packed bed is considered at uniform temperature and zero VOC concentration. The initial conditions of all other semi-cycles were considered identical with the states at the final moment of the preceding ones.

Equations of heat and mass balance (1) to (4) define a system of nonlinear partial differential equations (PDE) which was integrated numerically by finite difference method [7].

For the simulations, it was considered a commercial Pt/ γ -alumina catalyst having the Pt distributed in the outer zone of the pellet (0.5 wt % Pt on the average in the pellet). This distribution was approximated by a step function of radial coordinate, with Pt placed in a zone close to the external surface (Figure 2). The Pt concentration in the active zone was so calculated to match an average pellet concentration of 0.5 % by weight.

The chemical reaction considered in the study is the combustion of a hydrocarbon A (in the class of VOC's) having a first order kinetics:

$$r_A = k_0 e^{\left(-\frac{E_A}{RT}\right)} C_A \quad (10)$$

The Pt exploitation efficiency was expressed by the internal effectiveness factor. Due to the low hydrocarbon concentration, its transport inside the porous pellet is characterized by Fick's law with an effective diffusion coefficient incorporating the molecular and Knudsen diffusion.

The reactant concentration dependence on radial position, in the active spherical zone containing Pt, of thickness δ_c , (Figure 2), deduced from mass balance equation of A, is given by equation (11):

$$C_A(\xi) = \frac{C_{AS}}{\xi} \cdot \frac{\xi_1 \varphi \cosh \varphi(\xi - \xi_1) + \sinh \varphi(\xi - \xi_1)}{\xi_1 \varphi \cosh \varphi(1 - \xi_1) + \sinh \varphi(1 - \xi_1)}, \text{ for } \xi_1 \leq \xi \leq 1 \quad (11)$$

$$\varphi = R \sqrt{\frac{k_v}{D_{ef}}}; \quad \xi = \frac{r}{R}; \quad \xi_1 = \frac{r_1}{R}; \quad k_v = \rho_{cat} k \quad (12)$$

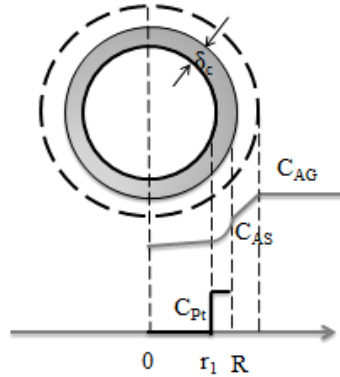


Figure 2. Pt distribution inside the catalyst pellet

Following the usual procedure, one obtains the expression of the effectiveness factor:

$$\eta_i = \frac{\bar{r}_A}{r_A(C_{AS})} = \frac{3}{(1-\xi_1^3)\varphi^2} \frac{(\xi_1\varphi^2 - 1)\sinh\varphi(1-\xi_1) + \varphi(1-\xi_1)\cosh\varphi(1-\xi_1)}{\xi_1\varphi\cosh\varphi(1-\xi_1) + \sinh\varphi(1-\xi_1)} \quad (13)$$

\bar{r}_A - average reaction rate in the active zone of the pellet;

C_{AS} – VOC concentration at the mouth (entry) of the pores.

The values of physical constants and parameters involved in the mathematical model are given in Table 1.

Considering the limited accuracy of the published correlations for the calculation of gas - solid mass and heat transfer coefficients and for the axial dispersion transport coefficients, these were evaluated by averaging the values calculated from several correlations [3, 8-14].

RESULTS AND DISCUSSION

Influence of internal diffusion

The evolutions of reactant concentration in the spherical catalyst pellet, for various thicknesses of active zone, are shown in Figure 3A (note that $\xi_1=0$ corresponds to uniform Pt distribution inside the pellet). The less pronounced concentration decrease throughout the pellet corresponds to uniform Pt concentration. When the active zone gets narrower, the decrease of reactant concentration becomes steeper. This result is explained by the

rise of Pt concentration and consequently rise of the combustion rate, combined with the shortening of the diffusion length, with the narrowing the active zone. This feature justifies the superiority of platinum distribution on a narrow area in the immediate vicinity of the external surface.

Table 1. Values of the model parameters

d_R (m)	0.14
L_t (m)	0.6
L_c (m)	0.3
d_p (m)	0.003
ε	0.4
λ_s ($J m^{-1} s^{-1} K^{-1}$)	0.18
ρ_s ($kg m^{-3}$)	1634
c_{ps} ($J kg^{-1} K^{-1}$)	1100
k_0 (s^{-1})	0.18
E_A ($J mol^{-1}$)	82900
ΔH_{RA} ($J mol^{-1}$)	- 802880
p ($N m^{-2}$)	100000
T_0 (K)	293
M ($kg kmol^{-1}$)	29
u_0 ($m s^{-1}$)	0.1
c_{pG} ($J kg^{-1} K^{-1}$)	1015
Y_{A0}	0.001
ΔT_{ad}	27
δ_c (mm)	0.4

The dependence of the internal effectiveness factor on the thickness of the active zone is shown in Figure 3B. The effectiveness factor decreases with the increase of active zone thickness, due to the increase of the diffusion distance (thickness δ_c of the active zone).

Startup and pseudo-steady-state

At the startup of operation, the temperature of the solid bed has to be sufficiently high in order to allow the reaction ignition. In practice, the non-stationary operated reactors are equipped with a solid preheating device, such as gas burners or electric sources [15].

The calculated profiles of hydrocarbon conversion and temperature along the reactor bed at different times during the first two half-cycles are presented in Figure 4. As seen, due to the gas heating, near the feed section appears a colder zone of solid, which is progressively extending in the direction of gas flow (Figures 4 - A2, B2, C2). Note also that the temperatures of the gas and solid are practically equal along the bed. In time, due to the heat generation in the chemical reaction, appears a temperature maximum along the catalyst zone, which is also moving slowly in the gas flow direction.

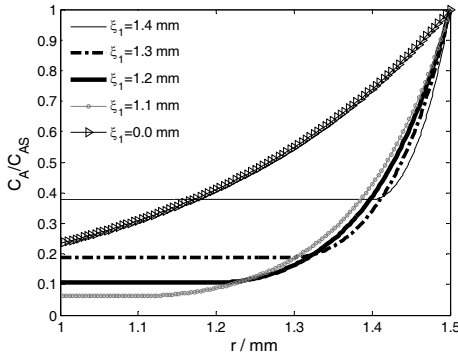


Figure 3A. Reactant concentration profiles in the spherical pellet with different thicknesses of active zone ($T=277\text{ }^{\circ}\text{C}$, $R=1.5\text{ mm}$)

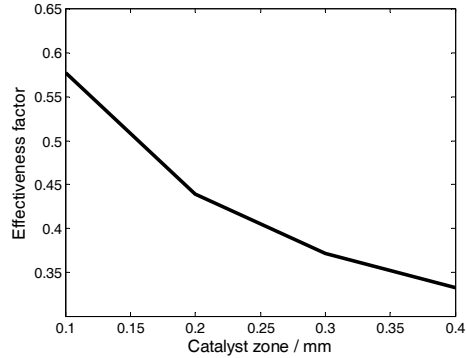


Figure 3B. The internal effectiveness factor versus the thickness of active zone, in the spherical pellet ($T=277\text{ }^{\circ}\text{C}$, $R=1.5\text{ mm}$)

In order to achieve a stable operation, the advancement of cooled zone has to be limited to the entry region of catalyst zone, thereafter the gas flow direction having to be reversed. After the gas flow direction is changed, a new cooled solid zone develops in the new flow direction. In addition, the former cooled zone of the bed is continuously heated, by the gaseous mixture leaving the reaction zone (Figure 4B).

If the half-cycle duration is not excessively high, after a sufficient number of changes of the gas flow direction, it can be achieved the so-called pseudo-steady-state regime. This regime is characterized by identical temperature and conversion profiles along the reactor, when traversed by the gas in the two directions. The computations evidenced that, depending on the operating conditions, the pseudo-steady state regime is practically achieved in the first 50 half-cycles. There are also two observations worth to be added, regarding the conversion profiles in Figure 4: (i) during the semi-cycle interval occurs a small decline of conversion, that can be limited by shortening the semi-cycle duration; (ii) for the duration of the first seconds after the gas flow reversal, appears a temporary zone with higher VOC concentration (smaller conversion values), due to the VOC hold-up retained in the voids of entry zone, in the preceding semi-cycle.

The mechanism of process stabilization can be illustrated through the heat balance terms around the reactor over a time interval, t , given by the equation:

$$Q_R(t) + Q_{CS}(t) = Q_P(t) \tag{14}$$

- ❖ the amount of heat withdrawn by gas mixture from the bed :

$$Q_P(t) = \int_0^t D_m c_{pG} [T_G(\tau, L) - T_{G0}] d\tau \quad (15)$$

- ❖ the amount of heat lost by the solid:

$$Q_{CS}(t) = \int_0^L S \rho_s (1 - \varepsilon) c_{ps} [T_s(0, z) - T_s(t, z)] dz \quad (16)$$

- ❖ amount of heat released in the combustion reaction:

$$Q_R(t) = \int_0^t D_{MA,0} (-\Delta H_{RA}) \cdot X_A(\tau, L) d\tau \quad (17)$$

Theoretically, the achievement of pseudo-steady state is demanding symmetrical solid temperature profiles along the bed, at the beginning and the end of a semi-cycle:

$$T_{(z)}^{(0)} = T_{(L-z)}^{(t_{sc})} \quad (18)$$

Consequently, the heat (enthalpy) content of the solid should be the same, at the beginning and at the end of a semi-cycle ($Q_{CS}(t_{sc})=0$). The percentage error in fulfilling the heat balance equation, on a pseudo-steady state semi-cycle, has the expression:

$$e = \frac{Q_{CS}(t_{sc}) + Q_R(t_{sc}) - Q_P(t_{sc})}{Q_{CS}(t_{sc}) + Q_R(t_{sc})} 100 \quad (19)$$

Considering a grid of 300 points along the packed bed axis, the calculated percentage error was less than 3% for all simulated semi-cycles, indicating an acceptable accuracy of numerical solution. The improvement of integration accuracy is possible by increasing the number of grid points along the reactor bed.

The diagrams in Figure 5 illustrate the time evolutions for Q_P , Q_R and Q_{CS} , during various semi-cycles, for a duration, $t_{sc}=2200$ s. The diagram in Figure 5A evidences that the quantity of heat removed from the bed by the gaseous mixture is negligible during a first time interval of the semi-cycle, all the heat generated in reaction being accumulated in the solid bed ($Q_{CS} < 0$). This is explained by existence of a final cold solid zone (ahead of the bed exit), which is cooling the gas down to the feed temperature, while the solid in this zone is gradually heated. After the final zone of the bed is heated above the feeding temperature (T_{G0}), the outlet gas temperature and the heat removed by the gas, start to rise.

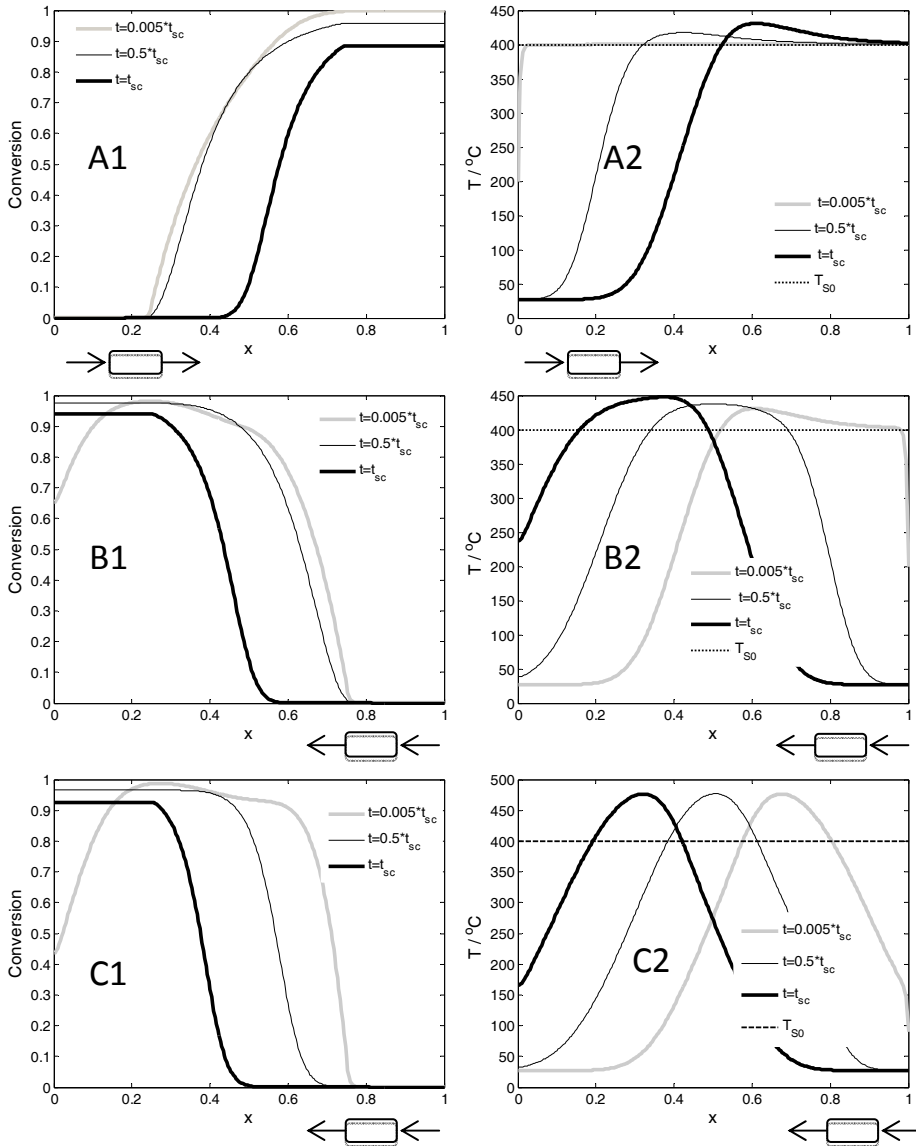


Figure 4. Axial evolutions of conversion and temperature in the reactor at different times during a semi-cycle : A –first semi-cycle; B–second semi-cycle; C – a semi-cycle of stabilized pseudo-steady state ($t_{sc}=2200$ s, $v_0=0.1$ m/s, $y_0=0.001$, $T_{si}=400$ °C, $L_c=0.3$ m, $L_t=0.6$ m, $x=z/L_t$)

In the semi-cycles prior to stabilization, the amount of the total heat withdrawn by gas from the bed is greater than the total amount of heat released in the chemical reaction ($Q_P(t_{sc}) > Q_R(t_{sc})$). As seen in diagrams of Figure 5, the stabilization consists in continuously decreasing the total amount of heat removed by the gas stream from the bed during the semi-cycle ($Q_P(t_{sc})$) until it equals the total amount of heat released in chemical reaction ($Q_R(t_{sc})$). At this point, the total heat lost from the solid becomes zero during a half cycle ($Q_{CS}(t_{sc}) = 0$), which means the same heat content of solid bed at the beginning of each half cycle (Figure 5B). The diagram in Figure 5C shows an approximately linear increase of total heat released in reaction with the time, due to the fact that the rate of heat generation is approximately constant (almost constant conversion of hydrocarbon during the semi-cycle).

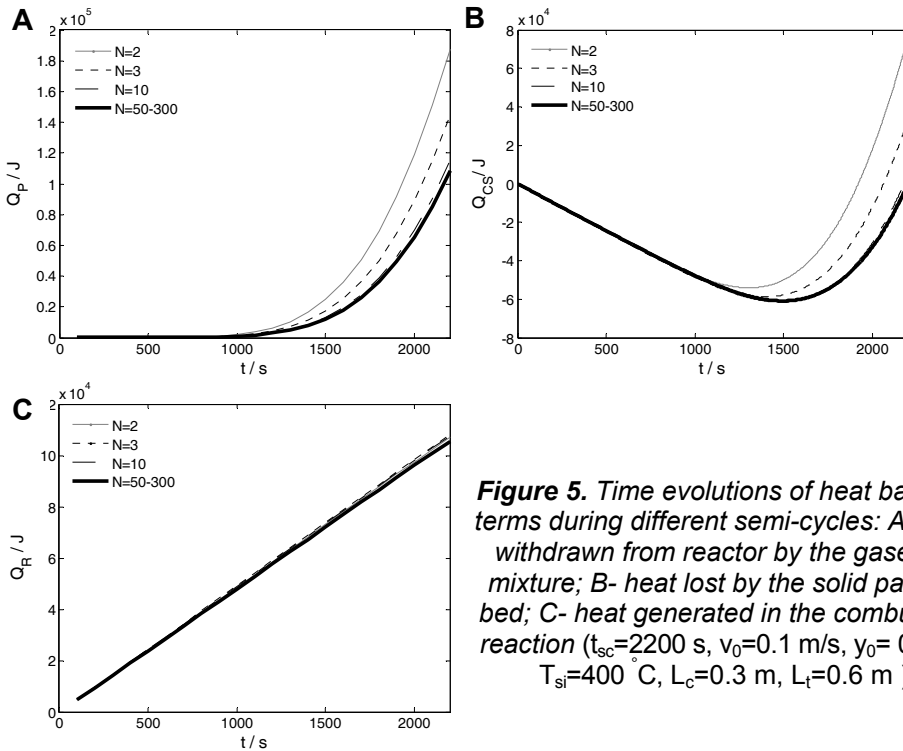


Figure 5. Time evolutions of heat balance terms during different semi-cycles: A- heat withdrawn from reactor by the gaseous mixture; B- heat lost by the solid packed bed; C- heat generated in the combustion reaction ($t_{sc}=2200$ s, $v_0=0.1$ m/s, $y_0=0.001$, $T_{sl}=400$ °C, $L_c=0.3$ m, $L_t=0.6$ m)

From the analysis presented above, it follows that the pseudo-steady state is achieved if total amount of heat removed by the gas from the bed during a half cycle equals the amount of heat released in the reaction during the same duration, $Q_P(t_{sc}) = Q_R(t_{sc})$.

If the total heat released in the reaction over a half cycle is smaller than the total heat removed by the gas ($Q_P(t_{sc}) > Q_R(t_{sc})$), the heat content of the bed and consequently its average temperature, gradually decrease, leading to reaction extinction.

These results show that the stable auto-thermal operation of the reverse flow reactor is achieved by continuously changing the solid temperature profile along the bed, keeping adequate levels and width to accomplish the chemical transformation. This occurs by successive heat accumulation and heat removal steps, leading to identical heat content of the bed at the beginning and the end of a semi-cycle.

During a stabilized semi-cycle, it is transferred a quantity of heat from the first zone of the bed contacted by gas, towards the final bed region, the gas acting as a heat carrier. On overall, as already emphasized, the amount of heat generated in reaction during a semi-cycle is entirely withdrawn from the bed by the gas. This is a feature worth to underline, some authors asserting that the principle of RFR operation consists simply in the accumulation of combustion heat into the bed.

An inconvenient of reverse flow reactor consists in small non-reacted VOC emissions occurring at changes in gas flow direction (Figure 6). At the end of each semi-cycle, throughout the cooled feed zone of solid is accumulated an amount of hydrocarbon, which is pushed out immediately after the change of the gas flow direction. The duration of this emission is very short, having the order of magnitude equal to the gas residence time into the cooled zone of the bed. In the simulated conditions, after approximately 1.5 seconds from the change of flow direction, there are no significant amounts of hydrocarbon eliminated from the reactor (Figure 6B), these being stabilized to a level dependent on VOC conversion achieved in the bed. Note that the top points in the diagram shown in Figure 6C represent the concentration of hydrocarbon at the exit of the bed, when changing the direction of gas flow. To minimize the unreacted VOC emissions, the duration of the semi-period should be kept close to its maximum possible value. However, the increase of semi-cycle duration could induce some decrease of hydrocarbon conversion, due to the extension of the cooled zone of the bed.

Influence of operating parameters

(i) Influence of main operating parameters on the maximum semi-cycle duration

As already mentioned, for a given set of operating parameters, the pseudo-steady state can be achieved for any duration of semi-cycle, inferior to a limit called maximum duration of semi-cycle. The simulation results presented in Figure 7 shows stabilized temperature evolutions along the packed bed (obtained

after 300 periods) in different working conditions and the corresponding maximum semi-period duration. These are evidencing that the maximum semi-period duration is increased by decreasing the gas velocity, increasing the feed hydrocarbon concentration, increasing the initial temperature of the packed bed and (in some limits) by increasing the catalyst to inert amounts ratio.

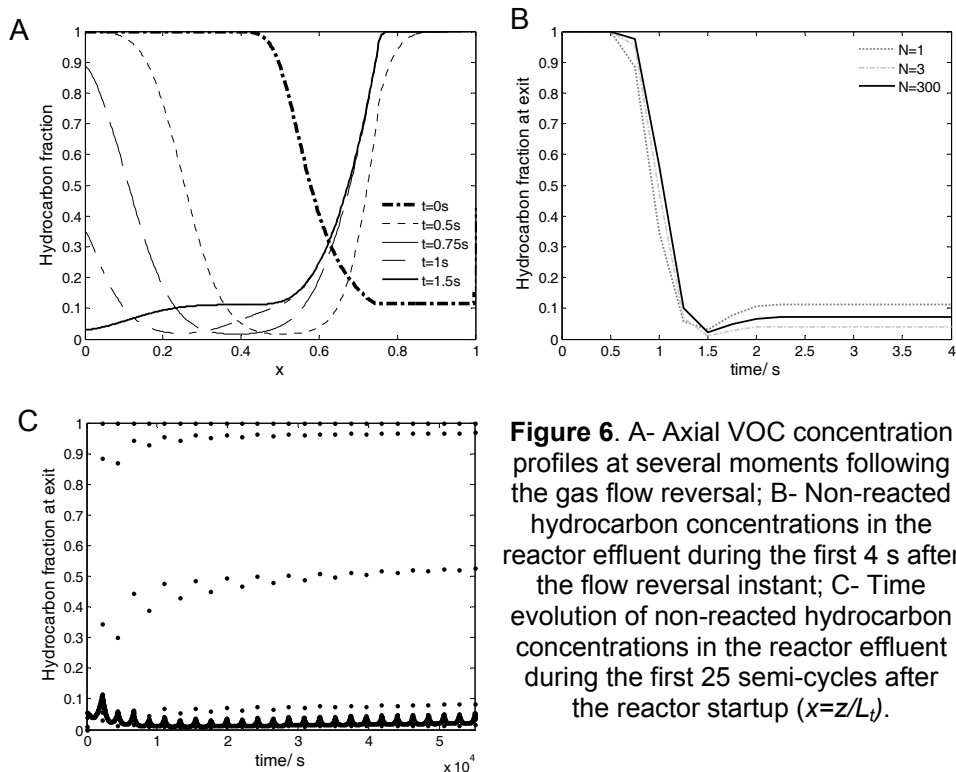


Figure 6. A- Axial VOC concentration profiles at several moments following the gas flow reversal; B- Non-reacted hydrocarbon concentrations in the reactor effluent during the first 4 s after the flow reversal instant; C- Time evolution of non-reacted hydrocarbon concentrations in the reactor effluent during the first 25 semi-cycles after the reactor startup ($x=z/L_t$).

The following general conclusions can be drawn from Figures 7 A, B, C and D: (i) By increasing the gas velocity (or equivalently the flow rate) the cooling capacity of the gas is raised and the velocity of cooled zone extension increases, narrowing the hot zone of the bed. (ii) Increasing the feed hydrocarbon concentration, it is also increased the amount of reactant consumed and consequently the amount of heat generated inside the bed, leading to the raise of maximum solid temperature. As known, the increase of temperature in a catalyst bed has to be controlled, as it may be harmful for the catalyst activity. A similar effect has also the increase of startup temperature of the solid. (iii) Extending the catalyst zone width in detriment of the inert zone, can also increase, in some limits, the maximum duration of

semi-cycle. Nevertheless, the cooling effect prevails, so that the duration of the half-cycle is subject to the phenomenon of overlapping the high-temperature front with catalytically active zone, which assure the occurrence of chemical reaction with adequate intensity.

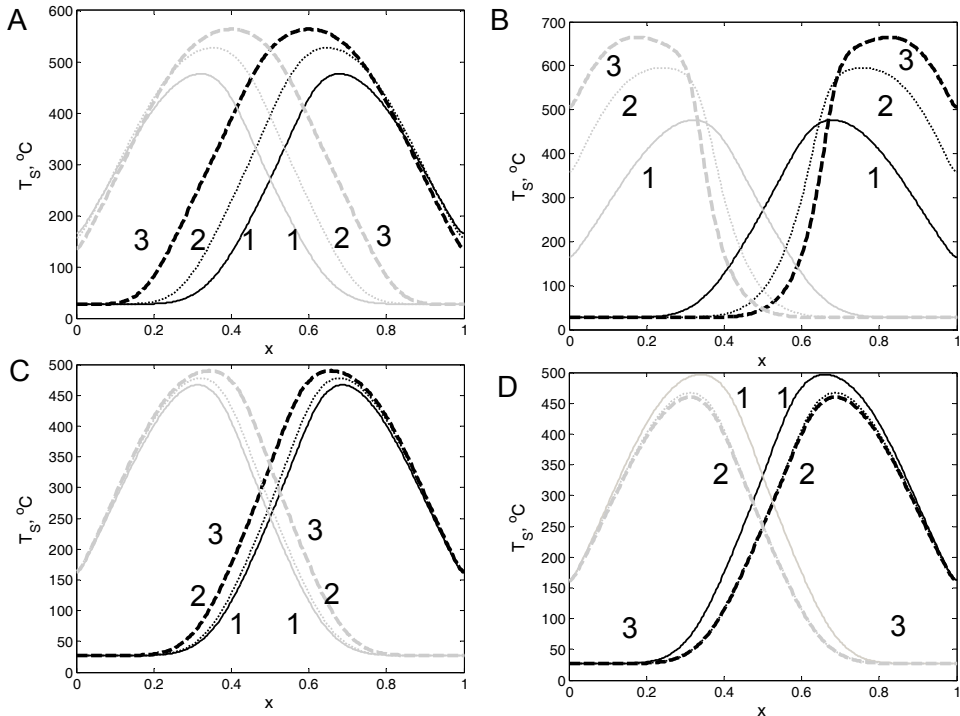


Figure 7. Stabilized axial temperature evolutions (achieved after 300 periods) and maximum semi-cycle durations in different working conditions (grey curves - direct feed, black curves - reverse feed, $x=z/L_f$). Nominal values: $T_{si}=400\text{ }^{\circ}\text{C}$, $y_0=0.001$, $v=0.1\text{ m/s}$, $L_f=0.6\text{ m}$, $L_c=0.3\text{ m}$. A (1- $v=0.1\text{ m/s}$, $t_{sc}=2200\text{ s}$; 2- $v=0.2\text{ m/s}$, $t_{sc}=900\text{ s}$; 3- $v=0.3\text{ m/s}$, $t_{sc}=400\text{ s}$); B (1- $y_0=0.001$, $t_{sc}=2200\text{ s}$; 2- $y_0=0.002$, $t_{sc}=3300\text{ s}$; 3- $y_0=0.003$, $t_{sc}=3800\text{ s}$); C (1- $T_{si}=400\text{ }^{\circ}\text{C}$, $t_{sc}=2250\text{ s}$; 2- $T_{si}=375\text{ }^{\circ}\text{C}$, $t_{sc}=2200\text{ s}$; 3- $T_{si}=350\text{ }^{\circ}\text{C}$, $t_{sc}=2000\text{ s}$); D (1- $L_c=0.24\text{ m}$, $t_{sc}=2000\text{ s}$; 2- $L_c=0.30\text{ m}$, $t_{sc}=2250\text{ s}$; 3- $L_c=0.42\text{ m}$, $t_{sc}=2250\text{ s}$)

(ii) Influence of operating parameters on process evolution at given semi-period duration

The curves in Figure 8A show the influence of gas flow rate on the final axial temperature profile, corresponding to a semi-period duration of 400 s. As the gas flow rate increases, the hot zone width decreases and the combustion reaction releases a significant quantity of heat in a narrower catalyst bed, leading to more significant peak temperature. As underlined

above, the maximum semi-period get lower with the increase of gas flow rate, so that it is preferred to operate at lower gas flow rates, in order to guarantee high conversions for higher maximum semi-period duration. The diagram in Figure 8B illustrates the influence of feed concentration on final temperature profiles along the bed. As expected, the width of hot zone and the maximum temperature augment with the rise of feed hydrocarbon concentration, as result of increasing the amount of heat generated in the bed.

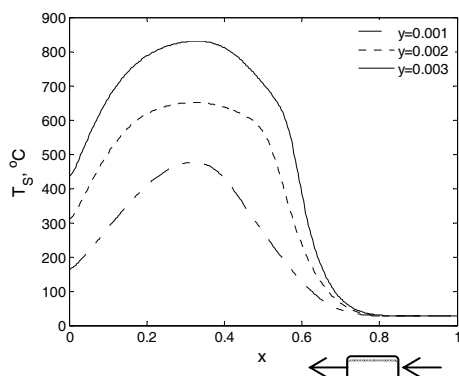


Figure 8B. Stable final temperature profiles along the bed at different feed concentrations and constant semi-period duration ($t_{sc}=2200$ s).

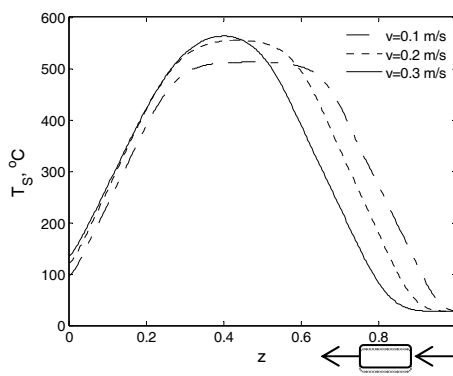


Figure 8A. Stable final temperature profiles along the bed at different gas flow rates and constant semi-period duration ($t_{sc}=400$ s).

As already underlined, unexpected increases of feed concentration present the danger of excessive temperatures in the bed, whereas the decrease of feed concentrations is inducing a decrease in hydrocarbon conversion, diminishing the heat released in the chemical reaction, with potential danger to light-off the chemical reaction. These effects can be compensated by changing (increasing or decreasing) the gas flow rate passing through the reactor.

Simulation calculations evidenced also that, for a given semi-period, the initial temperature of the solid bed (if adequate) does not influence the final temperature profile, it playing a role only in the process evolution toward the pseudo-steady state regime.

CONCLUSIONS

The operation of packed bed catalytic reactors with periodical change of flow direction is a technique that permits auto-thermal operation, even for very low feed concentration of reactant, a feature that makes it very attractive for gas cleaning by catalytic combustion. The stabilization of transient operation

is possible when the heat removed by the gas from the bed during a semi-cycle, equals the amount of heat generated in combustion reaction. For given values of working parameters, there exists a maximum semi-cycle duration, below which is possible the process stabilization. The simulation results of this work evidence the influences of the main process parameters on the process dynamics and on the maximum semi-cycle duration.

REFERENCES

1. Y.S. Matros, G.A. Bunimovich, *Catalysis Rev.-Sci. Eng.*, **1996**, 38, 1;
2. Y.S. Matros, "Catalytic Processes under Unsteady-State Conditions", Elsevier, **1989**, chapter 3;
3. B. van de Beld, "Air Purification by Catalytic Oxidation in an Adiabatic Packed Bed Reactor with Periodical Flow Reversal", PhD thesis, Twente University, The Netherlands, **1995**;
4. A.A. Barresi, M. Vanni, M. Brinkmann, G. Baldi, *AIChE Journal*, **1999**, 45, 1597;
5. A.A. Barresi, I. Mazzarino, Vanni M., G. Baldi, *The Chemical Engineering Journal*, **1993**, 52, 79-88;
6. G. Kolios, J. Frauhammer, G. Eigenberger, *Chemical Engineering Science*, **2000**, 55, 5945;
7. A.V. Wouwer, P. Saucez, W.E. Schiesser, "Adaptive method of lines", Chapman & Hall/CRC Press, **2001**, chapter 1;
8. K.R. Westerterp, W.C. Kusters, R.J. Wijngaarden, *Chem. Ing. Tech*, **1984**, 56, 621;
9. G. Bozga, O. Muntean, „Reactoare Chimice”, Ed. Tehnică, Bucharest, **2001**, chapter 5;
10. N. Wakao, S. Kaguei, „Heat and Mass Transfer in Packed Beds”, Gordon and Breach Science Publishers, Inc., New York, **1982**, chapter 4, 5;
11. S. Salomons, R.E. Hayes, M. Poirier, H. Sapoundjiev, *Computer and Chemical Engineering*, **2004**, 28, 1599;
12. B. Koning, "Heat and Mass Transport in Tubular Packed Bed Reactors at Reacting and Non-Reacting Conditions", PhD thesis, Twente University, The Netherlands, **2002**;
13. R.E. Hayes, „Introduction to catalytic combustion”, Gordon and Breach Science Publishers, Inc., Canada, **1997**, chapter 3;
14. J. Smit, M. van Sint Annaland, J.A.M. Kuipers, *Chemical Engineering Science*, **2005**, 60, 6971;
15. M. Brinkmann, A.A. Barresi, M. Vanni, G. Baldi, *Catalysis Today*, **1999**, 47, 263.

*Dedicated to Professor Liviu Literat
On the occasion of his 85th birthday*

NEW COPPER(I) COMPLEXES WITH ORGANOPHOSPHORUS LIGANDS WITH XPNSO SKELETON

CAMILLE STRADY^a, ADINA STEGARESCU^b,
CRISTIAN SILVESTRU^b AND ANCA SILVESTRU^{b,*}

ABSTRACT. Salt metathesis reactions between $K[\{SP(OEt)_2\}(O_2SC_6H_4Cl-4)N]$ and the copper(I) species $CuCl$ and $(Ph_3P)_2CuNO_3$, respectively, resulted in the new complexes $[Cu(\{SP(OEt)_2\}(O_2SC_6H_4Cl-4)N)]$ (**1**) and $[Cu(PPh_3)_2(\{SP(OEt)_2\}(O_2SC_6H_4Cl-4)N)]$ (**2**). The two compounds were characterized by multinuclear NMR (1H , ^{13}C , ^{31}P). Single-crystal X-ray diffraction studies revealed a monomeric structure with a bidentate, monometallic biconnective behavior of the organophosphorus(V) ligand in case of compound **2**. For compound **1** the NMR spectra suggest intermolecular associations in solution.

Keywords: *Organophosphorus ligands, copper(I) complexes, structure elucidation*

INTRODUCTION

The tetraorganodichalcogenoimidodiphosphinato ligands of type $[(XPR_2)(YPR'_2)N]^-$ (X, Y = chalcogen, R, R' = alkyl, aryl, OR) were intensively studied in last decades in relation with their versatility towards main group and transition metals, as well as due to the different applications of their metal complexes in catalysis, materials science and biology [1-9]. Copper complexes with such ligands were described as structural models for the active sites in copper containing enzymes [10-12] and found applications as precursors for nanomaterials for opto-electronic devices [13,14].

^a *Institut Universitaire de Technologie, Departement de Chimie Université de Rouen, Rue Lavoisier, 76821 Mont Saint Aignan Cedex, France*

^b *Universitatea Babeş-Bolyai, Facultatea de Chimie și Inginerie Chimică, Str. M. Kogălniceanu, Nr. 1, RO-400084 Cluj-Napoca, Romania, * ancas@chem.ubbcluj.ro*

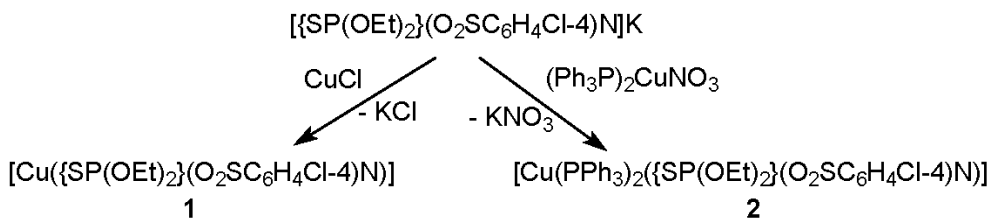
Bis(organosulfonyl)imides of type $(O_2SR)_2NH$ ($R = \text{alkyl, aryl}$) were also studied as ligands towards different metals, including also copper [15-17]. During last years we introduced a new type of organophosphorus ligands, respectively $[(XPR_2)(O_2SR')NH]$ ($X = S, O; R, R' = \text{alkyl, aryl, OR}$) and we obtained several complexes with late transition metals (Cu, Au, Ag, Pd) [15,18-20]. It was observed that such ligands behave as bidentate, monometallic biconnective, *O,S*- or *N,S*- chelating units.

In order to extend our studies upon ligands containing alkoxy groups attached to phosphorus, we investigated two $Cu(I)$ complexes with the anionic ligand $[\{SP(OEt)_2\}(O_2SC_6H_4Cl-4)N]^-$, one of them bearing two additional bulky triphenylphosphane ligands. We report here the synthesis of the complexes $[Cu(\{SP(OEt)_2\}(O_2SC_6H_4Cl-4)N)]$ (**1**) and $[Cu(PPh_3)_2(\{SP(OEt)_2\}(O_2SC_6H_4Cl-4)N)]$ (**2**), as well as their solution behavior and the single-crystal X-ray structure of compound **2**.

RESULTS AND DISCUSSION

Synthesis and spectroscopy

The new copper(I) complexes $[Cu(\{SP(OEt)_2\}(O_2SC_6H_4Cl-4)N)]$ (**1**) and $[Cu(PPh_3)_2(\{SP(OEt)_2\}(O_2SC_6H_4Cl-4)N)]$ (**2**) were prepared by salt metathesis reactions between $CuCl$ and $(PPh_3)_2CuNO_3$, respectively, and the potassium salt $[\{SP(OEt)_2\}(O_2SC_6H_4Cl-4)N]K$, as depicted in Scheme 1.



Scheme 1

Both copper(I) complexes are colorless solid species, soluble in common organic solvents. They were characterized by solution multinuclear NMR (1H , ^{13}C , ^{31}P). The proton NMR spectra have the expected pattern for the organic groups attached either to phosphorus or to sulfur: multiplet resonances for the *ortho*, *meta* and *para* C_6H_5 protons in PPh_3 , doublet resonances for the *ortho* and *meta*, respectively, protons in the C_6H_4Cl-4 group attached to sulfur. The ethoxy protons give two resonances in a 2:3 ratio, with aspect of a doublet of quartets (CH_2) and a triplet (CH_3), as result of the proton-proton and phosphorus-proton couplings. In case of the copper complex **1** the 1H NMR spectrum contains two sets of resonances both for the CH_2 and the

CH_3 protons, suggesting the non-equivalence of the ethyl groups in solution. Moreover, in both compounds the CH_2 protons in the ethyl groups appear as AB spin systems, due to diastereotopicity. In compound **1** two AB spin systems are present, one of them centered at δ 3.92 ppm and the other at δ 4.40 ppm, in accordance with the non-equivalent *OEt* groups, while in compound **2** one AB spin system centered at δ 3.73 ppm was observed. The aspect of the resonances corresponding to the CH_2 protons is complex, due to the proton-proton and phosphorus-proton couplings in combination with the AB spin systems.

For both species, the ^{13}C NMR resonances appear as singlets for the organic groups attached to sulfur and as doublets in case of the organic groups attached to phosphorus, due to the phosphorus-carbon couplings. The ^{13}C NMR spectrum of compound **1** contains in the aliphatic region a doublet resonance for the CH_3 carbons and two doublet resonances for the CH_2 carbons. This is in accordance with the nonequivalence of the *OEt* groups attached to the same phosphorus atom, assuming that the two CH_3 groups have, by coincidence, the same chemical shift.

Only one ^{31}P resonance was observed for complex **1** (δ 45.08 ppm), while for compound **2** two broad resonances were observed, one of them at δ 48.06 ppm, corresponding to the P(V) atom, and the other at δ -4.52 ppm, corresponding to the PPh_3 ligands, in a 1:2 ratio. The $\delta(^{31}P)$ values are shifted in comparison with the starting materials.

Copper(I) is expected to be either di-coordinated in a linear environment, trigonal-planar, or tetra-coordinated with a tetrahedral environment, depending on the ligands in a molecular unit. Such a coordination geometry can not be realized only by a bidentate chelating ligand. Taking into account the NMR observations for compound **1**, we assume that the non-equivalence of the *OEt* groups in the molecular unit might be the result of an intermolecular interaction of one *OEt* oxygen atom with a neighboring molecule, as was also previously observed in $K[(SPh_2)\{OP(OEt)_2\}N]\cdot H_2O$ [21]. The $[(SP(OEt)_2)\{O_2SC_6H_4Cl-4\}N]$ units can behave as a bimetallic triconnective ligand (Figure 1) resulting in an oligomeric (dimeric, trimeric, etc.) or a polymeric structure, the latter being less probable taking into account the good solubility of compound **1** in common organic solvents.

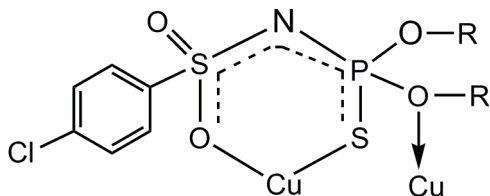


Figure 1. Proposed coordination pattern of the ligand in compound **1**

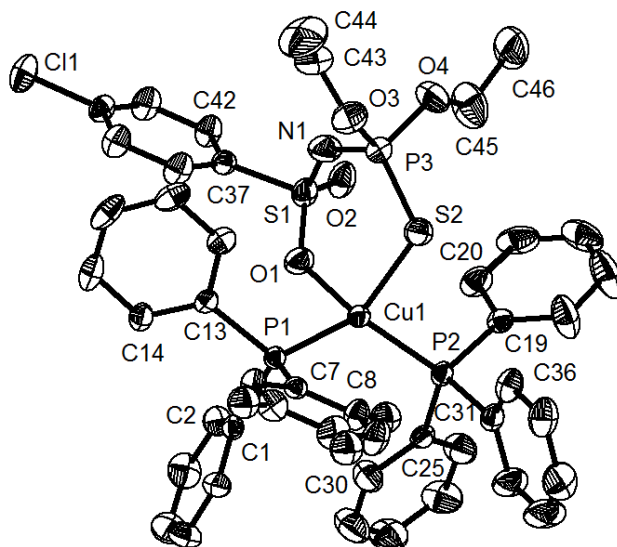
Single-crystal X-ray diffraction studies

For compound **2** the molecular structure was determined by single-crystal X-ray diffraction. The Ortep-like diagram with the atom numbering Scheme is given in Figure 2, while important interatomic distances and angles are given in Table 1.

Table 1. Important interatomic distances (Å) and angles (deg.) in **2**.

Cu(1)–O(1)	2.231(3)	O(1)–Cu(1)–P(1)	96.96(10)
Cu(1)–P(1)	2.2638(11)	O(1)–Cu(1)–P(2)	112.54(10)
Cu(1)–P(2)	2.2751(12)	P(1)–Cu(1)–P(2)	126.67(4)
Cu(1)–S(2)	2.3611(14)	O(1)–Cu(1)–S(2)	102.30(9)
N(1)–P(3)	1.527(5)	P(1)–Cu(1)–S(2)	115.04(5)
N(1)–S(1)	1.584(5)	P(2)–Cu(1)–S(2)	101.22(5)
O(1)–S(1)	1.437(4)	P(3)–N(1)–S(1)	136.3(3)
O(2)–S(1)	1.435(4)	P(3)–S(2)–Cu(1)	105.83(7)
O(3)–P(3)	1.612(4)	S(1)–O(1)–Cu(1)	127.3(2)
O(4)–P(3)	1.570(4)		
P(3)–S(2)	1.9364(18)		

The compound has a monomeric structure, with a distorted tetrahedral coordination geometry around copper. The anionic ligand acts as a S,O bidentate monometallic biconnective moiety.

**Figure 2.** Ortep-like diagram with 30% probability ellipsoids of compound **2**. Hydrogen atoms are omitted for clarity.

The Cu–S and Cu–O interatomic distances [Cu(1)–S(2) 2.3611(14) Å and Cu(1)–O(1) 2.231(3) Å] are of similar magnitude with those found in the related complexes [(Ph₃P)₂Cu{(SPPPh₂)(O₂SMe)N}] (Cu–S 2.3912(11) and Cu–O 2.188(2) Å) and [(Ph₃P)₂Cu{(SPPPh₂)(O₂STol-p)N}] 0.5C₆H₅CH₃ (Cu–S 2.3761(18) and Cu–O 2.160(4) Å) [19]. The phosphorus–sulfur bond length [P(3)–S(2) 1.9364(18) Å] and the phosphorus–nitrogen interatomic distance [P(3)–N(1) 1.527(5) Å] are shorter than those observed in the related compounds [(Ph₃P)₂Cu{(SPPPh₂)(O₂SMe)N}] [1.9886(14) and 1.602(3) Å] and [(Ph₃P)₂Cu{(SPPPh₂)(O₂STol-p)N}]·0.5C₆H₅CH₃ [1.995(2) and 1.605(6) Å]. They are also different than those found in the free acid {SP(OEt)₂}(O₂SC₆H₄Cl-4)NH [P–N 1.683(3) and P=S 1.9138(11) Å] [18].

The sulfur–nitrogen interatomic distance [S(1)–N(1) 1.584(5) Å] is longer than in the above mentioned complexes [1.552(3) and 1.558(6) Å]. The sulfur–oxygen bond lengths [S(1)–O(1) 1.437(4) and S(1)–O(2) 1.435(4) Å] are almost equal and in the range found for the other two copper complexes mentioned above [1.427(1) – 1.446(1) Å] [19]. The bond lengths suggest the delocalization of the π electrons on the SPNSO skeleton. The six-membered CuOS₂PN ring exhibits a twisted boat conformation with S(1) and S(2) in apices.

CONCLUSIONS

Our studies revealed a bidentate monometallic biconnective behavior of the anionic organophosphorus ligand [{SP(OEt)₂}(O₂SC₆H₄Cl-4)N][−] in compound **2**. The NMR spectra suggest that in the absence of the bulky PPh₃ groups the copper(I) atom in compound **1** tends to increase its coordination number by intermolecular interactions in which one OEt group is involved.

EXPERIMENTAL SECTION

Starting materials, *i.e.* K[{SP(OEt)₂}(O₂SC₆H₄Cl-4)N] [18] and (Ph₃P)₂CuNO₃ [22], were prepared according to literature procedures. Other reagents including ⁿBuLi, Ph₃P, CuCl and Cu(NO₃)₂ were purchased from Aldrich and used without further purification. All manipulations involving air sensitive compounds were carried out under vacuum or argon, using Schlenk techniques. Solvents were dried and distilled prior to use. Elemental analyses were performed on a Flash EA 1112 machine. Melting points have been determined with an ELECTROTHERMAL 9200 apparatus and they are not corrected. Multinuclear NMR spectra (¹H, ¹³C and ³¹P) were recorded on a BRUKER 300 Avance instrument operating at 300.11, 75.5 and 121.4 MHz, respectively, using CDCl₃ solutions. The chemical shifts are reported in δ units (ppm) relative to the residual peak of the deuterated solvent (ref. CHCl₃: ¹H 7.26, ¹³C 77.0 ppm) and H₃PO₄ 85%. The ¹H and ¹³C chemical shifts were

assigned based on 2D experiments (COSY, HSQC and HMBC) using standard BRUKER XWIN-NMR pulse sequences. The NMR spectra were processed using the MestReC and MestReNova software [23].

Preparation of [Cu{SP(OEt)₂}(O₂SC₆H₄Cl-4)N] (1)

A reaction mixture of CuCl (0.122 g, 1.23 mmol) and K[{SP(OEt)₂}(O₂SC₆H₄Cl-4)N] (0.47 g, 1.23 mmol) in 25 mL of anhydrous dichloromethane was stirred at room temperature for 16 hours. The solvent was removed under vacuum and the remained solid product was washed with n-hexane and dried under vacuum. The title compound was obtained as a colorless powder which was recrystallized from a dichloromethane/n-hexane mixture (1:3, v/v). Yield 0.361 g (72%), m.p. 199°C. Anal. Calc. for C₁₀H₁₄ClCuNO₄PS₂ (M = 406.32): C 29.56% H 3.47%, N 3.45%. Found: C 29.42%, H 3.32%, N 3.51%. ¹H NMR: δ 1.18t (3H, OCH₂CH₃, ³J_{HH} 6.5 Hz), 1.35t (3H, OCH₂CH₃, ³J_{HH} 6.5 Hz), 3.92 AB spin system with δ_A 3.78dq (1H, OCH₂CH₃, ³J_{HH} 7.5 Hz, ³J_{PH} 14.2 Hz) and δ_B 4.06dq (1H, OCH₂CH₃, ³J_{HH} 7.5 Hz, ³J_{PH} 14.7 Hz), 4.40 AB spin system with δ_A 4.39dq (1H, OCH₂CH₃, ³J_{HH} 7.3 Hz, ³J_{PH} 13.4 Hz) and δ_B 4.41dq (1H, OCH₂CH₃, ³J_{HH} 7.3 Hz, ³J_{PH} 13.5 Hz), 7.44d (2H, C₆H₄-meta, ³J_{HH} 8.3 Hz), 7.92d (2H, C₆H₄-ortho, ³J_{HH} 8.3 Hz). ¹³C NMR: δ 15.46d (OCH₂CH₃, ³J_{PC} 8.6 Hz), 66.26d (OCH₂CH₃, ²J_{PC} 6.9 Hz), 67.15d (OCH₂CH₃, ²J_{PC} 6.8 Hz), 128.66s (C₆H₄-meta), 128.87s (C₆H₄-ortho), 138.4s (C₆H₄-ipso), 141.9s (C₆H₄-para). ³¹P NMR: δ 45.08s.

Preparation of [Cu(PPh₃)₂{SP(OEt)₂}(O₂SC₆H₄Cl-4)N] (2)

A reaction mixture of (Ph₃P)₂CuNO₃ (0.289 g, 0.445 mmol) and K[{SP(OEt)₂}(O₂SC₆H₄Cl-4)N] (0.17 g, 0.445 mmol) in 25 mL of anhydrous dichloromethane was stirred at room temperature for 24 hours. The solvent was removed under vacuum, when a colorless viscous oil was obtained. After washing with n-hexane, the title compound resulted as a colorless microcrystalline solid. Yield 0.244 g (59%), m.p. 162°C. Anal. Calc. for C₄₆H₄₄ClCuNO₄P₃S₂ (M = 930.90): C 59.35%, H 4.76%, N 1.50%. Found: C 59.64%, H 4.92%, N 1.55%. ¹H NMR: δ 1.07t (6H, CH₃, ³J_{HH} 7.02 Hz); 3.73 AB spin system with δ_A 3.72dq (2H, CH₂, ³J_{HH} 7.5 Hz, ³J_{PH} 14.5 Hz) and δ_B 3.74dq (2H, CH₂, ³J_{HH} 7.5 Hz, ³J_{PH} 14.6 Hz); 7.04d (2H, C₆H₄, ³J_{HH} 8.3 Hz); 7.25m (12H, C₆H₅-ortho) 7.35m (18H, C₆H₅-meta+para); 7.51d (2H, C₆H₄, ³J_{HH} 8.3 Hz). ¹³C NMR: δ 15.76d (OCH₂CH₃, ³J_{PC} 8.8 Hz), 62.72d (OCH₂CH₃, ²J_{PC} 6.5 Hz), 127.95s (C₆H₄-para), 128.45d (C₆H₅-ortho, ²J_{PC} 7.3 Hz), 129.44s (C₆H₄-ortho + C₆H₄-meta), 133.5d (C₆H₅-ipso, ¹J_{PC} 106.3 Hz), 133.95d (C₆H₅-meta, ³J_{PC} 14.4 Hz), 136.28 (C₆H₄-ipso), 143.95 (C₆H₄-para). ³¹P NMR: δ -4.52s, br. (Ph₃P); 48.06s [(EtO)₂P(S)].

X-ray Crystallographic Studies

X-ray quality crystals of compound **2** were grown by slow diffusion from a mixture of CH₂Cl₂/n-hexane (1/5, v/v). The crystal was attached with paratone/N oil to a cryoloop. Data collection and processing was carried on a Bruker SMART APEX CCD system, using graphite-monochromated Mo K α radiation ($k = 0.71073 \text{ \AA}$). Details of the crystal structure determination and refinement for compound **2** are given in Table 2.

Table 2. Crystallographic data for compound **2**.

Empirical formula	C ₄₆ H ₄₄ ClCuNO ₄ P ₃ S ₂
Formula weight	930.84
Temperature, K	297(2)
Wavelength, \AA	0.71073
Crystal system	Triclinic
Space group	P-1
Crystal size, mm	0.60 x 0.48 x 0.38
Unit cell dimensions	
<i>a</i> , \AA	9.7281(9)
<i>b</i> , \AA	11.4567(10)
<i>c</i> , \AA	21.5866(19)
α , $^\circ$	103.838(2)
β , $^\circ$	93.523(2)
γ , $^\circ$	103.242(2)
<i>V</i> , \AA^3	2256.7(3)
<i>Z</i> , Calculated density	2, 1.370 Mg/m ³
<i>F</i> (000)	964
Refinement method	Full-matrix least-squares on F^2
Θ Range for data collection	0.98 to 25.00
Reflections collected	21771
Independent reflections [<i>R</i> _{int}]	7940 [<i>R</i> _{int} = 0.0312]
Data/restraints/parameters	7940 / 0 / 525
Goodness-of-fit on F^2	1.114
Final <i>R</i> indices [<i>I</i> > 2 σ (<i>I</i>)]	<i>R</i> 1 = 0.0674, <i>wR</i> 2 = 0.1519
<i>R</i> indices (all data)	<i>R</i> 1 = 0.0795, <i>wR</i> 2 = 0.1585
Largest diff. peak and hole, (e \AA^{-3})	1.274 and -0.621

The structure was refined with anisotropic thermal parameters. The hydrogen atoms were refined with a riding model and a mutual isotropic thermal parameter. The software package SHELX-97 was used for structure solving and refinement [24]. The drawings were created with the DIAMOND program [25].

ACKNOWLEDGMENTS

Financial support from the Ministry of Education and Research of Romania (CNCS, Research Project No. PN-II-ID-PCE-2011-3-0659) is greatly appreciated. Camille Strady is grateful for financial support from the *Région Haute-Normandie* (France).

SUPPLEMENTARY DATA

CCDC 961231 contains the supplementary crystallographic data for **2**. These data can be obtained free of charge via <http://www.ccdc.cam.ac.uk/conts/retrieving.html>, or from the Cambridge Crystallographic Data Centre, 12 Union Road, Cambridge CB2 1EZ, UK; fax: +44 1223 336 033; or e-mail: deposit@ccdc.cam.ac.uk.

REFERENCES

1. C. Silvestru, J.E. Drake, *Coord. Chem. Rev.*, **2001**, 223, 117, and references cited therein.
2. J.D. Woollins, *J. Chem. Soc., Dalton Trans.*, **1996**, 2893.
3. I. Haiduc, in: A.B.P. Lever (Ed.), *Comprehensive Coordination Chemistry II, Fundamentals: Ligands, Complexes, Synthesis, Purification and Structure*, vol. 1, Elsevier, Pergamon Press, Amsterdam, Oxford, **2004**, p. 323.
4. E. Ferentinos, D. Maganas, C.P. Raptopoulou, A. Terzis, V. Psycharis, N. Robertson, P. Kyritsis, *J. Chem. Soc., Dalton Trans.*, **2011**, 40, 169. and refs. therein.
5. T. Chivers, J.S. Ritch, S.D. Robertson, J. Konu, H.M. Tuononen, *Acc. Chem. Res.*, **2010**, 43, 1053.
6. J.S. Ritch, T. Chivers, *Inorg. Chem.*, **2009**, 48, 3857.
7. D. Maganas, A. Grigoropoulos, S.S. Staniland, S.D. Chatziefthimiou, A. Harrison, N. Robertson, P. Kyritsis, F. Neese, *Inorg. Chem.*, **2010**, 49, 5079.
8. A. Singhal, D.P. Dutta, S.K. Kulshreshtha, S.M. Mobin, P. Mathur, *J. Organomet. Chem.*, **2006**, 691, 4320.
9. P. Bhattacharyya, A.M.Z. Slawin, M.B. Smith, *J. Chem. Soc., Dalton Trans.*, **1998**, 2467 and refs. therein.
10. R.L. Lieberman, A.C. Rosenzweig, in: J. Que Jr., V.B. Tolman (Eds.), *Comprehensive Coordination Chemistry II, Bio-coordination Chemistry*, vol. 8, Elsevier, Pergamon Press, Amsterdam, Oxford, **2004**, p. 195.
11. K.R. Brown, G.L. Keller, I.J. Pickering, H.H. Harris, G.N. George, D.R. Winge, *Biochemistry*, **2002**, 41, 6469.
12. I.J. Pickering, G.N. George, C.T. Dameron, B. Kurz, D.R. Winge, I.G. Dance, *J. Am. Chem. Soc.*, **1993**, 115, 9498.
13. Y.-Y. Niu, Y.-L. Song, H.-G. Zheng, D.-L. Long, H.-K. Fun, X.-Q. Xin, *New J. Chem.*, **2001**, 25, 945.
14. M. Afzaal, D.J. Crouch, P. O'Brien, J. Raftery, P.J. Skabara, A.J.P. White, D.J. Williams, *J. Mater. Chem.*, **2004**, 14, 233.
15. M. Szabo, D. Ban, C. Rat, A. Silvestru, J.E. Drake, M.B. Hursthouse, M.E. Light, *Inorg. Chim. Acta*, **2004**, 357, 3595, and references cited there in.

16. D. Henschel, K. Linoh, K.-H. Nagel, A. Blaschette, P.G. Jones, *Z. Anorg, Allg. Chem.*, **1996**, 622, 1065.
17. K. Linoh, K.-H. Nagel, I. Lange, O. Moers, A. Blaschette, P.G. Jones, *Z. Anorg, Allg. Chem.*, **1997**, 623, 1175.
18. D. Oltean, A. Pöllnitz, A. Silvestru, *Polyhedron*, **2013**, 53, 67.
19. A. Pop, A. Rotar, C. I. Rat, A. Silvestru, *Inorg. Chim. Acta*, **2008**, 361, 255.
20. A. Pöllnitz, A. Silvestru, M. Concepción Gimeno, A. Laguna, *Inorg. Chim. Acta*, **2010**, 363, 346.
21. G. Balazs, J.E. Drake, C. Silvestru, I. Haiduc, *Inorg. Chim. Acta*, **1999**, 287, 61.
22. F.A. Cotton, D.M.L. Goodgame, *J. Chem. Soc.*, **1960**, 5267.
23. MestReC and MestReNova, Mestrelab Research S.L., A Coruña 15706, Santiago de Compostela.
24. G.M. Sheldrik, SHELX-97, University of Göttingen, Germany, **1997**.
25. DIAMOND – Visual Crystal Structure Information System, CRYSTAL IMPACT, Postfach 1251, 53002 Bonn, Germany, **2001**.

*Dedicated to Professor Liviu Literat
On the occasion of his 85th birthday*

CONCENTRATION OF PARTICULATE MATTER ASSOCIATED TO A CROSSROAD TRAFFIC FROM CLUJ-NAPOCA CITY

NICOLETA BICAN-BRIȘAN^{a,*}, TEODORA ENACHE^a, CRISTINA ROȘU^a

ABSTRACT. Large cities crossroads are areas with high pollution level generated by heavy traffic, especially during rush hours. Furthermore, pollution level is increased by heavy traffic through excessive releases of toxic gases and particulate matter. In order to highlight the quality of urban atmosphere in the area of major crossroads from Cluj-Napoca City, particulate matter concentration was monitored in an important crossroad from the southern part of the city, using a direct-reading instrument, the DustTrak Aerosol Monitor, model 8520. The obtained data include the concentration levels of the particulate matter with a diameter ranging between 0.1 and 10 μm . The results were discussed in relation to the crossroad traffic, thus highlighting the influence of heavy traffic on the particulate matter pollution level. The analysis of medium values showed the poor correlation with meteorological parameters (temperature, relative humidity, wind speed) during the measurement interval.

Key words: *particulate matter, PM_{10} , $PM_{2.5}$, PM_1 , urban air quality, crossroad*

INTRODUCTION

Airborne particulate matter (PM) or *aerosol*, is a complex mixture of solid and liquid particles of organic or inorganic origin suspended in the air, whose effective diameter is larger than that of a molecule, but smaller than 100 μm [1]. These result from both natural and anthropogenic processes, while the main sources are mineral dust, emissions from energy generation, transport and marine aerosols.

The various adverse effects associated to these particles have already been researched [2]. Moreover, numerous studies conducted in this field have revealed essential cause-and-effect relationships between PM and

^a *Babeș-Bolyai University Cluj-Napoca, Faculty of Environmental Science and Engineering, Cluj-Napoca, 30 Fântânele, RO-400294 * nicoleta.brisan@ubbcluj.ro*

an increase in the death rate [3, 4, 5]. Certain connections between fine PM and a series of health problems, such as asthma, bronchitis, and other respiratory symptoms, both acute and chronic were demonstrated [6].

The size of the PM, their concentration and chemical composition have the most significant influence on their behavior in the atmosphere, as well as on their impact on the respiratory tract [7]. Hence, the smaller dimensions of the PM are the bigger impact on human health [8, 9].

Concerning its impact both on the health and the environment (acid rains, fog and dry deposition, impact on Earth's radiative balance and subsequently on climate changes), the airborne PM pollution of the atmosphere represents one of the current global problems [10, 11, 12].

The analysis of the PM concentration evolution in a highly urban environment is a key activity in air quality assessment and an effective means to facilitate the monitoring and regulation of PM limit values in ambient air, in order to reduce the risk of respiratory illnesses.

Considering the gravity of the respiratory tract [13, 14, 9, 15] and cardiovascular system [16, 17] affections and depending on the dimension of the inhalable PM (PM_{10} , $PM_{2.5}$, PM_1), regulations limiting the emissions of PM were globally imposed.

Beginning with 1971, when the US Environmental Protection Agency (US-EPA) developed the first legislative regulations for PM, the established limits were subjected to countless modifications through time, depending on the outcomes achieved after the measurements (www.who.int; www.epa.gov; www.ec.europa.eu). Some specific regulations set by the World Health Organization (WHO) experts during the 2005 meeting in Bonn, included stricter standards for PM (the medium value of $PM_{2.5}$ within one year must not exceed $10 \mu\text{g}/\text{m}^3$ and $25 \mu\text{g}/\text{m}^3$ along 24 hours). In 2006, US-EPA included PM on the list of major pollutants, along with CO , Pb , NO_2 , SO_2 and O_3 . According to the international air quality standards, the average level over three consecutive years must not exceed $15 \mu\text{g}/\text{m}^3$ and the 24-hour mean is $35 \mu\text{g}/\text{m}^3$. In the European Union (EU), the Directive 2008/50/CE includes the latest amendments regarding the fine PM. This was transposed to the Romanian legislation through the law 104/2011, as the mean value of $PM_{2.5}$ in one year was established at $25 \mu\text{g}/\text{m}^3$. Concerning the 24-hour concentration level, in 2004, during the Clear Air for Europe program, a limit of $35 \mu\text{g}/\text{m}^3$ was proposed but this was not approved by the legislation. In terms of PM_{10} , the daily limit value is $50 \mu\text{g}/\text{m}^3$ which cannot be exceeded for more than 35 days within one year and the annual limit is $40 \mu\text{g}/\text{m}^3$.

The high amount of PM is an important problem that creates discomfort for the inhabitants in Cluj-Napoca City. Previous studies developed in different locations of the city represented by playgrounds, crossroads [18] and courtyards of buildings in different neighborhoods [19] have revealed high concentrations of atmospheric PM. Heavy traffic, activities in constructions and industry are supposed to be the main sources of PM_{10} and $PM_{2.5}$.

RESULTS AND DISCUSSIONS

The influence of traffic on PM during the working days

Road transport is an essential factor in the urban areas and it represents one of the major sources of PM [23, 24].

PM emission is a particularity of the diesel engine, as compared to the gasoline engine. Depending on the combustion process and the engine's operating mode, emissions largely contain carbon particles, such as aerosols or sulfites. In this case, PM emissions include the fuel and engine oil related to exhaust gases, particles resulted from friction processes associated with tire deterioration or traces of brake, as well as the dusting generated by vehicles movement, especially the large size vehicles.

The relation between the PM concentration and the number of vehicles which have passed through the crossroads during the measurement period is graphically presented in Figure 1.

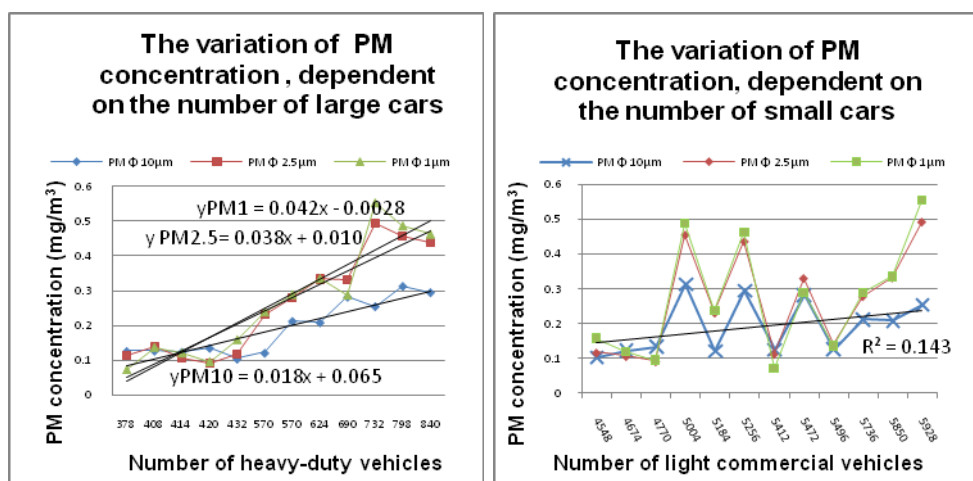


Figure 1. The variation of PM concentrations in relation to traffic

In the case of heavy-duty vehicles, a strong correlation is observed between the two types of values, for all PM sizes, especially for small diameter ones (PM₁ and PM_{2.5}). This fact is normal, because the fine PMs are the direct product of engine combustion, especially for the vehicles using Diesel fuel. The coarse particulate matter (PM₁₀) do not show such a spectacular increase related to the number of vehicles, therefore the increasing slope is much smaller (18% as compared to fine PM, whose increasing slope is 38% and 42%). This is explained by the rotation movement of the tires on the road, but also by the pressure of the exhaust gases, as they stimulate the nearby dust particles, although the lack of intense air-mass movement results in phenomenon decrease.

The analysis of the graph illustrating the relation between the number of light commercial vehicles and the PM concentration revealed a poor connection ($R^2=0,143$), especially in the median zone of the values. This can indicate the relative upgrade of these types of vehicles with non-pollutant equipment. However, in the case of extreme values of vehicles passing through the crossroad (4548 and 5928 vehicles), large variations of all PM types concentration were noticed, especially the fine ones. This can be explained by the passing of heavy-duty vehicles through the study area.

For a better understanding of the PM concentrations variation, Figure 2 includes the graphs illustrating the ratio between fine and coarse PM.

One can notice that this dependence is remarkable in terms of the heavy-duty cars, as it presents 8% slopes in the case of PM_1 and 7% slopes in the case of $PM_{2.5}$.

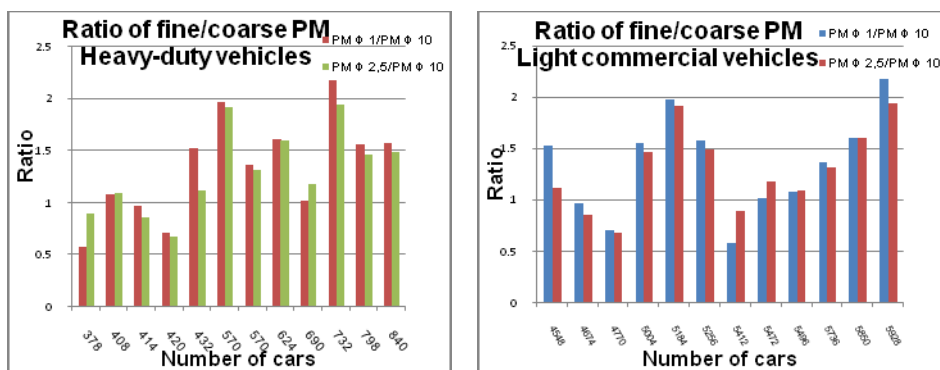


Figure 2. The ratio of fine/coarse PM concentrations in relation to vehicles types

One can state that a direct proportional connection has been emphasized between the number of heavy-duty vehicles and the PM concentrations of all types, as well as a poorer dependence between the two values, in the case of light commercial vehicles, which are less polluting. This difference can be accounted for by the fact that, according to literature data, the medium level of pollution caused by a heavy-duty vehicle is 20 times higher than that caused by light vehicles and, as a result, the immediate effect is much more visible and easier to record, in the case of heavy-duty vehicles.

The influence of weather conditions on the PM concentrations

Studies have revealed that the level of PM concentrations was not exclusively influenced by the local transport emissions, but by a function of the weather conditions [25, 26].

Hereinafter, the influence of each meteorological parameter on the PM_{10} , $PM_{2.5}$ and PM_1 values is presented in order to get a full comprehension of the way these exert a greater influence on the pollution level, as well as a relation (direct, inverted or indifferent) between them.

a. *The influence of the ambient temperature on PM emissions during the working days*

As the air temperature variations during the days of measurement were very small, the differences in the contaminant values, caused by this parameter are not likely to be significant. Generally, the instability and the thermo inversion are factors strongly influencing the PM concentration variations in the atmosphere. These phenomena did not occur during the days of measurement.

The difference between the temperature of pollutants emitted by polluting sources and the temperature of the ambient atmosphere influences the diffusion. In this case, the temperature of the pollutant, when emitted, is often similar to the temperature of exhaust systems, while the ambient temperature is low, close to 0°C. Therefore, insignificant variations of PM concentrations are expected to occur, depending on the ambient temperature.

The graphic representations and the associated analysis were conducted separately for the heavy-duty vehicles (high level of polluting) and for the much more eco-friendly light vehicles.

The analysis of the graphs in Figure 3 indicates a decrease of PM values along with the increase of temperature: the evolution curves of the trend lines are small and almost equal (1.73%, respectively 1.81%), and the R² indicator shows a poor dependence between the two parameters in the given conditions.

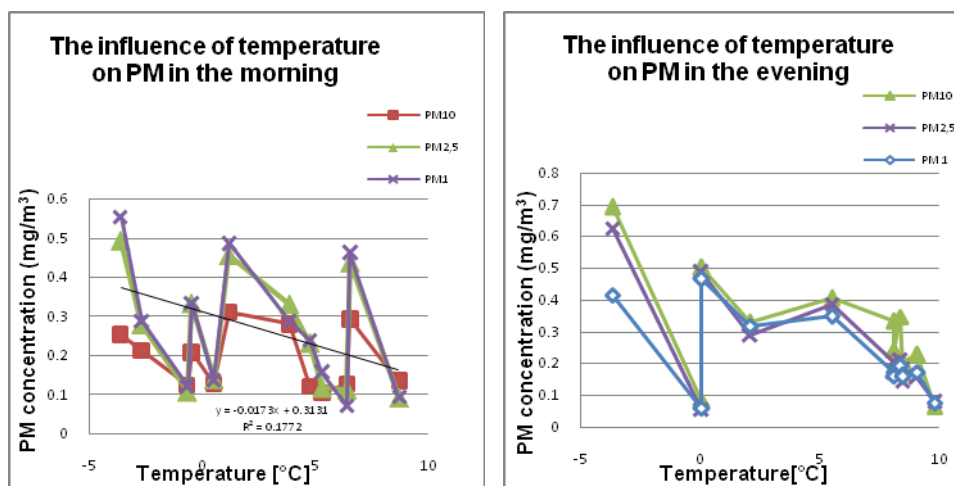


Figure 3. The variation of PM concentration in relation to temperature

It is important to observe the fact that the average morning and evening temperatures are different, but low (2.5°C in the morning, respectively 5.38°C in the evening). Negative values were recorded in 33.3% of the cases in the morning, respectively in 8% of the cases (once) in the evening. The difference

between the temperature of the air and that of the pollutant, when emitted (i.e. the temperature of exhaust gases) influences the dispersion of gases. As this difference is significant, the ascensional speed of the pollutant will increase.

b. The influence of wind speed on the PM emissions during the working days

The graphs in Figure 4 represent the variations of different PM concentrations, in order to observe whether the PM concentrations show determinable variations for small values of this parameter.

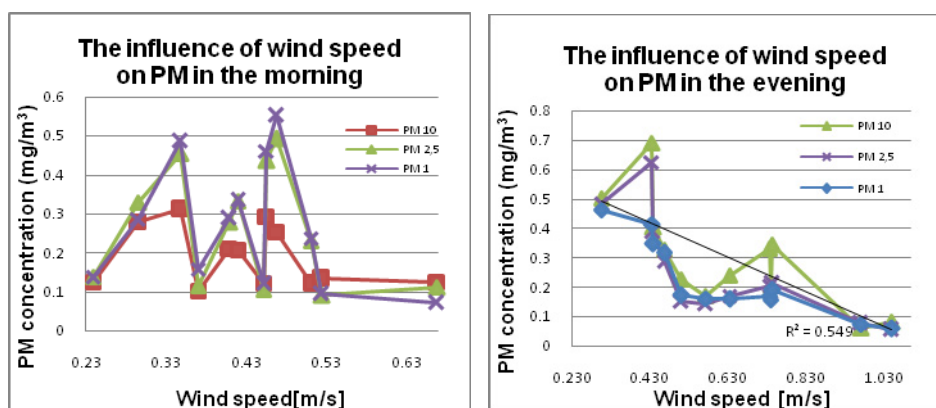


Figure 4. The variation of PM concentration in relation to wind speed

Generally, great wind speeds can have strong effects on the PM concentrations, due to dispersion and dilution phenomena. As this parameter had relatively small values in the field measurements, a very clear correlation between the two types of values has not been noticed.

Therefore, the expression $PM=f(ws)$ shows no correlation between the parameters (wind speed and PM).

The graphs in Figure 5 indicate a different evolution of PM concentrations, depending on the variations of air-mass speed, as follows: in the morning, the variation of PM concentrations shows no definitive trend, because of the very low wind speed. However, during the measuring interval, when the wind speed exceeds 0.5 m/s, the fine PM concentrations decrease to the minimum value corresponding to the measuring periods: $PM_{2.5}=0.092 \text{ mg/m}^3$, respectively $PM_1=0.073 \text{ mg/m}^3$, due to the dilution process. In the evening, when the measured values are higher, a clear decrease tendency of fine PM concentration can be noticed, along with the increase of wind speed ($R^2=0.76$ for PM_1 , respectively $R^2=0.58$ for $PM_{2.5}$). This does not apply to PM_{10} , because, in this case, the concentration increases ($PM_{10}=0.333 \text{ mg/m}^3$), as the air-mass velocity intensifies to the value of 0.737 m/s.

c. *The influence of humidity on the PM emission during the working days*

The influence of relative humidity on PM concentrations in Figure 5 is unclear. Therefore, can be notice that is not correlation between humidity and PM values.

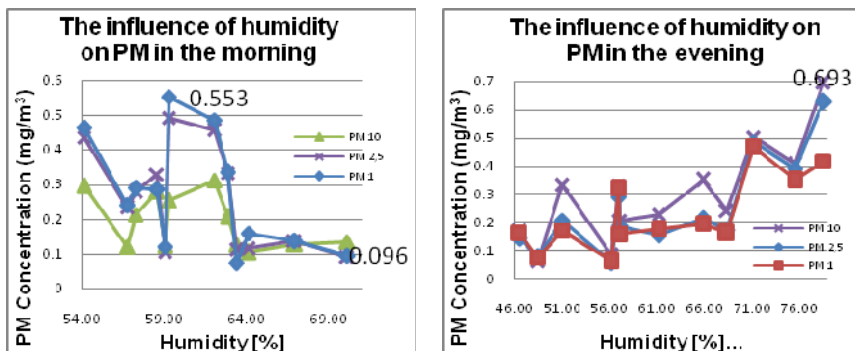


Figure 5. The variation of PM concentration in relation to relative humidity

The comparison between working days data and weekend days data

The objective of analyzing these measurements is to present a comparative study to reveal the similarities and differences in PM concentrations during the weekend days, in relation to the working days. Hence, the authors explain the reduced number of days when measurements were conducted (only two Saturdays), but also the different time schedule (during the 16¹⁰ - 17⁴⁰ interval).

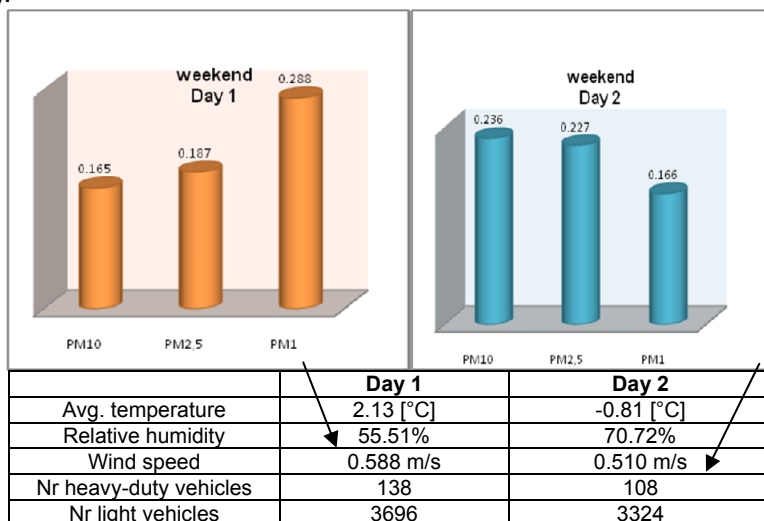


Figure 6. The PM values, weather conditions and traffic during the weekends

The measurements conducted during the weekends illustrate PM values when the traffic, in general, and the public transport traffic, in particular, are significantly reduced (an average of 123 heavy-duty vehicles during the weekends, counted in 90 minutes, representing 21.46% of the working days traffic). Moreover, the number of small cars which have passed through the crossroads was 29.7% smaller than recorded during the working days (3760 as compared to 5277 cars counted daily, in a 90-minutes interval).

The graphs indicate that the average PM value measured during the weekend is 2 or even 3 times smaller than the average PM values measured during the working days. This can be explained by the traffic reduction at the crossroads and also by the cease of several polluting activities in the proximity of the study area (industrial activities, construction works), during the above-mentioned period.

The objective of the two representations is to emphasize the differences that may occur during the low traffic days, but in non-identical meteorological conditions. Still, the number of measurements conducted during the non-working days is very small and therefore it is difficult to draw global conclusions.

CONCLUSIONS

The measurements highlighted the fact that the influence of traffic is important in relation to the PM concentrations, in the case of PM₁₀, but also for PM₁ and PM_{2.5}. Values of PM₁₀ (coarse particulates) concentrations were noticed to be 23.32% higher in the evening, as compared to those recorded in the morning, due to continuous dusting, but also to the ongoing pollutant activities (industrial activities, construction works etc.).

In the medium and long term, it is extremely important to continue the research on various diameters PM concentrations in the crowded crossroads of the Cluj-Napoca city, in order to observe the efficiency of the measures imposed by governmental policies concerning environmental protection, such as:

a. The stimulation of Romanian vehicle fleet replacement, by means of the RABLA program, but also by the acquisition of new non-polluting motor haulage vehicles.

b. The construction of belt highways for the large cities, in order to reduce the traffic and the residence times or extremely low speed traffic times, which induce strong polluting effects.

c. The use of alternative, less polluting runways, like railways existing in the area.

d. The promotion of the use of non-pollutant fuel motor vehicles equipped with efficient filters, type Euro 4, Euro 5, Euro 6.

e. The systematic washing of the road, in order to eliminate the dusting through the action of tires, corroborated by high wind speeds.

f. The implementation of more severe motor check-ups, along with the increase of fines and sanctions, concerning pollutants emissions, which can be accomplished by setting up mobile measurement laboratories.

g. The location of tire washing areas, to be used for the motor vehicles passing through back roads or fields, construction areas, in order to remove the most part of the different origin and size dust.

h. The start-up of intensive planting programs to green spaces or reforestation establishments, in order to protect and purify the environment.

i. The removal, to the possible extent, of the heavily polluting factories from the intensely inhabited areas, but also the relocation of some activities during the nighttime, in order to enable environmental self-purification.

In order to prevent environmental destruction, the environmental awareness of large cities inhabitants should be increasingly built, using all the necessary methods (school education, mass-media) to induce an adequate civil behavior and attitude, meant to sustain clean environment, healthy ecosystems and purified air to ensure human and environmental health.

EXPERIMENTAL SECTION

The study area is located in the proximity of the Calea Turzii and Observatorului crossroads roundabout, with the coordinates 46.75549° N and 23.596289° E and an average altitude of 360 m. This intersection belongs to the marginal area of the Zorilor neighborhood, also associated to the Observator area and located in the southern part of Cluj-Napoca City.

The measurement points selection criteria concern the architecture and morphology of the study area, as the main buildings located in this intersection are tall blocks of flats in the West, the Sigma Shopping Mall, along with the adjacent parking lot and the UTC-N Laboratories in the North, and house ensembles in the East and North-East, whereas the southern part is prevailed by the wide Calea Turzii. Therefore, this area is not located inside an enclosed neighborhood, in terms of circulation of the air-masses, as the small houses and the parking lots enable a loose circulation of the air. The velocity of the air streams is significantly reduced and these are even diverted in the western part and, partially, the northern part, due to the presence of tall and imposing buildings.

In order to highlight the range of PM concentration, the measurements were performed at 60 cm above the road surface after a well established schedule, as follows.

The measurements were conducted on a weekly basis during the 24th October 2011 – 20th November 2011 period. Throughout this period, the authors have chosen the Mondays, Wednesdays and Fridays together with two Saturdays for a good comparison between working days data and weekends data. During the working days, three 30 minutes measurements per day were performed, for each size category (PM₁, PM_{2.5} and PM₁₀), during the 7⁴⁰- 9¹⁰ time interval in the morning, and 19⁰⁰ - 20³⁰ in the evening. In order to compare the working days and weekend values, the measurement were also performed during the weekends, but only in the 16¹⁰- 17⁴⁰ time interval in the afternoon. Thus, PM₁, PM_{2.5} and PM₁₀, averages were obtained.

As the concentration level of PM generally depends on the atmosphere conditions and meteorological parameters [10, 20, 21], measurements of air temperature, relative humidity and wind speed were also performed. The vehicles passing through the roundabout were counted throughout the time of performing the measurements. These vehicles were classified in two types: light commercial vehicles and heavy-duty vehicles, last including buses and mini-buses).

The concentration of PM of different sizes (PM₁, PM_{2.5} and PM₁₀) was monitored with a direct-reading aerosol monitor - TSI's DustTrak Aerosol Monitor (Model 8520). The real-time measurements in milligrams per cubic meter (mg/m³) conducted by means of a laser photometer based on a 90° light scattering sensor type. They operate by illuminating a PM as it passes through an optic chamber (sensing volume) and by measuring the light scattered by all the particles at a given scattering angle relative to the incident beam. As the number of PM increases, the light reaching the detector increases. Moreover, the PMs are isolated in the chamber by a sheath air system in order to keep the optics clean and improve the reliability [22].

The data obtained by the DustTrak Aerosol Monitor was also analyzed by the *TRAKPRO™ Data Analysis Software* that generates time dependent PM concentration graphs and multiple reports of the measurements results.

The meteorological parameters were determined using the Testo 608-H1 Termohygrometer for temperature and humidity and AIRFLOW™ Model TA430 Thermal Anemometer for wind speed.

REFERENCES

1. Gh. Lăzăroiu, „Dispersia particulelor poluante”, Ed. Agir, 307 p., **2006**, București.
2. WHO „Air quality guidelines for particulate matter, ozone, nitrogen dioxide and sulfur dioxide”. *Global update 2005*. Summary of risk assessment. (www.who.int).
3. C.A. Pope, R.T. Burnett, M.J. Thun, E.E. Calle, D. Krewski, K. Ito, G.D. Thurston, *Lung cancer, cardiopulmonary mortality, and long-term exposure to fine particulate air pollution*. JAMA, **2002**, 287 (9), pp.1132-1141.

4. K. Katsouyanni, G. Touloumi, C. Spix, J. Schwartz, F. Balducci, S. Medina et al. *Short-term effects of ambient sulphur dioxide and particulate matter on mortality in 12 European cities: results from time series data from the APHEA project.* *BMJ.*, **1997**, 314:1658–1663.
5. J. M. Samet, F. Dominici, F. Curriero, I. Coursac, S.L. Zeger, *Fine Particulate air pollution and Mortality in 20 U.S. Cities: 1987-1994.* *New England Journal of Medicine* (with discussion), **2000**, 343, 24, 1742-1757.
6. C.A. Pope, D.W. Dockery, Health effects of fine particulate air pollution: Lines that connect. *Air & Waste Manage. Assoc.*, **2006**, 56, pp.709-742.
7. A.M. Moldoveanu, „Poluarea aerului cu particule”, Ed. Matrix Rom, **2005**, 169 p., București.
8. R.T. Burnett, M.S. Goldberg, *Size-fractionated particulate mass and daily mortality in eight Canadian cities.* Revised analyses of time-series studies of air pollution and health. Special report., **2003**, Health Effects Institute, Boston, pp. 85-90.
9. G.T. O`Connor, L. Neas, B. Vaughn, M. Kattan, H. Mitchell, E.F. Crain, R. Evans, R. Gruchalla, W. Morgan, J. Stout, G.K. Adams, M. Lippmann, Acute respiratory health effects of air pollution on children with asthma in US inner cities. *J. Allergy. Clin. Immunol.*, **2008**, 121(5), pp. 1133-1139.
10. J.E. Penner, M. Andreae, H. Annegam, L. Barrie, J. Feichter, D. Hegg, A. Jayaraman, R. Leaitch, D. Murphy, J. Nganga, G. Pitari, „Aerosols, their direct and indirect effects” in: *Climate Change, 2001: The Scientific Basis.* J. T. Houghton et al., Eds., Cambridge University Press, 289–348.
11. R.N. Halthore, S.E. Schwartz, D.G. Streets, D. Rind, H. Yu, P.L. DeCola, „Introduction in Atmospheric Aerosols Properties and Climate Impacts”, A report by the U.S. Climate Change Science Program and the Subcommittee on Global Change Research. National Aeronautics and Space Administration, Washington, **2009**, USA.
12. U.B. Gunturu, „Aerosol-Cloud Interactions: A New Perspective” in *Precipitation Enhancement* Massachusetts Institute of Tehnology, **2010**, Ph.D. Thesis, Department of Earth, Atmospheric and Planetary Sciences.
13. M.T. Kleinman, The health effects of air pollution on children. South coast air quality management district, **2000** (<http://www.aqmd.gov>).
14. M. M. Kulkarni, Source apportionment of human exposure to particulates in Mumbai, India, *Aerosol and Air Quality Research*, **2006**, 6(3), pp. 281-294.
15. P.T. Nastos, A.G. Paliatsos, M.B. Anthracopoulos, E.S. Roma, K.N. Priftis, Outdoor particulate matter and childhood asthma admissions in Athens, Greece: a time-series study. *Environmental Health*, **2010**, 9(45), pp.1-9.
16. A. Peters, M. Fröhlich, A. Döring et al., Particulate air pollution is associated with an acute phase response in men: results from the MONICA–Augsburg study. *Eur Heart J*, **2001**; 22: 1198–204.
17. B.Z. Simkhovich, M. T. Kleinman, R. A. Kloner, Air pollution and cardiovascular injury. Epidemiology, toxicology and mechanism. *Journal of the American College of Cardiology*, **2008**, 52 (9), pp.719-726.

18. N. Bican-Brișan, D. Costin, I.N. Pop, Light scattering in particulate matter monitoring as tool for health exposure. Case study: Central Park Cluj-Napoca, Romania, *Optoelectronic Techniques for Environmental Monitoring, Proceedings*, **2010**, pp. 134-142.
 19. A.B. Badea, N. Bican-Brișan, PM_{2.5} concentration values in urban atmosphere of Cluj-Napoca. *Studia UBB Ambientum*, **2011**, LVI, 2, pp. 3-20.
 20. M. Amodio, E. Andriani, I. Cafagna, M. Caselli, B. E. Daresta, G. Gennaro, A. Gilio. C.M. Placentino, M. Tutino, A statistical investigation about sources of PM in South Italy. *Atmospheric Research*, **2010**, 98, pp. 207-218.
 21. P.G. Satsangi, A. Kulshrestha, A.Taneyya, P.S.P. Rao, Measurements of PM₁₀ and PM_{2.5} aerosols in Agra, a semi-arid region of India. *Indian J. of Radio & Space Physics*, **2011**, 40, pp. 203-210.
 22. D. Johnson, D. Swift, *Air Sampling Instruments for evaluation of atmospheric contaminants*, 9th Edition, ACGIH Worldwide, 1330 Kemper Meadow Drive, Cincinnati, Ohio, Eds. Beverly, S., Charles, S., Mc, Cammon, Jr., **2001**.
 23. A. Charron, R.M. Harrison, Fine(PM_{2.5}) and coarse(PM₁₀) particulate matter on a heavily trafficked London highway: sources and processes, *Environ. Sci. Technol.*, **2005**, 39(20), pp. 7768-7776.
 24. M. Abu-Allaban, J.A., Gillies, A.W. Gertler, R. Clayton, D. Proffitt, Motor Vehicle Contribution to Ambient PM₁₀ and PM_{2.5} at Selected Urban Areas in the USA, *Environ. Monit. Assess.*, **2007**, 132, pp. 155-163.
 25. R.M. Harrison, A.M. Jones, R.G. Lawrence, Major component composition of PM₁₀ and PM_{2.5} from roadside and urban background sites. *Atmos. Environ.*, **2004**, 38, 4531-4538.
 26. E.K. Wise, A.C. Comrie, Meteorologically Adjusted Urban Air Quality Trends in the Southwestern United States, *Atmos. Environ.*, **2005**, 39, 2969-2980.
 - *** C.A.F.E. Working Group in Particulate Matter (2004), Second position paper on particulate matter (www.ec.europa.eu).
 - *** National Ambient Air Quality Standards (NAAQS) for Particulate Matter, US-EPA (www.epa.gov).
 - *** Directive 2008/50/EC of the European Parliament and of the Council of 21 May 2008 on ambient air quality and cleaner air for Europe (<http://eur-lex.europa.eu>).
 - *** Law no. 104/2011 on ambient air quality, published in Official Gazette of Romania no. 452 dated June 28, 2011.
- <http://www.epa.gov/particles/health.html> (Environmental Protection Agency - EPA), accessed on 15 of September, 2013.

*Dedicated to Professor Liviu Literat
On the occasion of his 85th birthday*

INTENSIFICATION OF CONVECTIVE HEAT TRANSFER IN STRAIGHT PIPES BY USING SOME TURBULENCE PROMOTERS

ANDRA TĂMAȘ^{a,*}, SORINA BORAN^a

ABSTRACT. In this paper was studied the influence of some turbulence promoters (annular or spiral baffles), placed in the inner tube of a double pipe heat exchanger, on heat transfer intensification. These studies were performed in order to enhance heat transfer by convection of the fluid that moves through these spaces, flowing in transient or turbulent regime. The quantitative determination of heat transfer intensification in the presence of turbulence promoters was performed by calculating, from the energy balance data, the total or partial heat transfer coefficients and comparing these values to the values calculated in the absence of promoters.

Keywords: *baffles, heat exchanger, heat transfer, partial/total heat transfer coefficient, turbulence promoters*

INTRODUCTION

Due to an insufficient high value of the heat transfer coefficient by convection, the heat transfer represents a limiting factor for the performance of heat exchangers. For this reason, any technical measure is useful, functionally and economically justified, which is able to improve the level of these performances. From among the methods that enhance convection, studied and partially implemented in practice, the following can be mentioned: increasing fluid velocity, vibration/pulsation of the fluid or of the heat exchanger surface, the use of electrostatic or electromagnetic fields, injection and absorption of

^a *Universitatea "Politehnica" Timisoara, Facultatea de Chimie Industrială și Ingineria Mediului, Bd. V. Parvan Nr. 6, RO-300223 Timisoara, Romania*

* *Corresponding author: andra.tamas@upt.ro*

the boundary layer, the use of additives or turbulence promoters (uniform or discrete artificial roughness, turbulence generators) [1-5].

Turbulence promoters cause an additional local turbulence which leads to the transfer speed increase. They can be surface or moving fluid promoters.

In the first case, heat transfer can be enhanced by modifying the surface state, respectively, by introducing artificial roughness (channel type, rib type or granular). These modify the boundary layer flow, which leads to the increase of superficial heat transfer and of friction coefficient as well.

Moving fluid promoters create an artificial turbulence throughout its mass. The elements are placed inside the pipe and can be flat spirals, turbulence pads, conical surfaces, twisted metallic bands. In practice, the highest efficiency is achieved by using turbulence pads, to Reynolds number values lower than 10^4 . Also, by placing turbulence promoters on the outer surface of the inner tube of an annulus, the heat flow increases up to 60 % compared to the case of their absence [1,2,6].

By using static mixer elements (non-moving elements with a helical form, combining alternating right and left hand) in each heat exchanger tube, film build-up on the inside walls is greatly reduced. Process fluid is continuously pushed from the center of each tube to the wall and back to the center, eliminating thermal gradients and boosting the inside film coefficient. Kenics static mixer elements produce a more uniform, consistent transfer process, with three to seven time greater heat transfer rates than empty tubes alone [7,8].

Addition of milli or micro sized particles to the heat transfer fluid is one of the techniques employed for improving heat transfer rate. This method presents some disadvantages: high pressure loss, clogging, erosion of the material of construction. These problems can be overcome by using nanofluids - dispersion of nanosized (below 50 nm) particles (Al_2O_3 , CuO , Cu_2O , TiO_2 , SiC , SiO_2 , copper, gold, silver) in a base fluid. Nanoparticles increase the thermal conductivity of the base fluid which in turn increases the heat transfer rate. The extent of enhancement depends on the nanoparticle material type and volume fraction. Unfortunately, nanoparticles also increase the viscosity of the base fluid, resulting in higher pressure drop for the nanofluid compared to the base fluid [9-13].

In this paper was studied the effect of some turbulence promoters placed on the air flow path of a coaxial tube heat exchanger on the intensification of heat transfer to it. The quantitative evaluation of heat transfer intensification was performed by calculating, from the energy balance data, the total heat transfer coefficient in the absence and presence of turbulence promoters, respectively.

The pressure loss caused by air flow through the central tube was measured with an inclined-tube manometer [14].

RESULTS AND DISCUSSION

The total heat transfer coefficient K is determined from the energy balance equation:

$$Q_1 = Q_2 + Q_3 = Q_4 \tag{1}$$

$$Q_2 = m_{air} \cdot c_{air} \cdot (\Delta t)_{air} \tag{2}$$

$$Q_4 = K \cdot A \cdot \Delta t_{med} \tag{3}$$

where Q_1 is the heat delivered by the hot fluid (water); Q_2 is the heat received by the cold fluid (air); Q_3 is the lost heat; Q_4 is the transmitted heat; m_{air} - the air flow rate, $kg \cdot s^{-1}$; c_{air} - specific heat of air to the average temperature, $J \cdot kg^{-1} \cdot K^{-1}$; $(\Delta t)_{air}$ - the temperature differences for air at the heat exchanger extremities, $^{\circ}C$; Δt_{med} - the average temperature difference between air and water, $^{\circ}C$. The heat transfer area A was calculated with the relationship $A = \pi \cdot d_{med} \cdot H_1$, where d_{med} and H_1 are the average diameter and the height of the inner pipe ($A = 0.05m^2$). The unit for Q_1 - Q_4 is $J s^{-1}(W)$.

The partial heat transfer coefficient for air α was determined from the values of total heat transfer coefficient K , taking into account the thermal resistance to conduction of the pipe wall ($2.6 \cdot 10^{-6} m^2 \cdot K \cdot W^{-1}$) and the partial heat transfer coefficient for water ($\alpha_w = 920 W \cdot m^{-2} \cdot K^{-1}$) analytically calculated in the case of heat transfer in laminar flow through vertical pipes, when the forced movement direction is reversed to the free convection ($Gr \cdot Pr > 5 \times 10^5$) [14,15], Gr and Pr being Grashof and Prandtl numbers.

For each analyzed case (absence, respectively, the presence of annular baffles), the increasing of air flow rate (therefore, hydrodynamic regime intensification) leads to the increasing of the heat received by the air. Also, the heat received is greater the more increases the number of annular baffles (n) placed in the inner tube (decreases their step, $l_1 = H_1/n$).

For the situation of transient flow regime, it was found that the dependence between the heat received by the air and the value of Reynolds number is linear, the established equations are presented in Table 1.

Table 1. Equations $Q_2=f(Re)$ in the presence of annular baffles in transient regime

Step, mm	Eq. $Q_2=aRe + b$	R^2
-	$Q_2=0.0028Re + 8.4$	0.9906
200	$Q_2=0.0046Re + 12.7$	0.9982
100	$Q_2=0.0048Re + 17.9$	0.9927
50	$Q_2=0.0054Re + 19.5$	0.9913

The favorable effect of the presence of annular baffles on the air path is also evidenced by the values' evolution for partial (α) and total (K) heat transfer coefficients. In Fig. 1 is comparatively shown the dependence $\alpha=f(Re)$ for air flow over annular baffles (placed at different steps), respectively, in their absence.

In the absence of annular baffles were analytically calculated the values of partial heat transfer coefficient for air α , using eq. (4) for transient flow regime and eq. (5) for turbulent regime. It was admitted $\varepsilon=1.15$ for the ratio $H_1/d_i=23.1$, where d_i is the inner diameter of the inner tube [15].

$$\frac{Nu}{Pr^{0.43} \cdot \left(\frac{Pr}{Pr_p}\right)^{0.25}} = -9.214 + 5.964 \cdot 10^{-3} \cdot Re - 1.786 \cdot 10^{-7} \cdot Re^2 \quad (4)$$

$$Nu = 0.018 \cdot \varepsilon_l \cdot Re^{0.8} \quad (5)$$

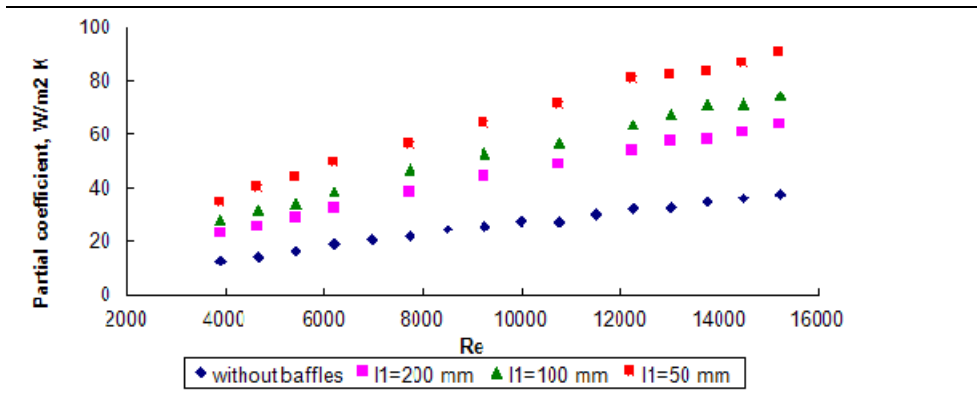


Figure 1. The variation of partial heat transfer coefficient for air vs. hydrodynamic regime in the presence of annular baffles

In Fig. 2 are comparatively presented the values of partial coefficient α analytically calculated and those established from experimental measurements. Lower values obtained from experimental measurements may be due to the existence of the lost heat.

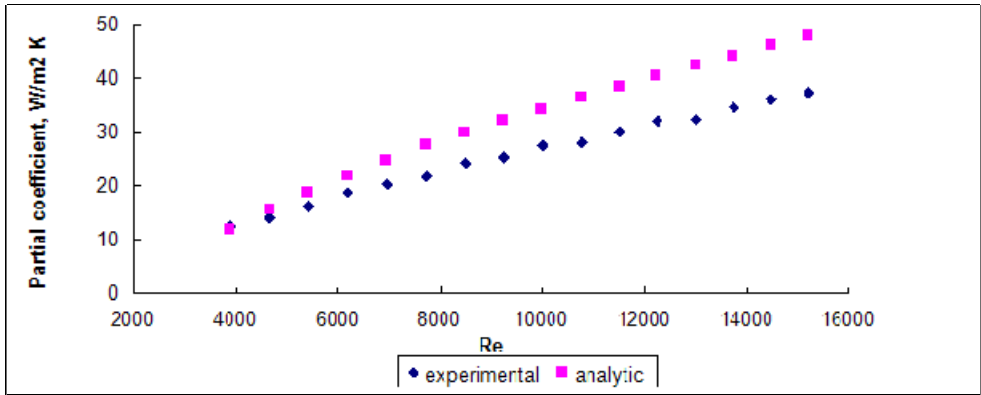


Figure 2. Analytical and experimental values for α in the absence of annular baffles

From the values of partial heat transfer coefficient experimentally determined were calculated the corresponding values of Nusselt number (Nu), both in the presence and absence of annular baffles. In the conditions of turbulent regime, from the $Nu=f(Re)$ dependence and admitting the value 0.8 for the exponent of Reynolds number in the relation $Nu=CRe^m$, the values of C constant were calculated.

The constant C is influenced by the geometrical dimensions of the baffles and, respectively, the ratio $l=\ l_1/\delta$. From Table 2 it is observed that the step reduction leads to the heat transfer intensification to the same hydrodynamic regime. From the measurements performed with a number of 3; 4; 6; 8 and 12 baffles, respectively, $20 \leq l \leq 80$, it was obtained that the constant C can be expressed in relation to the step, through the relationship $C=0.23(l/\delta)^{0.5}$.

Table 2. $Nu=f(Re)$ equations as a function of the annular baffles step

Step, mm	$Re > 10^4$	$Re < 10^4$	
	Eq. $Nu = C \cdot Re^{0.8}$	Eq. $Nu = a + b \cdot Re + c \cdot Re^2$	
200	$Nu = 0.027 \cdot Re^{0.8}$	$Nu = 6.9 + 3.8 \cdot 10^{-3} \cdot Re + 0.2 \cdot 10^{-8} \cdot Re^2$	
100	$Nu = 0.034 \cdot Re^{0.8}$	$Nu = 6.9 + 3.8 \cdot 10^{-3} \cdot Re + 0.2 \cdot 10^{-8} \cdot Re^2$	
50	$Nu = 0.051 \cdot Re^{0.8}$	$Nu = 5.7 + 7.6 \cdot 10^{-3} \cdot Re - 18 \cdot 10^{-8} \cdot Re^2$	
			R^2

In Fig. 3 are shown the values of Nu number calculated from the experimental values of the partial heat transfer coefficient, respectively, analytically calculated with equations derived above (Table 2), depending on the values of Re number ($Re > 10^4$). In the presence of annular baffles there is a great overlap between the two sets of values.

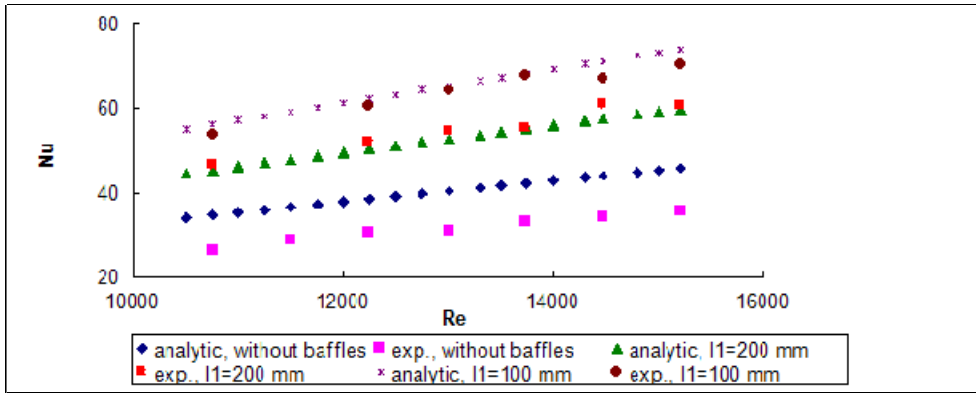


Figure 3. Analytical and experimental values of Nusselt number in the presence or absence of annular baffles, $Re > 10^4$

Fig. 4 shows the dependence $Nu=f(Re)$ calculated from experimental values, for air flow in transient regime. The corresponding equations are given in Table 2.

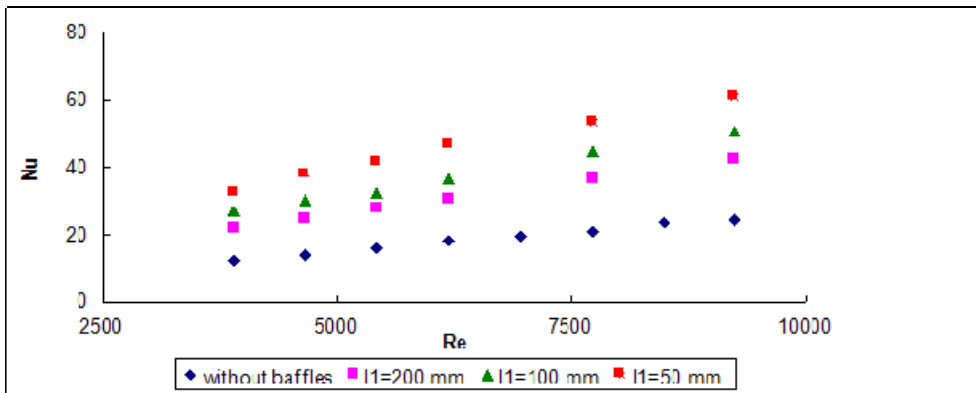


Figure 4. Experimental values of Nusselt number in the presence of annular baffles, $Re < 10^4$

Heat transfer intensification reflected by the ratio α_n/α_0 (n being the number of annular baffles, 0 the situation without baffles) is more effective the greater the number of turbulence promoters (decreases the step), regardless of flow regime. However, at the same l value, enhancing heat transfer is more pronounced when operating in transient flow regime, Fig. 5.

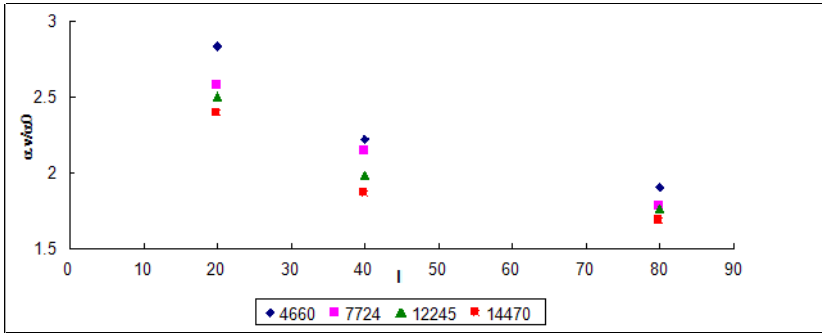


Figure 5. The dependence $\alpha_n/\alpha_0 = f(l)$ at different Re values

And if they were used copper spires with wire thickness $\delta=2.5$ mm as turbulence promoters, having the same winding step w_s (25 mm) but different lengths L (125 and 250 mm) and, respectively, the same length (250 mm) but different winding steps (25, 50 and 75 mm), it was found a benefic effect in terms of heat transfer to air. This fact is evidenced by the values evolution of air partial coefficient α depending on the hydrodynamic regime, Fig. 6a and 6b.

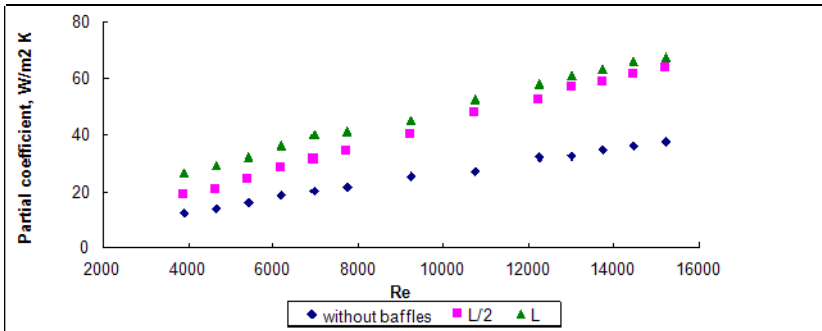


Fig. 6a

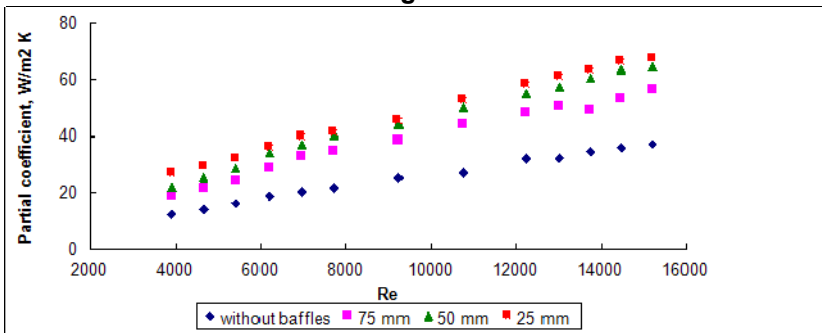


Fig. 6b

Figures 6a, b. The dependence $\alpha=f(Re)$ for spires with different: a) lengths; b) winding steps

The percentage increase in total heat transfer coefficient K , in each of the analyzed cases is shown in Fig. 7.

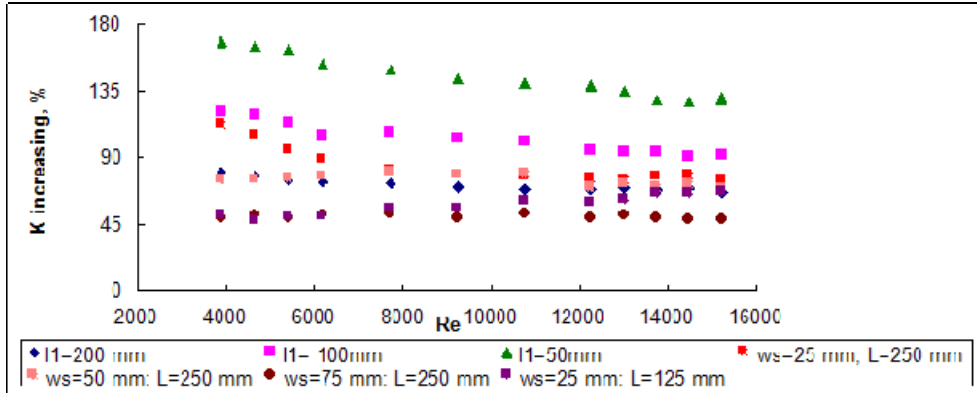


Figure 7. The increasing of the total heat transfer coefficient in the presence of turbulence promoters

CONCLUSIONS

Based on the information from literature on the role of turbulence promoters on the intensification of heat transfer with fluids flowing in transient and turbulent regime, a double pipe heat exchanger was designed and made, with annular or spiral baffles inside the inner pipe that caused a more efficient "mixing" of the hot fluid.

In all the analyzed cases, the air rate flow increasing leads to the decrease of the difference between the air temperature at the top and bottom of the inner pipe.

The heat received by the air Q_2 , the partial coefficient α and, respectively, the total heat transfer coefficient K increase with the air rate flow increasing and are higher in the presence of turbulence promoters.

In the case of annular baffles, the heat transfer to the air is more effective since their number is higher (total heat transfer coefficient increases between 60 and 160 %).

And the presence of spiral baffles on the air path has a benefic effect in terms of heat transfer intensification to it. The intensification of heat transfer in this case is influenced by both the length and the winding step of the spires used. However, in the experiments conducted under these conditions, the use of spires led to more modest results than those obtained when using annular baffles.

EXPERIMENTAL SECTION

The heat exchanger used is made of pipes with the following dimensions: the copper inner pipe-diameter $d = 28 \times 1 \text{ mm}$, height $H_1 = 600 \text{ mm}$, the outer pipe-diameter $D = 49 \times 1.5 \text{ mm}$, height $H = 580 \text{ mm}$. The inner tube is equipped with an additional part of 450 mm length to stabilize air flow. The turbulence promoters of the inner pipe were rings with dimension $25 \times 2 \text{ mm}$ placed at different distances (steps) or spires with different winding step and lengths. Both types of promoters were made of copper wire with a diameter $\delta = 2.5 \text{ mm}$.

The heat exchanger is vertically positioned. The air enters on the base of the inner pipe where is ensured its flow regulation and measurement. The heat required for the air warming is delivered by the hot water circulating through the annulus and is transmitted through the cylindrical surface of tubular wall. The air temperature was measured with thermometers placed at the top and bottom of the pipe.

The hot water from the annulus is provided by a thermostat and moves upward, being recycled with a constant rate flow of $0.145 \text{ m}^3 \cdot \text{h}^{-1}$. Its temperature was measured both at the entrance (constant value 65°C) and exit of the annulus, the water cooling has not been greater than 1°C . Experiments were performed at air flow rates from 5 to $20 \text{ m}^3 \cdot \text{h}^{-1}$, providing both a turbulent and transient flow.

Table 3 presents a set of experimental measurements in the case of annular baffles ($l_1 = 100 \text{ mm}$).

Table 3. Experimental data for annular baffles ($l_1 = 100 \text{ mm}$)

Air flow rate, $\text{m}^3 \text{ h}^{-1}$	Air temperature, $^\circ\text{C}$		Water temperature, $^\circ\text{C}$		$(\Delta t)_{air}$, $^\circ\text{C}$	Δt_{med} , $^\circ\text{C}$
	bottom	top	bottom	top		
5	26.5	50.0	65	64.5	23.5	24.9
6	28.0	49.5			21.5	24.7
7	29.5	49.0			19.5	24.5
8	30.0	49.0			19.0	24.3
10	31.0	49.0			18.0	23.9
12	32.5	49.0			16.5	23.3
14	34.5	49.0			14.5	22.5
16	35.0	49.0			14.0	22.3
17	36.0	49.5			13.5	21.5
18	37.0	50.0			13.0	20.8
19	38.0	50.0			12.0	20.4
20	39.0	50.5			11.5	19.7

REFERENCES

1. I.G. Carabogdan, A. Badea, L. Ionescu, A. Leca, V. Ghia, I. Nistor, I. Cserveny, "Instalatii termice industriale", Cap.1,3, Ed. Tehnica, Bucuresti, **1978**.
2. F. Chiriac, A. Leca, M. Pop, A. Badea, L. Luca, N. Antonescu, D. Peretz, "Procese de transfer de caldura si de masa in instalatiile industriale", Cap. 10, Ed. Tehnica, Bucuresti, **1982**.
3. A. Gupta, M. Uniyal, *J. Mech. Civ. Eng.*, **2012**, 1, 14.
4. M. Legay, N. Gondrexon, S. Le Person, P. Boldo, A. Bontemps, *Int. J. Chem. Eng.*, **2011**, DOI: 10.1155/2011/670108.
5. D.G. Kumbhar, N.K. Sane, "Enhancement in a Circular Tube Twisted with Swirl Generator" in *Proc. of 3rd Int. Conference on Advances in Mechanical Engineering*, India, **2010**, 188.
6. O. Floarea, G. Jinescu, "Procedee intensive in operatiile unitare de transfer", Cap. 3, Ed. Tehnica, Bucuresti, **1975**.
7. V. Kumar, V. Shirke, K.D.P. Nigam, *Chem. Eng. J.*, **2008**, 139, 284.
8. M. Gavrilescu, R.Z.Tudose, *Acta Biotechnol.*, **1995**, 15, 3.
9. Y. Ding, H. Chen, L. Wang, C-Y. Yang, Y. He, W.Yang, W.P. Lee, L. Zhang, R. Huo, *KONA*, **2007**, 25, 23.
10. X-Q. Wang, A.S. Mujumdar, *Int. J. Therm. Sci.*, **2007**, 46, 1.
11. D. Wen, G. Lin, S. Vafaei, K. Zhang, *Particuology* **2009**, 7, 141.
12. Y. Xuan, Q. Li, *Int. J. Heat Fluid Flow* **2000**, 21, 58.
13. P. Kumar, R. Ganesan, *Int. J. Civ. Environ. Eng.*, **2012**, 6, 385.
14. A. Tamas, S. Boran, *Studia UBB Chemia*, **2012**, LVII(4), 209.
15. C.F. Pavlov, P.G. Romankov, A.A. Noskov, "Procese si aparate in ingineria chimica-Exercitii si probleme", Cap. 4, Ed. Tehnica, Bucuresti, **1981**.

*Dedicated to Professor Liviu Literat
On the occasion of his 85th birthday*

STRUCTURAL FT-IR AND ¹³C CP/MAS NMR INVESTIGATION OF NATIVE STARCH WITH PLASTICIZERS BEFORE AND POST EXTRUSION PROCESS

ONUC COZAR^{a,b,*}, NICOLAE CIOICA^b, CLAUDIU FILIP^c,
CONSTANTIN COȚA^b, XENIA FILIP^c

ABSTRACT. Structural aspects of native corn starch samples with plasticizers are investigated by FT-IR, ¹³C CP/MAS NMR and XRD methods before and after extrusion process. The crystalline A, B and V – types structural phases prevail before extrusion in the prepared samples. The amorphous phase becomes dominant in both recent prepared formula and control specimen sample after extrusion.

Keywords: starch, extrusion, FT-IR, CP/MAS NMR, XRD

INTRODUCTION

Starch in one most studied biopolymers and many structural aspects involving the arrangement of the two component molecules, amylose and amylopectin, inside native starch granules and starchy materials are strongly investigated in the last years [1-4]. The both component molecules consist of $\alpha(1-4)$ linked D-glucose units, amylose being essentially linear, whereas amylopectin is a highly branched polymer due to 5-6% of $\alpha(1-6)$ links [3].

The native starch has a granular structure with an internal architecture characterized by concentric rings representing semi-crystalline shell (thickness 120-400nm) separated by essentially amorphous regions. There is much

^a Academy of Romanian Scientists, Splaiul Independentei 54, 050094, Bucharest, Romania

^b National Institute of Research – Development for Machines and Installations designed to Agriculture and Food Industry - INMA Bucuresti – Cluj-Napoca Branch, RO-400458 Cluj-Napoca, Romania

^c National Institute for Research and Development of Isotopic and Molecular Technologies, 65-103 Donath, 400293 Cluj-Napoca, Romania

* Corresponding author: onuc.cozar@phys.ubbcluj.ro

evidence that the semi-crystalline shells consist of regular alternating amorphous and crystalline lamellae repeating at 9-10 nm. In this structural organization, parallel double helices of amylopectin side chains are assembled into radially oriented clusters [4].

The amylose to amylopectin ratio influences strongly the physical-chemical characteristics and properties of starch, as viscosity, gelation power, adhesion etc [5].

The vibrational spectroscopic techniques, such as IR spectroscopy and Raman spectroscopy are successfully used in the quantitative investigation of control analysis of starch for the food industry, characterization of some medical polysaccharides and quantitative investigation of amylose and amylopectin content in different starch samples [6-11].

The vibrational spectroscopies were also used to investigate the retrogradation and gelation processes of some types of starches [6-8] and for characterization of some medical polysaccharides, including amylose and amylopectin [12].

Beside the vibrational methods the nuclear magnetic resonance (NMR) spectroscopy, especially nuclear magnetic relaxation method is a powerful method for studying the morphology, compatibility, chain conformation and dynamics of polymer systems [13-16].

NMR is sensitive to short-range order and according to the theory of NMR signals developed by Kulagina et al. [13] is possible by the analysis of NMR line area to determine the fractions of crystalline and amorphous phases in solid biodegradable polymers.

According with this method, the cross-polarization magic-angle spinning NMR (CP/MAS NMR) technique is also successfully used to crystallinity degree evaluation by inspecting the width of the resonance lines [7, 17-19].

Thermoplastic extrusion is a thermo-mechanical processing used to disrupt and transform the semi-crystalline structure of starch granules to form a homogeneous and amorphous material. This transformation is usually accomplished by small amounts of molecular substances commonly known as plasticizers. The most used plasticizers are water, a volatile plasticizer and glycerol, a non-volatile plasticizer [20, 21].

The plasticizing – antiplasticizing effects of water and glycerol contents on starch samples and also the amylose / amylopectin ratios were recently investigated by various methods [4, 9, 16, 20].

The following samples, blend formula (68% native starch, 17% glycerol, 15% water) before extrusion (a), extruded (previous blend (a) formula) sample (b) and a control extruded specimen (c) were investigated by FT-IR and ¹³C CP/MAS NMR spectroscopy in order to establish the prevalence of crystalline or amorphous domains after the extruding process.

RESULTS AND DISCUSSION

Fig.1. shows the IR spectra of the blend formula (a) and extruded starch samples (b, c). The two bands from 3300 cm^{-1} and 1650 cm^{-1} are ascribed to water stretching and bending vibrations and also to different OH groups present in starch and glycerol molecules [7, 8]. The other absorptions are originated from the vibrational modes of the amylose and amylopectin, the principal components of starch [7].

Thus the two absorption bands from at 2930 cm^{-1} and 2860 cm^{-1} are assigned to vibrations of CH_2 groups [7]. The absorptions from 1338 cm^{-1} region are due to bending modes of O-C-H, C-C-H and C-O-H angles from amylose and amylopectin formations [22].

The strong absorption peaks appeared in the $1150 - 900\text{ cm}^{-1}$ region are assigned to C-C and C-O stretching vibrations [23]. The bands from 1000 cm^{-1} region are sensitive to changes in crystallinity and the intensity of 1000 cm^{-1} band determines the orientation in intermolecular H – bonding of CH and CH_2 in CH_2OH [7, 24].

The band from 1106 cm^{-1} of the sample (a) is characteristic for glycerol and assigned to C-O stretching vibrations [25, 26]. As it is suggested by NMR spectrum of this sample (^{13}C line from 64 ppm) a complex between native starch and glycerol stabilized by hydrogen bonds appears. The disappearance of this band after extrusion may be due to the homogenization of the structural network.

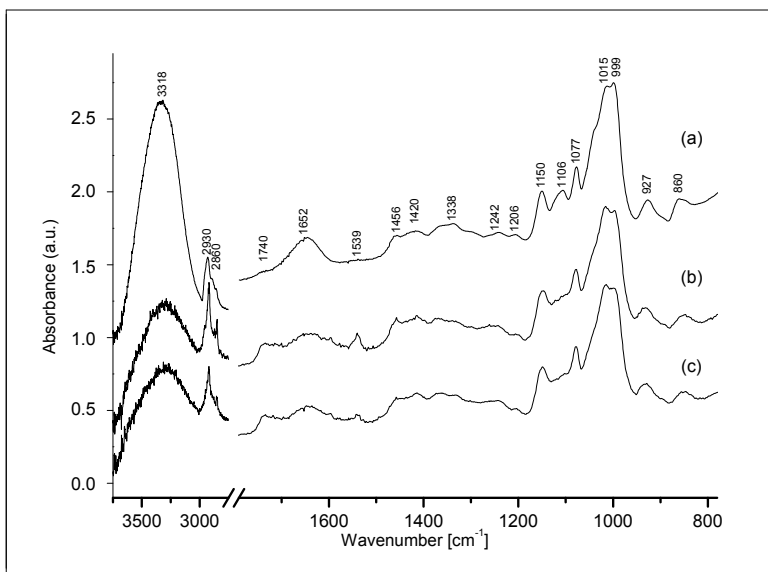


Figure 1. FT-IR spectra of blend formula before (a) and after extrusion (b) and of a control extruded specimen sample (c).

Many correlations between changes in the some band intensities from the 1000 cm^{-1} region ($994, 1000, 1022, 1040, 1047, 1053\text{ cm}^{-1}$) and the crystalline and amorphous phases (forms) of different starches are given in papers [4, 7, 9].

According to Capron et al. [4] the intense absorption from 998 cm^{-1} may be assigned to hydrated crystalline domains whereas the band at 1015 cm^{-1} reveals the amorphous contribution of plasticizers in starch formulas.

By analyzing the IR spectra (Figs. 1a, 2a) of blend formula before extrusion results that 999 cm^{-1} band correlated with crystalline domains is more intense than the 1015 cm^{-1} band characteristic of amorphous starch samples.

In the same time it can be observed (Figs. 1, 2b, c) that for extruded samples, the 1015 cm^{-1} band is more intense than 999 cm^{-1} band, thus resulting that in extruded starch samples (obtained by us (b) and control specimen (c)) the amorphous domains prevail.

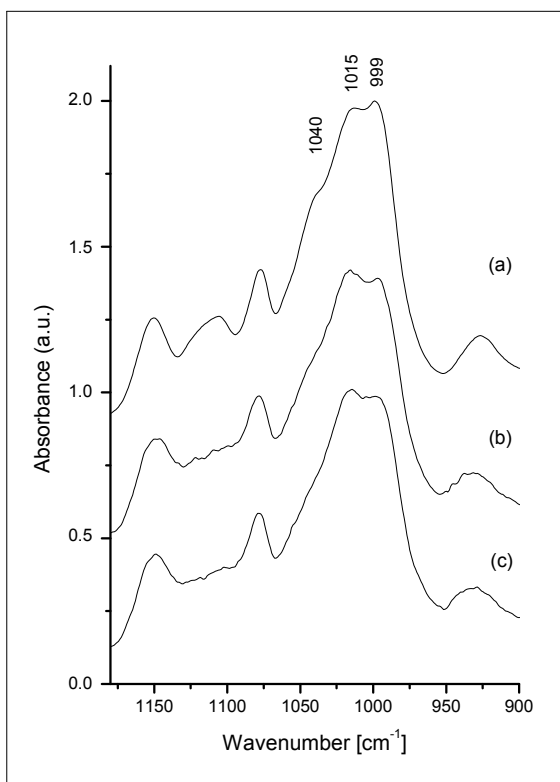


Figure 2. Extended 1000 cm^{-1} regions of the IR spectra shown in Figure 1.

The appearance of the weak band at 1539 cm^{-1} in Fig. 1b, c may be assigned to C-O vibrations from conjugated carbonyl and carboxyl groups after extruding or cooking processes (associated to the retrogradation in maize tortillas) of starch samples [7]. This fact may be ascribed to the partial amylose separation of amylopectin after the thermal treatment (gelatinization and retrogradation) of starch and also to the stress during extrusion process [2].

^{13}C CP/MAS NMR spectra of the investigated samples are shown in Fig. 3. The structural crystalline behavior of a starch granule is due to amylopectin, but also to the amylose/amylopectin ratio. According to Thérien-Aubin and Zhu [19], there are three types of crystalline starch structures: A, B, which are both formed by double helices of amylose and amylopectin, and V-type, composed of single helices.

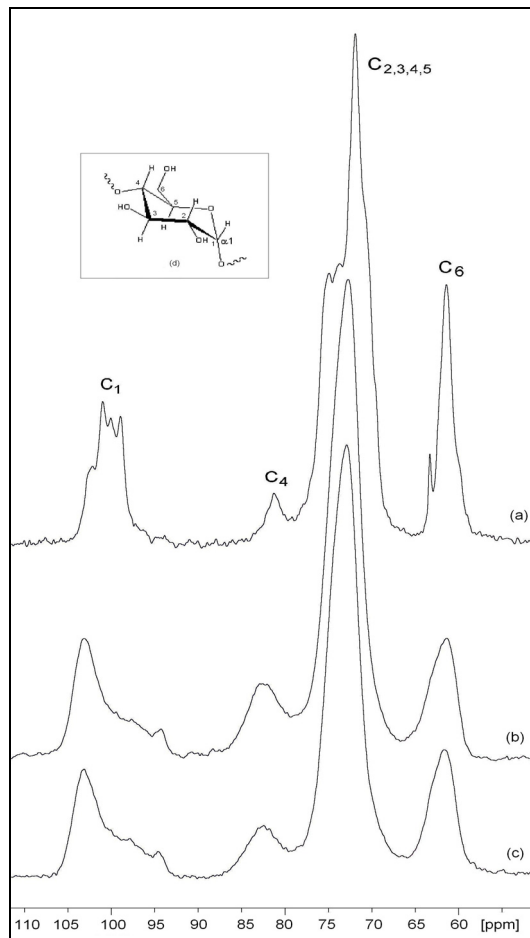


Figure 3. ^{13}C CP/MAS NMR spectra of blend formula before (a) and after extrusion (b) and of a control extruded specimen (c) recorded at room temperature and 14 kHz spinning speed. The insert (d) represents the chemical structure of $\alpha(1-4)$ glucopyranose.

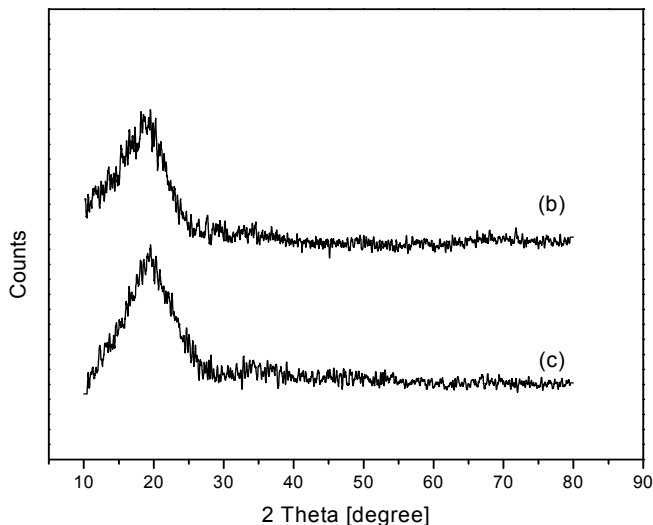


Figure 4. X-Ray Diffractograms of extruded samples (b, c).

Solid-state NMR spectroscopy, in particular ^{13}C CP/MAS NMR, is accurately used in distinguishing these three structural motifs (phases) [7,17-19]. Also, the degree of crystallinity can be easily probed by inspecting the shape and the width of the NMR resonance lines.

The most pronounced crystalline behavior is put in evidence in the spectrum of sample (a), blend formula (65% native starch, 17% glycerol, 15% water) before extrusion (Fig 3a). Thus, the ^{13}C CP/MAS spectrum of this sample shows the major presence of A, B and V- types of crystalline structures. In the region of the characteristic C_1 NMR resonance (glucose units [19]), an overlap of the triplet centered around 101 ppm specific to the A type – crystalline former with a doublet at 101 ppm characteristic of B type crystalline structure and a singlet at 104 ppm for the V- type structure appears.

The strong $\text{C}_{2,3,4,5}$ quadruplet signal from 73 ppm is also characteristic of A – type phase. We mention also that in the intense C_6 absorption region (62 ppm) the contributions of A, B, and V – types crystalline phases manifest, too.

The sharp ^{13}C line from 64 ppm belongs to glycerol, and suggest the formation of a complex between native starch and glycerol, most probably stabilized by hydrogen bonds.

The presence of a small amorphous phase in this sample (a) is suggested by the weak and broad NMR resonances at 104 ppm (C_1), 83 ppm (C_4) and 61 ppm (C_6).

In contrast with these results, the (b) and (c) NMR spectra of the extruded samples show the domination of the amorphous phase character. Both spectra are similar with ^{13}C CP/MAS NMR spectra reported by other authors for amorphous starch samples [18, 19].

The prevalence of amorphous domains after the extrusion suggested by IR and ^{13}C CP/MAS NMR data is also confirmed by XRD patterns (Fig.4) of extruded samples (b, c).

The absence of sharp peaks in the diffraction pattern of the extruded samples shows only the amorphous character without any crystalline form [27].

EXPERIMENTAL SECTION

The normal corn starch used in this study was obtained from SC Amylon Sibiu, Romania, having an water content on wet basis (wt.b) of 10.76 %, a density of 0.561 g/cm^3 and an amylose content of 21%. The glycerol used in formulas was purchased from SC Nordic Invest SRL Cluj Napoca and had a concentration of 99.5% and a density of 1.262 g/cm^3 . The water used was from the water supply system.

FT-IR/ATR spectra were recorded at room temperature on a conventional Equinox 55 (Bruker, Germany) spectrometer equipped with a DTGC detector, coupled with an ATR sampling device (Miracle, Pike Techn.). The resolution was of 2 cm^{-1} .

^{13}C solid state cross-polarization magic-angle-spinning (CP/MAS) NMR spectra were recorded on a Bruker Avance III wide-bore spectrometer operating at 500 MHz Larmor frequency for ^1H , and 125 MHz for ^{13}C , respectively, using a 4 mm double resonance probehead. Standard ^{13}C CP/MAS experiments were performed at room temperature, using a spinning frequency of 14 kHz and a ^1H 90° pulse of $2.3\ \mu\text{s}$. The spectra were acquired under two-pulse phase-modulated (TPPM) ^1H decoupling at 100 kHz by averaging 4000 scans, with a recycle delay of 5 s, and a 2 ms contact pulse. ^{13}C CP/MAS spectra are calibrated according to the $^{13}\text{CH}_3$ line in TMS through an indirect procedure which uses the carboxyl NMR line in α -glycine.

A laboratory twin-screw extruder with co-rotating intermeshing, self-wiping screws ZK 25, Collin, Germany) was used to conduct the extrusions. The extruder has 25 mm screw diameter, 30:1 length to diameter ratio, max. 400 rpm screw speed and six independent electric heating and cooling areas.

The starch was fed into the extruder hopper with a twin-screw volumetric feeder, DSV 020D, Definitive Inovation, Italy.

The dosing pump used to feed the plasticizers from the plasticizers tank was a peristaltic pump SP 311/12, VELP, Italy.

The plasticizers were added into the working area through a pipe connection located at 170 mm from axis of the supply hopper.

The screw speed was set at 150 rpm and the barrel temperatures were maintained during the experiment at 30, 50, 80, 100 and 120 °C, respectively, from the feeding port to the die section.

A circular die plate with one hole was used. The diameter of the hole in the die is 3 mm.

The extruding product was collected and cooled to room temperature. Each experimental samples were taken after the extruder had reached steady state.

X – ray diffractograms were obtained with a Bruker D8 Advanced X – ray diffractometer with a graphite monochromator for Cu - K α radiation with $\lambda = 1.54 \text{ \AA}$.

CONCLUSION

Both amorphous and crystalline structural phases are present in various proportions in the investigated starch samples.

The crystalline structural phases (A, B, V – types) prevail in the blend formula (68% native starch, 17% glycerol, 15% water) before extrusion.

After extrusion process the amorphous phase becomes dominant in both, recent prepared formula and control specimen sample.

ACKNOWLEDGMENTS

This work was supported by CNCSIS – UEFISCDI, project PN II-IDEI code 284/2011.

REFERENCES

1. M.R. Almeida, R.S. Alves, L.B.L.R. Nascimbem, R. Stephani, R.J. Poppi, L.F.C. de Oliveira, *Anal. Bioanal. Chem.*, **2010**, 397, 2693.
2. H. Liu, F. Xie, L. Yu, L. Chen, L. Li, *Progress in Polymer Science*, **2009**, **34**, 1348.
3. A. Buléon, P. Colonna, V. Planchot, S. Ball, *Int. J. Biol.Macromol.*, **1998**, 23, 85.
4. I. Capron, P. Robert, P. Colonna, M. Brogly, V. Planchot, *Carbohydrate Polymers*, **2007**, 68, 249.
5. E.R. Daiuto, M.P. Cereda, L.J.C.B. Carvalho, *Braz. J. Food Technol.*, **2002**, 5, 217.
6. P.M. Fechner, S. Wartewig, P. Kleinebudde, R.H.H. Neubert, *Carbohydrate Research*, **2005**, 340, 2563.

7. A.F. Morales, M.J. Estrada, R.M. Escobedo, *Carbohydrate Polymers*, **2012**, *87*, 61.
8. K. Iizuka, T. Aishima, *J. Food Science – Chemistry / Biochemistry*, **1999**, *64*, 653.
9. N. Katayama, M. Kondo, M. Miyazawa, *J. Molec. Struct.*, **2010**, *974*, 179.
10. O. Cozar, C. Cota, N. Cioica, E.M. Nagy, L. Tibre, *Studia UBB Chemia*, **2012**, *57*, 23.
11. O. Cozar, C. Filip, N. Cioica, C. Cota, C. Tripon, E.M. Nagy, *Processes in Isotopes and Molecules (PIM 2013)*, *AIP Conf. Proc.*, **2013**, 1565, 39;
DOI: 10.1063/1.4833692.
12. R.G. Zhabankov, S.P. Firsov, E.V. Korolik, P.T. Petrov, M.P. Lapkovski, V.M. Tsarenkov, M.K. Marchenwka, H. Ratajczak, *J. Mol. Struct.*, **2000**, *555*, 85.
13. T.P. Kulagina, P.S. Manikin, G.E. Kamaukh, L.P. Smirnov, *Russ. J. Phys. Chem. B*, **2011**, *5*, 674.
14. K. Tananuwong, D. S. Reid, *Carbohydr. Polym.*, **2004**, *58*, 345.
15. Yu. B. Grunin, L. Yu. Grunin, E. A. Nikol'skaya, V. I. Talantsev, *Polym. Sci., Ser. A*, **2012**, *54*, 201.
16. N. Cioica, R. Fechete, C. Cota, E.M. Nagy, L. David, O. Cozar, *J. Molec. Struct.*, **2013**, *1044*, 128.
17. Fl. H. Larsen, A. Blennow, S. B. Engelsen, *Food Biophys.*, **2008**, *3*, 25.
18. S. Wang, J. Yu, Q. Zhu, J. Yu, F. Jin, *Food Hydrocolloids*, **2009**, *23*, 426.
19. H. Therien-Aubin, X.X. Zhu, *Carbohydrate Polymers*, **2009**, *75*, 369.
20. I. Tan, C.C. Wee, P.A. Sopade, P.J. Halley, *Carbohydr. Polym.*, **2004**, *58*, 191.
21. R. Kizil, J. Irudayaraj, K. Seetharaman, *J. Agric. Food Chem.*, **2002**, *50*, 3912.
22. V. Bellon-Maurel, C. Vallat, D. Goffinet, *Appl. Spectroscopy*, **1995**, *49*, 556.
23. R.H. Wilson, P.S. Belton, *Carbohydr. Res.*, **1988**, *180*, 339.
24. M. Kacurakova, Mathlouthi, *Carbohydrate Res.*, **1996**, *284*, 145.
25. P. Huang, A. Dong, W.S. Caughey, *J. Pharm. Sciences*, **1995**, *84*, 387.
26. A. Mudalige, J.E. Pemberton, *Vibr. Spectroscopy*, **2007**, *45*, 27.
27. E. Corradini, A.J.F. de Carvalho, A.A.S. Curvelo, J.A.M. Agnelli, L.H.C. Mattoso, *Materials Research.*, **2007**, *10*, 227.

STUDIA UBB CHEMIA, LVIII, 4, 2013 (p. 285)
(RECOMMENDED CITATION)

==ERRATUM==

STUDIA UBB CHEMIA, Volume 58 (LVIII), 3, 2013 (pp. 7-18)

http://www.studia.ubbcluj.ro/arhiva/abstract_en.php?editie=CHEMIA&nr=3&an=2013&id_art=11928

The article entitled "DYNAMIC MODELING OF CARBONATOR FROM CALCIUM-LOOPING PROCESS USED FOR CARBON CAPTURE", Authors Ana-Maria Cormos and Abel Simon, was withdrawn based on authors' request.